UNIVERSITY OF
BIRMINGHAM

GAS PHASE VACUUM-ULTRAVIOLET (VUV) SPECTROSCOPY OF SMALL HALOGENATED POLYATOMIC MOLECULES

by

SAHANGIR ALI

A thesis submitted to
The University of Birmingham
for the degree of
DOCTOR OF PHILOSOPHY

School of Chemistry
The University of Birmingham
Birmingham
B15 2TT

March 2007

ABSTRACT

The work carried out in this thesis is concerned with photoexcitation of small and halogenated molecules in the gas phase with vacuum-ultraviolet (VUV) radiation. For all the experiments described in this thesis, the source of radiation was from tuneable VUV radiation from a synchrotron source. The majority of the experiments used the UK national source located at Daresbury Cheshire.

Fluorescence spectra were taken using the newly commissioned Wadsworth monochromator on beamline 3.1 of the Daresbury synchrotron radiation source. Dispersed fluorescence spectra were taken using a newly developed fluorescence apparatus incorporating a multi-channel CCD detection system. One of the objectives of this thesis is to compare the sensitivity and resolution of this new system with that of an apparatus used at the BESSY 1 synchrotron source in the 1990s. Many of the molecules studied here were chosen because previous data recorded at BESSY 1 were available for this comparison.

Molecules studied include the MCl_4 series (M = C, Si and Ge) where both the VUV photoabsorption and fluorescence spectra were recorded. A new analysis of the absorption spectra is presented. Emissions are observed in MCl_2, MCl and the parent ion of $SiCl_4^+$ and $GeCl_4^+$. The CF_3X series (X = H, F, Cl, Br, I and SF_5) have been studied and fluorescence spectra and some photoabsorption spectra were recorded. Emissions are observed in CF, CF_2, CF_3 and the ions CF_4^+, CF_3H^+. Undispersed and dispersed fluorescence spectra of BX_3 (X = F, Cl and Br) were also recorded. Emission was observed in BX_2, BX and the parent ion BX_3^+. Finally the fluorescence spectra of PX_3 (X = F, Cl and Br) were recorded and are presented here. Emission was observed in PX_2, PX and parent ion PX_3^+.

ACKNOWLEDGEMENTS

Firstly, I would like to thank my supervisor, Professor Richard Tuckett, for all his help and guidance during my PhD. I would also like to thank Dr Chris Howle for all his help during the early days of my PhD training. A special thank you goes to the other members of the Tuckett group Michael Parkes and Mathew Simpson. Their friendship and support both in Birmingham and at the Daresbury laboratory has been invaluable. All the Daresbury support staff and especially Dr David Shaw and Dr Andrew Malins also require a thank you.

I would like to thank all my friends and colleagues in Birmingham for making my time there both enjoyable and memorable. All the chemistry support staff, especially Stuart Arkless and Tony Rothin for their technical support.

I have to thank all my family, my brothers (Zahangir, Dosti, Jakir and Zubair), my sister (Fahima) and my mum, without their help and support this would not have been possible. My wife Milu for her constant encouragement and her tolerance of the many long runs at Daresbury. Finally, I would like to dedicate this thesis to two people who have left and came into my life during the course of my PhD, my father and my son Saji.

TABLE OF CONTENTS

CHAPTER 1 : INTRODUCTION

1.1 Primary excitation process

1.2 Secondary processes
    1.2.1 Radiative Processes
    1.2. 2 Non-radiative Processes

1.3 Energy sources
    1.3.1 Photon sources
        1.3.1.1 Lamp sources
        1.3.1.2 Synchrotron sources
        1.3.1.3 Lasers
    1.3.2 Non-Photon sources

1.4 Dispersing elements
    1.4.1 Prisms
    1.4.2 Diffraction gratings

1.5 Monochromators

1.6 Photodetectors

1.7 Experimental techniques in the VUV
    1.7.1 Absorption spectrsocopy
    1.7.2 Fluorescence spectroscopy
    1.7.3 Photoelectron spectroscopy
    1.7.4 Threshold photoelectron spectroscopy
    1.7.5 Photoionisation mass spectroscopy
    1.7.6 Coincidence spectroscopy

1.8 References

CHAPTER 2 : EXPERIMENTAL

2.1 Introduction

2.2 The new Wadsworth monochromator

2.3 Dispersed fluorescence apparatus
2.4 N_2 spectra
2.5 CO_2 spectra
2.6 Absorption apparatus
2.7 References

CHAPTER 3 : VUV ABSORPTION AND UNDISPERSED FLUORESCENCE EXCITATION SPECTROSCOPY OF CCl_4, $SiCl_4$ and $GeCl_4$

3.1 Introduction
3.2 Results
    3.2.1 CCl_4 Photoabsorption spectroscopy
    3.2.2 $SiCl_4$ Photoabsorption spectroscopy
    3.2.3 $GeCl_4$ Photoabsorption spectroscopy
3.3 Conclusions
3.4 References

CHAPTER 4 : VUV FLUORESCENCE SPECTROSCOPY OF CCl_4, $SiCl_4$ and $GeCl_4$

4.1 Introduction
4.2 Results
    4.2.1 CCl_4
    4.2.2 $SiCl_4$
    4.2.3 $GeCl_4$
4.3 Conclusions
4.4 References

CHAPTER 5 : VUV ABSORPTION AND UNDISPERSED FLUORESCENCE EXCITATION SPECTROSCOPY OF CF_3X (X=F, H, Cl and Br)

5.1 Introduction
5.2 Results
    5.2.1 CF_4

5.2.2 CF_3H
5.2.3 CF_3Cl
5.2.4 CF_3Br
5.3 Conclusions
5.4 References

CHAPTER 6 : VUV FLUORESCENCE SPECTROSCOPY OF CF_3X (X=F, H, Cl, Br and I)
6.1 Introduction
6.2 Results
6.2.1 CF_4
6.2.2 CF_3H
6.2.3 CF_3Cl
6.2.4 CF_3Br
6.2.5 CF_3I
6.3 Conclusions
6.3 References

CHAPTER 7 : VUV FLUORESCENCE SPECTROSCOPY OF SF_5CF_3
7.1 Introduction
7.2 Experimental
7.3 Results
7.3.1 Photoabsorption spectrum
7.3.2 Total fluorescence yield
7.3.3 Dispersed fluorescence
7.4 Discussion
7.5 Conclusions
7.6 References

CHAPTER 8 : VUV FLUORESCENCE SPECTROSCOPY OF BF_3, BCl_3 and BBr_3
8.1 Introduction
8.2 Results
8.2.1 BF_3
8.2.2 BCl_3
8.2.3 BBr_3

8.3 Conclusions
8.4 References

CHAPTER 9 : VUV FLUORESCENCE SPECTROSCOPY OF PF_3 and PCl_3

9.1 Introduction
9.2 Results
    9.2.1 PF_3
    9.2.2 PCl_3
9.3 Conclusions
9.4 References

CHAPTER 10 : CONCLUSIONS

1. Introduction

The work carried out in this thesis is concerned with photoexcitation of small and halogenated molecules in the gas phase with vacuum-ultraviolet (VUV) radiation. Such radiation has a wavelength range between 50 and 200 nm (*ca.* 6 – 30 eV) in the electromagnetic spectrum. For all the experiments described in this thesis, the source of radiation was from tuneable VUV radiation from a synchrotron source. The majority of the experiments used the UK national source located at Daresbury Cheshire, but some experiments were performed using the BESSY 1 source in Berlin. There are seven sections in this introductory chapter. First, the primary excitation process following absorption of a VUV photon by a molecule is described. In the second section, we talk about the processes than can occur after absorption of a photon has occurred. The third section of this chapter deals with the energy sources used to perform experiments in the VUV. In the fourth section, the dispersion of this energy using different dispersing elements is described. In the fifth section, various types of monochromators which use dispersing elements to separate VUV radiation are described. The sixth section deals with photon detection. The final section of this chapter deals with experimental techniques in the VUV relevant to work carried out in this thesis.

1.1 Primary excitation process

In the hierarchy of interaction of electromagnetic radiation with gas phase molecules the primary excitation process comes first. Atoms and molecules may change states when they absorb specific amounts of energy. Atomic and molecular states are defined by the arrangement of electrons in orbitals. An electron in some orbital may be excited to a more energetic orbital by absorbing exactly one photon which has energy equal to the energy difference of the two orbitals. When the absorbed energy is less than the ionisation energy, the molecule may be excited to a discrete excited state. Fragmentation of a molecule can then occur either to form neutral or ionic pairs. If the excitation energy exceeds the ionisation energy of the molecule, ionisation can occur, with production of a photoelectron [1].

$$AB + h\nu \rightarrow AB^* \qquad \textbf{equation 1.1}$$

$$AB + h\nu \rightarrow AB^* \rightarrow A + B \qquad \textbf{equation 1.2}$$

$$AB + h\nu \rightarrow AB^* \rightarrow A^+ + B^- \qquad \textbf{equation 1.3}$$

$$AB + h\nu \rightarrow AB^+ + e^- \qquad \textbf{equation 1.4}$$

AB is a generic description of a molecule which may be polyatomic, hν is the photon energy with h being Planck's constant and ν being the frequency of the radiation. This absorption of energy, equation 1.1, is called the primary excitation process. Note that in equation 1.2 and 1.3, fragmentation may occur to ground or electronically excited states of the fragments A, B, A^+ and B^-.

Equation 1.1 can be called a resonant process because the quantisation of energy insures only a discrete amount of energy can be transferred to the molecule. A and B can be molecular fragments, ions or atoms and the star denotes electronic excitation. In an absorption spectrum a resonant or non-resonant process can be identified by the shape of the peak. A resonant peak will show a large increase in signal and reach a peak before receding back to the baseline. By contrast a non-resonant peak will show an increase in signal at the threshold, and the signal will plateau, but remain high for energies well in excess of the threshold energy. Equation 1.4 is an example of a non-resonant process where any excess energy above threshold is carried away by the photoelectron as kinetic energy.

Low-lying electronic states are normally referred to as valence states whereas higher-energy states, where an electron is promoted to an unoccupied orbital with a higher principal quantum number n, are called a Rydberg states. The distinction between these two classes of states is sometimes hard to make and it is difficult to note where one ends and the other one begins. Here the Rydberg state will be defined as one which, at least approximately, follows the Rydberg formula

$$E = IE - R_H / (n-\delta)^2 \quad \textbf{equation 1.5}$$

Here, E is the energy of the transition, IE is the vertical ionisation energy to which the Rydberg states converge, n is the principle quantum number of the Rydberg orbital, R_H is the Rydberg constant and δ is the quantum defect of the core. δ can be described as the deviation of the core from an impenetrable point charge [2].

1.2 Secondary processes

Following photoexcitation of the molecule AB one of many secondary processes can occur. They can either result in the emission of radiation in which case they are termed radiative, or involve some other form of energy transfer in which case they are termed non-radiative. Fluorescence and phosphorescence are two types of radiative secondary processes. There are many possible non-radiative processes that can occur including internal conversion, intersystem crossing and dissociation. Rarely do any of these processes happen exclusively, and competition between different channels is usually observed.

1.2.1 Radiative processes

When an excited state of a molecule or ion relaxes radiatively fluorescence or phosphorescence occurs. An electronic transition between two states of the same multiplicity is called fluorescence whilst a transition between states of different multiplicities is given the name phosphorescence.

Excitation: $AB + h\nu \rightarrow AB^*$ **equation 1.1**

Fluorescence / Phosphorescence (emission): $AB^* \rightarrow AB + h\nu$ **equation 1.6**

The selection rule $\Delta S = 0$ strictly renders phosphorescent transitions to be forbidden [3]. However, they can acquire intensity via spin-orbit coupling, but these processes occur on a longer timescale than fluorescence transitions which are allowed. The time scales for fluorescence and phosphorescence range from $10^{-6} - 10^{-9}$ and $10^{0} - 10^{-6}$ s, respectively.

1.2.2 Non-radiative processes

Electronic energy can be converted to vibrational energy via an intramolecular process with no change in total internal energy. This process, sometimes called electronic relaxation, can occur between states of the same multiplicity which is termed internal conversion (IC). If the process occurs between states of different multiplicities, it is called intersystem crossing (ISC). Under formal selection rules ISC can be considered a forbidden transition and therefore the rate of IC is expected to be greater than the rate of ISC. In practice the overlap of the vibrational wavefunctions of the individual electronic states is more important in determining the rate of the process.

Fragmentation of the excited states can also take place. Excitation into a dissociative state result in rapid dissociation and this can be regarded as being part of the primary excitation process. Dissociation may also take place when there is a large geometry change between the ground and excited states. As a consequence the Franck-Condon region is spread over high vibrational levels of the excited state which may lie above the dissociation limit. Pre-dissociation is another form of dissociation. Dissociation results from curve crossing of the initially excited state populated below its dissociation limit into a state populated above a different dissociation limit (figure 1.1). In this thesis, we observe many examples of fragment fluorescence following rapid dissociation or pre-dissociation of AB^*. In other words, dissociation of highly excited states of AB^* occurs to A^* or B^* which can then emit radiation via fluorescence as it decays to ground state A or B. Further details are given in section 1.7.

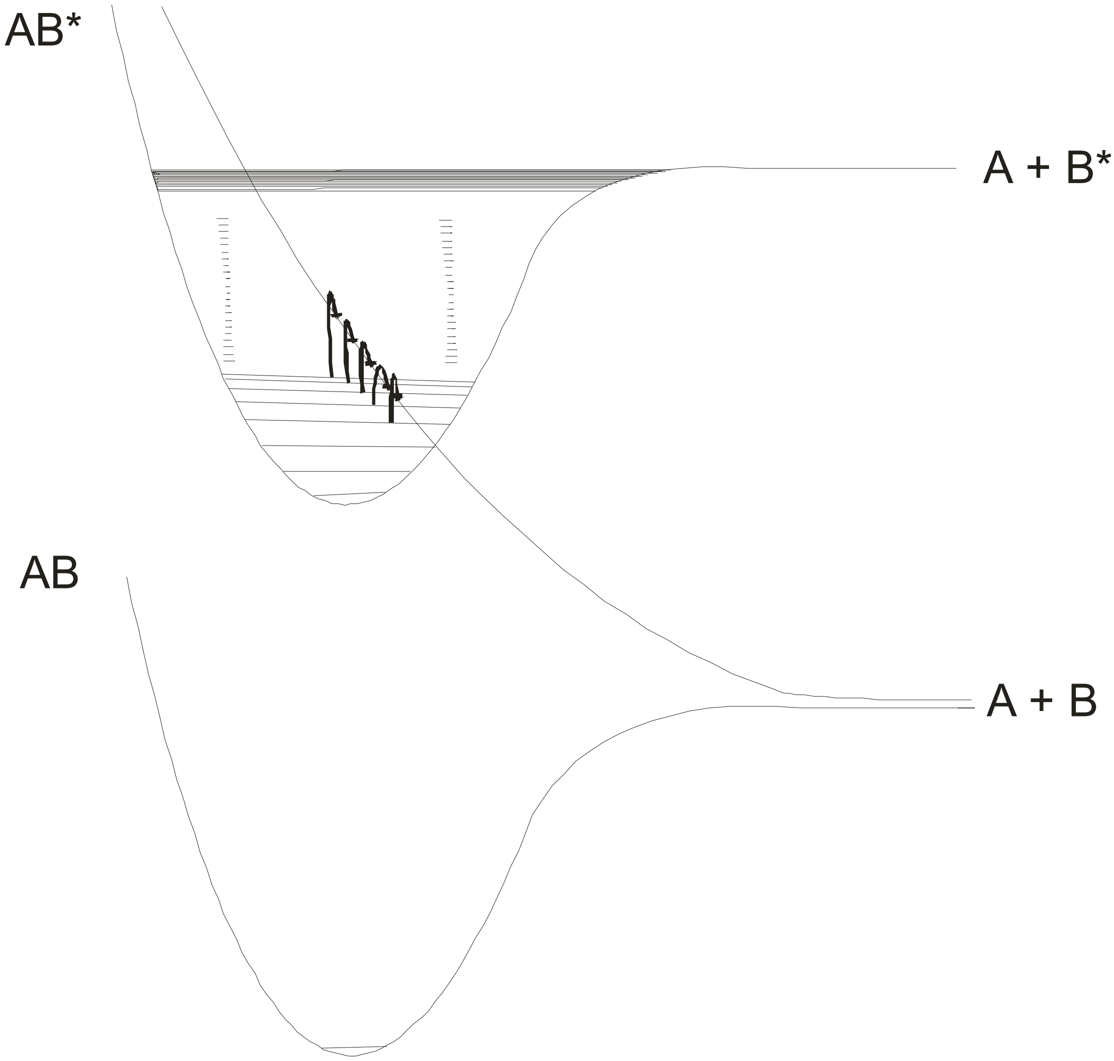

Figure 1.1 Diagram showing the process of pre-dissociation, Adapted from reference [7]

1.3 Energy Sources

There are a variety of excitation sources available to perform experiments in the VUV region of the electromagnetic spectrum. These sources can be divided into two categories, photon and non-photon sources.

1.3.1 Photon sources

1.3.1.1 Lamp sources

Gaseous discharge lamps are a family of light sources that generate light by passing an electric current through a gas. The hydrogen Lyman-α lamp is an example of a discharge line source. The lamp consists of a cylindrical quartz cell through which flows a mixture of 2 % H_2 in a He carrier gas. The gas is excited by a microwave discharge to produce the Lyman-α line ($n = 2 \rightarrow n = 1$ in atomic hydrogen, 121.59 nm or 10.195 eV). Line sources are produced from a transition between two bound states within an excited atom or molecule. An electrical discharge in a low pressure gas is used to provide the conditions which produce the radiation. The helium lamp is another very common line source. The helium lamp produces emission lines at 21.22 eV (He I) and 40.78 eV (He II). The He I line corresponds to the transitions between the excited state He ($1s^1\ 2p^1$) ^1P and the ground state He ($1s^2$) ^1S. At low pressure He^+ ions dominate and the He II emission line at 40.78 eV is produced. This line corresponds to the transition between the He^+ ($2p^1$) and the He^+ ($1s^1$) states. Other commonly used line sources include the Ar I, Xe I and the Ne I lamps [4].

Another type of lamp source is the continuum source; these are produced by a transition from a bound excited state of a molecule to a repulsive lower state. Continuum sources tend to be less intense than line sources and are only used when a large range of energies is required. The Hopfield continuum of helium is an example of such a continuum lamp. Its energy range extends from 11.8 eV to 20.6 eV.

1.3.1.2 Synchrotron radiation

Synchrotron radiation is the electromagnetic radiation emitted by charged particles that are moving in circular orbits at relativistic speeds in a magnetic field. It is the only real continuum source readily available as it emits radiation over a much wider energy range than discharge gas lamps. The energy range from a synchrotron source can span the whole electromagnetic spectrum. The total power emitted by a charged particle as it is accelerated through a path radius R is given by [5]

$$\text{Power} = \frac{2}{3c^7}\left(\frac{z^2E^4}{m^4R^2}\right)$$ **equation 1.7**

Here c is the speed of light, *R* is the radius of curvature, and *m*, *z* and *E* are the mass, charge and energy of the charged particle, respectively. In most synchrotron sources the electron is used for the charged particle, because it is easy to generate and has a high *z/m* ratio.

In such 'second generation' sources, electrons are injected into the storage ring at high energy where bending magnets maintain their orbit. The storage ring contains components such as magnets, insertion devices and radio frequency cavities, which respectively keep the electrons in their orbit, intensify the light beam produced by the electrons, and supply energy to the electrons to increase their energy. The circumference of the Daresbury ring is *ca.* 100 m. The universal synchrotron radiation is emitted tangentially to the circular motion of the electrons with a small horizontal angular divergence, *ca.* 15 milliradians, and energy-selected photon beams can be used for experiments. The radio-frequency cavity which replenishes the energy lost when radiation is emitted causes the electrons to bunch together. The radiation is linearly polarised in the plane of the ring, but becomes circularly polarised away from the horizontal plane. Ultra-high vacuum in the storage ring, *ca.* 10^{-10} mbar, minimises the scattering of electrons with background gas molecules. Lifetimes of such sources are typically 8-24 hours. The Daresbury source operates in two modes ; (a) multi-bunch mode where 160 electron bunches, 2 ns between bunches, are stored in the ring providing pseudo-continuous-wave radiation, and (b) single-bunch mode where only one bunch is in the ring, providing a temporal structure (pulse width *ca.* 0.2 ns and repitition rate *ca.* 3 MHz) for time-resolved experiments.

Thus SR is a continuous source of electromagnetic radiation covering the infrared through to the hard X-ray, and monochromators can be used to select the correct spectral region. The distribution of emitted radiation depends primarily on *E via* the critical wavelength, λ_c, which is given by

$$\lambda_c = 0.56R(m)/E^3$$ **equation 1.8**

The peak of the distribution occurs at $0.42\lambda_c$. Thus, lower values of *E* are needed for higher λ photons, and the best sources for VUV radiation occur with $E < 1$ GeV, whereas hard X-ray sources need larger values of *E*, typically > 5 GeV. Other factors that affect the intensity of the photon beam at the experiment include the beam current, the distance between the experiment and the tangent to the electron orbit, and the efficiencies of the beamline components. Insertion devices, such as multi-pole wigglers or multi-period undulators, produce SR of much greater intensity. They comprise arrays of magnets of alternating polarity where the electrons oscillate periodically, SR is emitted at each 'wiggle', and coherent interference leads to amplification. Undulators provide the majority of beamlines on the latest 'third-generation' sources such as Diamond, being built by the UK at the Rutherford and Appleton Laboratory and scheduled to open in 2007.

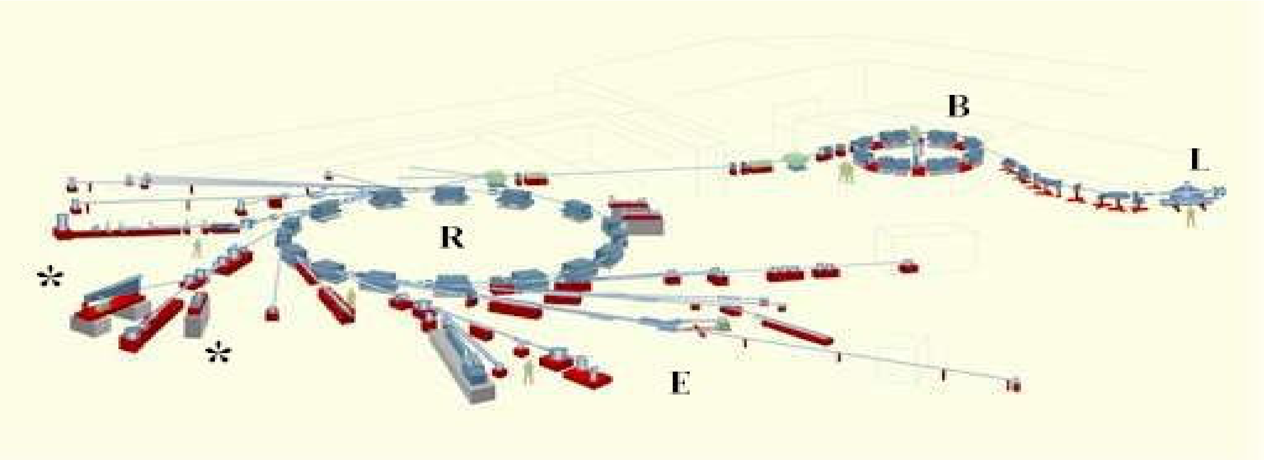

Figure 1.2 A schematic diagram of the Daresbury SRS taken from reference 6

1.3.1.3 Lasers

A Laser (Light Amplification by Stimulated Emission of Radiation) is an optical source that emits photons in a beam. Lasers are typically of high intensity, low divergence, highly monochromatic and coherent sources. These properties are not unique to lasers but their combination is most easily achieved in a laser. Highly monochromatic light can be obtained from a continuous source by filtering of the unwanted wavelengths by a grating monochromator. By doing this most of the light from the source may be rejected and the intensity will diminish. With lasers narrow bandwidths can be obtained with all of the light intensity concentrated into this narrow range. The laser action is based on stimulated rather than spontaneous emission. To obtain stimulated emission a population inversion of the electronic states of the lasing species has to be achieved [7].

A laser is composed of an active laser medium, or gain medium, and a resonant optical cavity. The gain medium is used to transfer external energy into the laser beam. The material used for the gain medium can be a solid, liquid or gas. The gain medium is energized, or pumped, by an external energy source. The pump energy is absorbed by the laser medium, putting some of its particles into high energy states. When the number of particles in one excited state exceeds the number of particles in some lower energy state, population inversion is achieved. In this condition, an optical beam passing through the medium produces more stimulated emission than the stimulated absorption so the beam is amplified. The stimulated emission is multi directional, but by placing the gain medium in a highly reflecting cavity, the direction of the beam can be controlled.

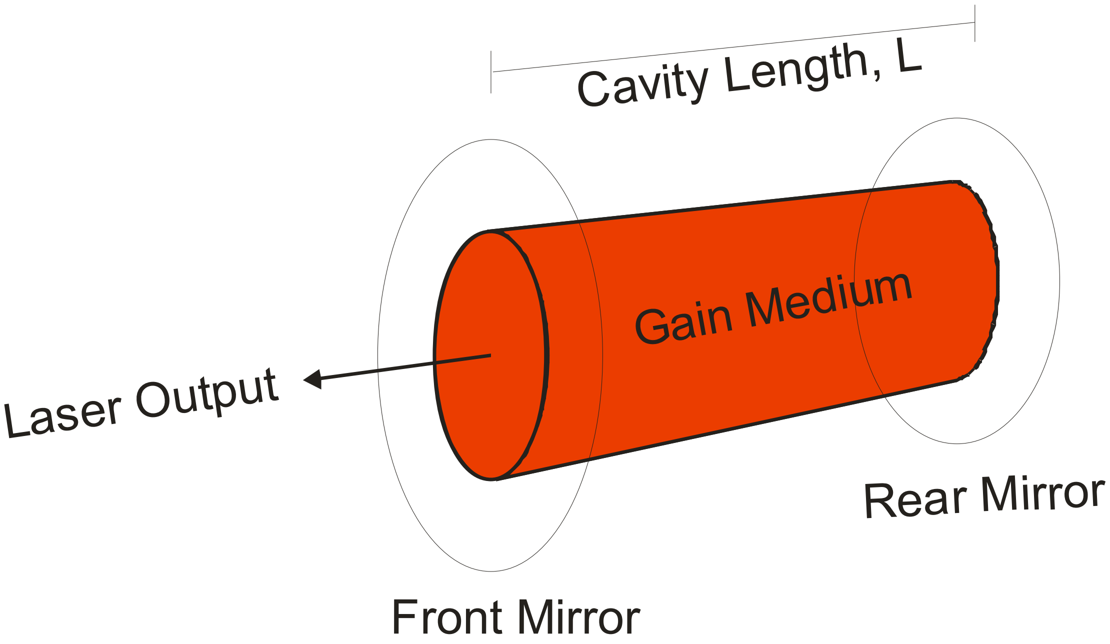

Figure 1.3 Principles of laser operation

There are many types of lasers available depending on the type of medium used for the amplification. Nd:YAG lasers where the gain medium is composed of Nd^{3+} ions trapped in a rod of yttrium aluminium garnet (YAG) is used mainly as a pump laser. Population inversion is achieved in the Nd^{3+} ion by optical pumping from a flashlamp. Nd:YAG lasers operate in both pulsed and continuous mode. Pulsed Nd:YAG lasers are typically operated in the so called Q-switching mode [7]. An optical switch is inserted in the laser cavity waiting for a maximum population inversion in the neodymium ions before it opens. Then the light wave can run through the cavity, depopulating the excited gain medium at maximum population inversion. In this Q-switched mode output powers of 200 MW and pulse durations of less than 10 nanoseconds are achieved.

Most excimer lasers are of the noble gas halide type. Laser action in an excimer molecule occurs because it has a bound excited state, but a repulsive ground state. This is because noble gases are highly inert and do not usually form chemical compounds. When in an excited state which can be induced by an electrical discharge or high energy electron beams, they can form temporary bound molecules with themselves or with halides. The excited compound can give up its excess energy by undergoing spontaneous or stimulated emission, resulting in a strongly-repulsive ground state molecule which dissociates very quickly back into two unbound atoms. This results in a population inversion between the two states. By changing the gas mixture the laser wavelength can be changed. Examples of some of the most commonly used excimer lasers include ArF (193 nm), KrF (248 nm) and XeCl (308 nm). The output of these lasers is pulsed with duration of 10 – 15 ns.

A dye laser is one that uses an organic dye in a solvent such as methanol as a gain medium. Compared to gases and most solid state gain media, a dye can usually be used for a much wider range of wavelengths. The wide bandwidth makes them particularly suitable as tuneable lasers. The dye can also be replaced by another type of dye molecule in order to generate different wavelengths within the same laser. Dye lasers are used in conjunction with a fixed energy source which initiates a radiative transition in the dye. The continuous nature is a result of the organic dye molecule being large with a very high density of energy levels. The levels are also broadened by collisions with the solvent molecules, resulting in the small gaps between levels effectively disappearing. Other laser types that are commonly available include ion lasers which are used for work in the visible region. Ti:sapphire lasers are tuneable solid state lasers normally operating in the range 660 – 1180 nm.

1.3.2 Non-Photon sources

Electrons and ions can be used extensively to excite or ionise molecules. Electrons can be produced by electrical heating of a filament. The electrons produced have a distribution of energies. An electron monochromator can be used to select monoenergetic beams of electrons for use in experiments such as absorption spectroscopy or ionisation mass spectrometry. Positively charged ions are used for effecting the dissociative or non dissociative ionisation of molecules. Some ions that can be used for this purpose include the species H^+, He^+, O^+ and H_2^+. At collision energies below 30 keV, electron capture and charge transfer processes are observed (equation 1.9 and 1.10). While at higher energies ionisation is favoured (equation 1.11). The products and kinetics of ion-molecule reactions can then be studied.

$$X^+ + AB \rightarrow X + A^+ + B$$ **equation 1.9**

$$X^+ + AB \rightarrow X + AB^+$$ **equation 1.10**

$$X^+ + AB \rightarrow X^+ + A^+ + B + e^- \qquad \textbf{equation 1.11}$$

Metastable states are excited states which have a relatively long lifetime due to slow radiative and non-radiative decay. Such states occur in situations where neither radiative nor non-radiative processes can lead to a rapid decay of the excited atoms or molecules. Radiative processes can be strongly reduced if all transitions to lower levels are forbidden. These metastables can then exist for long timescales and can therefore collisionally pass their excess energy to another species. As it is difficult to provide a narrow bandwidth source with metastable molecules as a multitude of vibrational and rotational levels are populated, the noble gases are the metastables of choice. Examples include the $He^*(^3S_1)$ state at 19.82 eV and the $Ar^*(^3P_0)$ state at 11.72 eV. In practice, good vacuum must be maintained in the reaction vessel to avoid collisional deactivation of the metastable.

1.4 Dispersing elements

Dispersion is a phenomenon that causes the separation of a wave into its spectral components with different wavelengths. Most light sources are not monochromatic or tuneable directly, therefore a dispersing element is required which separates the radiation and allows the experiment to be tuned to a particular wavelength. Dispersing elements ideally should have a high resolving power, good throughput and a high degree of tunability. Two commonly used types are described below.

1.4.1 Prisms

Refraction is the change in direction of radiation due to a change in its velocity and wavelength. This is most commonly seen when a wave passes from one medium to another. The optical prism uses the phenomenon of refraction to separate radiation of different wavelengths. How much this happens depends on the refractive index of the two mediums and the angle between the light ray and the line perpendicular (normal) to the surface separating the two mediums. The angle which the incident ray makes with the normal line is referred to as the angle of incidence (figure 1.4). Similarly the angle which the refracted ray makes with the normal line is referred to as the angle of refraction. The ratio of the speed of light in a vacuum to the speed of light in the medium gives the refractive index. It always takes a value greater than 1 and increases as the wavelength of the light decreases. Each medium has a different refractive index.

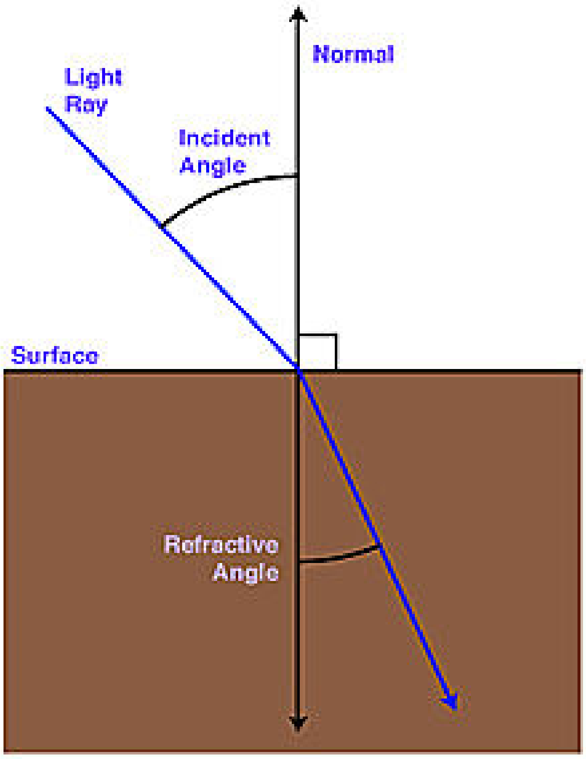

Figure 1.4. Diffraction at the edge of a surface.

Snells law is the formula used to calculate the refraction of light when travelling between two media of differing refractive index.

$$m_1 \sin\theta_1 = m_2 \sin\theta_1 \quad \textbf{equation 1.12}$$

where m_1, m_2 are the refractive indices of the two media and θ_1, θ_2 are the angles of incident and refraction. The refractive indices are functions of the wavelength of the radiation, and therefore the angle of refraction will also depend on the wavelength. It is then possible to monochromatise radiation by the separation of light of differing wavelengths. The device must be made of a material which has a significantly higher refractive index than air, and with a small path length which will allow the transmission of the radiation yet minimise optical losses. The most commonly used type is the triangular optical prism (figure 1.5).

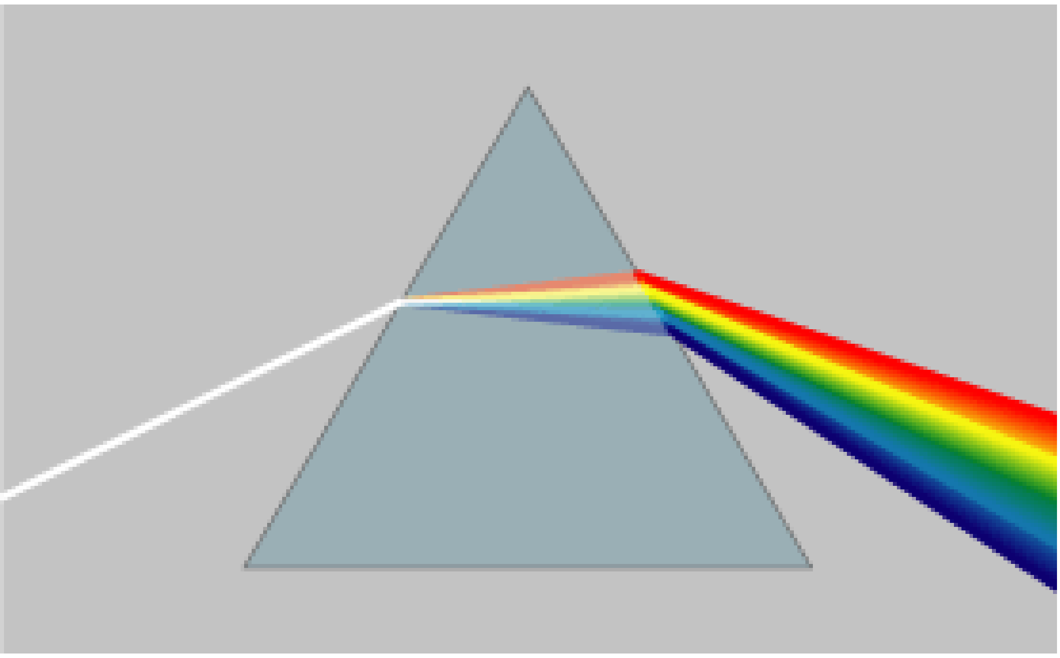

Figure 1.5 Dispersion in a prism

The resolving power, *R*, of the optical prism is given by

$$\text{Resolving power (R)} = \Delta L(dm/d\lambda) \quad \textbf{equation 1.13}$$

where ΔL is the difference in path length between the most and least refracted light. $dm/d\lambda$ is a property of the material, and is the rate of change of the refractive index with respect to wavelength. The material must be able to transmit the radiation that is analysed. As the wavelength of the radiation approaches the absorption region of the material, $dm/d\lambda$ increases. Therefore the resolving power of the material is highest at wavelengths just higher than the absorption wavelength. Quartz absorbs radiation below 185 nm, so when operating in the UV region of *ca.* 190 – 300 nm, quartz would be the most popular. The advantage of using optical prisms is that they have a high throughput and produce a clean dispersion of the radiation. Their disadvantages are the relatively low resolving power, the difficulty in tuning, and the limiting range over which they may be used.

1.4.2 Diffraction gratings

A diffraction grating consists of a series of equally spaced slits separated by a distance comparable to the wavelength of radiation to be dispersed. The slits may be supported on a material which can either transmit or reflect the radiation. A reflection grating consists of a grating superimposed on a reflective surface, whereas a transmission grating consists of a grating superimposed on a transparent surface [8]. When radiation is incident on a diffraction grating, diffractive and mutual interference effects can occur, and light is reflected or transmitted in discrete directions, called diffraction orders. The diffraction equation can give us the wavelength of the diffracted radiation.

$$n\lambda = d(\sin\theta + \sin i)$$ **equation 1.14**

where n and λ are the order and wavelength of the light, respectively, d is the distance between lines and θ and i are the angles of dispersed and incident radiation relative to the normal. It is sometimes convenient to write the equation as

$$Gn\lambda = \sin\theta + \sin i$$ **equation 1.15**

where G = 1/d is the groove frequency or groove density, more commonly called grooves per millimetre.

The sign of n is given by the grating equation and can be positive or negative. In a monochromator the angles i and θ are determined by the rotational position of the grating. The sign convention that all angles which are counter clockwise from the grating normal are positive, and all angles which are clockwise to the grating are negative is used. In experimental work usually only the first order is desired. All other wavelengths in higher orders need to be blocked. The desired input spectrum and detector sensitivity will determine whether filters can be used.

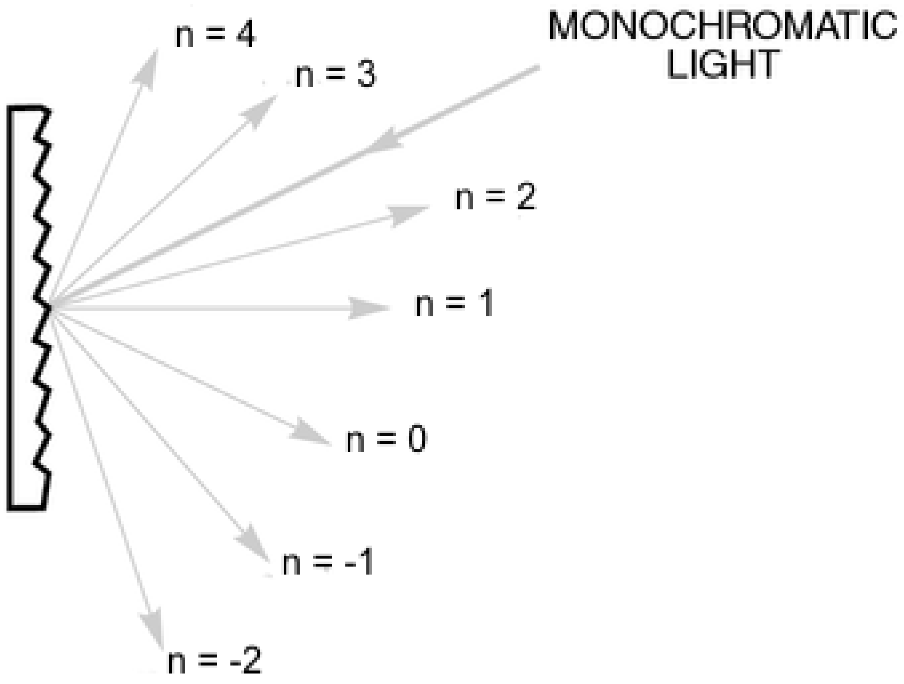

Figure 1.6 Orders in a diffraction grating

The angular dispersion ($d\theta/d\lambda$) is the amount of change of diffraction angle per unit change of the wavelength. It is a measure of the angular separation between beams of adjacent wavelengths and is given by

$$\text{Angular dispersion} = n/d \cos\theta \quad \textbf{equation 1.16}$$

The spectral resolution of an instrument is determined by the separation between two spectral peaks that can just barely be detected as separate with the instrument. The resolving power of a grating is given by [2]

$$R = \lambda/d\lambda = nN \quad \textbf{equation 1.17}$$

where n is the diffraction order and N is the total number of grooves on the entire grating surface.

1.5 Monochromators

A monochromator can use either the phenomenon of optical dispersion in a prism, or that of diffraction using a diffraction grating to separate polychromatic light. Although prisms are still used to disperse radiation in monochromators, grating monochromators is the favoured choice for most experimental work, and will be the only type discussed here.

The common Czerny-Turner design involves a classical plane grating illuminated by collimated light. The incident light is usually diverging from a source or slit and is collimated by a concave mirror before reaching the grating. The diffracted light is focused by a second concave mirror.

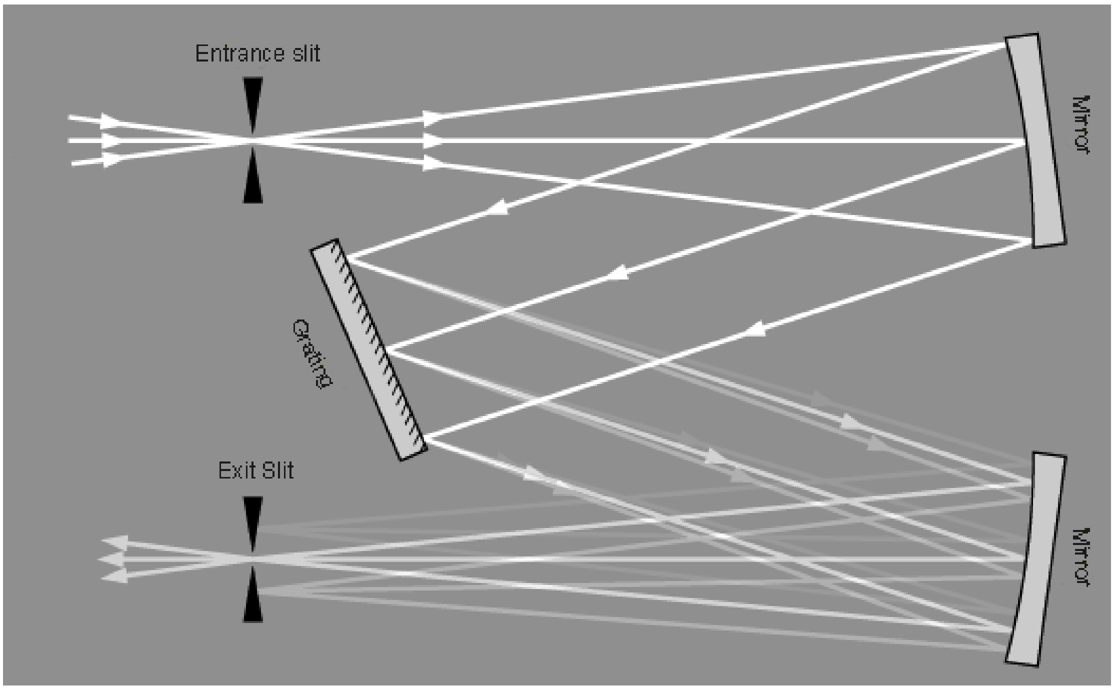

Figure 1.7 The Czerny-Turner monochromator

Molecular oxygen has absorption lines at wavelengths below *ca.* 185 nm. Monochromators that need to operate below this wavelength need to be evacuated, whereas those designed for higher wavelengths are not. Absorption by surfaces can also be a problem therefore arrangements of monochromators with fewer mirrors are sometimes preferred. A concave reflection grating can be used as a concave mirror that disperses. It can be thought to reflect and focus light because of its concave nature and to disperse light by use of its grooves. Configurations include the Seya-Namioka where mirrors at the entrance and exit slits conserve the polarisation of the light and the Wadsworth configuration where only a concave grating is used with no entrance slit.

1.6 Photodetectors

The purpose of any photodetector is to convert electromagnetic radiation into an electronic signal, ideally one that is proportional to incident light intensity. A photodiode is a semiconductor diode that functions as a photodetector. The most popular choices for the semiconductor material are silicon and gallium arsenide. When a photon is absorbed it excites an electron and produces a single pair of charge carriers, an electron and a hole, where a hole is simply the absence of an electron in the semiconductor lattice. Current passes through the semiconductor when the charge carriers separate and move in opposite directions. The electron current is then amplified and detected.

Photomultiplier tubes (PMTs) are extremely sensitive detectors of light. These detectors can multiply the signal produced by incident light by as much as 10^8. PMTs are constructed from a sealed glass vacuum tube which has a photocathode, a series of dynodes, and an anode. Incident photons strike the photocathode with electrons being released as a consequence of the photoelectric effect. The electrons are then directed by the focusing electrode towards the electron multiplier. The electron multiplier consists of a number of dynodes. Each dynode is held at a more positive voltage than the one before. The electrons leave the photocathode and move towards the first dynode where they are accelerated by the electric field and arrive with increased energy. On striking the first dynode more low energy electrons are emitted and these are accelerated towards the second dynode. The signal multiplication continues with an ever increasing number of electrons being produced at each stage. The anode is then reached where the accumulation of charge results in a sharp current pulse. The advantage of using PMTs is that the response to radiation over a large intensity range is linear. The amplification process essentially produces no noise since it takes place in an evacuated tube without degrading the signal to noise ratio. The dark count of the device is very low and can be lowered further by cooling. The use of a window means that PMTs are not suitable for the detection of VUV radiation. The radiation may be detected indirectly by use of a sodium salicylate coated window. When VUV light is incident upon the coating of sodium salicylate, visible fluorescence is emitted, which is then detectable using the PMT. It is assumed that the response of the sodium salicylate window is invariant to the VUV wavelength.

A Charge Coupled Device (CCD) is a highly sensitive photon detector [9]. The CCD is divided up into a large number of light sensitive small areas known as pixels. A photon of light which falls within the area defined by one of the pixels will be converted into one or more electrons and the number of electrons collected will be directly proportional to the intensity of the light at each pixel. Since many of the experiments described in this thesis use a CCD detector, it is described in some detail in the experimental chapter 2.

1.7 Experimental techniques in the VUV

1.7.1 Absorption spectroscopy

When a beam of light of known intensity is incident upon an absorbing sample, and provided a small fraction of this light is absorbed, with negligible losses caused by scattering. The relationship between the transmitted light intensity and the incident light intensity is given by the Beer-Lambert law

$$A = \log_{10}(I_o/I) = \varepsilon(\nu)cL \quad \textbf{equation 1.18}$$

where I_o is the intensity of light entering the cell and I is the intensity of the light on exiting the cell. A is the absorbance of the sample, c is the concentration of the absorbing species with units of mol dm^{-3}, L the optical path length in cm and ε is the molar absorption coefficient in dm^3 mol^{-1} cm^{-1}. The molar absorption coefficient can be thought as the absorbing power of the sample and is dependent on the frequency (ν). An alternative way of writing the Beer-Lambert law is

$$A' = \ln(I_o/I) = \sigma(\nu)\, cL \quad \textbf{equation 1.19}$$

Here σ is the absorption cross section in units of cm^2 $molecule^{-1}$, c the number density and now has units of molecules cm^{-3} and L is in cm. The value of the absorbance will be different depending on which of the two equations is used. Therefore care must be taken when interpreting data that the correct form of the law is used. The aim of an absorption experiment is to measure σ or ε as a function of energy. This is achieved by irradiating a closed cell containing a known amount of sample gas with monochromatic radiation of a desired frequency. The transmitted radiation (I_o) is detected using a PMT. The experiment is repeated without gas to obtain (I), the intensity of the incident radiation. The absorption cross-section can then be calculated using the Beer-Lambert law.

1.7.2 Fluorescence spectroscopy

After absorption of a photon, one of the possible secondary processes that can occur is fluorescence. There are several experimental techniques that use fluorescence detection to probe the nature of the excited state. Fluorescence excitation spectroscopy or undispersed fluorescence spectroscopy measures the total fluorescence given off as a function of the primary excitation energy. This experiment provides information on the parent molecular states that either fluoresce directly, or alternatively fragmentation of the molecule occurs and fluorescence results from one of these fragments. Fluorescence excitation spectroscopy essentially measures the absorption spectrum of the generic polyatomic molecule AB, with absorption being monitored by fluorescence of either the parent molecule or a fragment. It is an indirect detection technique with the advantage of having a zero background. Note that this experiment gives no indication of the quantum yield of the dissociation process, and therefore no indication of the extent of absorption that is being observed. The disadvantage is that no indication of the fluorescence yield is made therefore, no idea if fluorescence is a result of 0.1, 10 or 100 % of the flux. The shape of the excitation spectrum can indicate whether the primary excitation process is resonant or non-resonant. Resonant peaks have an onset, reach a peak, and then the signal recedes back to the baseline (figure 1.8). These types of peaks are an indication of fluorescence emanating from neutral states, either from the parent molecule or from one of its fragments.

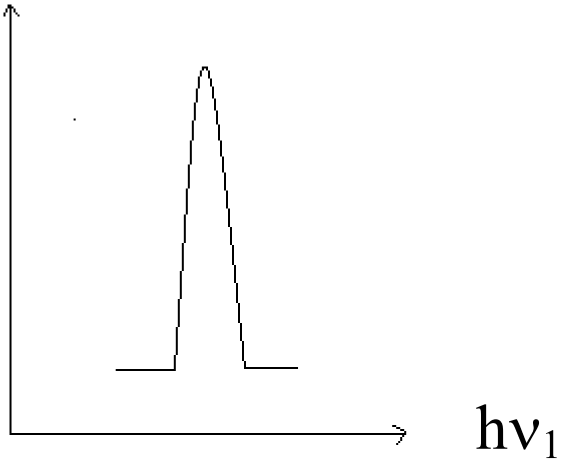

Figure 1.8 Resonant photon excitation, formation of a fluorescence fragment is via a dissociative Rydberg state of AB.

$$AB + h\nu_1 \rightarrow AB^* \quad \textbf{equation 1.1}$$

$$AB^* \rightarrow A^* + B \quad \textbf{equation 1.20}$$

$$A^* \rightarrow A + h\nu_2 \quad \textbf{equation 1.21}$$

The non-resonant peaks show no signal until an onset is reached where a rapid increase in signal is observed (figure 1.9). The signal is still observed at energies in excess of the threshold value. Peaks of this kind are normally an indication of emission from a parent ion, any excess energy supplied to the molecule being carried away by the associated photoelectron as kinetic energy.

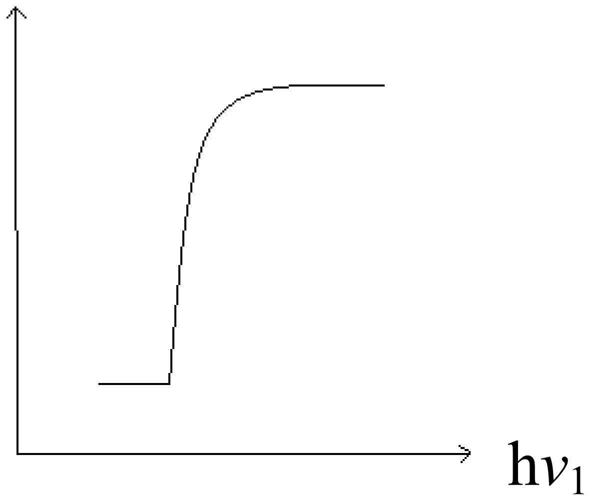

Figure 1.9 Non-resonant photon excitation. Sharp turn on of fluorescence, signal present for photon energies well in excess of threshold; electron carries away excess energy.

$$AB + h\nu \rightarrow (AB^+)^* + e^- \quad \textbf{equation 1.22}$$

$$(AB^+)^* \rightarrow AB^+ + h\nu_2 \quad \textbf{equation 1.23}$$

When the primary excitation energy is fixed, the resultant fluorescence can be collected and dispersed using a second monochromator. The experiments are then called dispersed fluorescence spectroscopy, and provide detailed information on each of the emitting states of the molecule, parent ion or the fragment produced by photodissociation. Dispersion of the fluorescence signal will always cause reduction in the intensity of the emission. Therefore intense photoexcitation sources along with sensitive collection devices are required to record dispersed fluorescence spectra with good signal to noise ration. In the dispersed fluorescence experiments carried out in this thesis, a synchrotron beam was used as the excitation source and a CCD has been used to detect the emission.

The presence of a secondary monochromator permits another type of experiment to be performed. If the primary monochromator is scanned, the photon energy is varied, and the wavelength range is fixed on the dispersing secondary monochromator. The signal is then monitored using a PMT. An action spectrum of the fluorescing species can then be obtained. This procedure allows the appearance energy, and hence the identity, of the fluorescing species to be determined. When photon sources such as the one used for the work in this thesis are used to do fluorescence experiments, detection of the fluorescence occurs perpendicular to the path of the synchrotron beam. This is done to prevent the incident light from the synchrotron beam being observed by the detector, thereby reducing the background signal of the spectrum. The inside of the fluorescence chamber is also black anodised to minimise scattered light. This has the added benefit of increasing the surface resistance of the walls to corrosion from samples.

1.7.3 Photoelectron spectroscopy

When a molecule interacts with electromagnetic radiation with sufficient energy ionisation can occur.

$$AB + h\nu \rightarrow \; AB^{+} + e^{-} \quad \textbf{equation 1.24}$$

The energy of the photon must exceed the ionisation energy of the molecule for the above process to take place. Several techniques are available to probe this process by analysing the kinetic energy of the electrons that are produced [10]. The kinetic energy of the recoiling ion can be ignored due to the large difference in mass between the ion and the electron. Then the excitation energy is related to the kinetic energy of the electron by

$$h\nu = IE_{i} + KE_{electron} \quad \textbf{equation 1.25}$$

where IE_i is the ionisation energy of an electron in orbital i and $KE_{electron}$ is the kinetic of the electron. If the energy of the radiation ($h\nu$) is accurately known, the orbital ionisation energies can be determined by measuring the kinetic energy of the emitted electrons. For molecules in the gas phase sometimes vibrational and rotational bands can be resolved. The structure of these bands observed in the photoelectron spectrum can also deduce other characteristics of the orbital from which the electron was removed.

Extended vibrational progressions can denote a large geometry change upon ionisation caused by the removal of an electron from a strongly bonding or anti-bonding orbital. The removal of a non bonding electron is suggested by the appearance of a narrow vibrational progression. Conventional photoelectron spectroscopy is taken by fixing $h\nu$, using a line source such as He I at 21.22 eV, the resultant electrons are then energy analysed using an electron energy analyser. The analyser can be based on electric or magnetic fields to distinguish the electrons according to their kinetic energies [7]. Analysers using electrical fields to allow the passage of electrons of a desired energy range to the detector are the most common. There are two main types of electrical field analysers, retarding field and deflection analysers. Retarding field devices allow transmission of electrons that have energies higher than the retarding potential. The spectrum is obtained by recording the photoelectron signal as a function of the retarding potential. Deflection analysers separate electrons by forcing them to follow different paths according to their kinetic energy. There are a number of different types, including the parallel plate analyser, the cylindrical mirror analyser and the hemispherical analyser.

1.7.4 Threshold photoelectron spectroscopy

Threshold photoelectron spectroscopy (TPES) studies the electrons with near zero kinetic energy or threshold electrons. These electrons normally do not have sufficient energy to travel towards the detector. A penetrating field technique [11] which focuses the electrons in the direction of an electron energy analyser is used to detect the low energy electrons. Some high energy electrons are directed towards the extracting electrode by travelling along a straight path and are not discriminated against. By use of the penetrating field technique along with a dispersive electron analyser, these erroneous signals can be suppressed. This configuration can result in very high collection efficiencies. The technique requires a tunable photon source and by scanning the photon energy while detecting the threshold electrons a threshold photoelectron spectrum can be taken.

1.7.5 Photoionisation mass spectroscopy

The process of photoionisation not only produces electrons which can be detected using the techniques described above, but also ions. The intensities of the mass of a selected ion can be recorded as a function of the excitation energy by photoionisation mass spectroscopy (PIMS). Mass analysis is generally achieved by the use of mass filter, such as a quadrupole mass spectrometer or time-of-flight mass spectrometer. The appearance energies of both parent and fragment ions can be determined as well as the ionisation energy of parent ion. Since electrons are not detected using PIMS this technique can be sensitive to formation of ion pairs. When carrying out experiments care must be taken to keep the operating pressures low to minimise secondary processes such as ion molecule reactions and electron attachment. From the appearance potential of either the fragment or parent ions thermochemical data can be derived.

1.7.6 Coincidence spectroscopy

Coincidence techniques are primarily concerned with the relationship between two events. Coincidence experiments can associate two events such as the primary excitation process, (example the excitation to a valence state of the parent ion) to a secondary process which subsequently occurs, such as dissociation of the valence state of the parent ion into fragments. Experiments involving the coincidence of two events more commonly associate two secondary processes. This normally involves detecting an ion and an electron after photoionisation has occurred. Examples include the photoelectron photoion coincidence (PEPICO) and threshold photoelectron photoion coincidence spectroscopy (TPEPICO). PEPICO is a combination of photoelectron and photoionisation mass spectroscopy. TPEPICO spectroscopy can be thought of as an amalgamation of the TPES and PIMS techniques.

TPEPICO spectroscopy investigates the dissociation pathways of a state selected ion defined by the photoexcitation energy. In a TPEPICO experiment a fragment ion is detected in coincidence with an electron. The technique has to ensure that the electron and ion arise from the same ionization event. Due to the electron having a lower mass it will arrive at the detector much quicker than the corresponding ion. When the electron reaches the detector a delayed electronic pulse is generated. The coincidence count is triggered by the registration of the ion pulse within a narrow time window. This is done to insure that the electron and ion arise from the same ionization event and to minimize any false coincidences. By measuring the coincidence count as a function of excitation energy the appearance energy of a fragment ion can be measured. Fixed energy experiments can be performed where the spectra obtained are two dimensional graphs where the coincidence count is plotted as a function of ion time of flight. The kinetic energy of the ions can be determined from this data thus allowing the determination of the decay dynamics of the excited states [12,13].

1.8 References

[1] J. Berkowitz, *Photoabsorption, Photoionisation and Photoelectron Spectroscopy*, Academic Press (1979).

[2] J.M. Hollas, *High Resolution Spectroscopy* (2nd edn.), Wiley (1998).

[3] M.B. Robin, *Higher Excited States of Polyatomic Molecules* (vol 1), Academic Press (1974).

[4] J.H. Moore, C.C. Davis and M.A. Coplan, *Building Scientific Apparatus* (2nd edn.), Addison-Wesley (1989)

[5] R.P. Tuckett, *Spectroscopy Europe*, Vol. 17 NO. 5 (2005)

[6] www.SRS.ac.uk

[7] A. Ellis, M. Feher and T. Wright, *electronic and photoelectron spectroscopy*, Cambridge press (2005)

[8] C. Palmer, *Diffraction grating handbook*, (5th ed), Thermo RGL (2002)

[9] P. Jacquinot, *J. Opt. Soc. Am.* **44** (1954) 761

[10] J.H.D. Eland, *Photoelectron Spectroscopy* (2nd ed.), Butterworths (1984).

[11] R I Hall, A McConkey, K Ellis, G Dawber, L Avaldi, M A MacDonald and *G* C King, *Meas. Sci. Technol.* **3** (1992) 316

[12] P.A. Hatherly, M. Stankiewicz, K. Codling, J.C. Creasey, H.M. Jones and R.P. Tuckett, *Meas. Sci. Technol.* **3** (1992) 891

[13] P.A. Hatherly, D.M. Smith and R.P. Tuckett, *Zeit. für Phys. Chem.* **97** (1996) 195.

[14] D. M. P. Holland, *Physia scripta*, **36** (1987) 22

[15] J. B. West, *Experimental methods in phys sci*, **31** (1998) 27

[16] E.Illenberger and J.Momigny, *Gaseous Molecular Ions*, Springer-Verlag (1992).

[17] E. W. Schlag, *ZEKE spectroscopy*, Cambridge press (1998)

[18] W. R. Hunter, *Experimental methods in phys chem*, **31** (1998) 305

[19] D. M. P. Holland, J. B. West, A. A. Macdowel, I. H. Munro and A. G. Beckett, *Nuclear instruments and methods in phys research B*, **44** (1989) 233

[20] J.B. West and H.A. Padmore in *Handbook of Synchrotron Radiation*, vol. 2, ed. G.V. Marr, North-Holland (1987

[21] C. Kunz, *Synchrotron Radiation: Techniques and Applications*, Spring-Verlag (1979)

2. Experimental

This chapter illustrates the experimental techniques used to record the spectra presented in this thesis. The first section starts with a description of beamline 3.1 of the Daresbury Synchrotron radiation source (SRS) which incorporates a new 1 m Wadsworth monochromator. This beamline has been used to carry out most of the fluorescence experiments shown in this thesis; a few fluorescence excitation spectra were also recorded at the BESSY 1 synchrotron source in Berlin. Then a description of the apparatus used to record both dispersed and undispersed fluorescence spectra at Daresbury is included. The VUV-excited spectra of N_2 and CO_2, which are used for the calibration of both the primary monochromator and the CCD triax system are then presented. Finally the apparatus used to record the absorption and some fluorescence excitation spectra by the Tuckett group at BESSY 1 will be described.

2.1 Introduction

Beamline 3.1 of the Daresbury SRS has recently been re-developed in order to provide *ca.* two orders of magnitude higher flux than it had in its previous manifestation. A major EPSRC grant to Tuckett and West funded this initiative. Following commissioning the monochromator became available for experimental use in May 2004, 7 months after the start of my PhD training. The improvement in flux has been achieved by a design that comprises a minimal number of optical components, thus substantially reducing the effect of transmission losses. The new monochromator has the Wadsworth configuration which contains only one optical component, a concave diffraction grating [1]. It is a great simplification over the previously-installed Seya monochromator, where concave mirrors were positioned both before and after the entrance and exit slits. A further feature of this new monochromator located on a bending magnet at the SRS is that it has no entrance slit, so it makes full use of the available horizontal aperture of the synchrotron radiation beamline.

In section 2.3 we describe the dispersed fluorescence apparatus which was used to aid the commissioning of this new beamline [2]. Previous dispersed fluorescence spectra taken by our group were carried out at the BESSY 1 synchrotron radiation source in Berlin [3]. The main improvement of our current equipment over that used in Berlin is the use of a charge-coupled device (CCD) detection system. This multi-channel detector permits the measurement of a wide range of wavelengths simultaneously, as opposed to the photomultiplier tubes used at BESSY1, where a grating must scan over a defined spectral range and successive wavelengths are focussed through an exit slit onto the photomultiplier tube. In essence, the CCD can attain the same signal/noise ratio as that achieved by single-channel detector in a much shorter acquisition time, *i.e.* the Jacquinot advantage [4].

2.2 The new Wadsworth monochromator

As noted earlier, this new monochromator was designed and built before the start of my PhD training, and I played negligible part in its construction. Many of the ideas highlighted here are given more fully in reference 2. The monochromator is based on the Wadsworth principle [1], and is similar in layout to that built for the DESY synchrotron over three decades ago [5]. The advantage in using this type of monochromator on a bending magnet of a synchrotron radiation source is that it has a large aperture, and by using the source as its entrance slit makes optimum use of the radiation available. This instrument operates in horizontal dispersion, so its resolution is limited by the horizontal electron beam size in the storage ring, FWHM *ca.* 1.8 mm in the case of the SRS, corresponding to a best resolution of *ca.* 0.05 nm. Although this is a factor of five inferior to that which could be obtained using vertical dispersion, it was sufficient for the kinds of experiments that are to be carried out on this beamline, and led to a much more convenient experimental arrangement. The scanning mechanism is by means of an off-axis pivot [6,7], which makes an approximate correction for the changing focus of the grating for different wavelengths. The main difference with this monochromator over previous instruments of this kind is that the length of the pivot arm can be varied externally to the vacuum. This means that different wavelength ranges can be covered without substantial loss in resolution; the user chooses the wavelength region required and adjusts the pivot arm to give optimum performance in that region. The position of the exit slit, *i.e.* the grating to exit slit distance, GS (figure 2.1), can also be changed externally, allowing further optimisation of the wavelength resolution over a given spectral range. Three gratings can be mounted, though only two have been fitted, both are interchangeable under vacuum, giving a wide range of wavelength coverage, currently *ca.* 40 – 200 nm. The high-energy grating (HEG), 2400 lines/mm, covers best the range 40 – 100 nm; the medium-energy grating (MEG), 1200 lines/mm, covers best the range 80 – 200 nm.

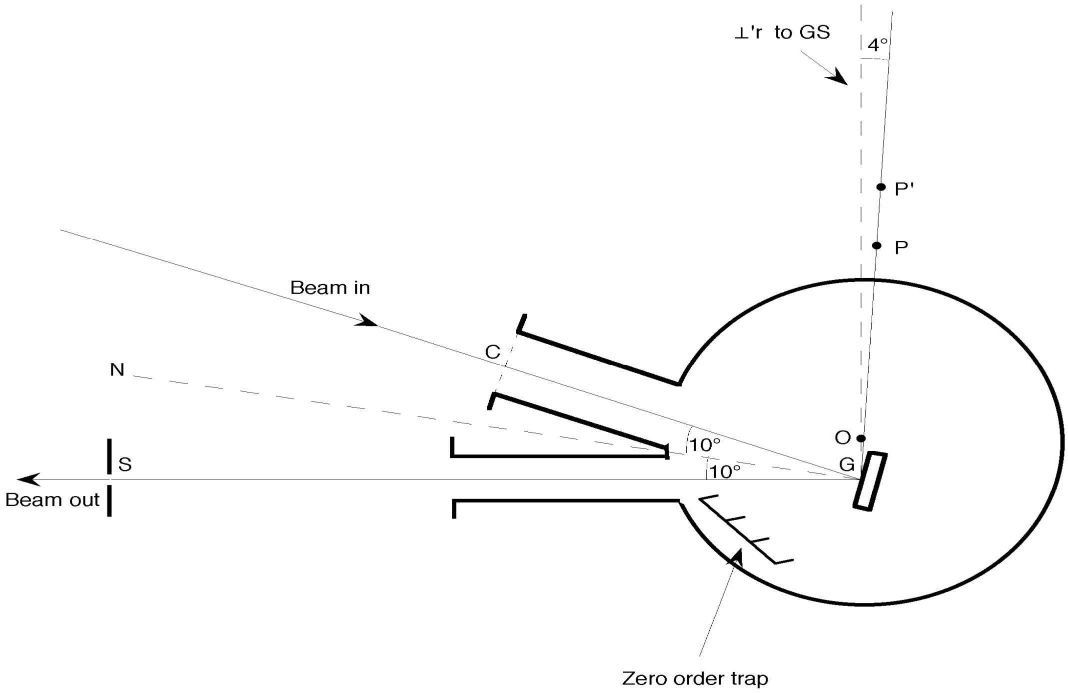

Figure 2.1 :The new monochromator of Wadsworth design. G – diffraction grating ; S – exit slit ; C – centre of entrance flange where collimating baffles are fitted ; O – vacuum chamber centre ; P – pivot point, movable between P and P’.

The optical layout, seen in plan view from above, is shown in Figure 1. The monochromator is preceded by a water-cooled metal plane mirror, which deflects the incident radiation through 20° onto the diffraction grating. Baffles are provided in the entrance tubing of the monochromator to define the area of illumination on the grating. The monochromator scans in positive order, in other words anticlockwise about the pivot point in the diagram which can be varied between P and P’. The 4° offset shown was chosen to minimise the change in direction of the output beam as the grating is moved. For the range of travel of the grating, the variation is within a range of ± 0.04°. A compact four-way cross fitted on to the exit slit of the monochromator incorporates a retractable LiF window for complete rejection of higher orders when operating with $\lambda > 105$ nm, and a retractable Si photodiode for absolute flux measurements. This cross is then attached to a mirror chamber which contains an elliptical mirror and a plane mirror, thereby focussing the exit slit with 1:1 demagnification at the centre of an exit flange. This arrangement preserves the horizontal direction of the output beam, and the plane mirror can be adjusted precisely to fine tune this alignment. A capillary light guide is mounted on to the exit flange. It serves the dual purpose of bringing the light efficiently to the experimental sample and also providing an efficient vacuum differential between the experimental chamber and the mirror box.

The absolute photon fluxes from the two gratings recorded at commissioning in March 2004 are shown in Figures 2 and 3. The flux curves were measured using a calibrated Si photodiode mounted on the exit slit of the monochromator. The experiments performed for this thesis used both gratings. The HEG was generally used for experiments involving excitation energies above 16 eV, while the MEG was used for excitation energies between 8 and 16 eV. Higher order effects are a problem for both gratings at lower energies. However this can be eliminated when operating at energies below 11.8 eV(105 nm), by having a LiF window in place between the exit slit of the monochromator and the post-focusing mirror box.

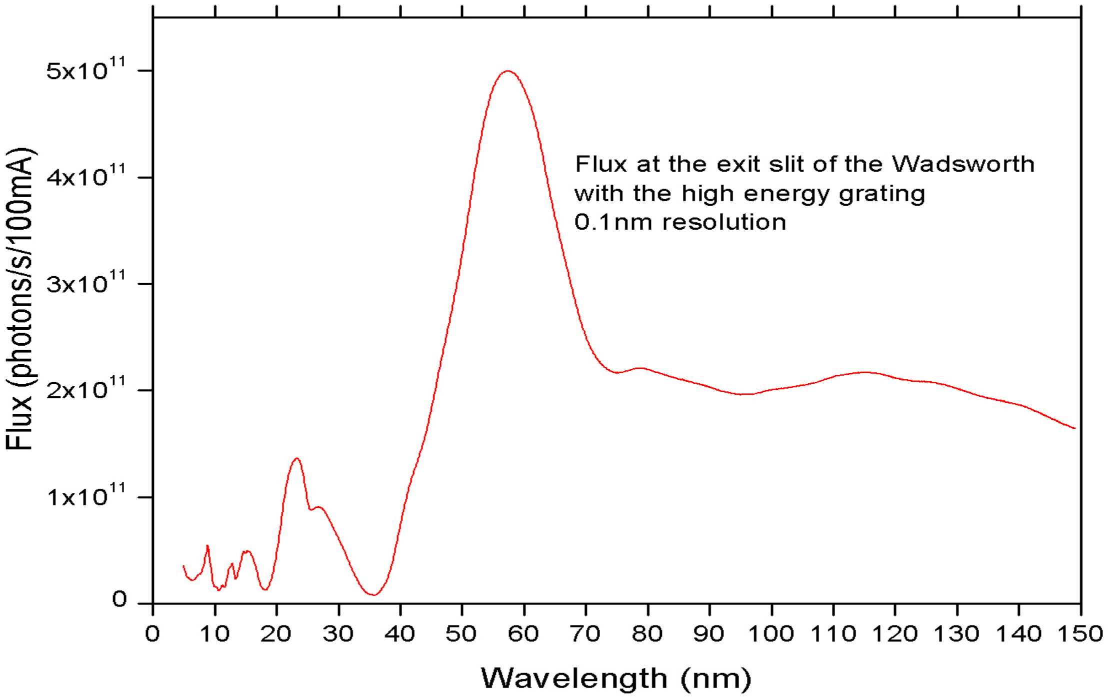

Figure 2.2: Absolute output flux from the HEG 2400 lines/mm, measured on a calibrated Si photodiode at the exit slit of the monochromator.

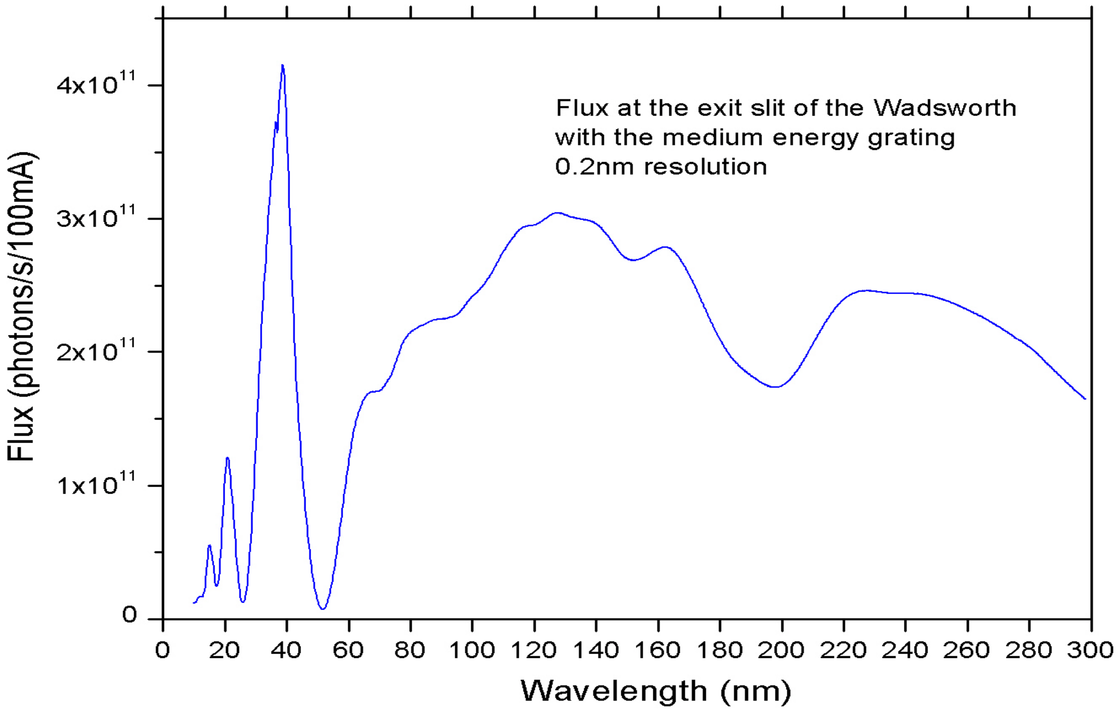

Figure 2.3: Absolute output flux from the HEG 1200 lines/mm, measured on a calibrated Si photodiode at the exit slit of the monochromator.

Unless otherwise stated, all VUV-excitation spectra in this thesis, whether absorption or fluorescence, are flux normalised using either a sodium salicylate window and a PMT or these absolute Si curves.

2.3 Dispersed fluorescence apparatus

The dispersed fluorescence apparatus used to perform these experiments consists of a 120 mm^3 black anodised aluminium cube, which is attached to the post-focusing mirror box by a set of flexible bellows (figure 2.4). The cube is partitioned into two separate sections divided by a 3 x 10 mm vertical slit, which can be opened or closed by a retractable plate on a vacuum-tight slider. The capillary light guide, length 330 mm and internal diameter 2 mm, ends *ca.* 5 mm from this slit. Rotary-backed Pfeiffer-Blazers TPU 260 KGT and TPD 064 turbo pumps are used to evacuate the two sections. A 50 mm^3 brass cube is connected to the opposite face of the aluminium cube, and is separated from it by a 3.5 mm diameter aperture. This arrangement of apertures and glass capillary allows extensive differential pumping to occur, in that the operating pressure in the interaction region is *ca.* six orders of magnitude higher than that in the post-focussing mirror box. Therefore, the optical coatings on the gratings of the monochromator are preserved. It is noted that the pressure in the two stages of the differential pumping can be measured by Edwards penning gauges, but it was not possible to measure *directly* the pressure in the brass cube interaction region. We estimate, however, it is one order of magnitude greater than in the adjacent pumping section.

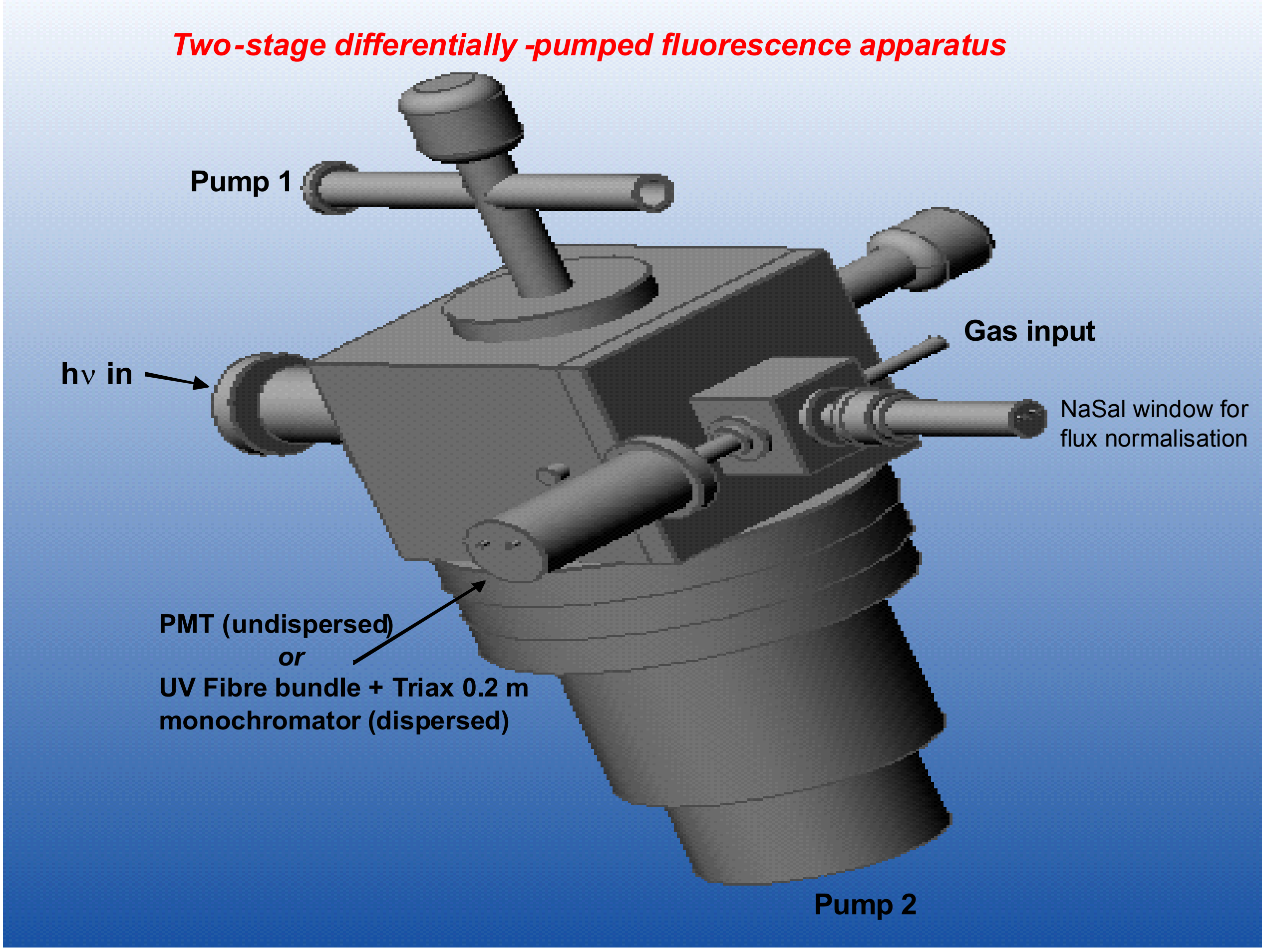

Figure 2.4: Fluorescence apparatus set up to record undispersed fluorescence excitation spectra. Dispersed fluorescence spectra is recorded by replacing the PMT with a UV fibre optic bundle attached to a 0.19 m triax monochromator.

The gaseous samples are admitted from one side of the interaction region *via* a needle valve. The resultant fluorescence is collected at 90° to the incident photon beam by a UV-grade fibre bundle of length 0.5 m containing 300 fibres attached to a Spectrosil-B window. This fibre displays > 50% transmittance in the 250 – 900 nm region, and is connected to the entrance slit of a 0.19 m focal length Jobin-Yvon Triax monochromator (figure 2.4). The collected signal is dispersed by one of either a UV or visible grating turret; each turret contains three gratings with 100, 300 or 1200 grooves mm^{-1}. A 1024 x 256 pixel open-electrode CCD collects the dispersed signal, which uses liquid nitrogen cooling to reduce the dark count level to < 1 count pixel^{-1} hour^{-1}. The standard parameters used to acquire dispersed fluorescence spectra were two consecutive accumulations with integration times of each ranging from 600 to 1800 s to effect cosmic ray removal. Although longer integration times were sometimes used, they often resulted in the appearance of larger quantities of cosmic rays that obscured the acquired data. Even though the cosmic ray removal routines were employed throughout, the benefits of increased integration times were often insignificant. All the dispersed spectra taken, using the liquid nitrogen cooled CCD, are seen with a constant background signal called the readout noise. The value of the readout noise can be between 900 and 1100 counts and is present for all wavelengths in the spectrum.

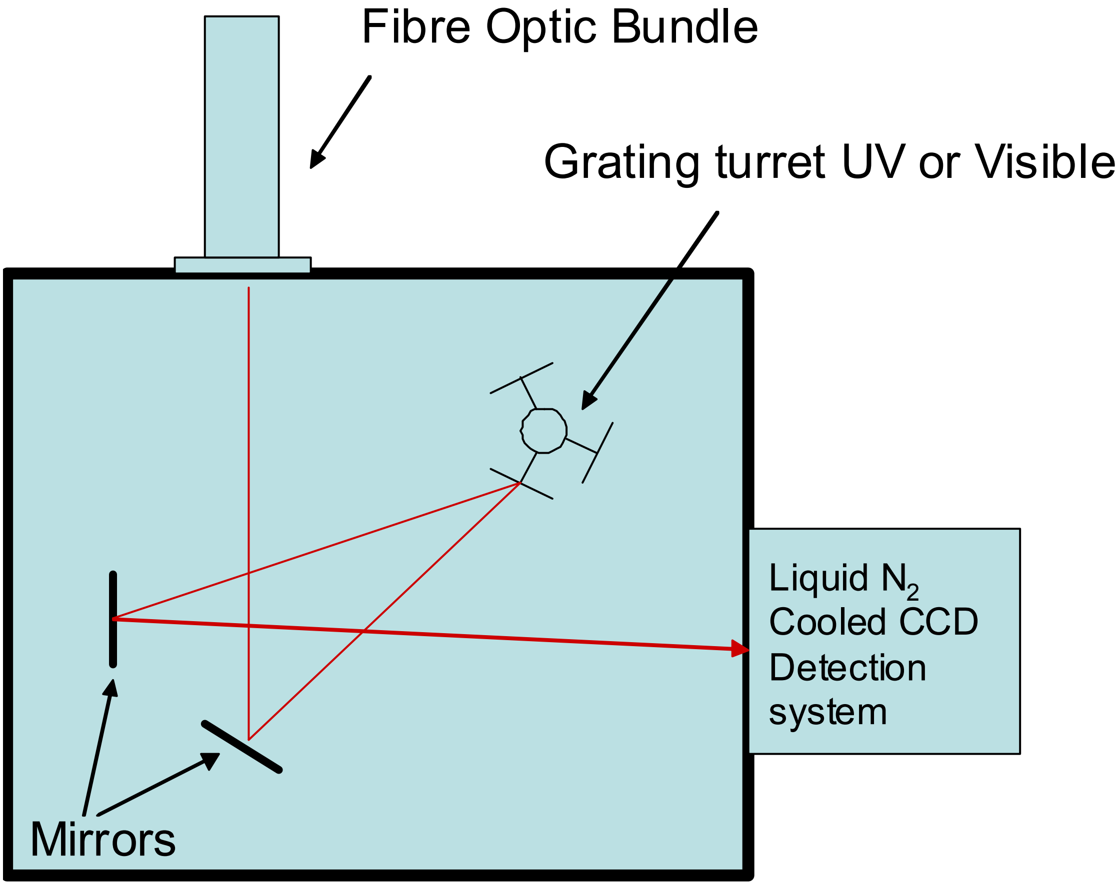

Figure 2.5: Schematic of the CCD/Triax dispersed fluorescence system.

For each sample an undispersed fluorescence spectrum was also recorded, using an uncooled EMI 9883QB photomultiplier tube in place of the fibre optic and Triax/CCD detection system. The undispersed fluorescence signal was acquired as a function of photon energy by scanning the Wadsworth monochromator. Well-established data for the ionisation thresholds of each of the fluorescing states allows calibration of the gratings to occur [9]. These scans are flux normalised using the signal from a sodium salicylate window monitored on a photomultiplier tube that is in line with the incident beam.

Most of the dispersed fluorescence spectra presented in this thesis have been normalised to the quantum efficiency (QE) of the open electrode CCD chip, and the efficiency of the different grating turrets. Both the QE of the CCD chip and the efficiency of the gratings are obtained from the manufacturer of the CCD/Triax monochromator, Jobin-Yvon.
The sensitivity curve of the CCD/Triax system is obtained by

Sensitivity Curve = QE (CCD) x Sensitivity of Grating: **equation 2.1**

Figure 2.6 shows the sensitivity curves obtained for the UV300 and UV100 gratings. The majority of the spectra in this thesis have been taken using one of these two gratings. These curves are then used to normalise the dispersed spectra. The range of the UV100 grating is 700 nm and the range of the UV300 grating is 380 nm. It was not necessary to apply this procedure to higher-resolution spectra recorded with the UV1200 grating, since the range across the CCD is only 95 nm.

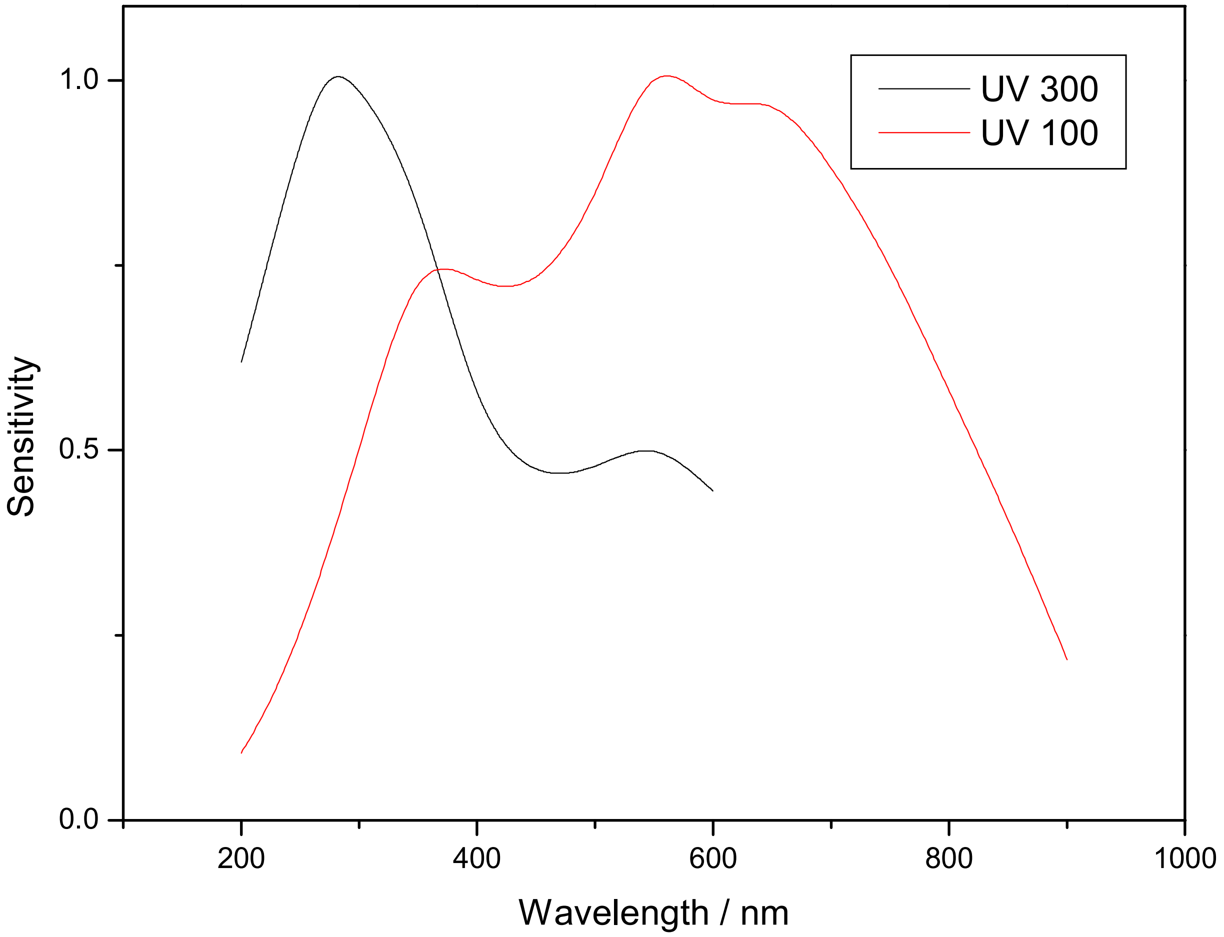

Figure 2.6: Sensitivity curves for the UV300 and UV100 grating, used to normalise disperse spectra

2.4 N_2

The fluorescence excitation spectrum of N_2 recorded on the high energy grating over the range 18.5 – 19.5 eV is shown in Figure 2.7. The optical resolution of the Wadsworth was set as 0.1 nm, corresponding to a resolution of 0.03 eV at a photon energy of 19 eV. Wavelength calibration of both the medium and high energy gratings can be performed using values obtained from this spectrum. Before the start of each run at the SRS a N_2 spectrum is taken to aid in this calibration process. The spectrum displays the profile of a non-resonant peak, with a steep rise from signal onsets at 18.75 ± 0.02 eV, the signal then remains above zero for excitation energies well in excess of threshold. This shape is characteristic of non-resonant photoionisation (see chapter 1), with fluorescence emanating from an excited state of the parent ion. The values correspond to fluorescence resulting from the N_2^+ $B^2\Sigma_u^+ - X^2\Sigma_g^+$ transition, starting in the v' = 0 level of the upper state. Further weak onsets are observed at 19.10 eV with emission now originating from the v' = 1 level of the B $^2\Sigma_u^+$ state of N_2^+.

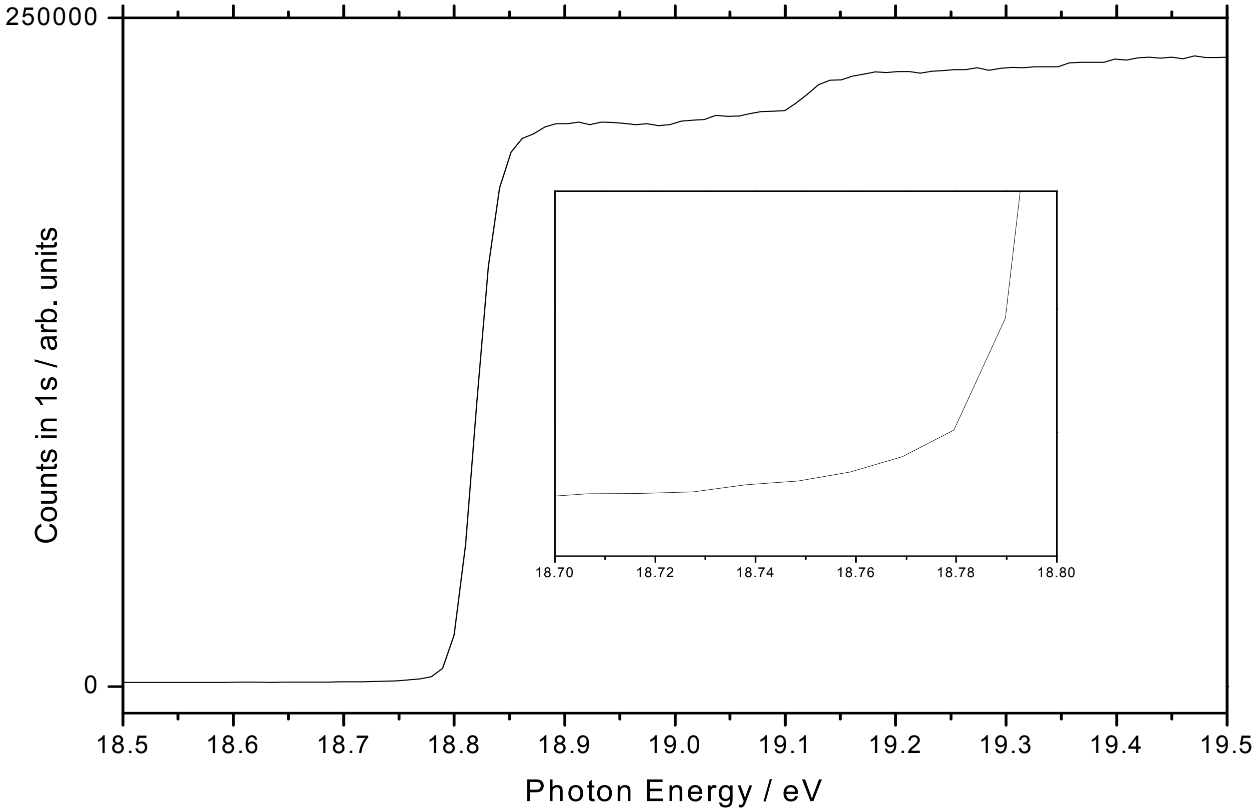

Figure 2.7: Fluorescence excitation spectrum of N_2 taken using the high energy grating with a resolution of 0.1 nm.

Dispersed fluorescence spectra shown in figure 2.8 were obtained using an entrance slit of 0.1 and 1 mm on the Triax secondary monochromator, corresponding to a resolution of 0.35

and 3.5 nm respectively. The spectra were acquired at photon energies of 18.8 eV (red) and 19.2 eV (blue). The dispersed spectrum at 18.8 eV shows two peaks at 391 and 428 nm, corresponding to the (0,0) and the (0,1) bands of the $B - X$ transition. The wavelength of these peaks can be used to calibrate the CCD Triax system. The insert in figure 2.7 shows the P-branch head and blue-degraded R-rotational envelope of each band, characteristic of an upper state rotational constant being greater than a lower state rotational constant, $B^{'} > B^{''}$. At the photon energy of 19.2 eV which is greater than the v' = 1 threshold, the (1,0) and (1,2) bands are also observed.

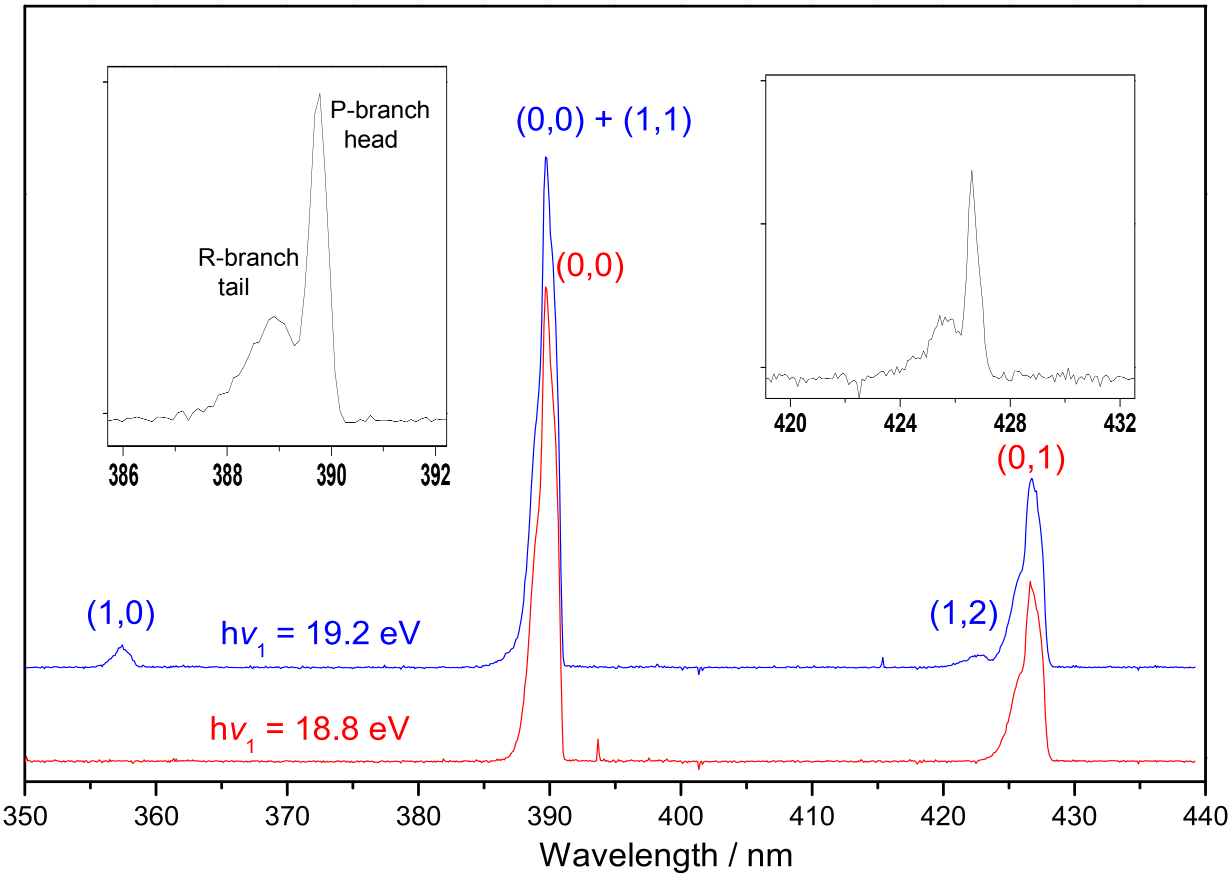

Figure 2.8: Dispersed fluorescence spectra of N_2^+ B $^2\Sigma_u^+$ - X $^2\Sigma_g^+$. The inserts shows a spectrum taken with slits on the Triax monochromator set at 0.1 mm corresponding to a resolution of 0.35 nm. The red and blue spectra were taken with slits of 1 mm corresponding to a resolution of 3.5 nm.

2.5 CO_2

The undispersed fluorescence excitation spectrum of CO_2 recorded over the 17 – 20 eV range using the HEG is shown in Figure 2.9. The signal onset is seen at 17.34 eV followed by a series of peaks at higher photoexcitation energies. This onset corresponds to the energy of the v' = 0 level of CO_2^+ $\tilde{A}^2\Pi_u$, with emission being due to the CO_2^+ $\tilde{A}^2\Pi_u - \tilde{X}^2\Pi_g$ transition. The majority of the peaks have been assigned by other groups [10,11] to higher vibrational levels of CO_2^+ $\tilde{A}^2\Pi_u$, a minority to Rydberg states of CO_2 which autoionise into the CO_2^+ $\tilde{A}$ state continuum. The most prominent peak is seen at 18.12 eV, this corresponds to the energy of the CO_2^+ $\tilde{B}^2\Sigma_u^+$ state, with the observed emission being now due to the CO_2^+ $\tilde{B}^2\Sigma_u^+ - \tilde{X}^2\Pi_g$ transition. The non-resonant nature of all these peaks, especially clear for the CO_2^+ $\tilde{B}$ threshold at 18.12 eV, is noted.

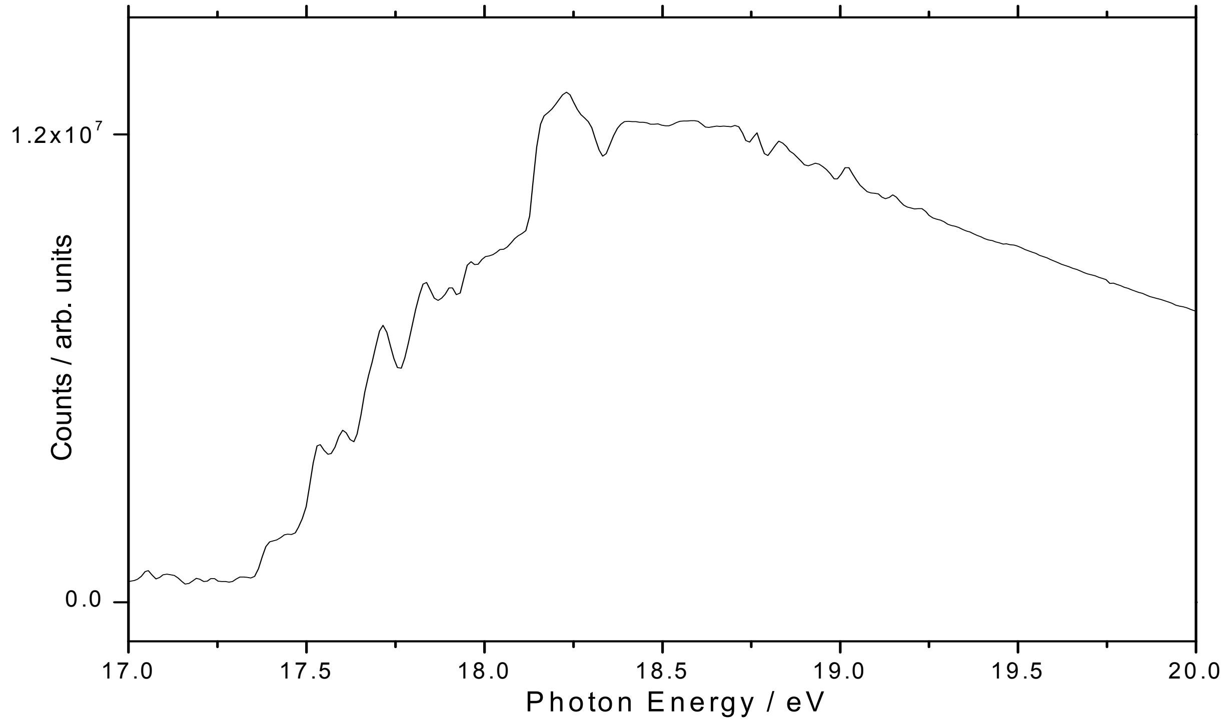

Figure 2.9: The undispersed fluorescence excitation spectrum of CO_2, taken using the HEG with a optical resolution of 0.1 nm, and a step size of 0.01 eV.

The dispersed fluorescence spectrum of CO_2^+ taken at a photoexcitation energy range between 17.33 and 18.10 eV is shown in Figure 2.10. In total five spectra are shown, increasing in energy from bottom to top. The first spectrum taken at 17.33 eV shows peaks originating from v' = 0 level of CO_2^+ $\tilde{A}^2\Pi_u$ state. The first peak seen at 352 nm corresponds to the $\tilde{A}^2\Pi_u(000) - \tilde{X}^2\Pi_g(000)$ transition. A second peak seen at 368 nm has been assigned as originating from the same vibrational level of the upper $\tilde{A}^2\Pi_u$ state as the previous peak but this time terminating on the (100) level of the CO_2^+ ground state. As the photoexcitation energy is increased higher vibrational levels of the $\tilde{A}^2\Pi_u$ state are populated, and more emission bands are observed at lower wavelengths.

At 18.1 eV there is sufficient energy available to populate the $\tilde{B}^2\Sigma_u^+$ state of CO_2^+, and figure 2.10 shows the spectrum taken at 18.1 eV. The peak seen at 289 nm is due to the $\tilde{B}^2\Sigma_u^+(000) - \tilde{X}^2\Pi_g(000)$ transition, which has high relative intensity because this transition involves negligible change in the C-O bond length. A higher resolution spectrum at this energy is shown in figure 2.11. The doublet splitting of 1.24 nm or 148 cm^{-1} is due to the spin-orbit splitting of CO_2^+ $\tilde{X}^2\Pi_g(000)$ [10,11]. This state shows a negative, 'inverted' spin-orbit splitting, but its sign cannot be determined from this spectrum.

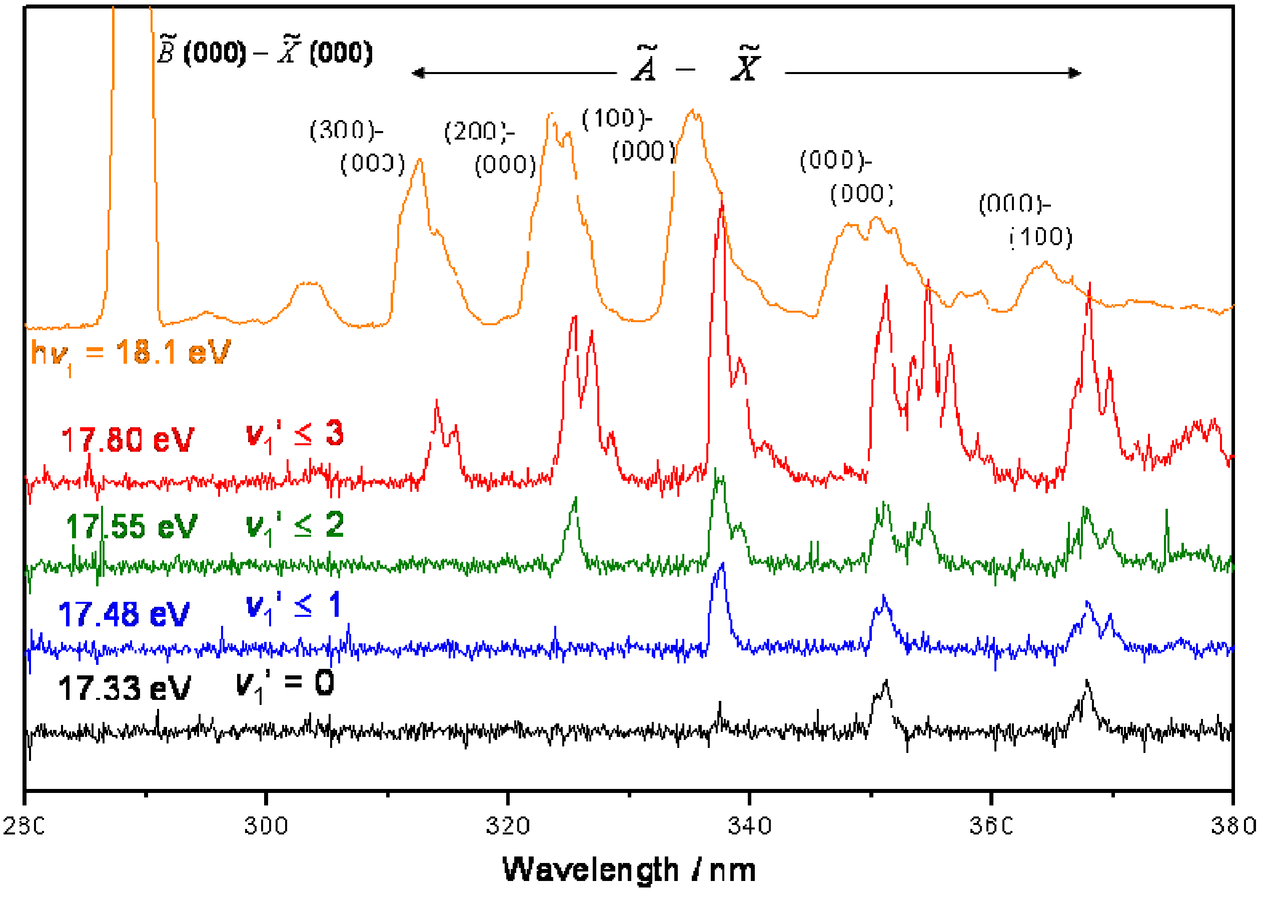

Figure 2.10: The dispersed fluorescence spectra of CO_2 taken in the range 17.33 to 18.1 eV.

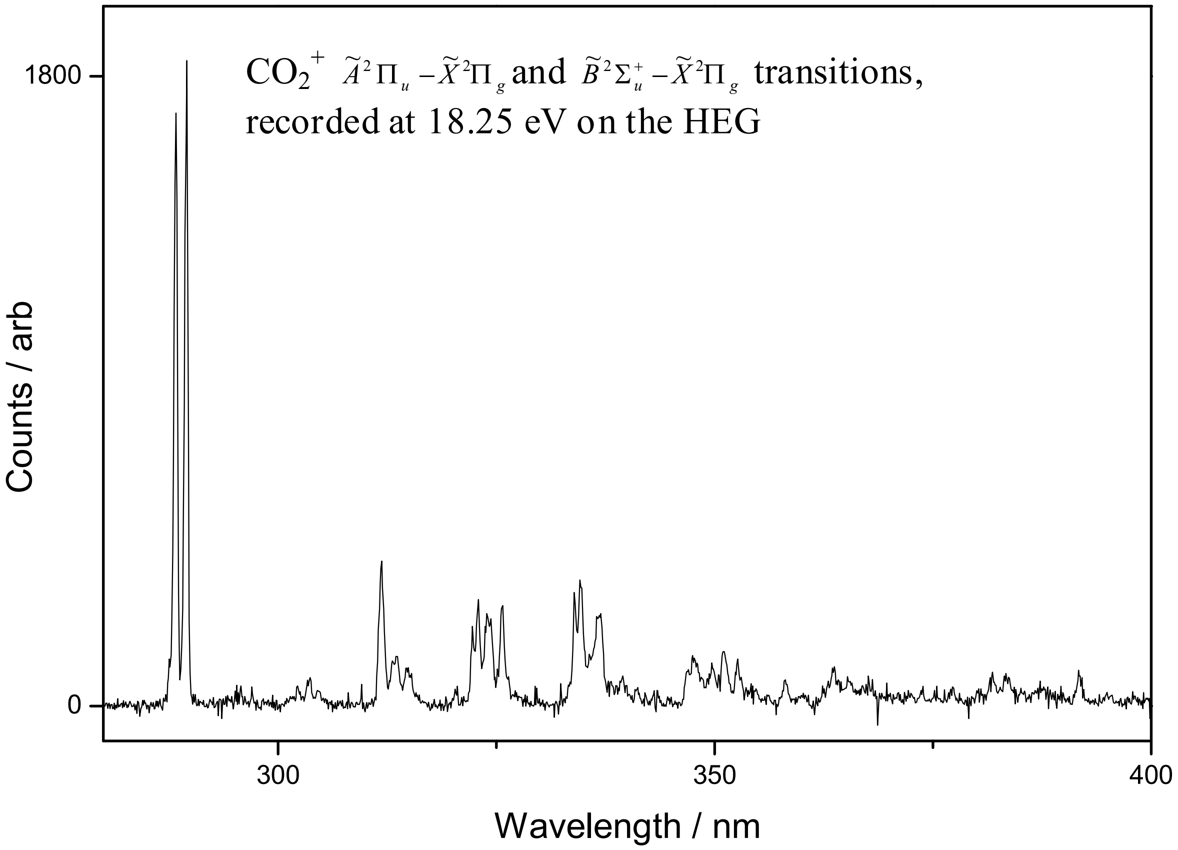

Figure 2.11: The dispersed fluorescence spectrum of CO_2 taken with 0.1 mm slits on the Triax monochromator, corresponding to a resolution of 0.35 nm.

2.6 Absorption Apparatus

All the absorption spectra presented in this thesis have been taken by previous members of the Tuckett group at the now decommissioned BESSY 1 synchrotron radiation source in Berlin. Briefly, radiation from the synchrotron passes through the exit slit of a VUV monochromator (a 1.5 m normal-incidence at Bessy-I), a two-stage differential pumping section, and a 1 mm thick stainless steel microchannel plate into an absorption cell of length, *L*, 300 mm(figure 2.12). A pressure differential of 1000:1 across the microchannel plate is possible. This plate can transmit wavelengths well below 100 nm, so this experiment can measure absorption spectra below the LiF cut-off, and yet the path length of the absorption 'cell' is defined. The gas pressure in the absorption cell, in the range 5-60 μbar, is maintained constant *via* a slow controlled flow of gas.

The VUV radiation at the end of the cell is detected through a sodium-salicylate-coated window and a visible photomultiplier tube. Since the pressure of gas and optical path length are known, measurement of the ratio of transmitted intensity observed for background (no gas) and sample spectra (with gas) can yield, *via* the Beer Lambert law $ln(I_o/I) = \sigma cL$, absolute absorption cross sections, σ, in units of cm^2 $molecule^{-1}$; *c* is the number density of the gas in units of molecules cm^{-3}, and *L* has units of cm. In the calculation of I_o/I at every value of the VUV energy, allowance is made for the natural decay of the VUV flux over the time of an experiment. No allowance is made for the small pressure gradient within the absorption cell due to gas leakage through the microchannel plate, and the small effects of second-order radiation from the VUV monochromator are ignored. We estimate that cross sections are accurate to *ca.* 15-20 %, and the ignorance of second-order effects may make this error greater at wavelengths close to twice the blaze wavelength of the grating in the VUV monochromator. Absorption spectra in the range *ca.* 50-200 nm at a resolution of better than 0.1 nm can routinely be measured. The range of cross sections that can be determined span ca 10^{-16} to 10^{-20} cm^2.

For the undispersed fluorescence excitation spectra of CCl_4, $SiCl_4$ and $GeCl_4$ shown in chapter 3, the absorption cell in figure 2.12 is replaced with a 50 mm^3 brass cube with a small aperture for differential pumping. Gas enters from one side of the cube and its opposite face has a small spectrosil B quartz window which mounts onto the entrance of a 0.2 m focal length scanning Jobon-Yvon H20VIS or H20UV monochromator. Dispersed radiation is detected through an exit slit by a cooled single photon-counting PMT. Clearly our apparatus used at Daresbury (figure 2.4) is modelled on this earlier design, but we believe the later apparatus has significant improvements:

(a) The aluminised cube is machined out of one solid piece of metal, where the BESSY cube incorporates two pieces joined together with araldite (epoxy glue).
(b) The Daresbury apparatus can incorporate in situ a sodium salicylate window for flux normalisation, whereas this was not possible with the BESSY apparatus.
(c) The Daresbury apparatus incorporates a CCD multi-channel detector with the Jacquinot advantage, whereas the Berlin dispersion monochromator involves the scanning of a grating.

Disadvantages:

(a) To take action spectra is difficult. Can only use undispersed spectra and filter.
(b) Time-resolved measurements with CCD are impossible. Lifetimes of emitting states cannot be measured [3].

One of the main purposes of this research project was to compare the relative sensitivities of these two different approaches to measuring dispersed fluorescence spectra. This has proved very difficult to quantify because other aspects of the experiment have changed (e.g. different synchrotron sources). However, the results shown in chapters 3 – 9 indicate strongly that the multi-channel detector approach is at least as sensitive as the dispersed approach using a photon-counting PMT, and in certain circumstances the CCD can provide superior spectra.

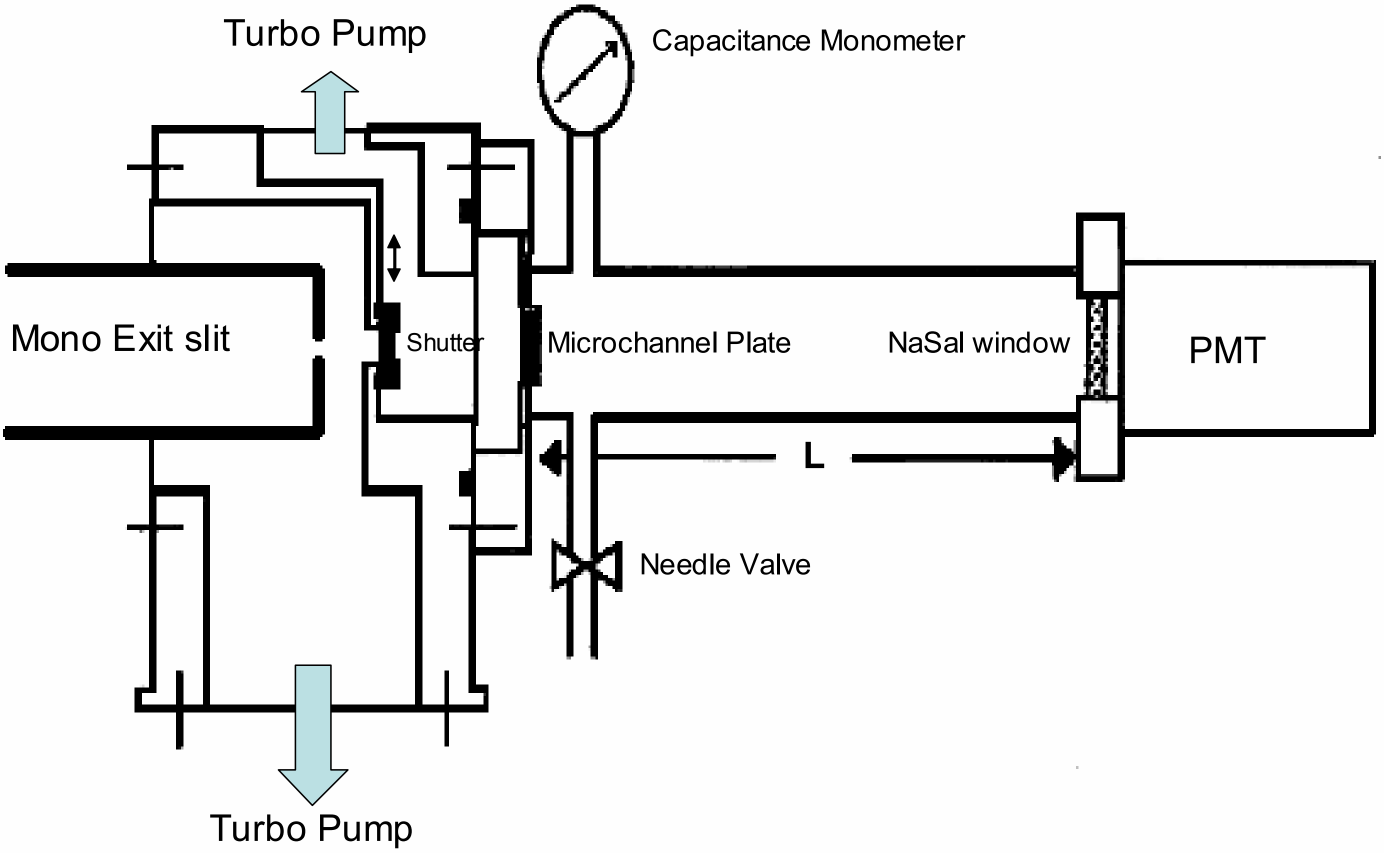

Figure 2.12: A schematic of the absorption apparatus at BESSY 1.

2.7 References

[1] F.L.O. Wadsworth, *AstroPhys. J.* **3** (1896) 54.

[2] C.R. Howle, S. Ali, R.P. Tuckett, D.A. Shaw and J.B. West, *Nucl. Instr and Methods B*, **237** (2005) 656.

[3] H. Biehl, K. J. Boyle, D. P. Seccombe, R. P. Tuckett, H. Baumgärtel and H. W. Jochims, *J. Chem. Phys,* **108** (1998) 857

[4] P. Jacquinot, *J. Opt. Soc. Am.* **44** (1954) 761.

[5] M. Skibowski, W. Steinmann, *J. Opt. Soc. Amer.,* **57** (1967) 112.

[6] P. D. Johnson, *Rev. Sci. Instr.*, **28** (1957) 833.

[7] R. Onaka, *Sci. Light (Tokyo),* **7** (1958) 23.

[8] H. Biehl, J.C. Creasey, D.M. Smith, R.P. Tuckett, K.R. Yoxall, H. Baumgartel, H.W. Jochims, U. Rockland, *J. Chem. Soc. Faraday Trans.* **91**, (1995) 3073.

[9] NIST website http://webbook.nist.gov

[10] L.C. Lee, *J. Phys. B.: At. Mol. Opt. Phys.* **10** (1977) 3033.

[11] L.C. Lee, R.W. Carlson, D.L. Judge, *J. Phys. B.: At. Mol. Opt. Phys.* **9** (1976) 855.

[12] A. Carrington, R.P. Tuckett, *Chem. Phys. Lett.* **74** (1980) 19.

[13] E.D. Poliakoff, Ming-Hang Ho, G.E. Leroi, M.G. White, *J. Chem. Phys.* **84** (1986) 4779.

[14] C.R. Howle, PhD Thesis, University of Birmingham (2004).

[15] P. Erman, A. Karawajczyk, U Koble, E. Rachlew, K. Yoshiki Franzen, L. Veseth, *Phys. Rev. Lett.* **76** (1996) 4136.

[16] R.E. Huffman, Y. Tanaka, J.C. Larrabee, *J. Chem. Phys.* **38** (1963) 1920.

[17] M.A. Johnson, R.N. Zare, J. Rostas, S. Leach, *J. Chem. Phys.* **80** (1984) 2407.

[18] J. Rostas, R.P. Tuckett, *J. Mol. Spec.* **96** (1982) 77.

[19] Ikuo Tokue, Takeyuki Kudo, Masaaki Kobayasi, Katsuyoshi Yamasaki, Bull. *Chem. Soc. Jpn.* **70** (1997) 71.

[20] L.C. Lee, Xiuyan Wang, Masako Suto, *J. Chem. Phys.* **85** (1986) 6294.

[21] H. Biehl, K.J. Boyle, R.P. Tuckett, H. Baumgartel, H.W. Jochims, *Chem. Phys.* **214** (1997) 367.

[22] A. J. Yencha, A. Hopkirk, A. Hiraya, G. Dujardin, A. Kvaran, L. Hellner, M. J. Besnard-Ramage, R. J. Donovan, J. G. Goode, R. R. J. Maier, G. C. King, S. Spyrou, *J. Elec. Spec. Rel. Phen.*, **70** (1994) 29.

[23] J.F.M. Aarts, *Chem. Phys. Lett.* **114** (1985) 114.

[24] G. Dujardin, S. Leach, *Faraday Discuss. Chem. Soc.* **75** (1983) 23.

[25] G. Dujardin, S. Leach, O. Dutuit, T. Govers, P.M. Guyon, *J. Chem. Phys.* **79** (1983) 644.

[26] Chuanyong Wu, E.D. Poliakoff, *Chem. Phys. Lett.* **292** (1998) 167.

[27] R.P. Tuckett, *Chem. Phys.* **58** (1981) 151.

[28] T.J. Sears, T.A. Miller, V.E. Bondybey, *J. Am. Chem. Soc.* **103** (1981) 326.

[29] C. Cossart-Magos, D. Cossart, S. Leach, *Mol. Phys.* **37** (1979) 793.

3: VUV absorption and undispersed fluorescence excitation spectroscopy of CCl_4, $SiCl_4$ and $GeCl_4$

In this chapter we present the VUV photoabsorption spectra of CCl_4, $SiCl_4$ and $GeCl_4$ which have been recorded by our group at the BESSY 1 synchrotron radiation source in Berlin. The data was recorded in the last year of the operation of BESSY 1, but had remained unassigned untill now. The absorption peaks have been assigned using the Rydberg formula and compared to the literature. The undispersed fluorescence excitation spectra of the molecules were recorded at the Daresbury synchrotron radiation source (SRS), and they are compared to the absorption spectra.

3.1 Introduction

All the titled molecules are important gases in atmospheric chemistry. The photolysis of these chemicals can produce atomic Cl which has implications for the chemistry of the ozone layer. Prior to the Montreal Protocol of 1987, large quantities of carbon tetrachloride were used to produce refrigerants, which contained chlorofluorocarbons (CFCs). Due to their role in ozone depletion, these refrigerants have now been phased out of use. CCl_4 has also been used in a variety of other applications before it was discovered to be a carcinogen. One such use was as a fire extinguisher agent. Besides the carcinogenic hazard this poses, an additional danger is that carbon tetrachloride can form phosgene gas (Cl_2CO, used as a chemical weapon in World War I) when used on electrical fires. The gas was also used as an industrial solvent and in the dry cleaning industry before its health hazards became known. $SiCl_4$ and $GeCl_4$ are used widely in the manufacture of semiconductors. $SiCl_4$ is used to make optical fibres which are in turn used to make fibre optic cables in the communications industry.

Previous studies on the VUV absorption spectroscopy of these molecules were mostly recorded at wavelengths above the LiF window cutoff of 105 nm. Causley and Russell [1] observed the photoabsorption spectra of CCl_4, $SiCl_4$ and $GeCl_4$ between 115 and 150 nm. The majority of the transitions were assigned as either valence in nature or Rydberg excitations of the electron from the non-bonding halogen $1t_1$, $3t_2$ and 1e molecular orbitals. Using a synchrotron as the radiation source, Ho [2] obtained the photoabsorption cross-sections of CCl_4, between 6 and 250 eV. Work was done on photoabsorption and fluorescence cross-sections of CCl_4, by Lee and Suto [3]. Ibuki et al [4] using synchrotron radiation has recorded absolute photoabsorption cross-sections and fluorescence excitation spectra of CCl_4 down to 100 nm, these fluorescence cross-sections are on a relative scale.

This group have recorded both absolute photoabsorption and absolute fluorescence cross-sections of $SiCl_4$ between 40 and 200 nm [5]. The absolute fluorescence cross-sections are normally much more difficult to determine (see section 3.2.1). They used a LiF widow to remove higher order radiation at excitation wavelengths > 105nm, and thin metal films of Te, Sn and In were used as windows at wavelengths < 105nm. Ibuki et al [6] have also observed absolute photoabsorption and fluorescence cross-sections for $GeCl_4$ between 40 and 200nm. Assignments for these molecules have been given as transitions to Rydberg states from the Cl 3pπ non-bonding molecular orbitals.

3.2 Results

The photoabsorption spectra of these molecules were recorded at the BESSY 1 synchrotron radiation source. The radiation was dispersed using a VUV normal incidence 225 McPherson monochromator, containing a 1200 g/mm laminar Zeiss grating which has an energy range of 6 to 25 eV. The spectra obtained had a resolution of 0.08 nm. The resonant peaks seen in the spectra are mainly due to absorption to the Rydberg states. The Rydberg transitions are assigned using the ionisation energies (IE) of the state of the parent ion to which the Rydberg state converges using the well known Rydberg formula

$$E = IE - R_H/(n-\delta)^2$$

where E is the energy of the transition, IE is the vertical ionisation energy to which the Rydberg states converge, n is the principal quantum number of the Rydberg orbital, and δ is the quantum defect of the core. δ can be described as the deviation of the core from an impenetrable point charge. Choosing whether vertical or adiabatic ionisation energies should be used can make a significant difference to the assignment of the Rydberg state. In the work done in this thesis vertical ionisation energies are used for two reasons. The first reason is that no vibrational structures are seen in any of the Rydberg transitions. Each band in the photoabsorption spectrum will represent a convolution of many vibrational components. Each of these components will have an appropriate Franck-Condon factor. There is a negligible geometry change between the Rydberg state and the state of the parent ion to which it converges. In a photoelectron spectrum with an unresolved band the peak will correspond to the maximum in the Franck-Condon-weighted vibrational envelope. This is equivalent to the vertical ionisation energy. It is sensible to assume that under these conditions the peaks in the Rydberg spectra can then be assigned by their convergence on the vertical ionisation energy of the parent ion. Secondly the adiabatic ionisation energy is taken to be the energy at which the signal rises above the background. This point of signal increase is often called the onset. Adiabatic ionisation energy is defined as the transition from the v = 0 of the neutral molecule to the v = 0 of the ion. If the Franck-Condon factors at threshold are very low the signal onset can be seen at a higher energy than the true adiabatic ionisation energy. Therefore in a vibrationally unresolved photoelectron band it is probably unwise to use the first signal onset as the true adiabatic ionisation energy. For both these reasons and because the spectra presented in this thesis generally are of a modest resolution we use vertical ionisation energies to assign Rydberg transitions.

3.2.1 CCl_4 photoabsorption spectroscopy

The electronic configuration of the outer valence molecular orbitals of CCl_4 is …..$(2a_1)^2$ $(2t_2)^6$ $(1e)^4$ $(3t_2)^6$ $(1t_1)^6$. The numbering scheme does not include core orbitals. These orbitals arise from the overlap of the 16 chlorine atom valence orbitals, Cl 3s 3p, with the central atom valence orbitals, C 2s 2p. The vertical ionisation energies for the five outermost occupied valence orbitals have been measured to be 11.64 ($1t_1$), 12.51 ($3t_2$), 13.37 (1e), 16.68 ($2t_2$), and 19.9 ($2a_1$) using He(I) and He(II) photoelectron spectroscopy [7]. The quantum defects of ns, np and nd Rydberg orbitals centred on C (Cl) atoms are predicted to be 0.98 (2.01), 0.58 (1.57), and 0.01 (0.09) [8]. The molecular orbitals 1e, $3t_2$ and $1t_1$ are all Cl 3pπ non-bonding in character. These molecular orbitals have no contribution from the C atom and therefore their quantum defects should have characteristics of an isolated Cl atom. The photoabsorption spectrum was taken in the 6 to 25 eV energy range and with a resolution of 0.08 nm on the primary monochromator. The features of our spectrum are broadly in line with previous work with our spectra having a slightly better resolution.

Resonant peaks are seen from 6 to 14 eV; the shapes of the peaks are characteristic of a resonant primary excitation process. Most of the literature has assigned the first peak at 7.04 eV as a valence transition originating from the $3t_2$ orbital of CCl_4. Our assignment is in agreement with these papers and have assigned this peak to the $(3t_2)^{-1}$ $3a_1$ transition. The next peak at 8.94 eV also originates from the $3t_2$ orbital of CCl_4 but this peak is assigned to a Rydberg transition. Using the Rydberg formula a quantum defect δ value of 2.03 is obtained. The quantum defect value expected for an isolated chlorine atom to a 4s Rydberg orbital is 2.01, therefore we can assign this peak to the $(3t_2)^{-1}$ 4s transition.

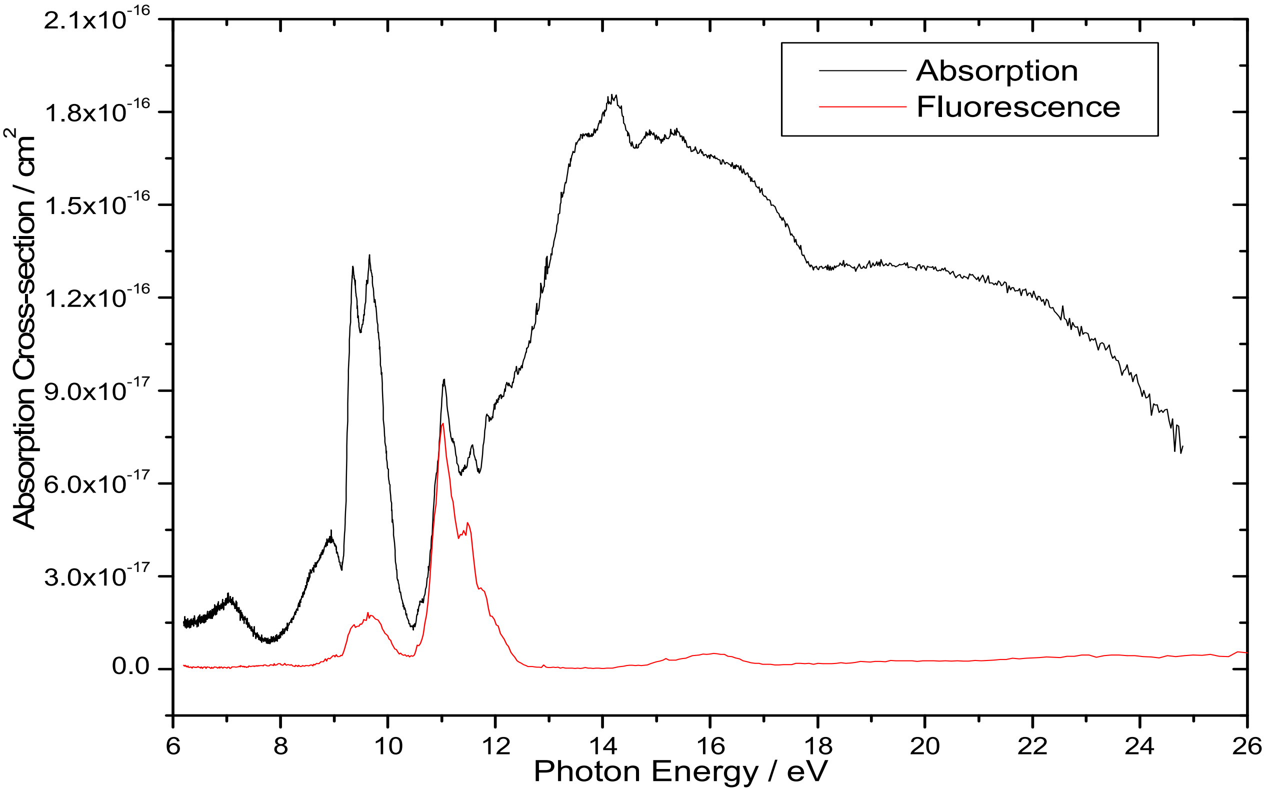

Figure 1: The absolute photoabsorption cross-section of CCl_4 taken at Bessy1 is shown. The fluorescence excitation spectrum measured at Daresbury is also shown to compare qualitatively the importance of the fluorescence decay channel. Absorption cross-sections shown are absolute, whereas the fluorescence signal is arbitrary

The two peaks seen at energies of 9.35 and 9.66 eV have also been assigned as due to Rydberg transitions. This time the first peak at 9.35 eV originates from the $1t_1$ orbital, while the peak at 9.66 eV has its origins in the $3t_2$ molecular orbital. Both transitions result in excitation of the electron to the 4p Rydberg orbital. The obtained quantum defect values of 1.57 and 1.81 are compared to the value for an isolated chlorine atom at 1.57. Another possible assignment for the 9.66 eV peak is the $(1t_1)^{-1}$ 5d transition. By comparing the fluorescence excitation and photoabsorption spectrum of CCl_4, it is observed that at these energies there is good correlation between the two spectra. In the fluorescence excitation spectrum there are two distinctive peaks at 9.42 and 9.70 eV. The fluorescence is a result of emission from the CCl_2 fragment (chapter 4). As the fragmentation of CCl_4 occurs through a dissociative Rydberg state of the molecule it is sensible to assume that this fragmentation occurs from the same Rydberg state for both transitions. The quantum defect value obtained for the transition $(1t_1)^{-1}$ 5d is 0.38. This is a higher value than what would be expected for an isolated chlorine atom (0.09). For both these reasons we can discount this assignment as a possibility. Full assignments for all the peaks in the spectrum are presented in table 1.

Between the excitation energies of 8.8 and *ca* 12 eV the profile of the fluorescence excitation and the photoabsorption spectra are very similar with the relative intensities of the 10 eV and 11 eV bands differing. Above 12 eV there is very little resemblance between the two. While we see some broad non resonant bands in the photoabsorption spectrum no such features are seen in the fluorescence excitation spectrum. In fact apart from a small peak around *ca* 16 eV very little fluorescence is observed for CCl_4 above *ca* 12 eV.

For the photoabsorption spectra absolute cross-sections were measured. Recording the absolute fluorescence cross-sections is more difficult. To do this calibration would be required with a well studied system which fluoresces in the VUV. An ideal system would be the N_2^+ ($B\ ^2\Sigma_u^+ \rightarrow X\ ^2\Sigma_g^+$) fluorescence signal. By normalising the fluorescence intensity for the system of study to the N_2^+ signal, fluorescence cross-sections can be determined. The absolute quantum yields to produce fluorescing fragments from an excited state were not determined either. The fluorescence yield can be defined as the ratio of fluorescence cross-section to the absorption cross-section. It is a measure of the interaction strength between the initial excited state and the repulsive state that produces the emitting species. When a molecule is excited by a photon to determine the fluorescence quantum yield both the absolute photoabsorption and fluorescence excitation cross-sections need to be known.

E(eV)	Upper state configuration	IE-E(eV)	n-δ	δ
7.04	$(3t_2)^{-1}$ 3a$_1$	5.47		
8.94	$(3t_2)^{-1}$ 4s	3.57	1.95	2.04
9.35	$(1t_1)^{-1}$ 4p	2.29	2.44	1.56
9.66	$(3t_2)^{-1}$ 4p	2.85	2.18	1.81
10.63	$(3t_2)^{-1}$ 3d	1.88	2.69	0.31
11.05	$(1e)^{-1}$ 4p	2.32	2.42	1.58
11.58	$(3t_2)^{-1}$ 6s	0.93	3.82	2.17
11.85	$(1e)^{-1}$ 5s	1.52	2.99	2.01
13.68	$(2t_2)^{-1}$ 4s	3.00	2.13	1.87
14.17	$(2t_2)^{-1}$ 4p	2.51	2.33	1.67
14.87	$(2t_2)^{-1}$ 3d	1.81	2.74	0.26
15.39	$(2t_2)^{-1}$ 5p	1.29	3.25	1.75

Table 1: CCl_4 Photoabsorption assignments and quantum defect values.

3.2.2 $SiCl_4$ Photoabsorption spectrum

The electronic configuration of the outer valence molecular orbitals of $SiCl_4$ is also …..$(2a_1)^2$ $(2t_2)^6$ $(1e)^4$ $(3t_2)^6$ $(1t_1)^6$. The numbering scheme does not include core orbitals. . The vertical ionisation energies for the five outermost occupied valence orbitals have been measured to be 12.12 ($1t_1$), 13.03 ($3t_2$), 13.51 (1e), 15.27 ($2t_2$), and 18.10 ($2a_1$) using He(I) and He(II) photoelectron spectroscopy [7]. The quantum defects of ns, np and nd Rydberg orbitals centred on Si (Cl) atoms are predicted to be 1.80 (2.01), 1.36 (1.57), and 0.10 (0.09) [8]. Just as for the CCl_4 molecule, the molecular orbitals 1e, $3t_2$ and $1t_1$ are all Cl 3pπ non-bonding in character. These molecular orbitals have no contribution from the Si atom and therefore their quantum defects should have characteristics of an isolated Cl atom.

The photoabsorption spectrum of $SiCl_4$ taken at the BESSY 1 with a resolution of 0.08 nm is shown in figure 2. The fluorescence excitation spectrum of $SiCl_4$ taken at BESSY 1 is also shown to provide a qualitative comparison with the photoabsorption spectrum. Between the excitation energies of 8 and 16 eV numerous resonant peaks are observed. At *ca.* 16 eV there is a broad non resonant band which peaks at *ca* 17 eV with signal still being observed well after the onset. The first peak we see is at 8.84 eV: a fit to the Rydberg formula gives an assignment to the $(3t_2)^{-1}$ 4s transition with a quantum defect of 2.2. This is in reasonable agreement with the value of 2.01 for an isolated chlorine atom. Although we do get a better fit if we assign it as a $(1t_1)^{-1}$ 4s transition, which gives us a quantum defect value of 1.96. In tetrahedral (T_d) symmetry a $t_1 \rightarrow s$ transition is forbidden [27] therefore we can discount this as a possible assignment.

The next peak at 9.62 eV now originates from the 1e molecular orbital of $SiCl_4$ and has been assigned to the $(1e)^{-1}$ 4s transition. There are two further peaks seen at energies of 9.78 and 10.08 eV. They are shown to terminate in the 4p and 4p' Rydberg orbitals of $SiCl_4$. The transitions originate from the $3t_2$ molecular orbital, which is split in the Rydberg excited state by the Jahn-Teller effect [26]. Similarly the photoabsorption peaks at 11.11 and 11.39 eV terminate in the 5s and 5s' Rydberg states with its origins in the $3t_2$ molecular orbital. A full list of all assignments are presented in table 2.

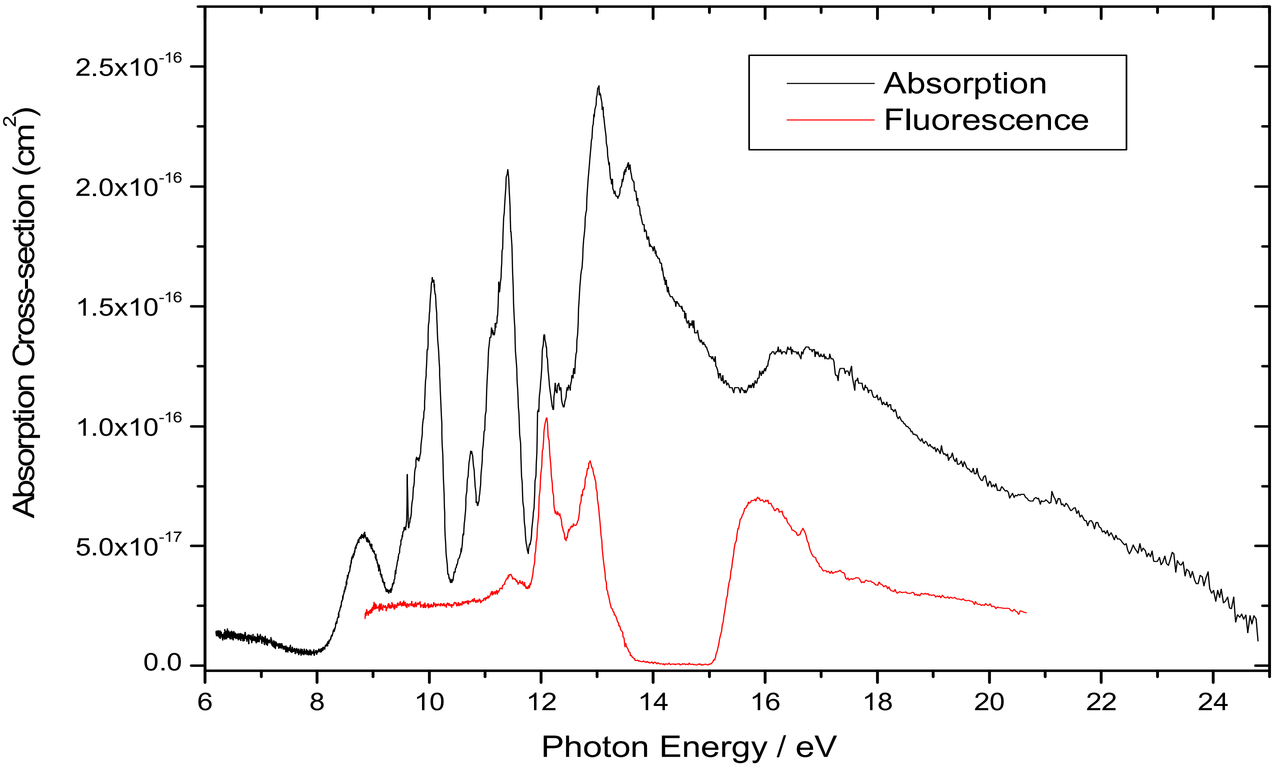

Figure 2: The photoabsorption spectrum of $SiCl_4$ taken at BESSY 1 with a resolution of 0.08 nm, the fluorescence excitation spectrum is shown for a qualitative comparison. Absorption cross-sections shown are absolute, whereas the fluorescence signal is arbitrary

The photoabsorption spectrum of $SiCl_4$ is compared to the fluorescence excitation spectrum in figure 2 above. Below 11 eV there is little resemblance between the two spectra. The first peak we see in the fluorescence excitation spectrum is a broad resonant peak at 11.45 eV. The fluorescence signal has been attributed to a transition emanating from the triplet state of the $SiCl_2$ radical (chapter 4). Production of the 5s and 5s' Rydberg states result in fragmentation of the $SiCl_4$ molecule. This in turn produces fluorescence originating from the $SiCl_2$ $\tilde{a}\,^3B_1$ triplet state.

There is very good correlation between the two spectra in the energy range *ca* 11.75 and 13.5 eV. The relative intensities of the two spectra do not match but the profiles are a very similar. The fluorescence signal is also a result of emission from the $SiCl_2$ radical. This time the resultant signal originates from the $SiCl_2$ $\tilde{A}\,^1B_1$ singlet state. A further broad non resonant band is seen above 15.1 eV with a peak at 15.9 eV. The emission is from the parent ion and has its origins in the $SiCl_4^+$ $\tilde{C}\,^2T_2$ state.

E(eV)	Upper state configuration	IE-E(eV)	n-δ	δ
8.84	$(3t_2)^{-1}$ 4s	4.19	1.80	2.20
9.62	$(1e)^{-1}$ 4s	3.89	1.87	2.13
9.78	$(3t_2)^{-1}$ 4p	3.25	2.05	1.95
10.08	$(3t_2)^{-1}$ 4p'	2.95	2.15	1.85
10.74	$(1e)^{-1}$ 4p	2.77	2.22	1.78
11.11	$(3t_2)^{-1}$ 5s	1.92	2.66	2.34
11.39	$(3t_2)^{-1}$ 5s'	1.64	2.88	2.12
12.03	$(1e)^{-1}$ 5p	1.48	3.03	1.97
12.25	$(2t_2)^{-1}$ 4s	3.02	2.12	1.88
13.00	$(2t_2)^{-1}$ 4p	2.27	2.45	1.55
13.58	$(2t_2)^{-1}$ 3d	1.69	2.84	0.16

Table 2: $SiCl_4$ Photoabsorption assignments and quantum defect values.

3.2.3 $GeCl_4$ Photoabsorption spectrum

The final chemical in this series of photoabsorption spectra is $GeCl_4$. Like the two preceding molecules $GeCl_4$ has tetrahedral symmetry and has an electronic configuration of …..$(2a_1)^2$ $(2t_2)^6$ $(1e)^4$ $(3t_2)^6$ $(1t_1)^6$. The numbering scheme does not include core orbitals. The vertical ionisation energies for the five outermost occupied valence orbitals have been measured to be 12.17 ($1t_1$), 12.64 ($3t_2$), 13.05 (1e), 14.88 ($2t_2$), and 18.38 ($2a_1$) using He(I) and He(II) photoelectron spectroscopy [7]. The quantum defects of ns, np and nd Rydberg orbitals centred on Ge (Cl) atoms are predicted to be 2.81 (2.01), 2.34 (1.57), and 1.05 (0.09) [8]. The three molecular orbitals 1e, $3t_2$ and $1t_1$ are all Cl 3pπ non-bonding in character. These molecular orbitals have no contribution from the Ge atom and therefore their quantum defects should have characteristics of an isolated Cl atom.

The photoabsorption spectrum of $GeCl_4$ taken between 9 and 15.5 eV and with a resolution of 0.08 nm is shown in figure 3. The undispersed fluorescence excitation spectrum is also shown for a qualitative comparison. The first peak we see in our spectrum is at 9.53 eV. Again the shape of the peak would imply that this process is of a resonant nature. This feature is again assigned as a transition from one of the chlorine lone pair molecular orbitals, specifically the $1t_1$ orbital. The second feature in our spectrum is at 9.99 eV this time the peak has been assigned to the $3t_2$ molecular orbital of $GeCl_4$. Both of these peaks are a result of the two transitions converging on the 4p Rydberg orbital. The quantum defect values obtained for these two peaks are 1.73 for both the $(3t_2)^{-1}$ 4p and $(1t_1)^{-1}$ 4p transitions. The peak at 10.39 eV also belongs to the 4p Rydberg orbital but this time originating from the 1e molecular orbital the quantum defect value for this peak is 1.74. Resonant peaks are seen up to *ca* 12.5 eV with some broad non resonant features appearing after 13 eV. The assignments for theses peaks are fully listed in table 3.

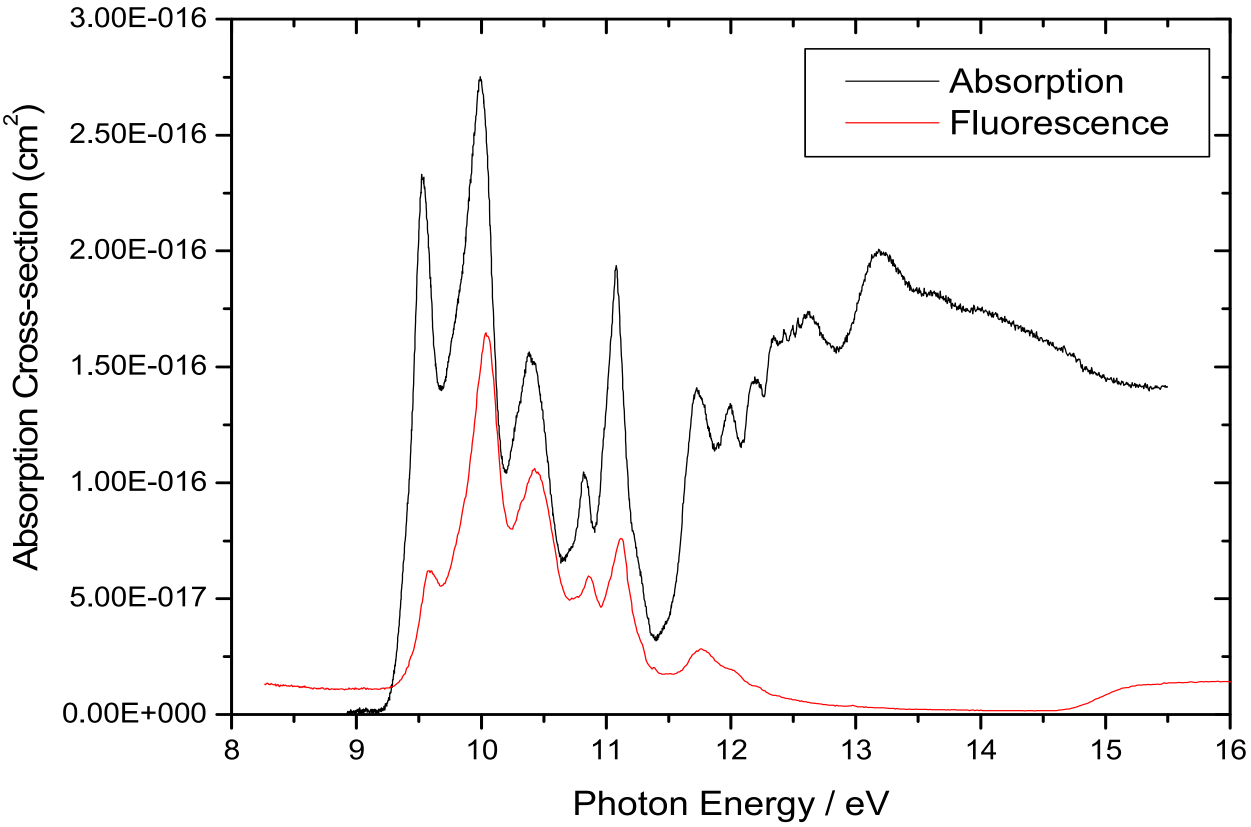

Figure 3: The photoabsorption and fluorescence excitation spectrum of $GeCl_4$. Absorption cross-sections shown are absolute, whereas the fluorescence signal is arbitrary

Figure 3 also shows the fluorescence excitation spectrum of $GeCl_4$. The two spectra have a very similar profile up to the energy of *ca* 12 eV. There is much more agreement between the photoabsorption and fluorescence spectra of $GeCl_4$ from 9 – 11 eV than either of the other two molecules. This would suggest that the path to dissociation of $GeCl_4^*$ to fluorescing states of $GeCl_2$ is a major channel, more significant than equivalent channels of $SiCl_4^*$ and CCl_4^*. The fluorescence excitation peaks have been attributed to emission emanating from either the $GeCl_2$ $\tilde{a}\ ^3B_1$ triplet or the $GeCl_2$ $\tilde{A}\ ^1B_1$ singlet state with the triplet state being the dominant channel. At the lowest energy of 9.51 eV no signal from the singlet state is observed at all. So we can say that the Rydberg states in the photoabsorption spectrum of $GeCl_4$ at energies below 12 eV dissociate producing $GeCl_2$ radicals. The resulting fluorescence from $GeCl_2$ radical is a result of a transition from the triplet $\tilde{a}\ ^3B_1$ and the singlet $\tilde{A}\ ^1B_1$ to the ground $\tilde{X}\ ^1A_1$ state. The fluorescence excitation spectrum also shows a non resonant feature with a threshold at *ca* 14.7 eV. This has been attributed to fluorescence emanating from the parent ion $GeCl_4^+$(chapter 4).

E(eV)	**Upper state configuration**	**IE-E(eV)**	**n-δ**	**δ**
9.53	$(1t_1)^{-1}$ 4p	2.64	2.27	1.73
9.99	$(3t_2)^{-1}$ 4p	2.65	2.27	1.73
10.39	$(1e)^{-1}$ 4p	2.66	2.26	1.74
10.82	$(1t_1)^{-1}$ 5p	1.35	3.17	1.83
11.07	$(3t_2)^{-1}$ 5s	1.57	2.94	2.06
11.72	$(1e)^{-1}$ 5p or	1.33	3.20	1.80
	$(3t_2)^{-1}$ 6s	0.92	3.85	2.15
11.99	$(1e)^{-1}$ 6s	1.06	3.58	2.42
12.20	$(1e)^{-1}$ 6p	0.85	4.00	2.00
12.34	$(2t_2)^{-1}$ 4p	2.54	2.31	1.69
12.62	$(1e)^{-1}$ 6d	0.43	5.62	0.38
13.19	$(2t_2)^{-1}$ 5s	1.69	2.84	2.16

Table 3: $GeCl_4$ Photoabsorption assignments and quantum defect values.

3.3 Conclusions

In this chapter we have presented the photoabsorption spectra of CCl_4, $SiCl_4$ and $GeCl_4$. The peaks in the spectra have been assigned mainly to transitions that produce a Rydberg state. The fluorescence excitation spectra have also been presented to show the fluorescence decay channels that are available. The average quantum defect values obtained were, CCl_4 (δ) ns = 2.02 ± 0.15, (δ) np = 1.64 ± 0.15, $SiCl_4$ (δ) ns = 2.13 ± 0.21, (δ) np = 1.82 ± 0.27, $GeCl_4$ (δ) ns = 2.20 ± 0.14, (δ) np = 1.79 ± 0.21.

3.4 References

[1] G.C. Causley and B.R. Russell, *J. Electron Spec and Related. Phenom*, **11**, (1977), 383

[2] G.H. Ho, *Chemical Physics*, **226**, (1998), 101

[3] L.C. Lee, X.Wang and M. Suto, *J. Chem. Phys*, **85**, (1986), 6294.

[4] T.Ibuki . Takahashi, A. Hiraya and K. Shobatake, *J. Chem. Phys*, **85**, (1986), 5717

[5] T. Ibuki, M. Kono, Y. Asari, A. Hiraya and K. Shobatake, *J. Chem. Phys*, **106**, (1997), 4853.

[6] T. Ibuki and A. Kamamoto, *Chem. Phys*. Lett, **260**, (1996), 314

[7] P.J. Bassett and D.R. Loyd, *J. Chem. Soc. A,* **641**, (1971)

[8] C.E. Theodosiou, M. Inokuti and S.T. Mason,
Atomic Data and Nuclear Data Tables, **35** (1986), 473.

[9] W. Zhang, G. Cooper, T Ibuki and C.E. Brion, *Chem. Phys*, **160**, (1992), 435

[10] W. Zhang, G. Cooper, T Ibuki and C.E. Brion, *Chem. Phys*, **153**, (1991), 491

[11] W. Zhang, G. Cooper, T Ibuki and C.E. Brion, *Chem. Phys*, **151**, (1991), 343

[12] L.C. Lee, J.C. Han, C. Ye and M. Suto, *J. Chem. Phys*, **214**, (1990), 367.

[13] L.C. Lee, J.C. Han, C. Ye and M. Suto, *J. Chem. Phys*, **92**, (1990), 133.

[14] H. Biehl. K.J. Boyle, D.P. Seccombe, D.M. Smith, R.P. Tuckett, H. Baumgartel and H. W. Jochims, *J. Electron Spec and Related. Phenom*, **97**, (1998), 89

[15] H. Biehl. K.J. Boyle, R.P. Tuckett, H. Baumgartel and H.W. Jochims,
Chemical Physics, **214**, (1997), 367

[16] D.P Seccombe, R.P. Tuckett, H. Baumgartel and H.W. Jochims,
Phys. Chem. Chem. Phys, **1**, (1999), 773

[17] A.W. Potts, H.J. Lempka, D.G. Streets and W.C. Price,
Phil. Trans. Roy. Soc. Lond.A, **268**, (1970), 59

[18] J.C. Green, M.L.H. Green, P.J. Joachim, A.F. Orchard and D.W. Turner,
Phil. Trans. Roy. Soc. Lond.A, **268**, (*1970*), 111

[19] T. Cvitas, H Gusten and L Klansic, J. Chem. Phys, **67**, (1977), 2687

[20] T. Cvitas, H Gusten, L Klansic, I. Novak, H. Vancik and Z. Naturforsch, *J. Chem. Phys*, **33a**, (1978), 1528.

[21] C.R.Brundle, M.B.Robin and H.Basch, *J. Chem. Phys*, **53**, (1971), 2196.

[22] I. Tokue, T. Honda, Y. Ito, *Chem. Phys*, **140**, (1990), 157.

[23] M. Kusakabe, Y. Ito, I. Tokue, *Chem. Phys*, **179**, (1993), 243.

[24] K.Kamata, M. Ukai, T. Numazawa, N. Terazawa, Y. Chikahiro, N. Kouchi, Y. Hatano, K. Tanake, *J. Chem. Phys*, **99**, (1993), 2487.

[25] J. W. Au, G. R. Burton, C. E. Brion, *Chem. Phys*, **221**, (1997),151.

[26] M. B. Robin, *Higher excited states of polyatomic molecules*, **Vol 3**

[27] G. Herzberg, *Molecular spectra and molecular structure III, Electronic spectra and electronic structure of polyatomic molecules.*

4: VUV fluorescence spectroscopy of CCl_4, $SiCl_4$ and $GeCl_4$

4.1 Introduction

VUV fluorescence excitation spectra of the titled molecules have been studied before by the Tuckett group at Daresbury, using the 1 m Seya-Namioka monochromator on beamline 3.1 [1]. These spectra were taken in the energy range 9 to 25 eV with an optical resolution of 0.4 nm on the Seya. The spectra presented in this chapter were taken using the newly commissioned Wadsworth monochromator which replaced the Seya.

Fluorescence excitation spectra were taken using both the high energy grating (HEG) and medium energy grating (MEG), the optical resolution of the Wadsworth being set at 0.1 nm and 0.2 nm on the two gratings respectively. Dispersed fluorescence spectra and lifetime measurements of the same molecules were performed at BESSY 1, using a 1.5 m normal incidence monochromator attached to the 800 MeV electron storage ring [1]. The fluorescence was dispersed using one of two secondary monochromators, a 0.2 m focal length Jobin Yvon H20UV with an effective range of 190 to 500 nm, and a Jobin Yvon H20VIS with an effective range of 190 to 700 nm. The former detection system was used to disperse UV fluorescence bands at wavelengths less than 400 nm, the latter to disperse visible bands at wavelengths greater than 400 nm. The dispersed fluorescence spectra presented in this chapter were taken using the 0.19 m Jobin Yvon Triax monochromator described in chapter 2.3. At BESSY the dispersed fluorescence was detected using one of two photomultiplier tubes (PMT) depending on which secondary monochromator was used. The H20UV monochromator was used with an EMI 9789 QB at 298 K, while the H20VIS monochromator was used with a red-sensitive Hamamatsu R6060 tube cooled to 280 K. This new dispersed study at Daresbury used a liquid nitrogen cooled CCD detection system which had an effective range of between 200 and 900 nm. This work was done in the early days of my PhD. Its main aim was to compare sensitivities of the different detection systems.

Other groups have also studied the fluorescence spectroscopy of the three molecules CCl_4, $SiCl_4$ and $GeCl_4$. Of the three, CCl_4 has been the most extensively studied in the VUV range. Ibuki *et al.* [2] recorded the absolute absorption cross sections and the fluorescence excitation spectra of CCl_4 for λ 100 ‹ λ ‹ 200 nm. A similar experiment was performed by Lee *et al.* [3] where absolute values for the fluorescence cross-sections and quantum yields were measured. Fluorescence spectroscopy of $SiCl_4$ has been studied by Ibuki *et al.* [4] where they measure the absolute fluorescence cross-sections down to 40 nm (31 eV). The absolute absorption and fluorescence cross-sections of $GeCl_4$ between 6 and 31 eV has been measured, using synchrotron radiation by Ibuki and Kamamoto [5].

4.2 Results

4.2.1 CCl_4

The flux normalised fluorescence excitation spectrum of CCl_4 recorded at a resolution of 0.1 nm is shown in figure 4.1. Peaks are observed between 9 and 13 eV and more weakly at 16 eV. Their shape is characteristic of a dissociative process, where the initially populated Rydberg state of the neutral molecule pre-dissociates to the fluorescing fragment. Thus for each peak the fluorescence signal increases from threshold, reaches a maximum at the Frank-Condon maximum of the Rydberg state, and recedes to the baseline. The first band is seen between 9 and 10.5 eV, this is a broad resonant band with a peak at 9.7 eV. The first ionisation energy of CCl_4 is at 11.64 eV [5], therefore any fluorescence signal seen at photoexcitation energies below this value will be due to neutral fragments of CCl_4. Table 1 shows the energetics of the possible dissociation channels for the CCl_4 neutral and parent ion. The thermochemical threshold for the production of CCl_2 $\tilde{A}$ $^1B_1$ + 2Cl is 8.05 eV. The threshold for the production of CCl_3 $\tilde{C}$ $^2A_1$ + Cl is at 7.80 eV. Therefore the fluorescence observed can be due to either one of these fragments. Three further peaks are seen between 10.5 and 13 eV with the intensity of these peaks decreasing as the photoexcitation energy increases. A broad resonant band is seen between 14.3 and 17 eV, with a peak at 16.25 eV. The thermochemical threshold for the production of CCl A $^2\Delta$ + 3Cl is at 14.32 eV. The photoexcitation energy is also above the ionisation energy of CCl_4. The possibility that the fluorescence is a result of emission from the parent ion can be discounted due to the resonant nature of this band. The emission more likely emanates from the CCl A $^2\Delta$ state, as the experimental and thermochemical thresholds are very close. There is good agreement of the peak energies with spectra recorded at BESSY (figure 3.1), although relative intensities agree less well. The difference may be explained by differing sensitivities of the two detection systems as a function of the wavelength.

The dispersed fluorescence spectra recorded at the Daresbury SRS are shown in figures 4.2 and 4.3. The spectra were taken with the new Wadsworth monochromator which was used to select the photoexcitation energy. As described in chapter 2, the resultant fluorescence was collected using a fibre optic bundle attached to the interaction region, and then dispersed using a 0.19 m Jobin-Yvon Triax monochromator. The dispersed signal was detected with a 1024 x 256 pixel, liquid N_2 cooled, open-electrode CCD. A choice of turrets and gratings is available depending on the wavelengths of the dispersed signal. For the dispersed spectra taken between 9 and 13 eV, the visible turret and the 150 grooves mm^{-1} grating provided the best combination. The spectrum taken at 16.0 eV was dispersed using the UV turret and the 300 grooves mm^{-1} grating.

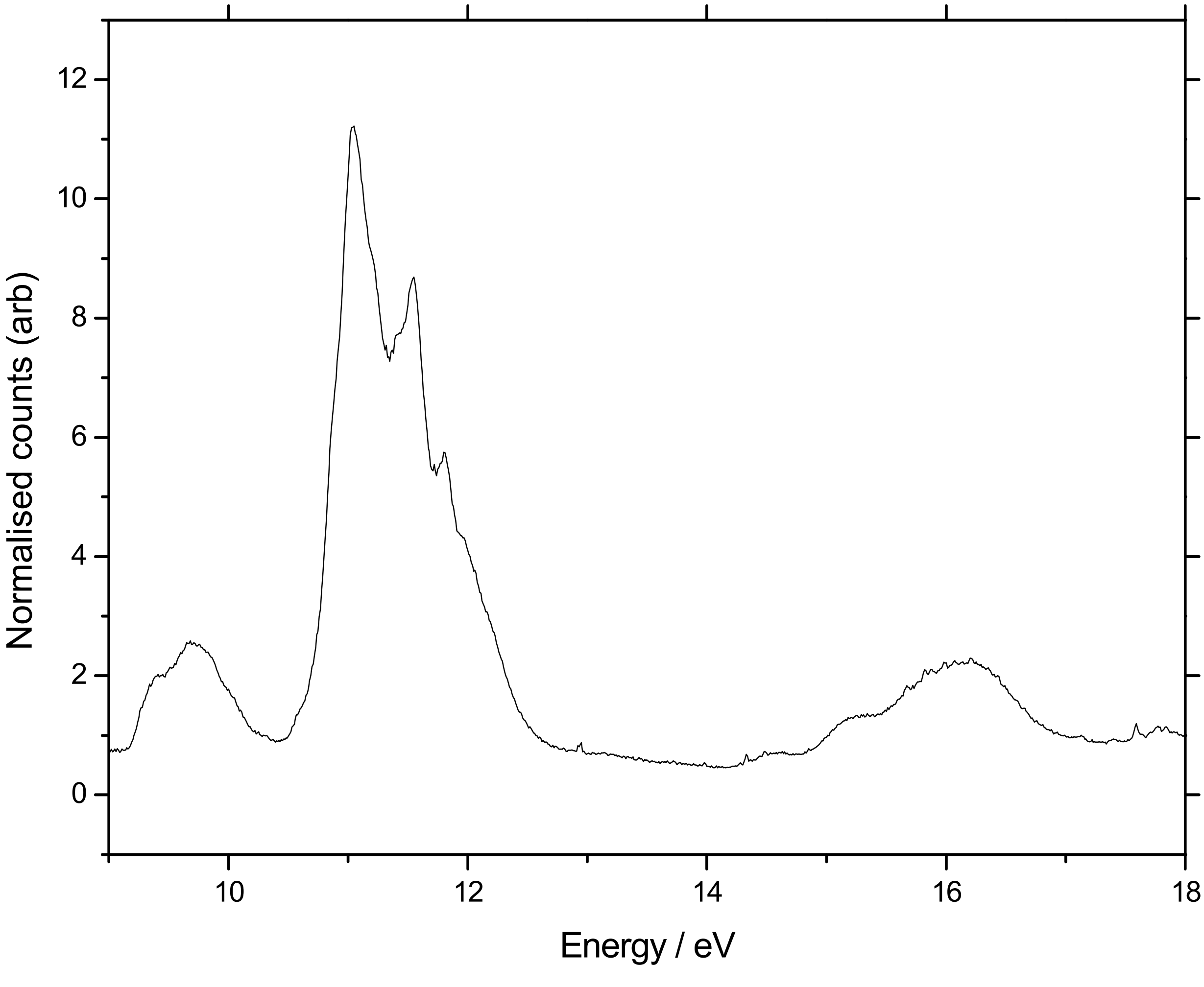

Figure 4.1: The undispersed fluorescence excitation spectrum of CCl_4, taken using the HEG at a resolution of 0.1 nm.

Neutral/parent ion		Dissociation channel	Dissociation energy / eV	Vertical IE / eV
CCl_4^+	$\tilde{D}\ ^2A_1$			19.9
	$\tilde{C}\ ^2T_2$			16.68
		CCl A $^2\Delta$ + 3Cl	14.32	
	$\tilde{B}\ ^2E$			13.37
	$\tilde{A}\ ^2T_2$			12.51
		CCl A $^2\Delta$ + Cl_2 + Cl	11.84	
CCl_4^+	$\tilde{X}\ ^2T_1$			11.64
		CCl X $^2\Pi$ + 3Cl	9.86	
		CCl X $^2\Pi$ + Cl_2 + Cl	7.38	
		CCl_2 $\tilde{A}\ ^1B_1$ + 2Cl	8.05	
		CCl_2 $\tilde{X}\ ^1A_1$ + 2Cl	5.91	
		CCl_2 $\tilde{A}\ ^1B_1$ + Cl_2	5.57	
		CCl_2 $\tilde{X}\ ^1A_1$ + Cl_2	3.43	
		CCl_3 $\tilde{C}\ ^2A_1$ + Cl	7.8	
		CCl_3 $\tilde{X}\ ^2A_1$ + Cl	2.94	
CCl_4	$\tilde{X}\ ^1A_1$			0

Table 1: Dissociation channels of CCl_4

Both dispersed spectra shown in figure 4.2 are dominated by a broad band between *ca.* 400 and 700 nm. As the photoexcitation energy is increased the peak of this band appears to move slightly to lower wavelengths. The fluorescence can be due to either the CCl_2 or CCl_3 fragments. Most of the literature [1-4,12] have attributed this signal to the CCl_2 fragment. The only exception has been Bretbarth et al [7] who suggest that the emission may be due to CCl_3.

The origin of the CCl_2 $\tilde{A}\ ^1B_1$ - $\tilde{X}\ ^1A_1$ band occurs at 579 nm [8]. The peaks in our spectra are seen at lower wavelengths *ca.* 520 nm. This shift to lower wavelength can be caused by the $\tilde{A}\ ^1B_1$ state of CCl_2 being produced vibrationally hot. The shift is a consequence of the large change in bond angle between the CCl_4 (109°) Rydberg state and the $\tilde{A}\ ^1B_1$ state of

CCl_2 (131°). Combined with the large change in bond angle between the $\tilde{A}$ $^1B_1$ state and the $\tilde{X}$ $^1A_1$ state of CCl_2 ($\Delta\theta = 22°$) [8], this shifts the maximum in the $\tilde{A}$ - $\tilde{X}$ Franck-Condon envelope to a wavelength much less than $\lambda_{0,0}$. Bretbarth et al [7] were concerned that this peak occurs at a much lower wavelength than the electronic origin of CCl_2 $\tilde{A}$ $^1B_1$ - $\tilde{X}$ $^1A_1$ and therefore believed that CCl_2 was not the emitter. Ab initio calculations [9] have predicted excited states of CCl_3 around 400 nm above the ground state. The lifetime of the CCl_2 $\tilde{A}$ $^1B_1$ state has been measured by Ibuki *et al* [2] using synchrotron radiation and is compatible with values obtained by other methods such as laser-induced fluorescence [10]. We agree with most of the literature and assign this band to the CCl_2 $\tilde{A}$ $^1B_1$ - $\tilde{X}$ $^1A_1$ transition.

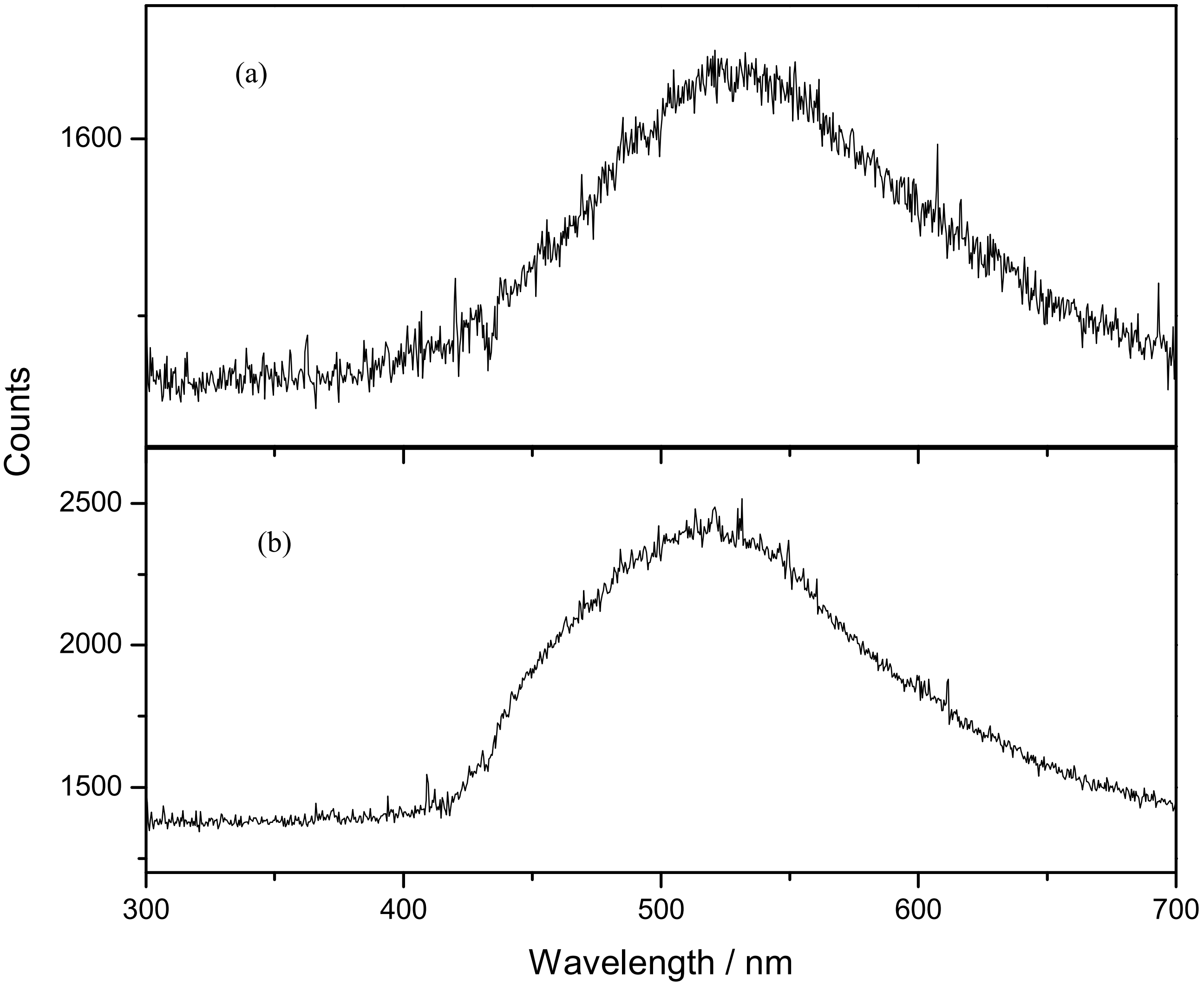

Figure 4.2: (a) Dispersed fluorescence spectra of CCl_4 taken with a photoexcitation energy of 9.7 eV (b) taken with a photoexcitation energy of 11.05 eV. Both spectra were taken using the visible turret and 100 grooves mm^{-1} grating. Note the readout noise of 900 to 1100 counts for all wavelengths.

Figure 4.3 shows the dispersed fluorescence spectrum of CCl_4 taken with a photoexcitation energy of 16 eV. The broad band between *ca*. 400 – 700 nm seen at photoexcitation energies below 13 eV disappears and is replaced by a narrow sharp band at 278 nm.
This band has been assigned as a CCl $A\ ^2\Delta - X\ ^2\Pi$ transition.

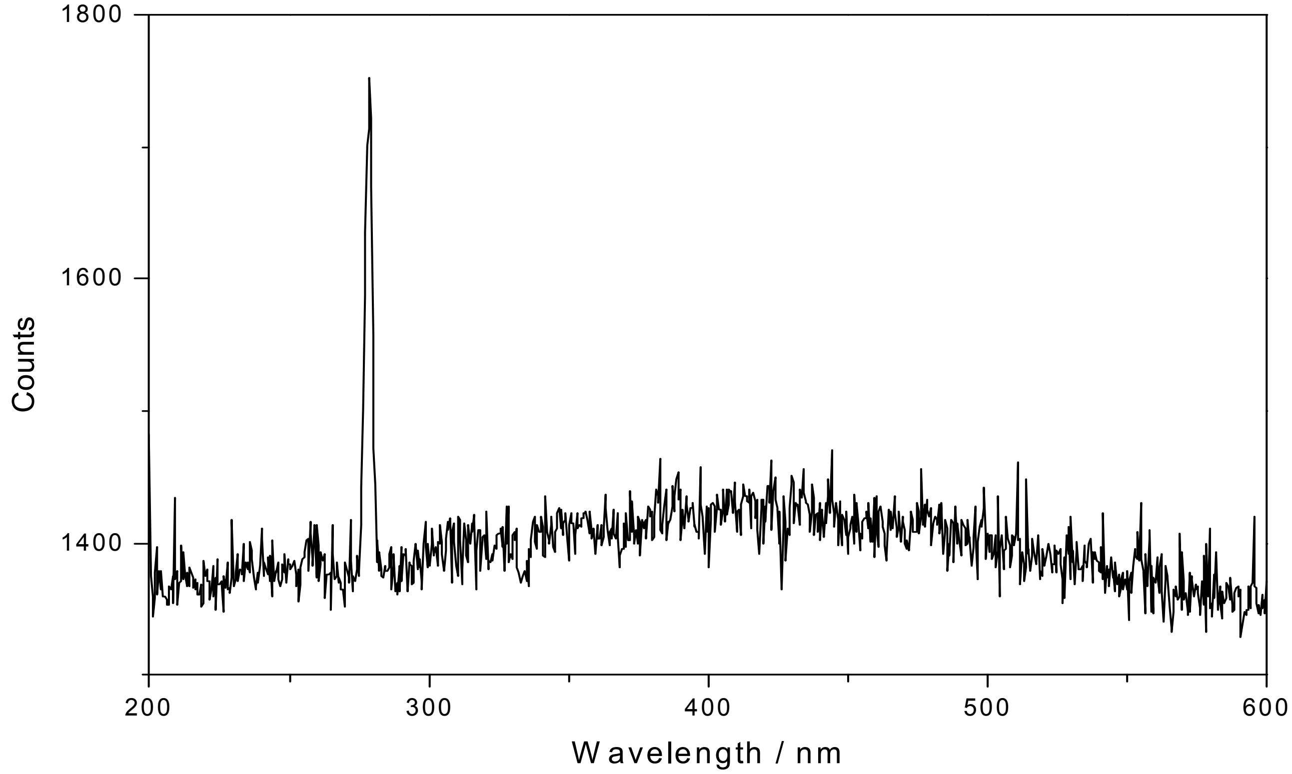

Figure 4.3: Dispersed fluorescence spectrum of CCl_4 taken with a photoexcitation energy of 16.0 eV. The UV turret and the 300 grooves mm^{-1} grating combination was used on the Jobin-Yvon triax secondary monochromator.

4.2.2 $SiCl_4$

The flux normalised fluorescence excitation spectrum of $SiCl_4$ is shown in figure 4.4. The spectrum was recorded at Daresbury with a resolution of 0.2 nm using the medium MEG on the Wadsworth monochromator. Resonant peaks are observed at energies between 11 and 14 eV. The first band is seen very weakly and has a peak at 11.35 eV. Table 2 shows the energetics of the possible dissociation channels for the $SiCl_4$ neutral and parent ion. No emission spectra have been assigned to the $SiCl_3$ radical, although energetically this is the most favourable dissociation fragment. We assume all excited states of $SiCl_3$ are repulsive and do not fluoresce. The thermochemical thresholds for $SiCl_2\ \tilde{A}\ ^1B_1$ + 2Cl and $SiCl_2\ \tilde{a}\ ^3B_1$ + 2Cl are 11.3 and 9.9 eV respectively. Therefore the observed fluorescence at 11.35 eV could be from either one of these states. It is noted that direct dissociation of $SiCl_4^*$ to form the $SiCl_2$ $\tilde{a}\,^3B_1$ triplet state is formally spin-forbidden. If the $SiCl_2$ $\tilde{a}\,^3B_1$ state acquires some singlet character through spin-orbit mixing this selection rule is relaxed. Alternatively, photodissociation can occur sequentially through two steps. First an excited state of $SiCl_3^*$ is produced with doublet symmetry ($SiCl_4^* \rightarrow SiCl_3^* + Cl$). The next step produces the triplet state of $SiCl_2$ which is now spin-allowed ($SiCl_3^* \rightarrow SiCl_2\ \tilde{a}\,^3B_1 + Cl$). A non-resonant peak is observed at higher energies, which has a signal onset at *ca.* 15 eV. The shape of this peak would suggest that fluorescence results from an excited state of the parent molecular ion. Note that the structure in the spectrum between 16 and 18 eV is also observed when the HEG is used, so it is genuine. There is good agreement between the peak energies of this spectrum with the spectrum taken at BESSY. The relative intensities of the peaks are very different, similar differences are observed in the CCl_4 spectra, showing greater intensity in the high energy range.

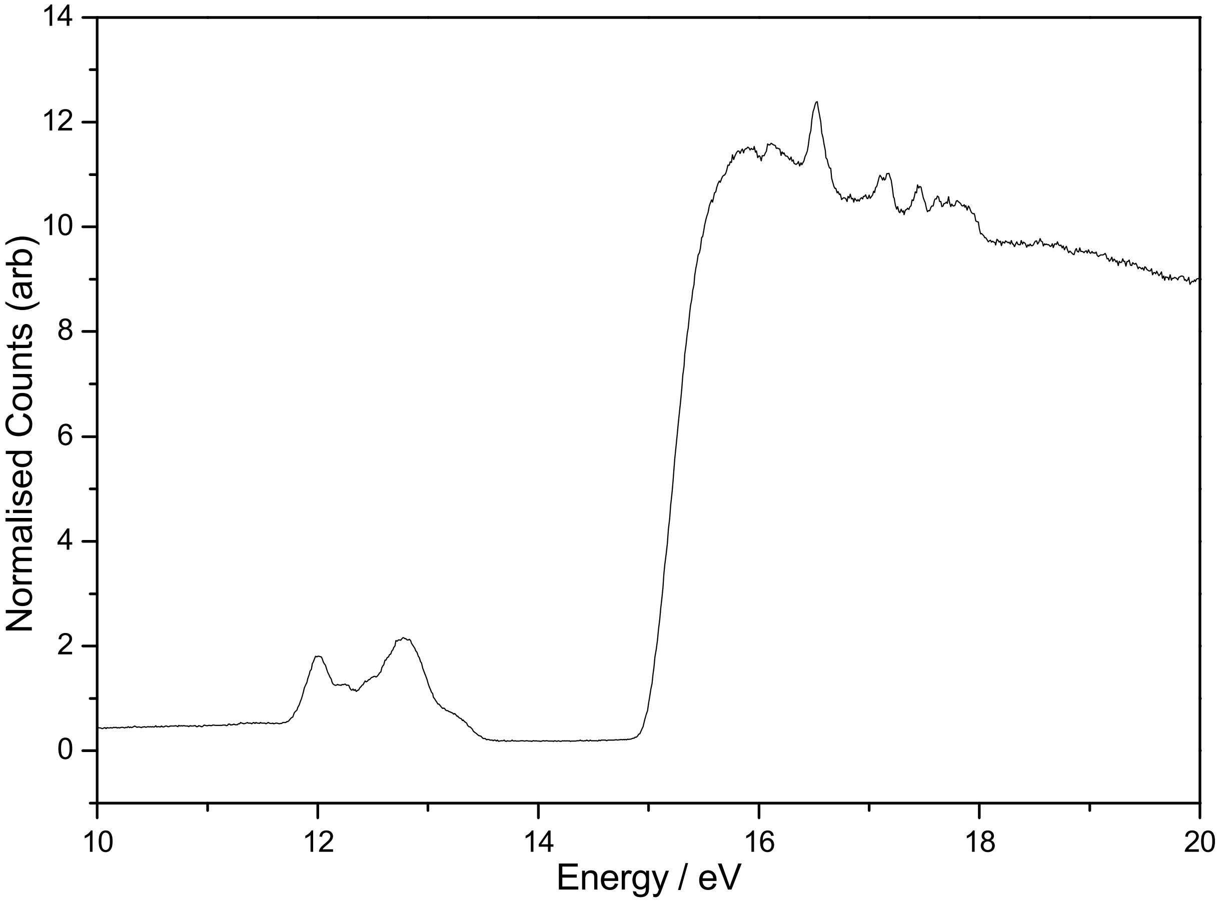

Figure 4.4: The undispersed fluorescence excitation spectrum of $SiCl_4$, taken using the MEG at a resolution of 0.2 nm.

Neutral/parent ion		Dissociation channel	Dissociation energy / eV	Vertical IE / eV
$SiCl_4^+$	$\tilde{D}\ {}^2A_1$			18.1
	$\tilde{C}\ {}^2T_2$			15.3
	$\tilde{B}\ {}^2E$			13.5
	$\tilde{A}\ {}^2T_2$			13.0
$SiCl_4^+$	$\tilde{X}\ {}^2T_1$			12.1
		$SiCl + 3Cl$	12.6	
		$SiCl + Cl_2 + Cl$	10.1	
		$SiCl_2\ \tilde{A}\ {}^1B_1 + 2Cl$	11.3	
		$SiCl_2\ \tilde{a}\ {}^3B_1 + 2Cl$	9.9	
		$SiCl_2\ \tilde{A}\ {}^1B_1 + Cl_2$	8.8	
		$SiCl_2\ \tilde{X}\ {}^1A_1 + 2Cl$	7.5	
		$SiCl_2\ \tilde{a}\ {}^3B_1 + Cl_2$	7.4	
		$SiCl_2\ \tilde{X}\ {}^1A_1 + Cl_2$	5.1	
		$SiCl_3 + Cl$	4.1	
$SiCl_4$	$\tilde{X}\ {}^1A_1$			0

Table 2: Dissociation channels of $SiCl_4$

The dispersed emission spectra of $SiCl_4$ recorded at the Daresbury SRS photoexcited at 11.35 eV, and using the MEG is shown in figure 4.5. Notice in figure 4.4 the peak at 11.35 eV is very weak. The fluorescence was dispersed using the UV turret and the 100 grooves mm^{-1} gratings on the Jobin-Yvon triax monochromator. The Lithium fluoride window was in place before the post-focusing mirror box of the Wadsworth to remove higher-order radiation when operating below *ca*. 11.8 eV. Figure 4.6 shows the dispersed spectra taken at photoexcitation energies of 12.8 and 15.9 eV. As before the spectra were taken using the UV turret and the 100 grooves mm^{-1} gratings on the Triax. However, on this occasion the lithium fluoride window is removed, as we are now operating above the cut-off energy for this window. The spectrum shown in figure 4.7 was taken at a photoexcitation energy of 22.5 eV using the HEG. The UV turret in combination with the 300 grooves mm^{-1} grating was used to disperse the spectrum. The insert shows the same spectrum taken at a higher resolution, this time using the UV turret with the 1200 grooves mm^{-1} grating.

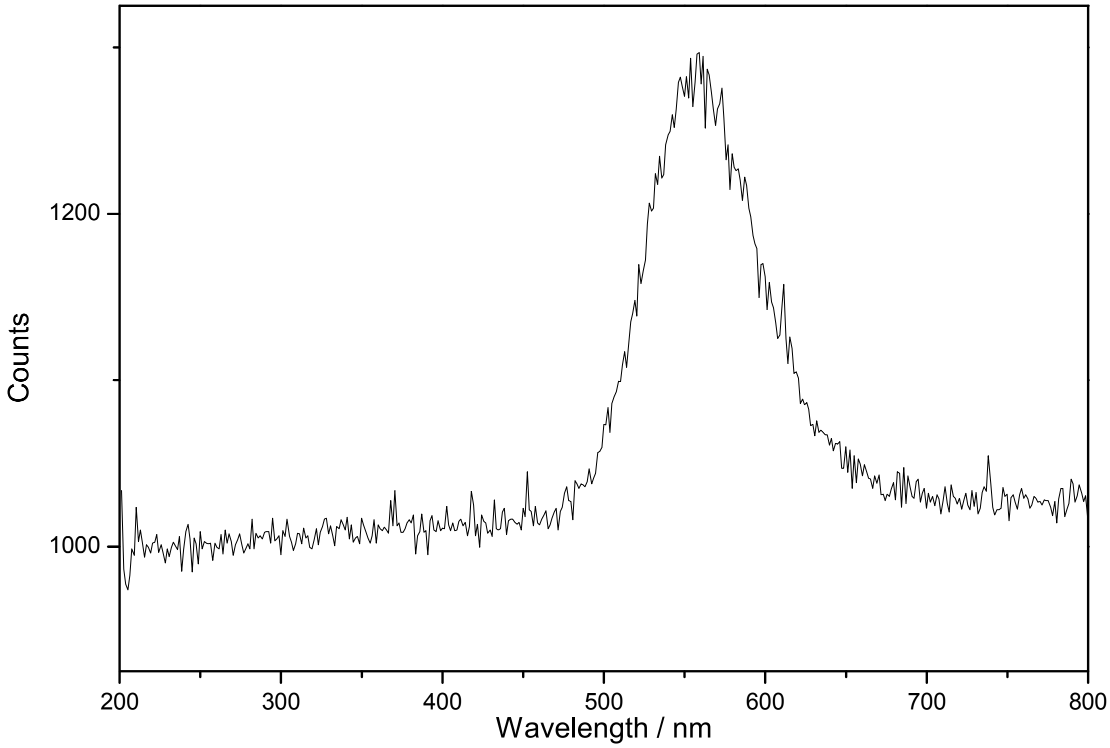

Figure 4.5: Dispersed fluorescence spectrum of $SiCl_4$ taken with a photoexcitation energy of 11.35 eV. The UV turret and the 100 grooves mm^{-1} grating combination was used on the Jobin-Yvon triax secondary monochromator.

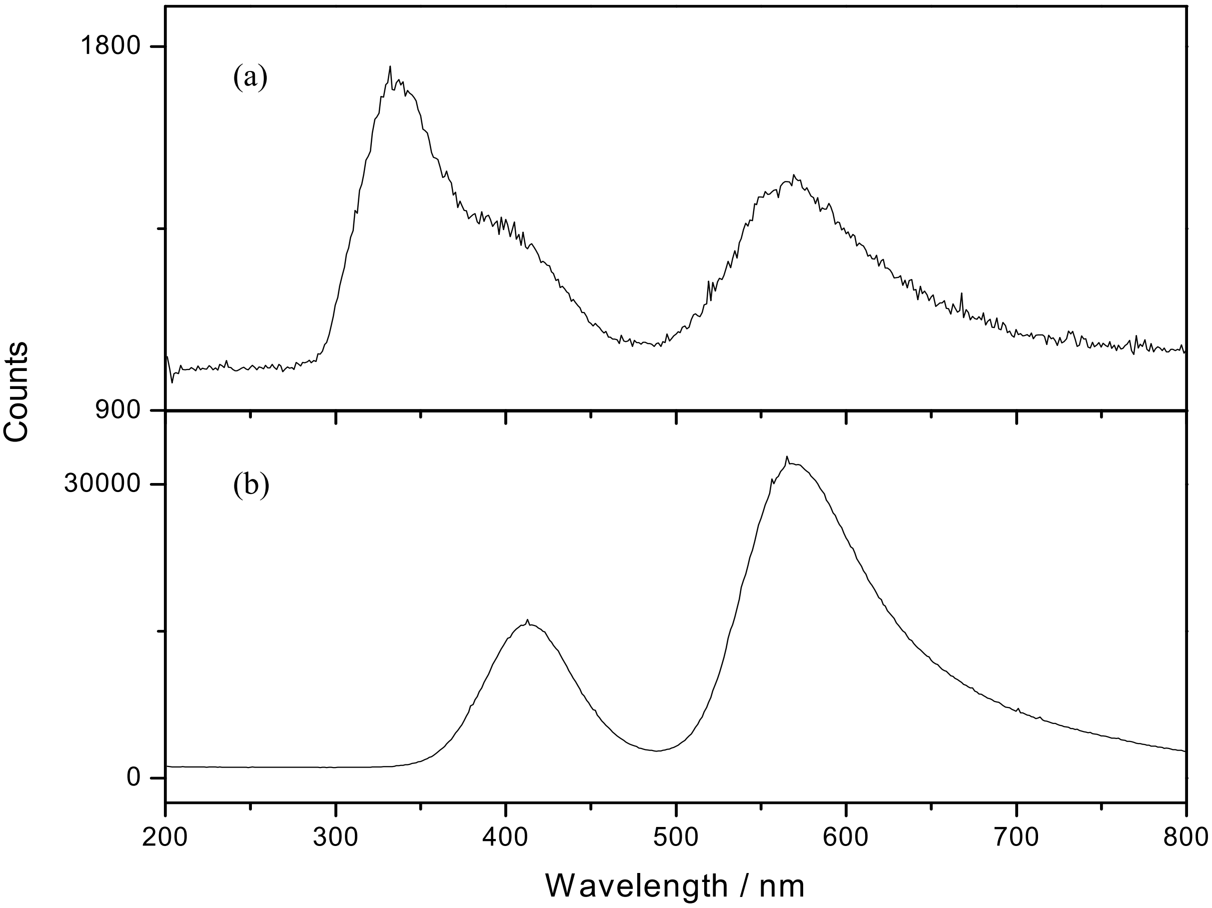

Figure 4.6: (a) Dispersed fluorescence spectra of $SiCl_4$ taken with a photoexcitation energy of 12.8 eV (b) taken with a photoexcitation energy of 15.9 eV. Both spectra were taken using the UV turret and 100 grooves mm^{-1} grating.

Second order radiation complicated the spectra at energies above *ca.* 11.8 eV. Figure 4.5 shows a clean spectrum with no second-order radiation coming from the primary monochromator. One broad band is observed with a peak at 550 nm, this has been assigned to emission from the $SiCl_2$ $\tilde{a}\ {}^3B_1$ - $\tilde{X}\ {}^1A_1$ band system [3,4]. This is the first time this band has been seen. In our previous work [1] the dispersed spectrum taken at 11.4 eV, where no system was available to incorporate a lithium fluoride window, was complicated by second order signal from 22.8 eV. At this energy two bands are seen with peaks at 410 and 560 nm. If $SiCl_2$ $\tilde{a}\ {}^3B_1$ - $\tilde{X}\ {}^1A_1$ signal was present it would be obscured by the second order signal from 22.8 eV. The presence of the $SiCl_2$ $\tilde{a}\ {}^3B_1$ - $\tilde{X}\ {}^1A_1$ signal was deduced from the different ratio of the two peaks in either spectrum. At 22.8 eV the ratio of the peak height at 410 nm to the peak height at 560 nm was *ca.* 3:2.The peak height ratios for the spectrum at 11.4 eV are almost 1:1.

Figure 4.6(a) shows the dispersed fluorescence spectrum of $SiCl_4$ taken with a photoexcitation energy of 12.8 eV. The lithium fluoride window has been removed, hence the spectrum is now complicated by second-order effects. The spectrum shown in figure 4.6(b) has been taken at a photoexcitation energy of 15.9 eV. Two broad bands are seen with peaks at 410 and 560 nm. The shape of the peak in the fluorescence excitation spectrum (figure 4.4) would suggest that fluorescence is due to emission from the parent ion. The band at 410 nm has been attributed to fluorescence resulting from the $SiCl_4^+$ $\tilde{C}\ {}^2T_2$ - $\tilde{X}\ {}^2T_1$ transition. The band with a peak at 560 nm has been assigned as $SiCl_4^+$ $\tilde{C}\ {}^2T_2$ - $\tilde{A}\ {}^2T_2$ emission. Dispersed fluorescence spectra taken at higher excitation energies, figure 4.7 shows the spectra taken at 22.5 eV, show the parent ion bands at 410 and 560 nm as well as some sharp lines due to atomic Si. These occur between 200 and 300 nm and the assignments are presented in reference [1]. Returning to the spectrum taken at 12.8 eV(figure 4.6(a)), we can see three bands with peaks at 330, 410 and 560 nm. We assign the bands with peaks at 410 and 560 nm to second-order parent ion emission from 25.6 eV. This leaves us with the band with a peak at 330 nm. From other work [1,3,4,] we know that the $SiCl_2$ $\tilde{A}\ {}^1B_1$ - $\tilde{X}\ {}^1A_1$ emission has an origin at 333 nm. We can therefore conclude that the band at 330 nm is due to $SiCl_2$ $\tilde{A}\ {}^1B_1$ - $\tilde{X}\ {}^1A_1$ transition.

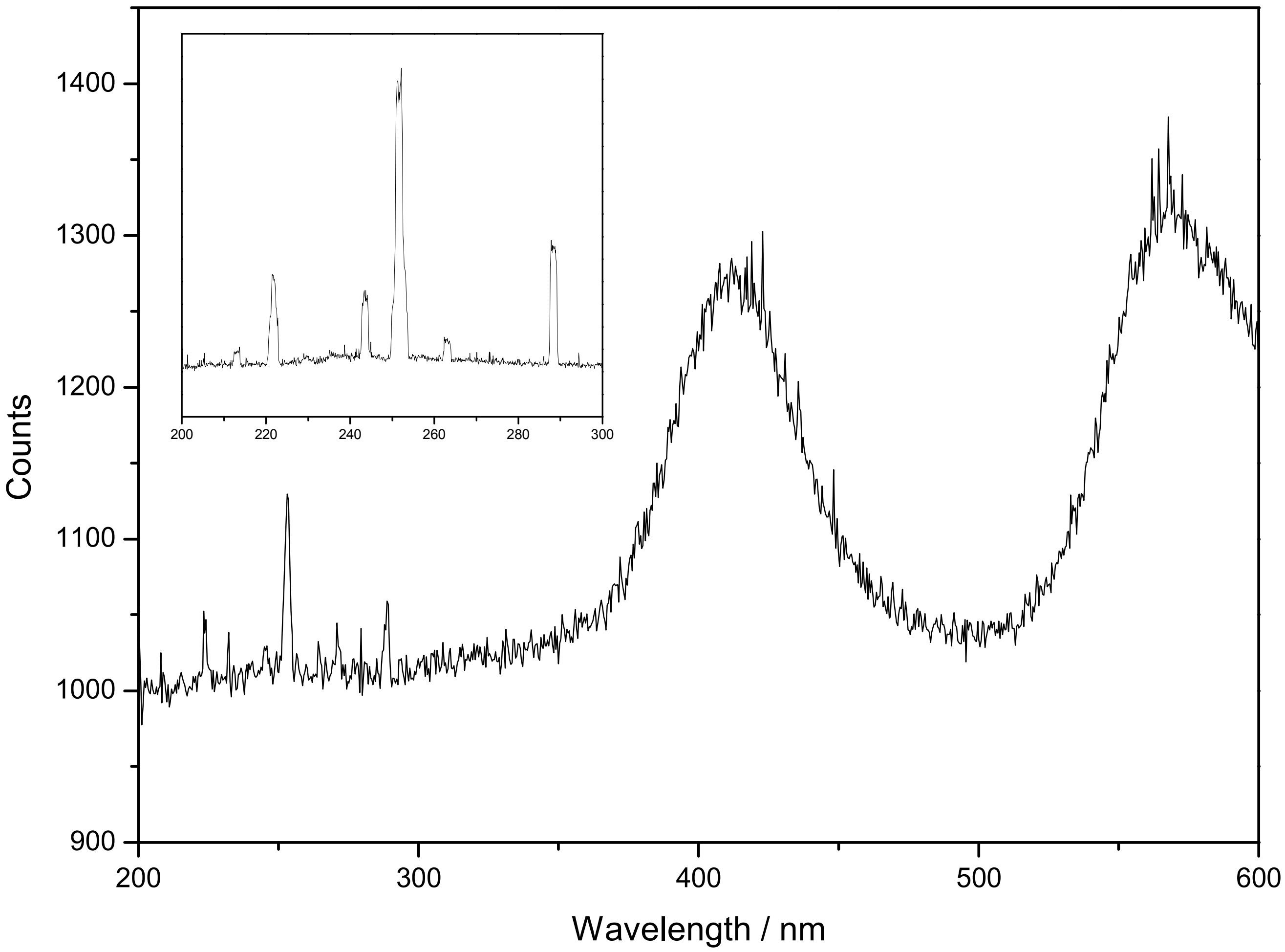

Figure 4.7: Dispersed fluorescence spectrum of $SiCl_4$ taken with a photoexcitation energy of 22.5 eV. The UV turret and the 300 grooves mm^{-1} grating combination was used on the Jobin-Yvon triax secondary monochromator. The insert shows the same spectra taken at a higher resolution using the 1200 grooves mm^{-1} gratings.

4.2.3 $GeCl_4$

The fluorescence excitation spectrum of $GeCl_4$ recorded using the MEG on the Wadsworth monochromator and a resolution of 0.1 nm is shown in figure 4.8. Resonant peaks are seen between 9 and 12 eV. A non-resonant feature with a signal onset at 14.6 eV is also observed. Previous undispersed work on this molecule [1] carried out at the Daresbury SRS used a set of filters in an attempt to identify the range of the collected fluorescence. These filters showed that the first peak at 9.59 eV is a result of photodissociation from a Rydberg state that emits radiation exclusively in the visible region. The other peaks between 9 and 12 eV have been shown to have both visible and UV components. If we compare the two spectra, we see good correlation with the peak energies, but the relative intensities of the spectra are different. The high energy peaks in the present spectrum have greater intensity than the previous work. The peak at 9.59 eV is much clearer in the earlier work.

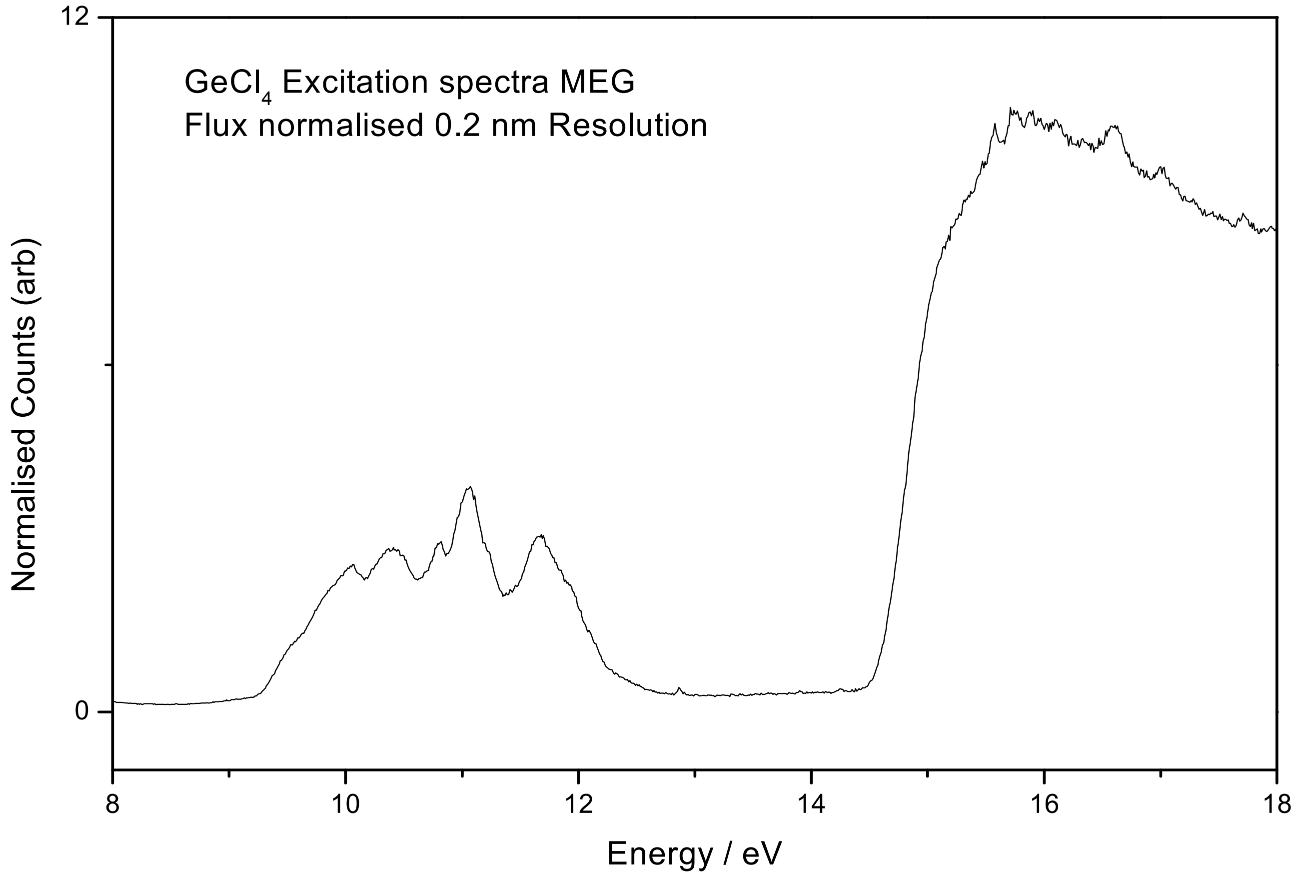

Figure 4.8: The undispersed fluorescence excitation spectrum of $GeCl_4$, taken using the MEG at a resolution of 0.2 nm.

Dispersed fluorescence spectra of $GeCl_4$ recorded with photoexcitation energies between 9 and 12 eV are shown in figure 4.9. The spectra were dispersed using the UV turret and the 100 grooves mm^{-1} grating. The parameters used for all the spectra shown were the same, 600 s integration time with two accumulations to effect cosmic ray removal. The non-resonant peak was dispersed using the UV turret and the 300 groves mm^{-1} gratings. The spectra taken for hν < 11.8 eV were recorded with the LiF window in front of the exit slit of the Wadsworth monochromator to ensure no second-order radiation was present.

Neutral/parent ion	Dissociation channel	Dissociation energy / eV	Vertical IE / eV
$GeCl_4^+$ $\tilde{D}\ ^2A_1$			18.2
$\tilde{C}\ ^2T_2$			14.9
$\tilde{B}\ ^2E$			13.1
$\tilde{A}\ ^2T_2$			12.6
$GeCl_4^+$ $\tilde{X}\ ^2T_1$			12.0
	GeCl + 3Cl	10.4	
	GeCl + Cl_2 + Cl	7.9	
	$GeCl_2$ $\tilde{A}\ ^1B_1$ + 2Cl	9.8	
	$GeCl_2$ $\tilde{a}\ ^3B_1$ + 2Cl	8.8	
	$GeCl_2$ $\tilde{A}\ ^1B_1$ + Cl_2	7.3	
	$GeCl_2$ $\tilde{X}\ ^1A_1$ + 2Cl	6.3	
	$GeCl_2$ $\tilde{a}\ ^3B_1$ + Cl_2	6.0	
	$GeCl_2$ $\tilde{X}\ ^1A_1$ + Cl_2	3.5	
	$GeCl_3$ + Cl	2.8	
$GeCl_4$ $\tilde{X}\ ^1A_1$			0

Table 3: Dissociation channels of $GeCl_4$

The first spectrum taken at 9.51 eV (figure 4.9(a)) shows a broad band between 400 and 560 nm with a peak at 480 nm. The experiments using filters to select particular energy ranges implied that this signal should be exclusively in the visible [1]. This assumption has been proven to be correct with visible emission between 400 and 560 nm and no peaks seen in the UV. This band has been assigned to $GeCl_2$ $\tilde{a}\ ^3B_1$ - $\tilde{X}\ ^1A_1$. Figure 4.9(b)-(d) shows the dispersed fluorescence spectra taken at photoexcitation energies of 9.99, 10.35 and 11.05 eV. These spectra show the same broad band between 400 and 560 nm attributed to $GeCl_2$ $\tilde{a}\ ^3B_1$ - $\tilde{X}\ ^1A_1$ emission. This time a very weak band between 330 and 380 nm is also observed. This emission, just as in the $SiCl_4$ spectra dispersed at 12.8 eV, has been assigned to a transition from the singlet state of $GeCl_2$, essentially the $\tilde{A}\ ^1B_1$ - $\tilde{X}\ ^1A_1$ emission. From this work we can assume that the fluorescence resulting from the Rydberg state at 9.51 eV leads exclusively to the production of the triplet $GeCl_2$ $\tilde{a}\ ^3B_1$ state. The other resonant peaks in the excitation spectra also photodissociate to this triplet state with the channels to the $GeCl_2$ $\tilde{A}$

$^1B_1$ state being minor. Note the spin-selection rule is relaxed due to the large spin-orbit splitting caused by the heavy Ge atom [1].

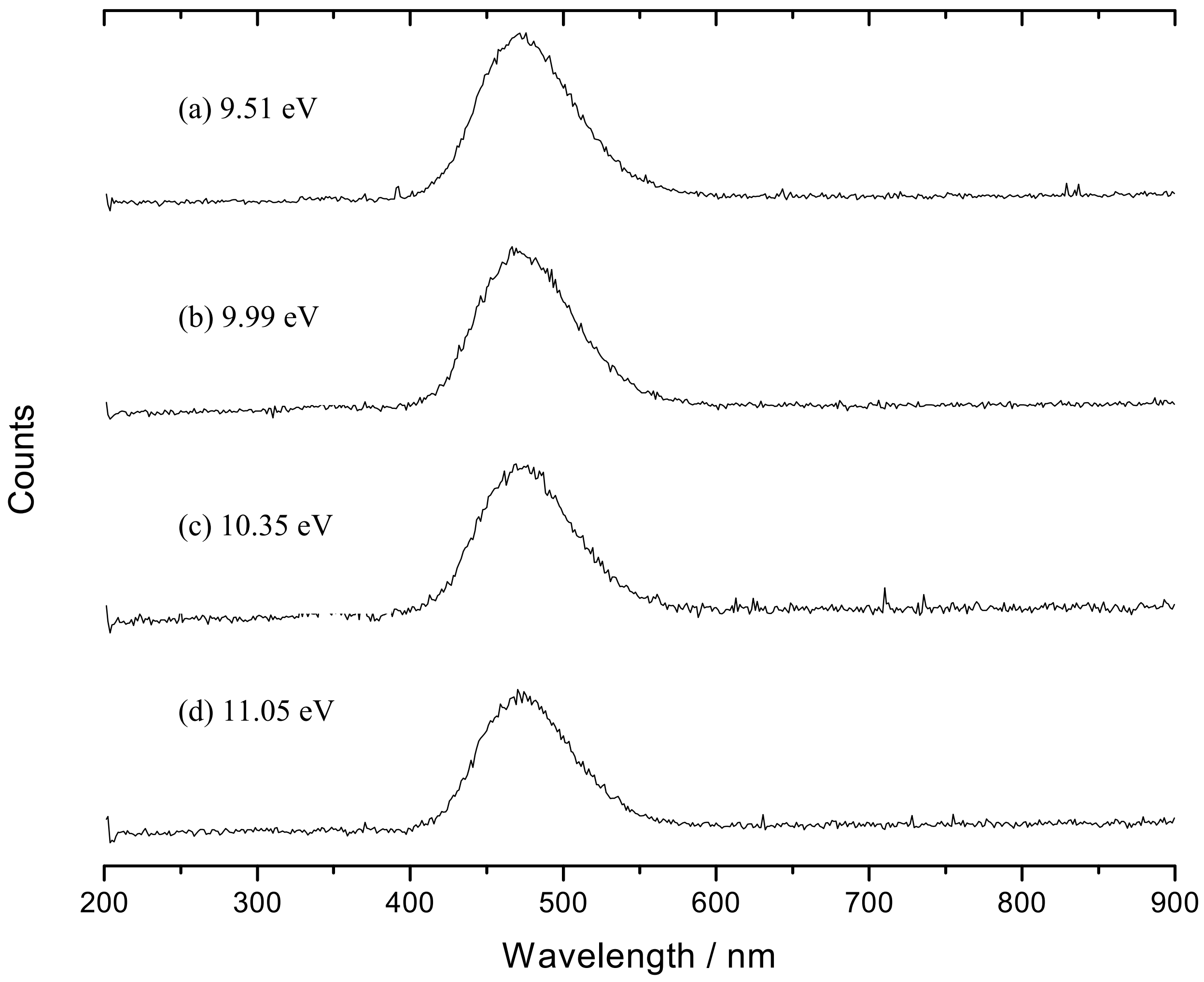

Figure 4.9: Dispersed fluorescence spectra of $GeCl_4$ taken with photoexcitation energies of (a) 9.51 eV (b) 9.99 eV (c) 10.35 eV (d) 11.05 eV. All the spectra were taken using the UV turret and 100 grooves mm^{-1} grating.

The dispersed emission spectrum taken at a photoexcitation energy of 15.1 eV shows two broad bands with a ranging from 400 to 550 nm and 560 to 750 nm. The band between 400 and 550 nm is due to the $GeCl_4^+$ $\tilde{C}$ $^2T_2$ - $\tilde{X}$ $^2T_1$ transition. This band was seen in the previous dispersed work carried out at BESSY 1. The band between 560 and 750 nm, which has been assigned to the $\tilde{C}$ $^2T_2$ - $\tilde{A}$ $^2T_2$ transition, is observed here for the first time. Due to the rapid loss of sensitivity of the dispersed detection system used at BESSY 1 for wavelengths greater than 500 nm, this peak was not detected in earlier experiments [1]. No dispersed spectra at higher energies were taken, 18 – 25 eV, but we expect to see atomic lines of Ge as in the $SiCl_4$ spectra.

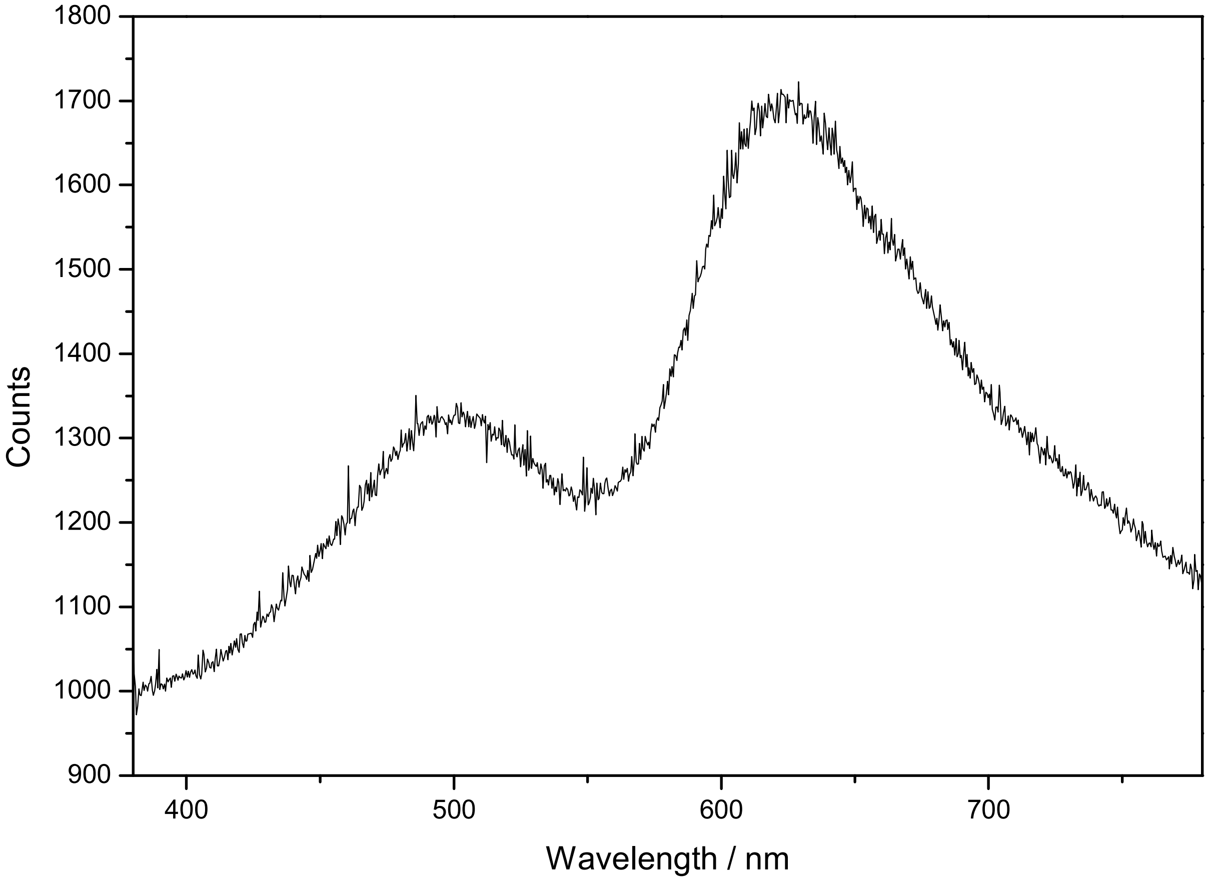

Figure 4.10: Dispersed fluorescence spectrum of $GeCl_4$ taken with a photoexcitation energy of 15.1 eV. The UV turret and the 300 grooves mm^{-1} grating combination was used on the Jobin-Yvon triax secondary monochromator.

4.3 Conclusions

Fluorescence from CCl_4, $SiCl_4$ and $GeCl_4$ has been recorded with five different decay channels being observed CCl_2 $\tilde{A}\ {}^1B_1 - \tilde{X}\ {}^1A_1$ emission at ca. 420-600 nm from CCl_4 excited in the range 9-12 eV. CCl $A\ {}^2\Delta - X\ {}^2\Pi$ emission at ca. 276-280 nm from CCl_4 excited in the range 14-18 eV. $SiCl_2/GeCl_2$ $\tilde{a}\ {}^3B_1 - \tilde{X}\ {}^1A_1$ and $\tilde{A}\ {}^1B_1 - \tilde{X}\ {}^1A_1$ emission from $SiCl_4/GeCl_4$ excited in the range 9-14 eV. $SiCl_4^+/GeCl_4^+$ $\tilde{C}\ {}^2T_2 - \tilde{X}\ {}^2T_1$ and $\tilde{C}\ {}^2T_2 - \tilde{A}\ {}^2T_2$ emission at ca. 350-700 nm from $SiCl_4/GeCl_4$ excited above the ionisation energy. Finally, Si* and Ge* atomic emission lines at wavelengths below 310 nm from $SiCl_4/GeCl_4$ excited in the range 19-25 eV.

4.4 References

[1] H. Biehl, K.J. Boyle, D.P. Seccombe, R.P. Tuckett, H. Baumgartel, H.W. Jochims, *J. Elec. Spec. Rel. Phen.*, **97** (1997) 89

[2] T.Ibuki . Takahashi, A. Hiraya and K. Shobatake, *J. Chem. Phys,* **85** (1996) 5717

[3] L.C. Lee and M. Suto, *Chem. Phys*, **114** (1997) 423

[4] T. Ibuki, M. Kono, Y. Asari, A. Hiraya and K. Shobatake, *J. Chem. Phys,* **106** (1997) 4853

[5] T. Ibuki and A. Kamamoto, *Chem. Phys. Lett,* **260** (1996) 314

[6] P.J. Bassett and D.R. Loyd, J. *Chem. Soc*. A, (1977) 641

[7] F.W. Breitbarth, D. Berg, *Chem. Phys. Lett*. **149** (1988) 334

[8] D.J. Clouthier, J. Karolczak, *J. Chem. Phys.* **94** (1991) 1

[9] J.W. Hudgens, R. D. Johnson, B. P. Tsai, S. A. Kafafi. *J. Am. Chem. Soc*. **112** (1990) 5763

[10] R.E. Huie, N.J.T. Long, B.A. Thrush. *Chem. Phys. Lett*. **51** (1977) 197

[11] C.H. Howle, S. Ali, R.P. Tuckett, D.A. Shaw, J.B. West, *NIM B*, **237** (2005) 656.

[12] G.H. Ho, *Chemical Physics*, **226** (1998) 101

[13] W. Zhang, G. Cooper, T Ibuki and C.E. Brion, *Chem. Phys*, **160** (1992) 435

[14] G.C. Causley and B.R. Russell, *J. Electron Spec and Related. Phenom*, **11** (1977) 383

[15] C.E. Theodosiou, M. Inokuti and S.T. Mason,
Atomic Data and Nuclear Data Tables, **35** (1996) 473

[16] A.W. Potts, H.J. Lempka, D.G. Streets and W.C. Price,
Phil. Trans. Roy. Soc. Lond.A, **268** (1970) 59

[17] J.C. Green, M.L.H. Green, P.J. Joachim, A.F. Orchard and D.W. Turner,
Phil. Trans. Roy. Soc. Lond.A, **268** (1970)111

[18] I. Tokue, T. Honda, Y. Ito, *Chem. Phys*, **140** (1990) 157.

[19] M. Kusakabe, Y. Ito, I. Tokue, *Chem. Phys*, **170** (1993) 243.

[20] K.Kamata, M. Ukai, T. Numazawa, N. Terazawa, Y. Chikahiro, N. Kouchi, Y. Hatano, K. Tanake, *J. Chem. Phys*, **99** (1993) 2487.

[21] M. Tsuji, M Furusawa, T. Mizuguchi, T Muraoka and Y. Nishimura,
J. Chem. Phys, **97** (1992) 245.

[22] G. Burton, W. Chan, G. Cooper and C. Brion, *Chem. Phys,* **181** (1994)147

[23] R. Dixon and R. Tuckett, *Chem. Phys. Lett,* **140** (1987) 553.

[24] N. Chandra, *J. Phys. B. At. Mol. Phys,* **20** (1987) 3417

[25] T. Ibuki, N. Washida, U. Itoh, Y. Toyoshima and H. Onuki,
Chem. Phys. Lett, **136** (1987) 447

[26] L. Cooper, L. Shpinkova, D. Holland and D. Shaw, *J. Chem. Phys*, **270** (2001) 363.

[27] C. R. Brundle, M. B. Robin, *J. Chem. Phys.,* **53**, (1970), 2196

[28] J.H. Seinfeld, S.N. Pandis, *Atmospheric Chemistry and Physics*,
Wiley, New York, (1998)

5. VUV absorption and undispersed fluorescence excitation spectroscopy of CF_3X (X = F, H, Cl, Br)

In this chapter we present the VUV photoabsorption spectra of CF_3X, where X = F, H, Cl and Br. These have been recorded by our group at the BESSY 1 synchrotron radiation source in Berlin. The data were recorded in the last year of the operation of BESSY 1, but had remained unassigned untill now. The absorption peaks have been assigned using the Rydberg formula and compared to the literature. The undispersed fluorescence excitation spectra of the molecules were recorded at the Daresbury synchrotron radiation source (SRS), using the Seya monochromator on station 3.1 and they are compared to the absorption spectra.

5.1 Introduction

Due to their significant global warming and ozone depleting properties, the production and use of CF_3Br and CF_3Cl are banned under the terms of the Montreal Protocol. The sources of both these molecules in the atmosphere are purely anthropogenic [1]. CF_3Br was formerly used as a fire suppressant and CF_3Cl as a refrigerant. Despite this legislation preventing its use, the relatively long atmospheric lifetimes of CF_3Br and CF_3Cl, *ca.* 65 and 640 years, and the gradual release of gas from old fire-extinguishing equipment and cooling systems means that these molecules will continue to play a role in environmentally-damaging processes for many years. The halomethanes CF_4 and CHF_3 are two of the most widely used gases for a variety of plasma assisted material processing and many other industrial applications.

5.2 Results

5.2.1 CF_4

The electronic configuration of the outer valence molecular orbitals of CF_4 is …..$(4a_1)^2$ $(3t_2)^6$ $(1e)^4$ $(4t_2)^6$ $(1t_1)^6$. The numbering scheme does include the C 1s and F 1s core orbitals. The vertical ionisation energies for the five outermost occupied valence orbitals have been measured to be 16.23 ($1t_1$), 17.47 ($4t_2$), 18.50 (1e), 21.95 ($3t_2$), and 25.10 ($4a_1$) using He(I) and He(II) photoelectron spectroscopy [2]. The quantum defects of ns, np and nd Rydberg orbitals centred on C (F) atoms are predicted to be 0.98 (1.20), 0.58 (0.75), and 0.01 (0.003) [3].

The photoabsorption spectrum of CF_4 taken in the 9 to 40 eV energy range and with a resolution of 0.08 nm on the primary monochromator is shown in figure 5.1. Resonant peaks are seen between 10 and 20 eV, the shapes of these peaks are characteristic of a resonant primary excitation process. The first peak is seen at 12.65 eV followed by a much larger peak at 13.79 eV with a shoulder at 14.05 eV. The peak at 12.65 eV, using quantum defect values, was initially assigned to the $(1t_1)^{-1}$ 3s transition. In tetrahedral (T_d) symmetry a $t_1 \rightarrow s$ transition is optically forbidden [4], therefore we can possibly discount this as a possible assignment. This peak is more likely due to a valence transition. The peak at 13.79 eV originates from the $1t_1$ orbital of CF_4, and using the Rydberg formula this has been assigned as an excitation to the $(1t_1)^{-1}$ 3p state. The shoulder at 14.05 eV has its origins in the $4t_2$ orbital, and absorption of a photon leads to the formation of a 3s Rydberg state. A sharp resonant peak is then seen at 16.05 eV which is followed by series of broad peaks between the energies of 16.5 and 20.3 eV. The peak assignments are presented in table 5.1.

Figure 5.2 shows an expanded region of the absorption spectrum between 20 and 23 eV. In this spectrum we can clearly observe vibrational structure. Table 5.2 shows the position of these peaks together with their vibrational spacing. This structure has been assigned before by Lee et al. [5] to sequences involving the v_1 C-F symmetric stretching vibration in three different Rydberg states which converge on either the $\tilde{C}\ ^2T_2$ or $\tilde{D}\ ^2A_1$ states of CF_4^+. The v_1 vibration has frequency of 729 and 800 cm^{-1} in CF_4^+ $\tilde{C}\ ^2T_2$ and $\tilde{D}\ ^2A_1$ states, respectively [6]. The peaks between 20.3 and 21.4 eV have an average spacing of 725 cm^{-1}, and probably is a series converging on the $\tilde{C}\ ^2T_2$ state of the ion. The average spacing of peaks above 21.4 eV is 715 cm^{-1} substantially less than 800 cm^{-1} which is the value of v_1 in CF_4^+ $\tilde{D}\ ^2A_1$. For this reason we cannot with complete confidence assign these peaks to CF_4^+ $\tilde{D}\ ^2A_1$.

Figure 5.1 also shows a comparison of the photoabsorption and fluorescence excitation spectra of CF_4. There is very little resemblance between the two spectra. In the fluorescence excitation spectrum the peak at lowest energy, with an onset of 10.8 eV and a peak at 11.4 eV, is a lower-intensity replica of the peak at 22.8 eV, due to second-order radiation from the primary monochromator, and even reproduces the fine structure to high energy of the peak. The first genuine peak is seen at 13.7 eV and is due to emission from the neutral CF_3^* fragment (chapter 6). Dissociation of the CF_4 molecule occurs via the 3p Rydberg state to form the CF_3^* fragment. The observed fluorescence is a result of emission from this fragment. A weak emission band is seen at 15.9 eV followed by very strong band with a peak at 22.6 eV. The band at 15.9 eV is probably due to the $(4t_2)^{-1}$ 3d Rydberg state. These emissions have been assigned and further details can be found in chapter 6.

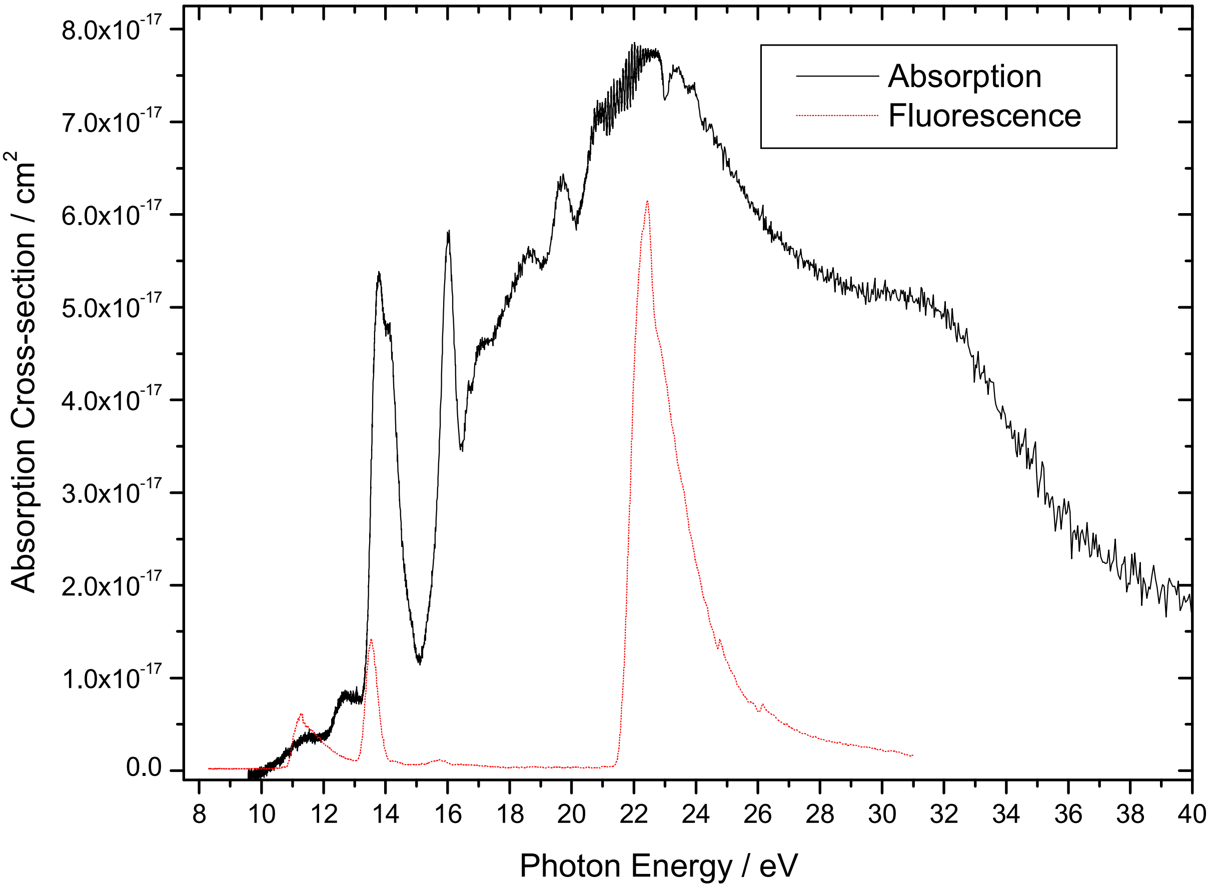

Figure 5. 1: The absolute photoabsorption cross-section of CF_4 taken at Bessy1 is shown. The fluorescence excitation spectrum measured at Daresbury is also shown to compare qualitatively the importance of the fluorescence decay channel. Absorption cross-sections shown are absolute, whereas the fluorescence signal is arbitrary

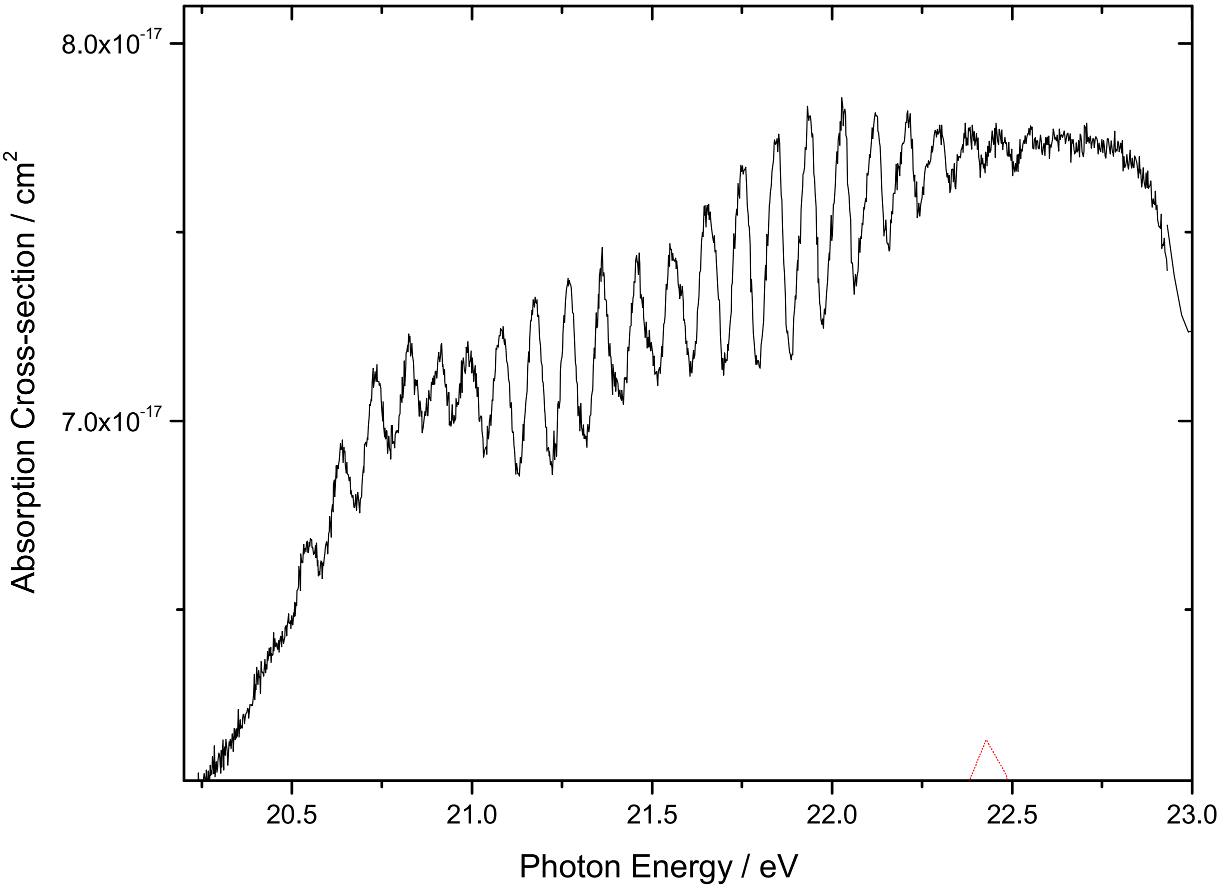

Figure 5.2: Absorption spectrum of CF_4 between 20.0 and 23.0 eV.

E(eV)	Upper state configuration	IE-E(eV)	$n-\delta$	δ
12.65	$(1t_1)^{-1}$ 3s	3.58	1.95	1.05
13.79	$(1t_1)^{-1}$ 3p	2.44	2.36	0.63
14.05	$(4t_2)^{-1}$ 3s	3.42	1.99	1.01
16.05	$(4t_2)^{-1}$ 3d	1.42	3.10	-0.10
16.68	$(1e)^{-1}$ 3p	1.82	2.73	0.27
17.12	$(1e)^{-1}$ 3d	1.38	3.14	-0.14
18.63	$(3t_2)^{-1}$ 3s	3.49	1.97	1.03
19.73	$(3t_2)^{-1}$ 3p	2.39	2.39	0.61

Table 5.1: CF_4 Photoabsorption assignments and quantum defect values. Vertical Ionisation energy values taken from Basset and Lloyd [2].

E (eV)	λ (nm)	Wavenumber (cm^{-1})	Separation (cm^{-1})
20.55	60.33	165745	
20.64	60.07	166471	725
20.73	59.81	167196	725
20.83	59.52	168003	806
20.92	59.27	168729	725
20.99	59.07	169293	564
21.09	58.79	170100	806
21.18	58.54	170826	725
21.27	58.29	171552	725
21.36	58.05	172278	725
21.46	57.78	173084	806
21.55	57.53	173810	725
21.65	57.27	174617	806
21.75	57.00	175423	806
21.85	56.74	176230	806
21.93	56.54	176875	645
22.03	56.28	177682	806
22.12	56.05	178407	725
22.22	55.80	179214	806
22.30	55.60	179859	645
22.38	55.40	180504	645
22.45	55.23	181069	564
22.56	54.96	181956	887

Table 5.2: Wavelength (nm) and energies (eV) of the photoabsorption peaks in CF_4 between 20.0 and 23.0 eV

5.2.2 CF_3H

CF_3H has C_{3v} geometry with the electronic configuration of its outer valence molecular orbitals being … $(4a_1)^2$ $(5a_1)^2$ $(3e)^4$ $(4e)^4$ $(5e)^4$ $(1a_2)^2$ $(6a_1)^2$. The numbering scheme does not include core orbitals. The vertical ionisation energies of the outer valence orbitals have been measured by high resolution He I and He II photoelectron spectroscopy [7] and are reported to be 14.80, 15.50, 16.16, 17.25, 20.50 and 24.40 eV.

The photoabsorption spectrum of CF_3H taken in the 6 to 25 eV energy range and with a resolution of 0.08 nm on the primary monochromator is shown in figure 5.3. Resonant peaks are seen between 10 and 19 eV. The first two peaks are seen at 10.87 and 11.95 eV. Using the Rydberg formula these two peaks have been assigned as originating from the $6a_1$ molecular orbital of CF_3H. Quantum defect values of 1.13 and 0.82 have been obtained, with the first peak at 10.87 eV assigned as an excititation to the $(6a_1)^{-1}$ 3s state and the peak at 11.95 eV assigned as an excitation to the $(6a_1)^{-1}$ 3p Rydberg state. The next peak at 12.58 eV has been attributed to the $(1a_2)^{-1}$ 3p transition. Full assignments are presented in table 5.3.

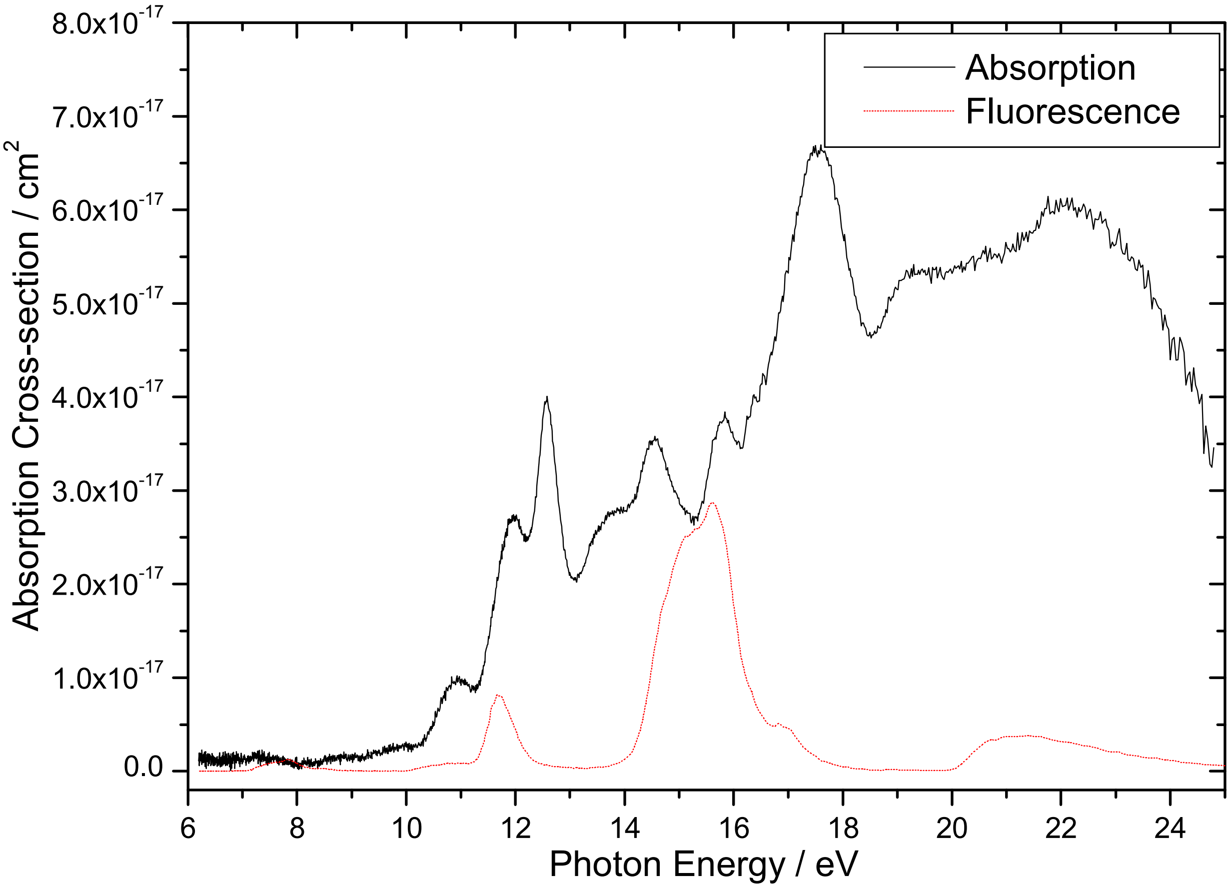

Figure 5.3: The absolute photoabsorption cross-section of CF_3H taken at Bessy1 is shown. The fluorescence excitation spectrum measured at Daresbury is also shown to compare qualitatively the importance of the

fluorescence decay channel. Absorption cross-sections shown are absolute, whereas the fluorescence signal is arbitrary

Figure 5.3 shows a comparison between the photoabsorption and fluorescence excitation spectra of CF_3H. There are some similarities between the two spectra. In the fluorescence excitation spectrum peaks are observed at 11.7 and 15.5 eV with a shoulder at 16.7 eV. In the absorption spectrum peaks are observed at 11.95 and 15.84 eV, these tally with the fluorescence peaks at 11.7 and 15.5 eV. The 11.7 eV fluorescence peak is due to CF_3^* emission resulting from dissociation of the molecule from the $(6a_1)^{-1}$ 3p Rydberg state of CF_3H. CF_2^* emission is seen at 15.5 and 16.7 eV and parent ion CF_3H^+ emission observed above *ca.* 20 eV (chapter 6).

E(eV)	Upper state configuration	IE-E(eV)	n-δ	δ
10.87	$(6a_1)^{-1}$ 3s	3.93	1.86	1.13
11.95	$(6a_1)^{-1}$ 3p	2.85	2.18	0.82
12.58	$(1a_2)^{-1}$ 3p	2.92	2.16	0.84
13.69	$(5e)^{-1}$ 3p	2.47	2.37	0.65
14.55	$(4e)^{-1}$ 3p	2.7	2.24	0.76
15.84	$(3e)^{-1}$ 3s	4.66	1.71	1.29
17.57	$(3e)^{-1}$ 3p	2.93	2.15	0.85

Table 5.3: CF_3H Photoabsorption assignments and quantum defect values. Vertical ionisation energies from Brundle and Robin [7]

5.2.3 CF_3Cl

CF_3Cl is of C_{3v} symmetry with an electronic configuration of the valence shell as …..$(1a_1)^2(1e)^4(2a_1)^2(3a_1)^2(2e)^4(4a_1)^2(3e)^4(4e)^4(1a_2)^2(5a_1)^2(5e)^4$. Vertical ionisation energies of the outer valence orbitals have been measured by high resolution He I and He II photoelectron spectroscopy [8] and are reported to be 13.08, 15.20, 15.80, 16.72, 17.71, 20.20, 21.2 and 23.8 eV. These result in the ionic states $\tilde{X}\ ^2E$, $\tilde{A}\ ^2A_1$, $\tilde{B}\ ^2A_2$, $\tilde{C}\ ^2E$, $\tilde{D}\ ^2E$, $\tilde{E}\ ^2A_1$, $\tilde{F}\ ^2E$, and $\tilde{G}\ ^2A_1$.

The photoabsorption spectrum of CF_3Cl taken in the 6 to 25 eV energy range and with a resolution of 0.08 nm on the primary monochromator is shown in figure 5.4. Resonant peaks are seen between 9 and 15 eV, some non-resonant features are seen at higher energies. The first peak is at 9.69 eV, using the Rydberg formula a quantum defect value of 2.00 is obtained. The 5e molecular orbital is of Cl non-bonding in character [8]. The quantum defect value expected for an isolated chlorine atom to a 4s Rydberg orbital is 2.01, therefore we can assign this peak as an excitation to the $(5e)^{-1}$ 4s Rydberg state. The second peak is seen at 10.64 eV, again using the Rydberg formula we can also assign this peak to a transition originating from the 5e molecular orbital terminating in the 4p Rydberg state. The $5a_1$ molecular orbital is of C-Cl bonding character [8]. If we assign the next peak at 11.60 eV to the $5a_1$ molecular orbital we get a quantum defect value of 2.06, higher than the value obtained for the 5e molecular orbital we assigned to the 9.69 eV peak. We would expect the quantum defect value for a molecular orbital with mixture of C and Cl character to have a lower value than an isolated chlorine atom. If the assignment is made to the $(5e)^{-1}$ 5s Rydberg state, the quantum defect value obtained is 1.97. Therefore the first three peaks in the absorption spectra of CF_3Cl are all assigned to transitions originating from the Cl non-bonding molecular orbital 5e. The peak at 13.38 eV has its origin in the C-Cl bonding molecular orbital, $5a_{1,}$ and has been assigned as an excitation to the $(5a_1)^{-1}$ 4s Rydberg state. The higher-energy structures are much more difficult to assign due to the high number of states available. Most of these bands are probably due to Rydberg transitions from either one of the fluorine lone pair orbitals 15.80 ($1a_2$), 16.72 (4e), and 17.71 eV (3e) or one of the other higher-energy valence orbitals.

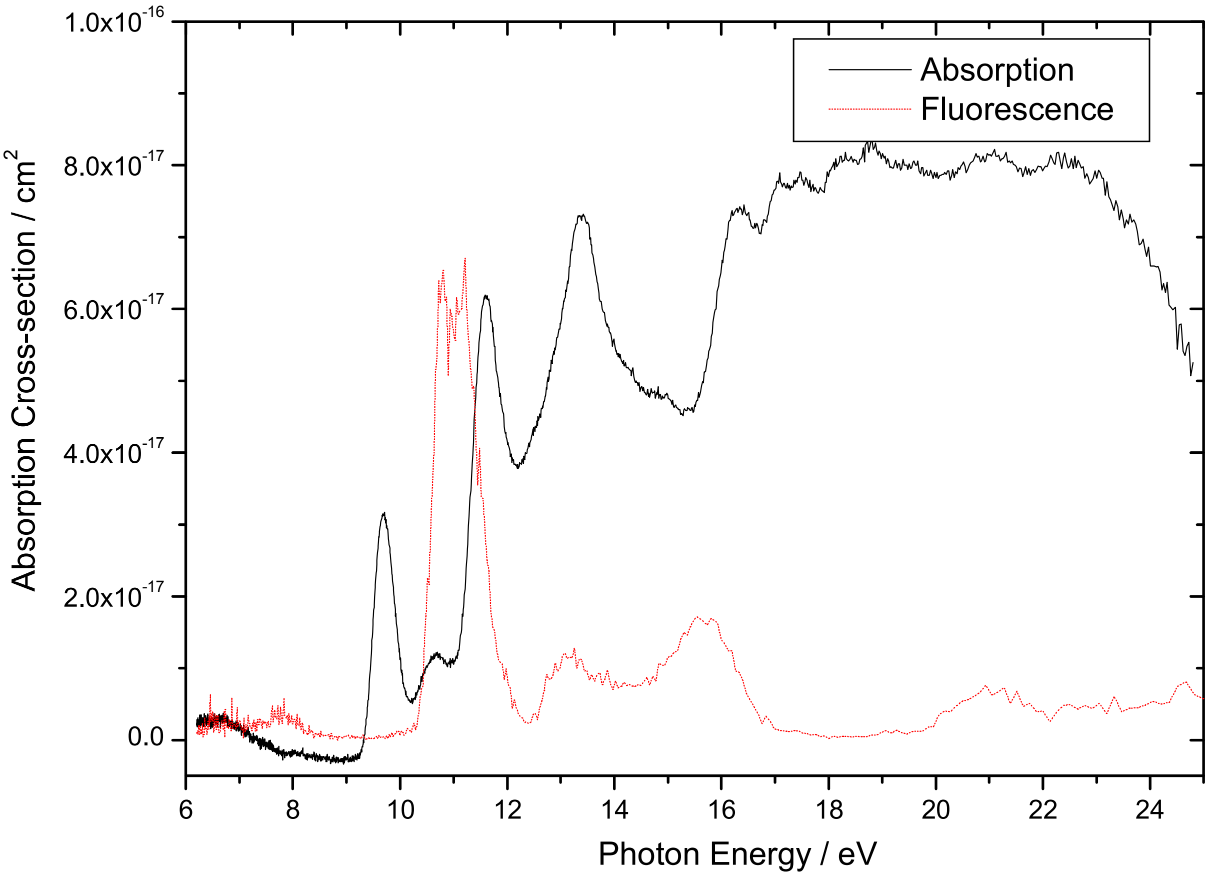

Figure 5.4: The photoabsorption spectrum of CF_3Cl taken at BESSY 1 with a resolution of 0.08 nm, the fluorescence excitation spectrum is shown for a qualitative comparison. Absorption cross-sections shown are absolute, whereas the fluorescence signal is arbitrary

The photoabsorption and fluorescence excitation spectra of CF_3Cl are compared in figure 5.4. There is some similarity between the two spectra. The first peak in the fluorescence excitation spectrum is a strong doublet seen at 10.7 and 11.1 eV. This emission could be a result of fluorescence related to either the $(5e)^{-1}$ 4p or the $(5e)^{-1}$ 5s Rydberg states. The fluorescence excitation spectrum shows broad peaks at 13.2 and 15.7 eV which presumably tally with absorption peaks at 13.38 and 16.39 eV.

E(eV)	Assignment	IE-E(eV)	(n-δ)	δ
9.69	$(5e)^{-1}$ 4s	3.39	2.00	2.00
10.64	$(5e)^{-1}$ 4p	2.44	2.36	1.64
11.60	$(5e)^{-1}$ 5s	1.48	3.03	1.97
13.38	$(5a_1)^{-1}$ 4s	1.82	2.73	1.27
16.39	$(4a_1)^{-1}$ 3s	3.81	1.89	1.11

Table 5.4: CF_3Cl Photoabsorption assignments and quantum defect values.

5.2.4 CF_3Br

CF_3Br is also of C_{3v} symmetry with an electronic configuration of the valence shell as ……$(1a_1)^2(1e)^4(2a_1)^2(3a_1)^2(2e)^4(4a_1)^2(3e)^4(4e)^4(1a_2)^2(5a_1)^2(5e)^4$, identical to that of CF_3Cl. The vertical ionisation energy of the outer valence orbitals have been measured by high resolution He I and He II photoelectron spectroscopy [9] and are reported to be 12.08, 14.28, 15.86, 16.55, 17.57, 19.80, 20.90 and 23.70 eV. Of the orbitals directly relevant to this work the 5e orbital is comprised essentially of a lone pair Br atom, the $5a_1$ orbital is associated with C-Br bonding and the $1a_1$, 4e, 3e and $4a_1$ orbitals are essentially fluorine 2p lone pair orbitals [9]. The quantum defects of ns, np and nd Rydberg orbitals centred on C (F) Br atoms are predicted to be 0.98 (1.20) 2.96, 0.58 (0.75) 2.51, and 0.01 (0.003) 1.1 [3].

The photoabsorption spectrum of CF_3Br taken in the 6 to 30 eV energy range and with a resolution of 0.08 nm on the primary monochromator is shown in figure 5.4. Resonant peaks are seen between 8 and 15 eV, non-resonant features are seen at higher energies. The first peak seen at 8.43 eV is assigned to the $(5a_1)^{-1}$ 4p Rydberg transition. A quantum defect value of 2.47 is obtained using the Rydberg formula. The $5a_1$ orbital has mixed C and Br character therefore the quantum defect value obtained should reflect that. The second peak has been assigned to the Br lone pair orbital 5e, giving a quantum defect value of 2.96, very close to what is expected for an isolated Br atom. Subsequent peaks are assigned to Rydberg transitions with origins in the 5e, $5a_1$, $1a_2$, 4e and 3e orbitals. The high energy peaks from *ca.* 16 eV onwards are very broad in nature and therefore not easily assigned to a particular Rydberg transition. These bands are probably due to more than one Rydberg transition, with origins from one of the fluorine lone pair orbitals.

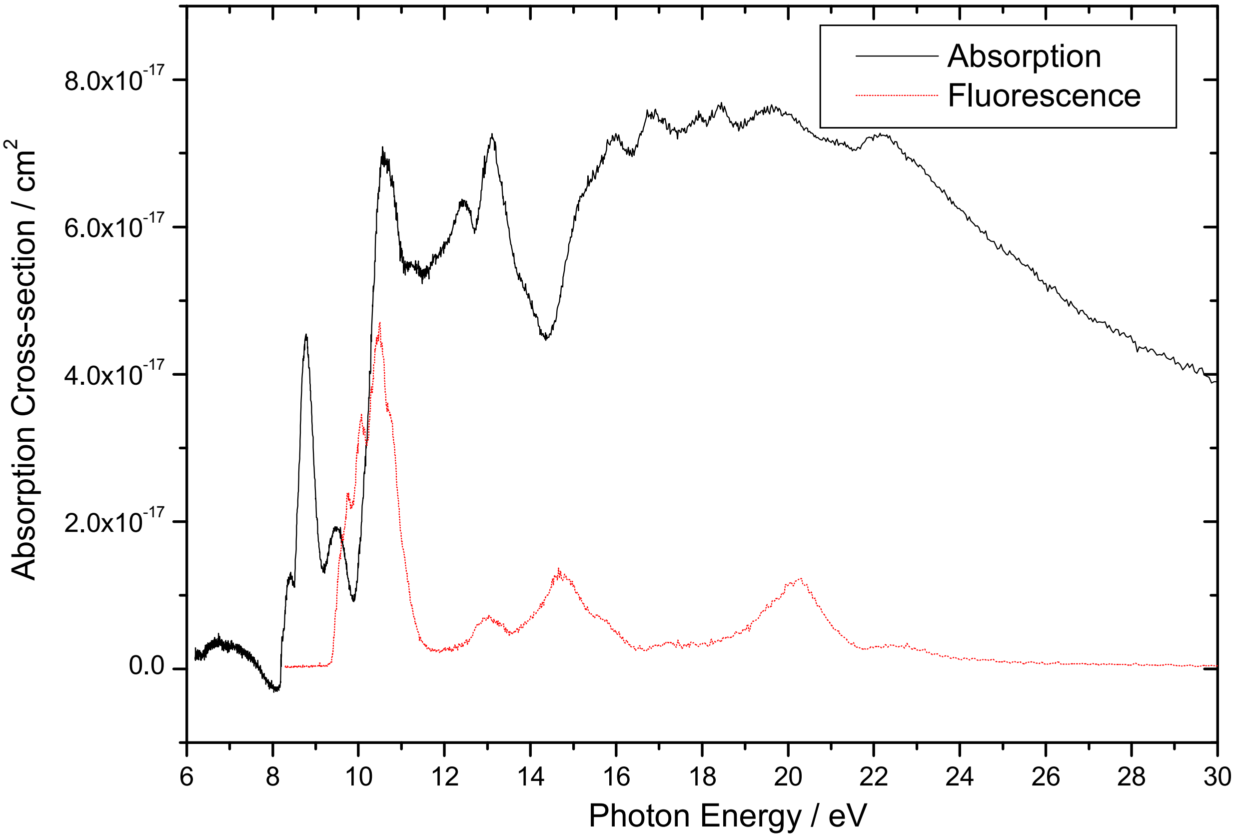

Figure 5.5: The photoabsorption and fluorescence excitation spectrum of CF_3Br. Absorption cross-sections shown are absolute, whereas the fluorescence signal is arbitrary

Again there is limited similarity between the absorption spectrum and the fluorescence excitation spectrum. Fluorescence excitation peaks are observed at 10.5, 13.0 and 14.7 eV with shoulders at 9.7 and 10.0 eV. The shoulders at 9.7 and 10.0 eV and the peak at 10.5 eV are all due to emission from CF_3^*. The peaks at 13.0 and 14.7 eV are a result of emission from the CF_2^* fragment (chapter 6).

E(eV)	Assignment	IE-E(eV)	(n-δ)	δ
8.43	$(5a_1)^{-1}$ 4p	5.85	1.53	2.47
8.80	$(5e)^{-1}$ 5s	3.28	2.04	2.96
9.50	$(1a_2)^{-1}$ 4p	6.36	1.46	2.54
10.57	$(5e)^{-1}$ 4d	1.51	3.00	1.00
11.23	$(5a_1)^{-1}$ 5s	3.05	2.11	2.89
12.43	$(1a_2)^{-1}$ 5s	3.43	1.99	3.01
13.11	$(4e)^{-1}$ 5s	3.44	1.99	3.01
16.03	$(3e)^{-1}$ 4d	1.54	2.97	1.03
16.92	$(3a_1)^{-1}$ 4p	6.78	1.41	2.58

Table 5.5: CF_3Br Photoabsorption assignments and quantum defect values.

5.3 Conclusions

In this chapter we present the VUV photoabsorption spectra of CF_3X (X=F,H,Cl,Br). Assignments were based primarily on quantum defect analysis using the Rydberg formula. The peaks in the photoabsorption spectra were mainly assigned to Rydberg transitions. Fluorescence excitation spectra taken at BESSY 1 are also shown for comparison.

5.4 References:

[1] J.H. Seinfeld, S.N. Pandis, *Atmospheric Chemistry and Physics*, Wiley, New York, (1998)

[2] P.J. Bassett and D.R. Lloyd, *J. Chem. Soc. A,* (1971) 641

[3] C.E. Theodosiou, M. Inokuti and S.T. Mason, *Atomic Data and Nuclear Data Tables*, **35** (1986) 473.

[4] G. Herzberg, *Molecular spectra and molecular structure III, Electronic spectra and electronic structure of polyatomic molecules.*

[5] L.C. Lee, E. Phillips and D.L. Judge, *J. Chem. Phys*. **67** (1977) 1237.

[6] J.F.M. Arts, S.M. Mason and R.P. Tuckett , *J. Chem. Phys*. **60** (1987) 761.

[7] C. R. Brundle, M. B. Robin, *J. Chem. Phys.,* **53**, (1970), 2196

[8] T. Cvitas, H. Gusten and L. Klasinc, *J. Chem. Phys*. **67** (1977) 2687.

[9] T. Cvitas, H. Gusten, L. Klasinc, I. Novak and H. Vancik, *Z. Naturforsch.* **33a** (1978) 1528

[10] L.C. Lee, J.C. Han, C. Ye and M. Suto, *J. Chem. Phys*. **92** (1990) 133.

[11] M Suto and L C Lee , *J Chem. Phys*, **79** (1983) 1127

[12] I.R. Lambert, S.M. Mason, R.P. Tuckett and A. Hopkirk, *J. Chem. Phys*. **89** (1988) 2683.

[13] H. Biehl a, K.J. Boyle a, R.P. Tuckett a,*, H. BaumgErtel b, H.W. Jochims *Chemical Physics* **214** (1997) 367

[14] J.C. Creasey, I.R. Lambert, R.P. Tuckett and A. Hopkirk, *Mol. Phys*. **71** (1990) 1355.

[15] J.C. Creasey, I.R. Lambert, R.P. Tuckett and A. Hopkirk, *Mol. Phys*. **71** (1990) 1367.

[16] J.C. Creasey, P.A. Hatherly, I.R. Lambert and R.P. Tuckett, *Chem. Phys. Lett*. **188** (1992) 223.

[17] H. Biehl, K.J. Boyle, D.M. Smith and R.P. Tuckett, *Chem. Phys*. **214** (1997) 357.

6. VUV fluorescence spectroscopy of CF_3X (X = F, H, Cl, Br, I)

6.1 Introduction

In this chapter we present the VUV fluorescence spectra of CF_3X, where X = F, H, Cl, Br or I. The spectra presented in this chapter were taken using beamline 3.1 at the Daresbury SRS. The fluorescence excitation spectra were taken using either the medium energy grating (MEG) or the high energy grating (HEG) at a resolution of 0.2 nm and 0.1 nm, respectively. Of the five samples CF_4 has been the most extensively studied molecule in the VUV range. Fluorescence studies using synchrotron radiation have been performed by Lee *et al* [1,2], Lambert *et al* [3] and by the Tuckett group [4-8]. Mason *et al* [9] recorded the photoabsorption spectrum of CF_3I using synchrotron radiation between 3.9 and 10.8 eV. As far we know there has been no previous work done on the fluorescence spectroscopy of CF_3I.

6.2 Results

6.2.1 CF_4

The electronic configuration of the outer valence molecular orbitals of CF_4 is …..$(4a_1)^2$ $(3t_2)^6$ $(1e)^4$ $(4t_2)^6$ $(1t_1)^6$. This numbering scheme includes C 1s and F 1s core orbitals. The flux-normalised fluorescence excitation spectrum of CF_4 taken using the HEG with a resolution of 0.1 nm is shown in figure 6.1. The first feature is a non-resonant peak seen between the photoexcitation energies of *ca.*11 and 13 eV. A second feature is a resonant peak with a peak at 13.68 eV. A weak resonant structure which peaks at 15.70 eV is seen between *ca.* 15 and 17 eV. The last major structure we see is a non-resonant feature with an onset at 21.75 eV. Resonant and non-resonant peaks and their properties are described in chapter 2. The band at lowest energy, with an onset of 10.80 eV and a peak at 11.4 eV, is a lower-intensity replica of the peak at 22.80 eV, due to second-order radiation from the primary monochromator, and even reproduces the fine structure to high energy of the peak. The first ionisation energy of CF_4 is at 16.23 eV [10], therefore any fluorescence signal seen at photoexcitation energies below this value will be due to neutral fragments of CF_4. Table 6.1 shows the energetics of the possible dissociation channels for the CF_4 neutral and parent ion. The thermochemical threshold for the production of CF_2 $\tilde{A}$ $^1B_1$ + F_2 is 12.34 eV. The threshold for the production of CF_3 $^2A_1$' (4s) + F is at 11.98 eV. Therefore the fluorescence observed at 13.68 eV could be due to either one of these fragments. The weak resonant peak at 15.70 eV is still below the first ionisation energy of CF_4 and below the threshold energy for production of CF A $^2\Sigma^+$ + F + F_2 at 18.31 eV, therefore this signal is probably also due to either the CF_3* or CF_2*

fragments. The final non-resonant peak which has an onset at 21.75 eV and peaks at 22.88 eV is most probably due to parent ion emission.

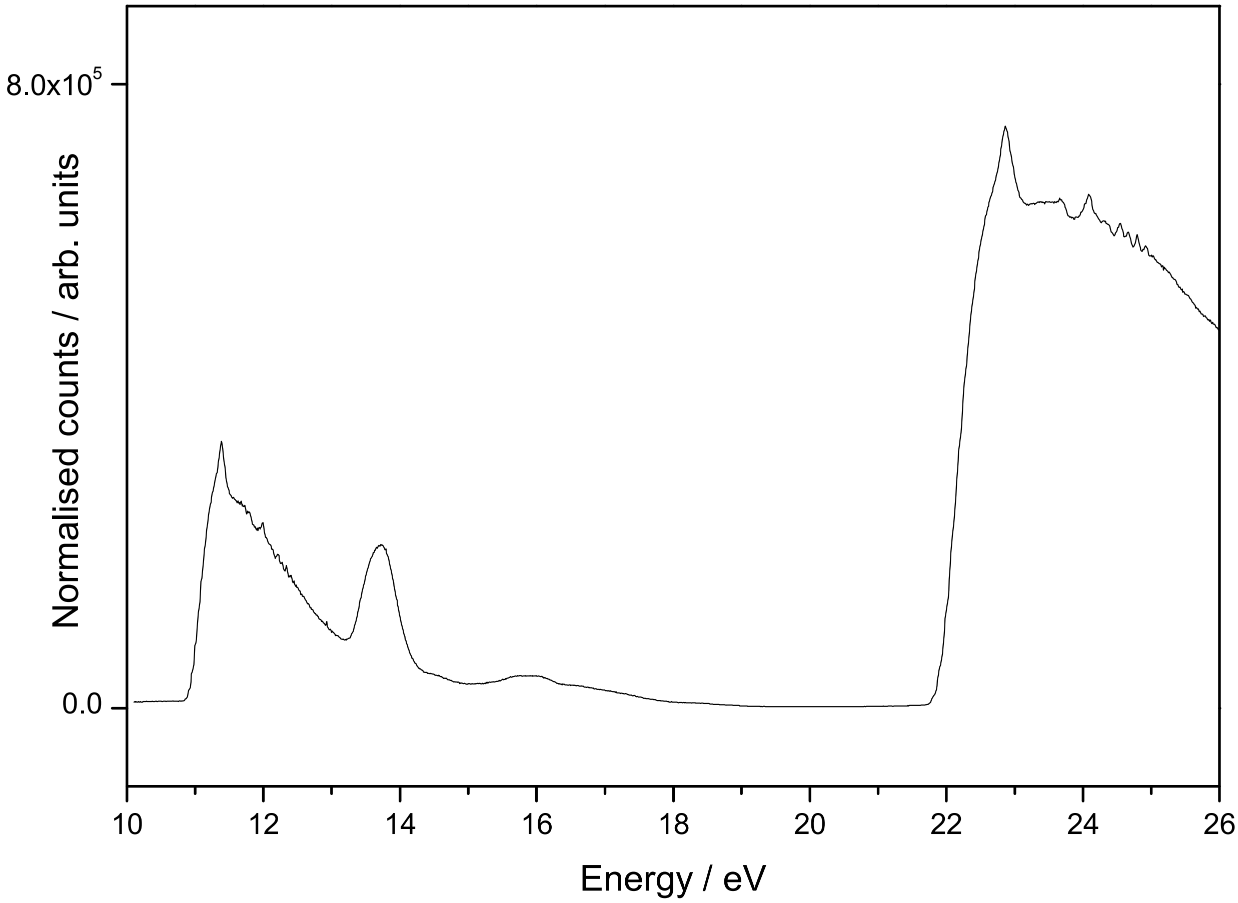

Figure 6.1: The undispersed fluorescence excitation spectrum of CF_4, taken using the HEG at a resolution of 0.1 nm.

The dispersed fluorescence spectra recorded at the Daresbury SRS are shown in figures 6.2, 6.3 and 6.4. The spectra were taken with the new Wadsworth monochromator which was used to select the photoexcitation energy. As described in chapter 2, the resultant fluorescence was collected using a fibre optic bundle attached to the interaction region, and then dispersed using a 0.19 m Jobin-Yvon Triax monochromator. The dispersed signal was detected with a 1024 x 256 pixel, liquid N_2 cooled, open-electrode CCD. A choice of turrets and gratings is available depending on the wavelengths of the dispersed signal. For the dispersed spectra taken below the peak at 22.88 eV the UV turret and the 300 grooves mm^{-1} grating provided the best combination. The spectrum taken at 22.88 eV was dispersed using the UV turret and the 1200 grooves mm^{-1} grating.

Neutral/parent ion		Dissociation channel	Dissociation energy / eV	Vertical IE / eV
	$\tilde{D}\ ^2A_1$			25.10
	$\tilde{C}\ ^2T_2$			21.95
		CF B $^2\Delta$ + 3F	20.74	
		CF A $^2\Sigma^+$ + 3F	19.91	
		CF B $^2\Delta$ + F + F_2	19.14	
	$\tilde{B}\ ^2E$			18.50
		CF A $^2\Sigma^+$ + F + F_2	18.31	
	$\tilde{A}\ ^2T_2$			17.47
CF_4^+	$\tilde{X}\ ^2T_1$			16.23
		CF X $^2\Pi$ + 3F	14.62	
		CF X $^2\Pi$ + F_2 + F	13.02	
		CF_2 $\tilde{A}\ ^1B_1$ + 2F	13.94	
		CF_2 $\tilde{X}\ ^1A_1$ + 2F	9.32	
		CF_2 $\tilde{A}\ ^1B_1$ + F_2	12.34	
		CF_2 $\tilde{X}\ ^1A_1$ + F_2	7.72	
		CF_3 $^2A_1^{'}$ (4s) + F	11.98	
		CF_3 $^2A_2^{''}$ / $^2E^{'}$ (3p) + F	11.97	
		CF_3 $\tilde{X}\ ^2A_1$ + F	5.57	
CF_4	$\tilde{X}\ ^1A_1$			

Table 6.1. Dissociation channels of CF_4

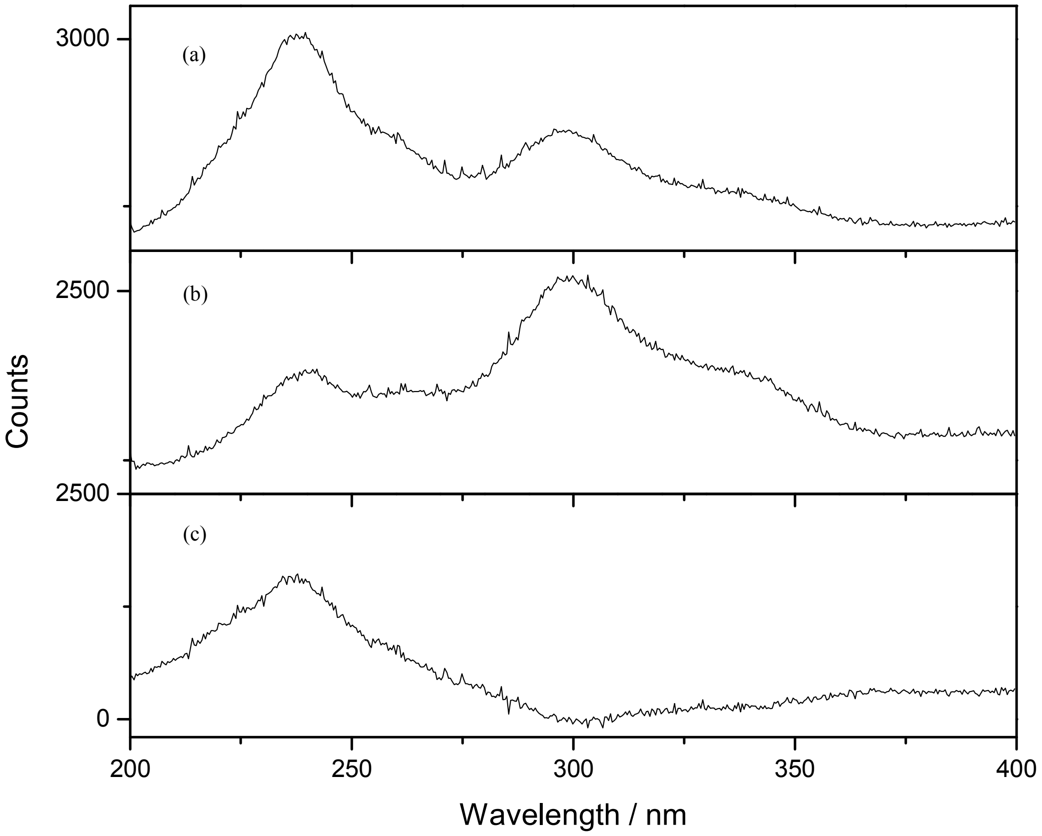

Figure 6.2: (a) Dispersed fluorescence spectra of CF_4 taken with a photoexcitation energy of 13.68 eV (b) taken with a photoexcitation energy of 13.20 eV. Both spectra were taken using the UV turret and 100 grooves mm^{-1} grating. (c) Difference spectrum of CF_4 spectrum (a) – (b).

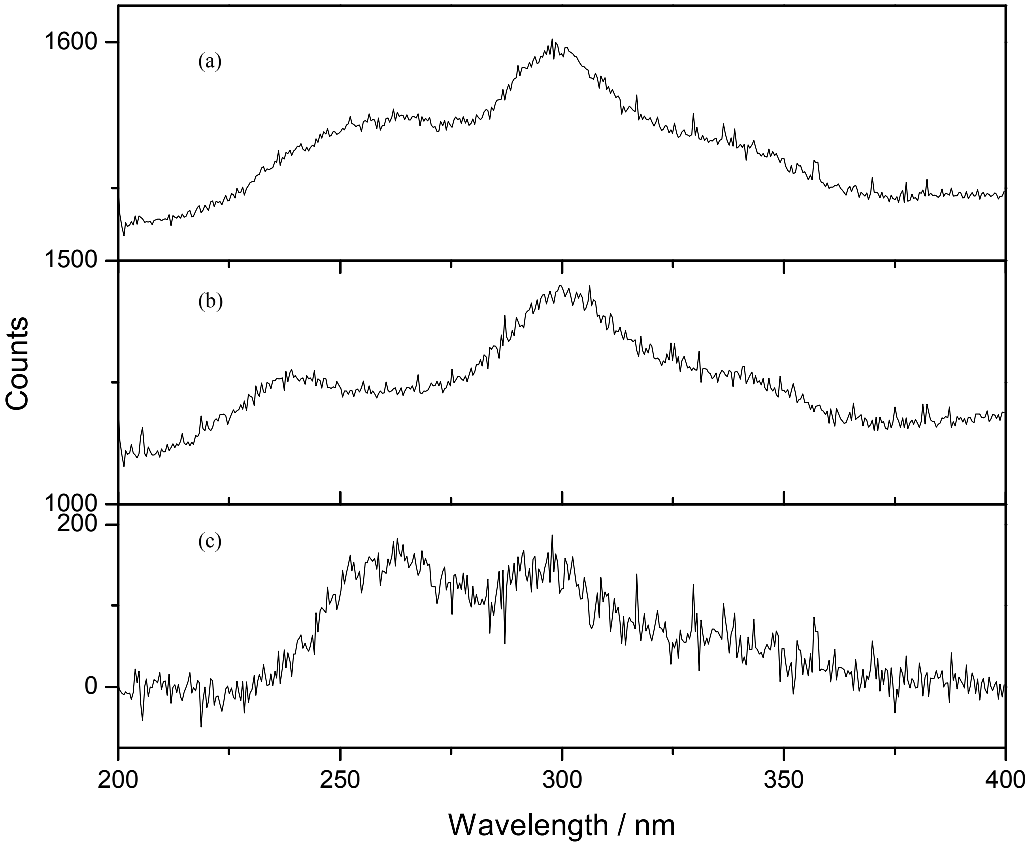

Figure 6.3: (a) Dispersed fluorescence spectra of CF_4 taken with a photoexcitation energy of 15.7 eV (b) taken with a photoexcitation energy of 15.0 eV. Both spectra were taken using the UV turret and 100 grooves mm^{-1} grating. (c) Difference spectrum of CF_4 spectrum (a) – (b).

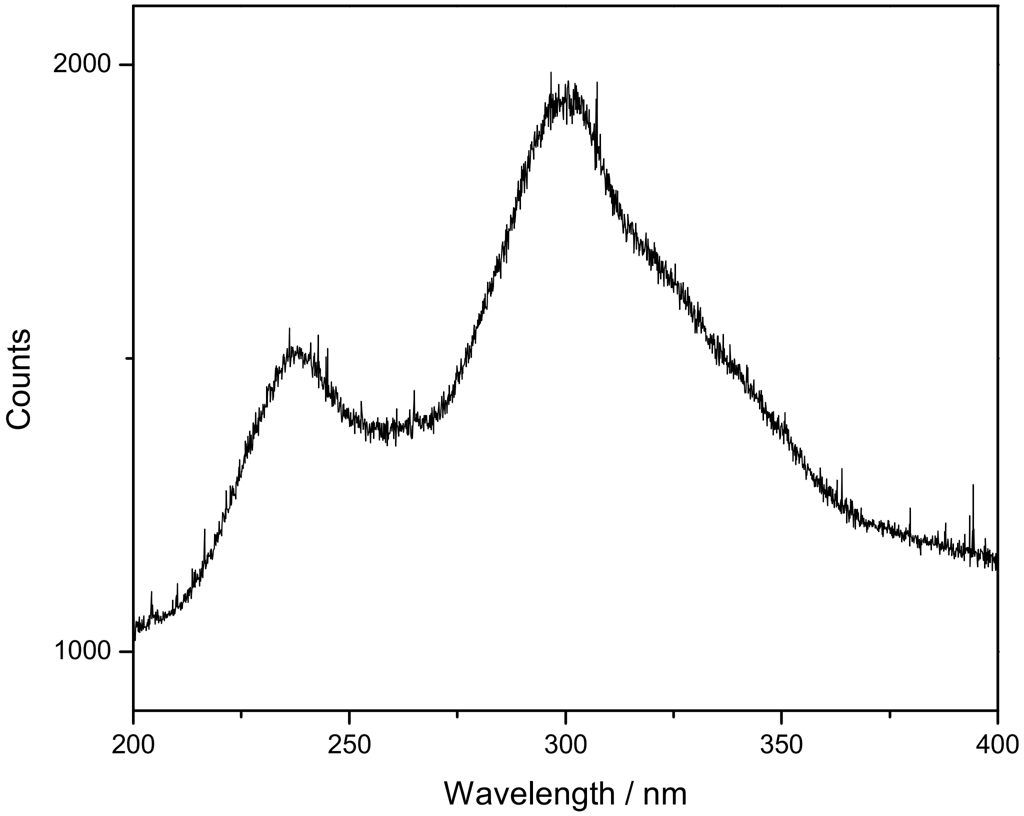

Figure 6.4: Dispersed fluorescence spectra of CF_4 taken with a photoexcitation energy of 22.88 eV, using the UV turret and 1200 grooves mm^{-1} grating.

Figure 6.2 shows the dispersed fluorescence spectra of CF_4 taken with a photoexcitation energy of 13.20 eV, below the onset of the first peak, and at the peak energy of 13.68 eV. The dispersed spectrum at 13.20 eV is an almost exact replica of the fluorescence signal seen at 22.88 eV (figure 6.4). The spectrum at 13.20 eV is below the signal threshold of the peak at 13.68 eV and is almost certainly due to second-order signal from the primary monochromator at 26.40 eV. Figure 6.2 (c) shows the difference spectrum of 6.2 (a) and (b). A broad band is seen between 200 and 300 nm with a peak at 237 nm. This peak is assigned as emission from the CF_3 radical between the $^2A_1$' (4s) Rydberg state and the $\tilde{X}$ $^2A_1$ ground state [3].

Figure 6.3 shows the dispersed fluorescence spectra of CF_4 taken below the onset of the second peak at 15 0 eV and at the peak 15.7 eV. Figure 6.3 (c) shows the difference spectrum of 6.3 (a) and (b). Two peaks are seen with wavelengths at 260 and 300 nm. The first peak at 260 nm is probably due to the CF_2 $\tilde{A}$ $^1B_1$ - $\tilde{X}$ $^1A_1$ transition. The second peak at 300 nm is much more difficult to assign. One possibility is that the emission arises from the CF_2 $\tilde{B}$ state. This transition, if real, should be observed at *ca.* 280 nm, although there is dispute in the literature as to whether the $\tilde{B}$ state has actually been seen. Mathews [11] claimed to have observed a CF_2 $\tilde{B}$ - $\tilde{A}$ transition between 131 and 138 nm, but it has been argued that this assignment is possibly incorrect and instead the transition could be due to the

CF_3* radical [3]. On the other hand, the two peaks could be a result of emission from CF_2 $\tilde{A}$ $^1B_1$ produced via two different dissociation channels. The CF_2 $\tilde{A}$ $^1B_1$ + F_2 channel has a thermochemical threshold of 12.34 eV and the CF_2 $\tilde{A}$ $^1B_1$ + 2F channel has a thermochemical threshold of 13.94 eV. If dissociation were to occur via the former channel, the excess energy available, could result in the CF_2 $\tilde{A}$ $^1B_1$ state being produced with substantial rovibrational energy. If dissociation were to occur via the latter channel, the experimental and thermochemical threshold are much closer in energy, and CF_2 $\tilde{A}$ $^1B_1$, will be produced with less internal energy. If both channels are operative at an excess energy at 15.7 eV, a bimodal populaton of CF_2 $\tilde{A}$ $^1B_1$ vibrational levels may be produced, thereby producing two peaks in the $\tilde{A}$ - $\tilde{X}$ emission spectrum. The third possibility is that the emission is from the CF^* radical. However the first excited state of CF is 5.29 eV above the ground state, and this energy difference is probably too high for the peak at 300 nm to be CF A – X emission.

This double peaked signal is seen for all the molecules in the CF_3X series described in this chapter. We conclude that the emission is probably from a common emitter, therefore we can eliminate the possibility that it is a result of CH or CFH emission. This feature has not been seen before in any previous work [1-8]. This is not surprising due to the extra sensitivity of our detection system in comparison to detection systems used in other work. However the possibility that these features are a result of some instrumental effect of the secondary monochromator and CCD Triax system cannot completely be discounted.

Figure 6.4 shows the dispersed spectrum taken with a photoexcitation energy of 22.4 eV using the HEG and the UV turret with the 1200 grooves mm^{-1} grating. We now have enough energy to excite to the CF_4^+ $\tilde{C}$ $^2T_2$. The two peaks seen at 239 and 298 nm in figure 6.4 are assigned to the CF_4^+ $\tilde{C}\,^2T_2 - \tilde{X}\,^2T_1$ and $\tilde{C}\,^2T_2 - \tilde{A}\,^2T_2$ transitions respectively.

6.2.2 CF_3H

CF_3H has C_{3v} geometry with the electronic configuration of its outer valence molecular orbitals being … $(4a_1)^2$ $(5a_1)^2$ $(3e)^4$ $(4e)^4$ $(5e)^4$ $(1a_2)^2$ $(6a_1)^2$ [12]. The numbering scheme does not include core orbitals. The fluorescence excitation spectrum of CF_3H taken using the HEG and with a resolution of 0.1 nm is shown in figure 6.5. Three main features are seen between the photoexcitation energies of 10 and 22 eV. The first band is resonant in nature with a peak at 11.70 eV. The signal onset is at *ca.* 11.10 eV; there is enough energy here to populate either the CF_2 $\tilde{A}$ $^1B_1$ state via the CF_2 $\tilde{X}$ $^1A_1$ + HF dissociation channel or the CF_3 $^2A_1{}'$ (4s) Rydberg state. Therefore the fluorescence observed could be a result of emission from either one of these fragments. The second feature is also a resonant peak seen between *ca.* 14 and 18 eV with a peak at 15.70 eV and a shoulder at 17.0 eV. The thermochemical threshold for the production of the CF_2 $\tilde{A}$ $^1B_1$ + H + F is at 12.92 eV. The fluorescence seen between *ca.* 14 and 18 eV is probably due to emission from this state or alternatively emission from either the CF_3^* or CF^* radical. The non-resonant peak with an onset at 20.0 eV has the characteristics of parent ion emission from CF_3H^+. At the photoexcitation energy of 20 eV we can populate the $\tilde{D}$ $^2A_1$ state and emission probably emanates from there.

The dispersed fluorescence spectra taken at 11.70 eV was taken using the UV turret and 100 grooves mm^{-1} grating on the secondary Triax monochromator. A higher-resolution spectrum taken using the UV turret in combination with the 1200 grooves mm^{-1} grating was also taken at this energy to observe the vibrational structure. The spectra taken at higher energies were taken using the UV turret and the 300 grooves mm^{-1} grating.

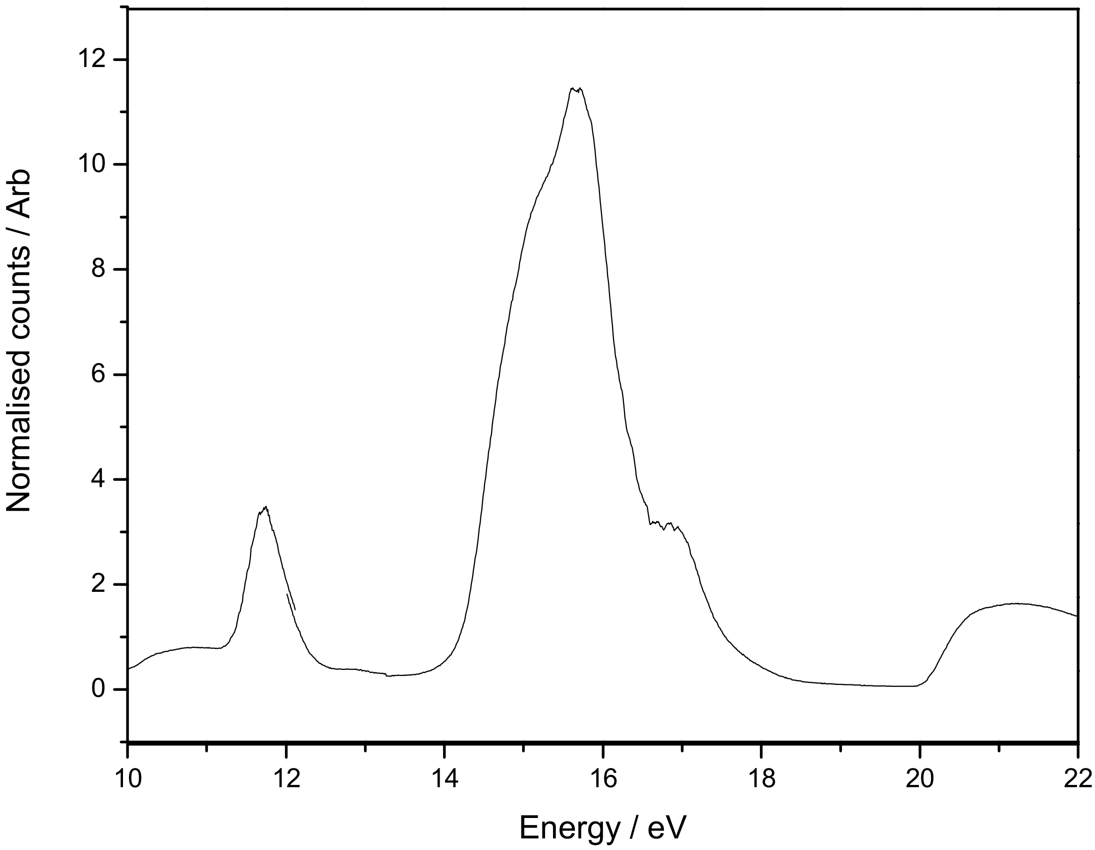

Figure 6.5: The undispersed fluorescence excitation spectrum of CF_3H, taken using the HEG at a resolution of 0.1 nm.

The dispersed fluorescence spectrum of CF_3H taken with a photoexcitation energy of 11.7 eV is shown in figure 6.6. In the spectrum we can see two broad bands with the first band between *ca.* 200 to 280 nm which has a peak at 240 nm. The second is a much broader band between *ca.* 400 and 800 nm which has a peak at 630 nm. Both these bands have been assigned as emission from the CF_3* radical. The first band is a result of a transition between the $^2A_1$' (4s) Rydberg state and the $\tilde{X}$ $^2A_1$ ground state of CF_3. This same band is seen in the CF_4 dispersed spectrum taken at a photoexcitation energy of 13.68 eV. The second band is also due to emission from the CF_3 radical. This time the emission is assigned, based on *ab initio* calculations, [13] to a Rydberg – Rydberg transition between an excited state of either ^2E' or $^2A_2$" symmetry and a repulsive lower state of $^2A_1$' symmetry. A higher-resolution scan of the first band was taken using the UV turret and the 1200 grooves mm^{-1} grating and is shown in figure 6.7. The slit width on the secondary Triax monochromator was set at 1 mm corresponding to a resolution of 3.5 nm. In this spectrum we can clearly see the vibrational progressions, due to the v_2 bending umbrella mode of CF_3 in its ground electronic state. The vibrational spacing of 890 cm^{-1} is in good agreement with previous studies [3].

Figure 6.8 (a) and (b) shows the dispersed fluorescence spectra of CF_3H taken with photoexcitation energies of 15.7 and 21.7 eV respectively. The spectrum taken with a photoexcitation energy of 15.7 eV (figure 6.8 (a)) shows two bands with peaks at 280 and 300 nm. The two bands are also seen in the CF_4 spectrum taken at 15.7 eV, but that much weaker spectrum is complicated by second-order signal from the primary monochromator. The much stronger CF_3H spectrum shows no signs of second-order signal coming from the primary monochromator, therefore this spectrum is probably a clean spectrum showing only first-order signal from 15.7 eV. These two bands have been assigned to CF_2 $\tilde{A}\ ^1B_1$ - $\tilde{X}\ ^1A_1$ emission. The two bands are a result of bimodal distribution resulting from two different dissociation channels of CF_3H to produce the CF_2^* radical. The thermochemical threshold for the production of CF_2 $\tilde{A}$ state via the two different dissociation channels are 8.30 eV for CF_2 $\tilde{A}\ ^1B_1$ + HF and 12.92 eV for CF_2 $\tilde{A}\ ^1B_1$ + H + F. If dissociation occurs via the former channel, more excess energy is available to populate higher vibrational levels of the CF_2 $\tilde{A}$ state.

The spectra taken with a photoexcitation energy of 21.7 eV is shown in figure 6.8 (b). There are several bands seen between 220 and 550 nm. The main bands appear at 260, 300 and 335 nm with some sharp atomic-like peaks seen at 430 and 482 nm. The bands between 220 and 375 nm have been assigned as emission from the parent ion CF_3H^+ originating from the $\tilde{D}$ $^2A_1$ state. These peaks are a result of transitions between the $\tilde{D}\ ^2A_1$ - $\tilde{X}\ ^2A_1$, $\tilde{D}\ ^2A_1$ - $\tilde{B}\ ^2E$ and $\tilde{D}\ ^2A_1$ - $\tilde{C}\ ^2E$ states of CF_3H^+. A_1 - E transitions are allowed under electronic dipole selection rules, but the $\tilde{D}\ ^2A_1$ - $\tilde{A}\ ^2A_2$ transition is formally forbidden. The two sharp peaks at 430 and 482 nm are due to hydrogen $n = 4 – 2$ and $n = 5 – 2$ transitions.

Neutral/parent ion	Dissociation channel	Dissociation energy / eV	Vertical IE / eV
$\tilde{D}\ ^2A_1$			20.5
	CF B $^2\Delta$ + H + 2F	19.73	
	CF A $^2\Sigma^+$ + H + 2F	18.89	
$\tilde{C}\ ^2E$			17.25
$\tilde{B}\ ^2E$			16.16
$\tilde{A}\ ^2A_2$			15.50
CF_3H^+ $\tilde{X}\ ^2A_1$			14.80
	CF B $^2\Delta$ + HF + F	13.87	
	CF X $^2\Pi$ + H + 2F	13.60	
	CF A $^2\Sigma^+$ + HF + F	13.03	
	CF X $^2\Pi$ + F_2 + H	12.00	
	CF X $^2\Pi$ + HF + F	7.74	
	CFH + $\tilde{X}\ ^1A'$ 2F	10.17	
	CFH + $\tilde{X}\ ^1A'$ F_2	8.53	
	CF_2 $\tilde{A}\ ^1B_1$ + H + F	12.92	
	CF_2 $\tilde{B}$ + HF	11.46	
	CF_2 $\tilde{X}\ ^1A_1$ + H + F	8.30	
	CF_2 $\tilde{A}\ ^1B_1$ + HF	7.06	
	CF_2 $\tilde{X}\ ^1A_1$ + HF	2.44	
	$CF_3\ ^2A_1'$ (4s) + H	10.96	
	$CF_3\ ^2A_2''$ / $^2E'$ (3p) + H	10.95	
	CF_3 $\tilde{X}\ ^2A_1$ + H	4.55	
CF_3H $\tilde{X}\ ^1A_1$			

Table 6.2: Dissociation channels of CF_3H

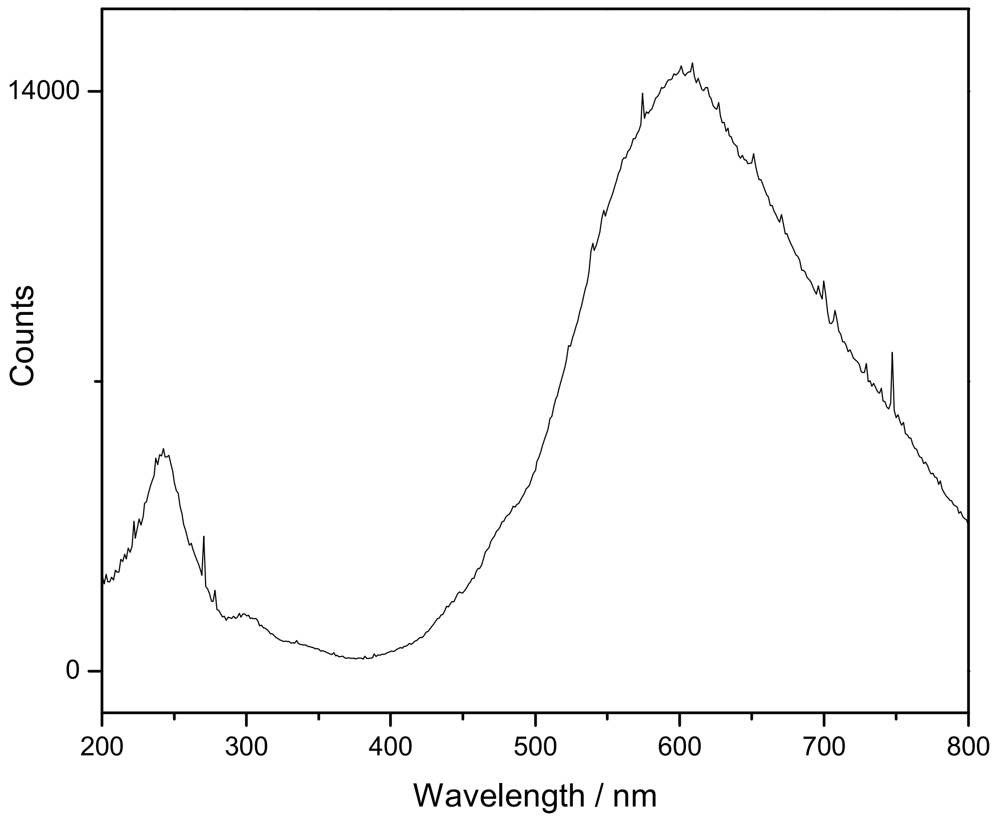

Figure 6.6: Dispersed fluorescence spectra of CF_3H taken with photoexcitation energy of 11.7 eV, using the UV turret and 100 grooves mm^{-1} grating.

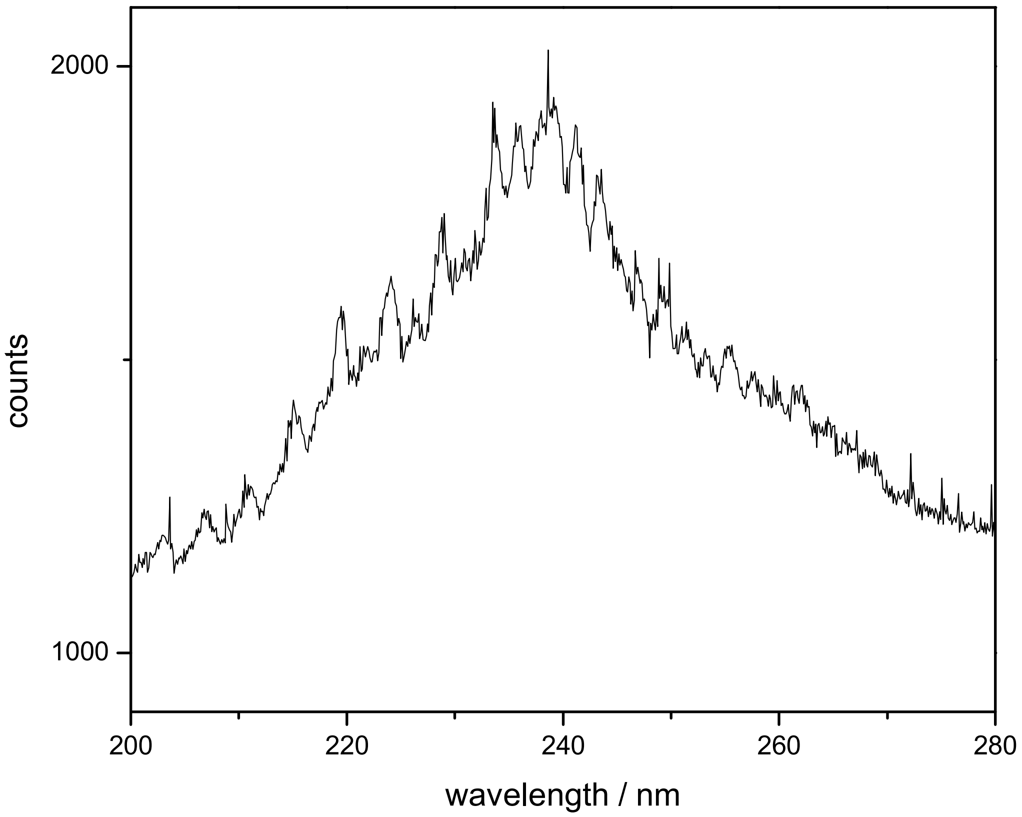

Figure 6.7: Dispersed fluorescence spectra of CF_3H taken with a photoexcitation energy of 11.7 eV, using the UV turret and 1200 grooves mm^{-1} grating.

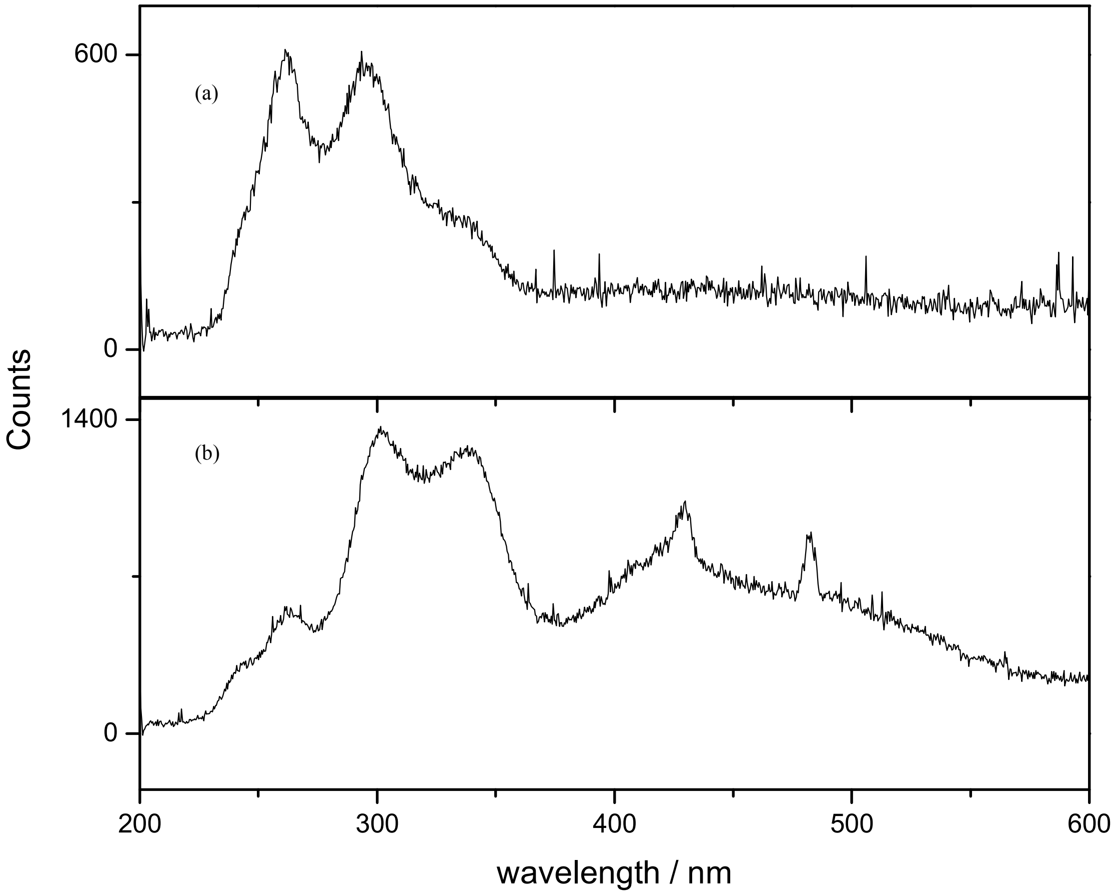

Figure 6.8: (a) Dispersed fluorescence spectra of CF_3H taken with a photoexcitation energy of 15.7 eV (b) taken with a photoexcitation energy of 21.7 eV. Both spectra were taken using the UV turret and 300 grooves mm^{-1} grating.

6.2.3 CF_3Cl

The VUV fluorescence excitation spectrum of CF_3Cl taken using the MEG at a resolution of 0.2 nm is shown in figure 6.9. Resonant peaks are seen between *ca.* 10 and 18 eV with peak energies of 11.29 and 15.90 eV and shoulders at 10.9 and 13.2 eV. A further non-resonant band with a peak at 21.0 eV is also seen. The lowest-energy peak in both the CF_4 and CF_3H fluorescence excitation spectra were assigned to emission from the CF_3^* radical. The thermochemical threshold for production of the CF_3^* radical lies below the experimental onset of *ca.* 10 eV, therefore this peak should be due to emission emanating from this radical. The two peaks at 13.2 and 15.9 are in a very similar energy range, to that in the CF_4 and CF_3H excitation spectra where emission from CF_2^* was observed. The peak at 21.0 eV lies above the energy of the $\tilde{E}\ ^2A_1$ state of CF_3Cl^+ at 20.2 eV [10]. This peak we would expect to be a result of emission emanating from the parent ion CF_3Cl^+.

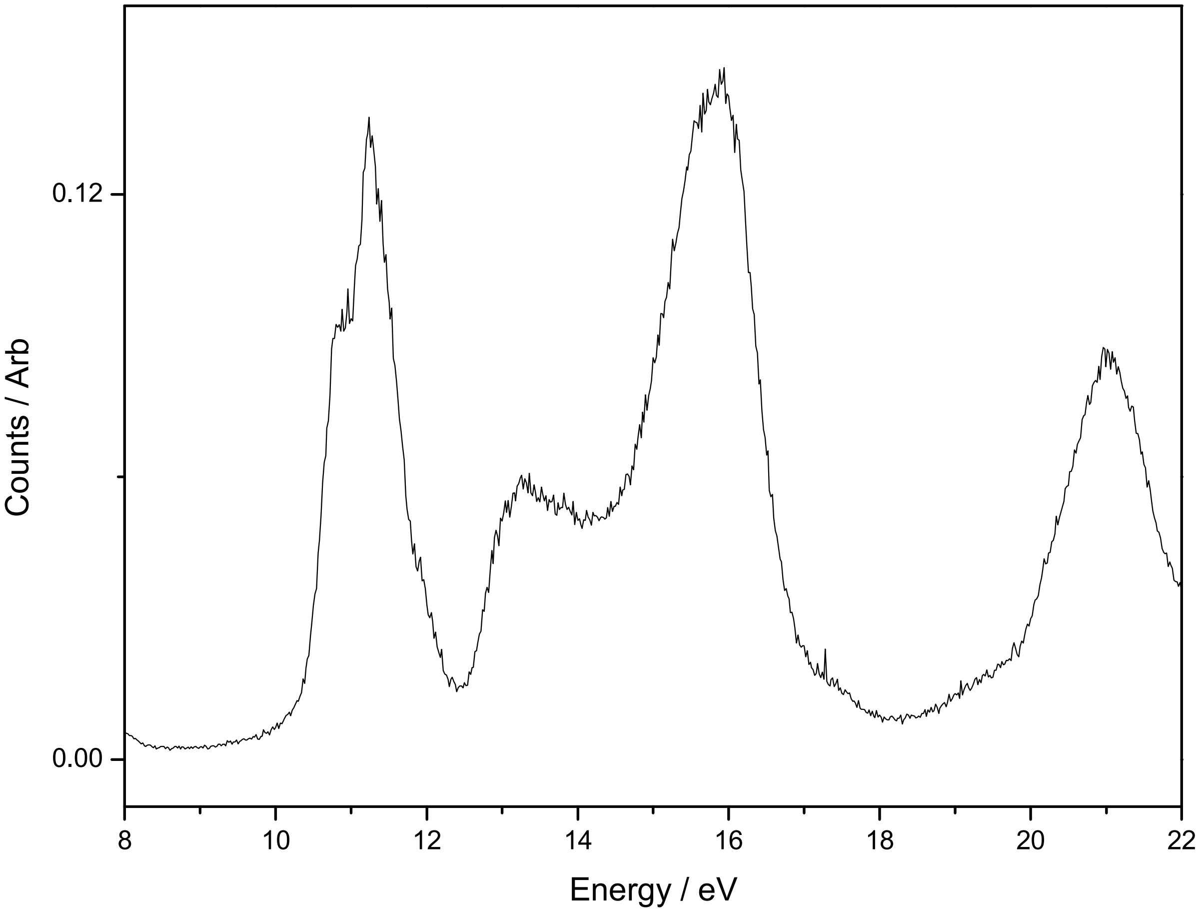

Figure 6.9: The undispersed fluorescence excitation spectrum of CF_3Cl, taken using the MEG at a resolution of 0.2 nm.

Neutral/parent ion	Dissociation channel	Dissociation energy / eV	Vertical IE / eV
$\tilde{E}\ ^2A_1$			20.20
	CF B $^2\Delta$ + Cl + 2F	18.85	
	CF A $^2\Sigma^+$ + Cl + 2F	18.02	
	CF B $^2\Delta$ + ClF + F	16.28	
	CF X $^2\Pi$ + Cl + 2F	18.85	
$\tilde{D}\ ^2E$			17.71
$\tilde{C}\ ^2E$			16.72
$\tilde{B}\ ^2A_2$			15.80
	CF A $^2\Sigma^+$ + ClF + F	15.45	
$\tilde{A}\ ^2A_1$			15.20
	CF X $^2\Pi$ + F_2 + Cl	11.12	
	CF X $^2\Pi$ + ClF + F	10.16	
	CF_2 $\tilde{B}$ + ClF	13.88	
CF_3Cl^+ $\tilde{X}\ ^2E$			13.08
	CF_2 $\tilde{A}\ ^1B_1$ + Cl + F	12.04	
	CF_2 $\tilde{A}\ ^1B_1$ + ClF	9.48	
	CF_2 $\tilde{X}\ ^1A_1$ + Cl + F	7.42	
	CF_2 $\tilde{X}\ ^1A_1$ + ClF	4.86	
	CFCl $\tilde{A}\ ^1A''$ + 2F	11.91	
	CFCl $\tilde{X}\ ^1A'$ + 2F	8.78	
	CFCl $\tilde{A}\ ^1A''$ + F_2	10.26	
	CFCl $\tilde{X}\ ^1A_1'$ + F_2	7.13	
	CF_3 $^2A_1'$ (4s) + Cl	10.08	
	CF_3 $^2A_2''$ / $^2E'$ (3p) + Cl	10.07	
	CF_3 $\tilde{X}\ ^2A_1$ + Cl	3.67	
CF_3Cl $\tilde{X}\ ^1A_1$			

Table 6.3: Dissociation channels of CF_3Cl

Figure 6.10 shows the dispersed fluorescence spectrum of CF_3Cl taken with a photoexcitation energy of 11.0 eV[1]. This spectrum was dispersed using the UV turret and the 100 grooves mm^{-1} grating on the secondary Triax monochromator. This spectrum has not been normalised to the sensitivity of the CCD (chapter 2) due to the weakness of the dispersed signal. Two bands are seen, the first band is a weak band between 200 and 275 nm with a peak at *ca.* 250 nm. The second band is a much stronger band between 450 and 800 nm with a peak at 600 nm. These bands are both seen in the CF_3H spectrum taken with a photoexcitation energy of 11.7 eV. The bands are also assigned to emission from the CF_3* radical. The first band is a result of a transition between the $^2A_1$' (4s) Rydberg state and the $\tilde{X}$ $^2A_1$ ground state of CF_3. Based on *ab initio* calculations [13], the second band is assigned to a Rydberg – Rydberg transition between an excited state of either ^2E' or $^2A_2$" symmetry and a repulsive lower state of $^2A_1$' symmetry.

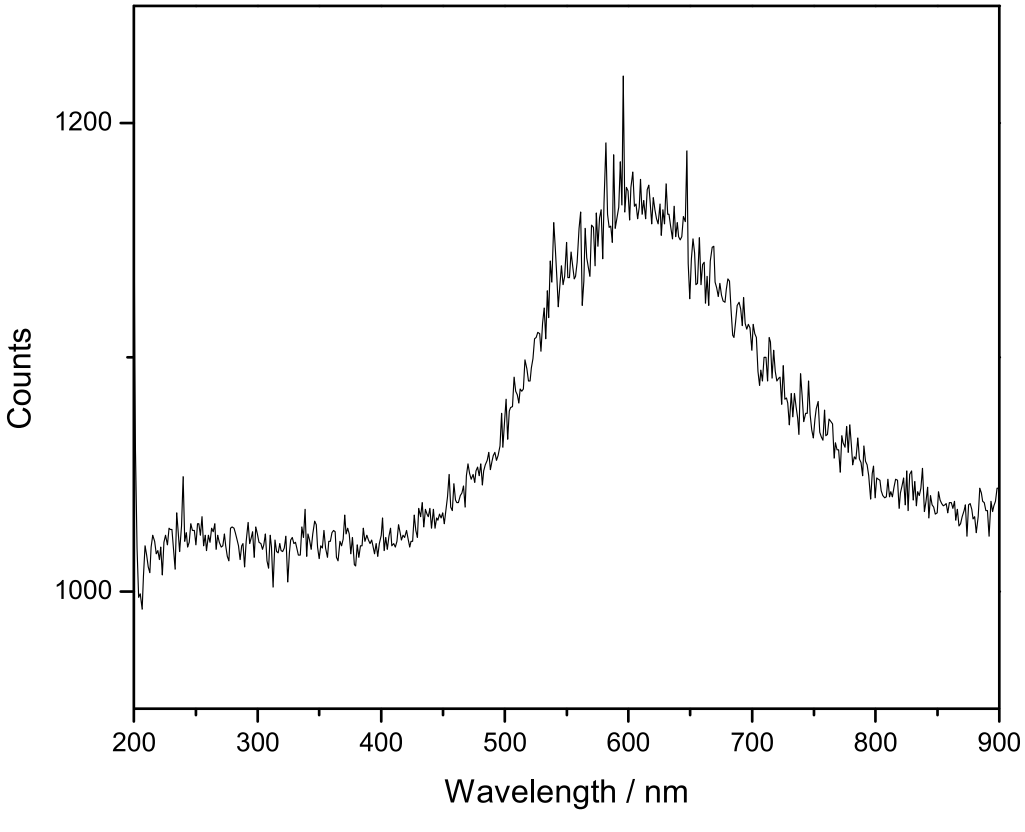

Figure 6.10: Dispersed fluorescence spectra of CF_3Cl taken with photoexcitation energy of 11.0 eV, using the UV turret and 100 grooves mm^{-1} grating. This spectrum has not been normalised to the sensitivity of the CCD Triax system.

---

[1] It is important to note that both the CF_3Cl and CF_3Br (section 6.2.4) samples were only available in a limited amount due to a ban on their production under the Montreal protocol. Our group probably had the last two bottles of these samples in the country. Further work on ion-pair production following VUV photoexcitation were planned for a later date, hence it was essential to preserve the samples. This is reflected on the poor quality of the dispersed fluorescence spectra compared to the other molecules in this series.

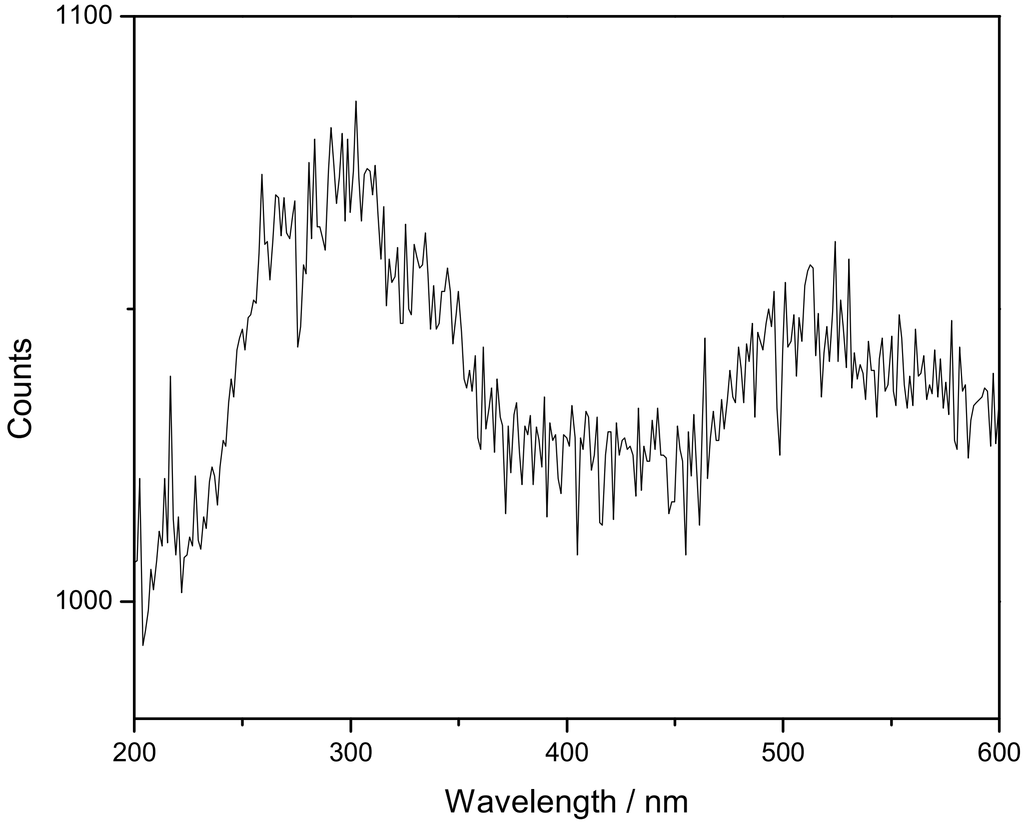

Figure 6.11: Dispersed fluorescence spectra of CF_3Cl taken with photoexcitation energy of 15.9 eV, using the UV turret and 100 grooves mm^{-1} grating. This spectrum has not been normalised to the sensitivity of the CCD Triax system.

The dispersed fluorescence spectrum of CF_3Cl taken with a photoexcitation energy of 15.9 eV is shown in figure 6.11. The spectrum shows bands with peaks at 280 and 300 nm. These bands are also seen in the dispersed fluorescence spectra of CF_4 and CF_3H taken at a photoexcitation energy of 15.7 eV for both molecules. Both these peaks have been assigned as emission from CF_2 $\tilde{A}\ ^1B_1$ - $\tilde{X}\ ^1A_1$. As discussed earlier the two bands are possibly a result of a bimodal vibrational distribution resulting from two different dissociation channels of CF_3Cl^* to CF_2^*. A further weaker shoulder is seen at *ca.* 340 nm. This peak is not seen in the either the CF_4 or CF_3H spectra taken at15.7 eV. This would suggest that the emitter probably contains a Cl atom. Previous studies involving VUV photoexcitation of C_2F_3Cl [14] has detected $CFCl^*$ emission in the 350 – 550 nm region. This shoulder at *ca.* 340 nm is probably due to this emission from the $CFCl^*$ radical. Figure 6.11 also shows a band between 450 and 600 nm. This could be due to second-order signal from the primary monochromator from 31.8 eV. In the absence of further dispersed spectra at higher energies, due to the reasons explained in the earlier footnote, no dispersed spectra were recorded at higher VUV energies above 20 eV so this possibility cannot be confirmed.

6.2.4 CF_3Br

The VUV fluorescence excitation spectrum of CF_3Br taken between 8 and 24 eV using the MEG at a resolution of 0.2 nm is shown in figure 6.9. Resonant peaks are seen at 10.54, 13.50, 14.90 and 21.00 eV. Following patterns seen previously in the fluorescence spectra of CF_4, CF_3H and CF_3Cl we would expect the lowest-energy peak at 10.54 eV to be due mainly to emission from the CF_3* radical. The second and third peak peaks at 13.50 and 14.90 eV are probably mainly due to emission from the CF_2^* radical. The energetics of the various dissociation channels are given in table 6.4. The resonant peak at 21 eV is probably due to emission from more than one fragment. Energetically, we can now also have emission emanating from both the A $^2\Sigma^+$ and B $^2\Delta$ states of the CF radical as well as parent ion emission from CF_3Br^+. Fluorescence work done previously on this molecule has observed CF emission in the 190 – 500 nm range. Lee *et al* [2] assigned dispersed signal from photoexcitation at 19.46 eV to emission from the parent ion CF_3Br^+. These assignments cannot be confirmed by our work as no dispersed spectra were taken at 21.00 eV, due to the reasons explained earlier.

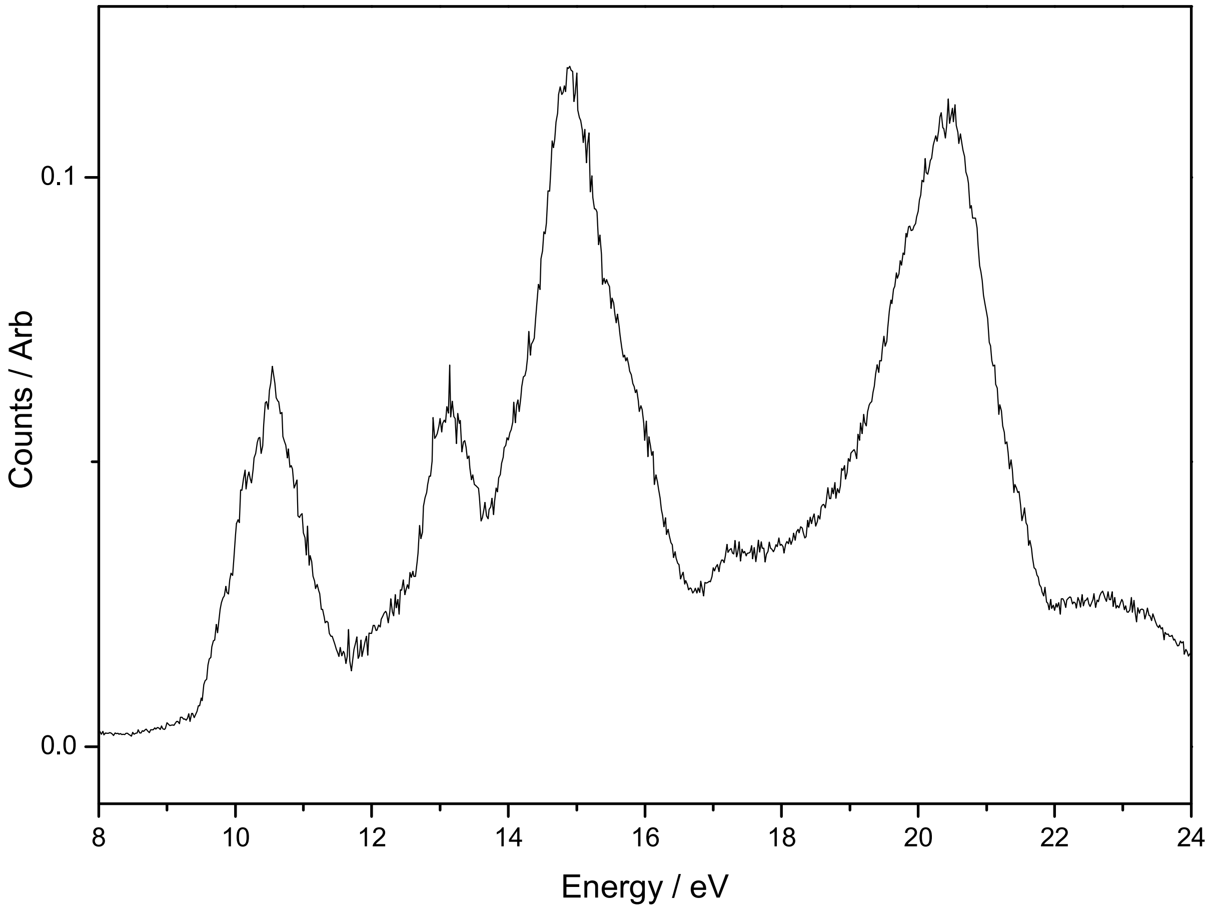

Figure 6.12: The undispersed fluorescence excitation spectrum of CF_3Br , taken using the MEG at a resolution of 0.2 nm.

Neutral/parent ion		Dissociation channel	Dissociation energy / eV	Vertical IE / eV
	$\tilde{E}\ ^2A_1$			19.80
		CF B $^2\Delta$ + Br + F_2	16.56	
		CF A $^2\Sigma^+$ + Br + 2F	17.32	
		CF B $^2\Delta$ + FBr + F	15.61	
		CF X $^2\Pi$ + Br + 2F	18.16	
	$\tilde{D}\ ^2E$			17.57
	$\tilde{C}\ ^2E$			15.86
		CF A $^2\Sigma^+$ + FBr + F	14.77	
	$\tilde{A}\ ^2A_1$			14.28
CF_3Br^+	$\tilde{X}\ ^2E$			12.08
		CF X $^2\Pi$ + F_2 + Br	10.43	
		CF X $^2\Pi$ + FBr + F	9.48	
		CF_2 $\tilde{A}\ ^1B_1$ + Br + F	11.35	
		CF_2 $\tilde{B}$ + FBr		
		CF_2 $\tilde{X}\ ^1A_1$ + Br + F	6.73	
		CF_2 $\tilde{A}\ ^1B_1$ + FBr	8.80	
		CF_2 $\tilde{X}\ ^1A_1$ + FBr	4.18	
		CF_3 $^2A_1{}'$ (4s) + Br	9.39	
		CF_3 $^2A_2{}''$ / $^2E'$ (3p) + Br	9.38	
		CF_3 $\tilde{X}\ ^2A_1$ + Br	2.98	
CF_3Br	$\tilde{X}\ ^1A_1$			

Table 6.4: Dissociation channels of CF_3Br

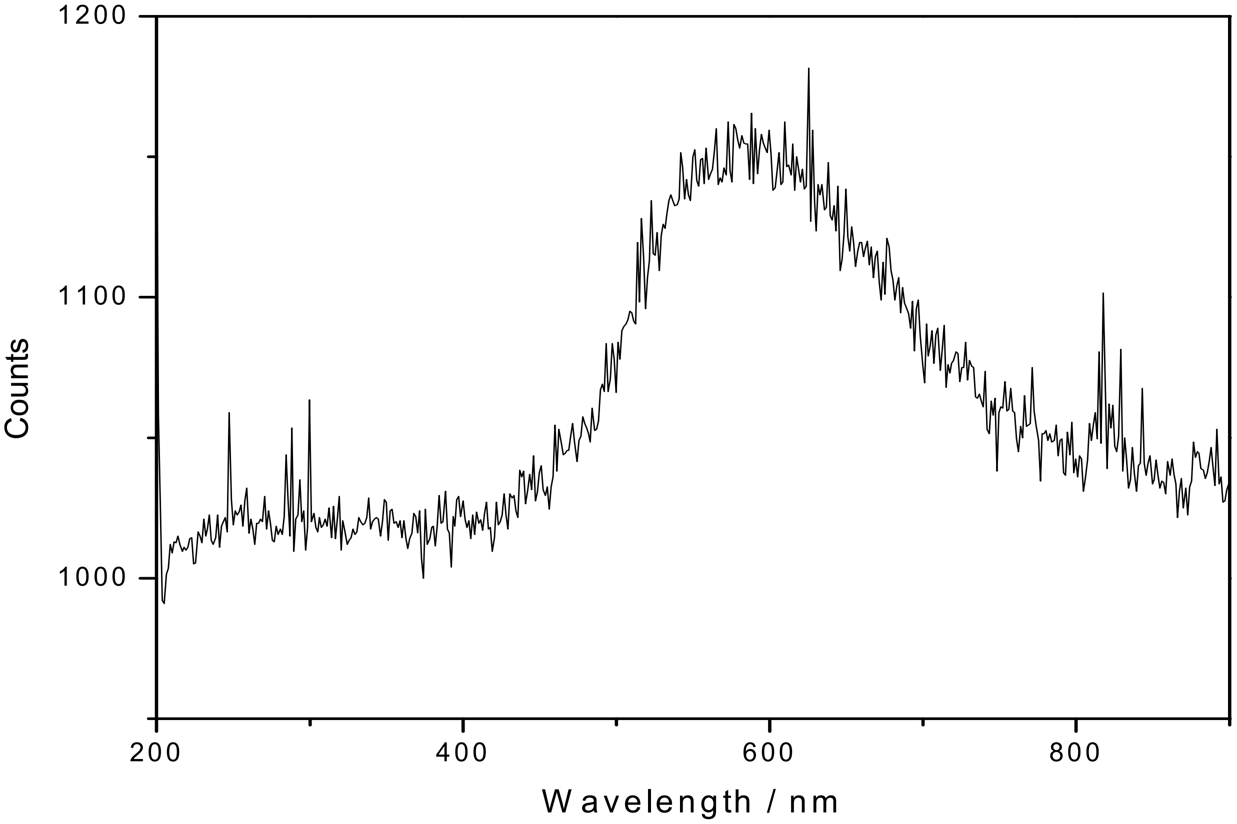

Figure 6.13: Dispersed fluorescence spectra of CF_3Br taken with photoexcitation energy of 10.54 eV, using the UV turret and 100 grooves mm^{-1} grating.

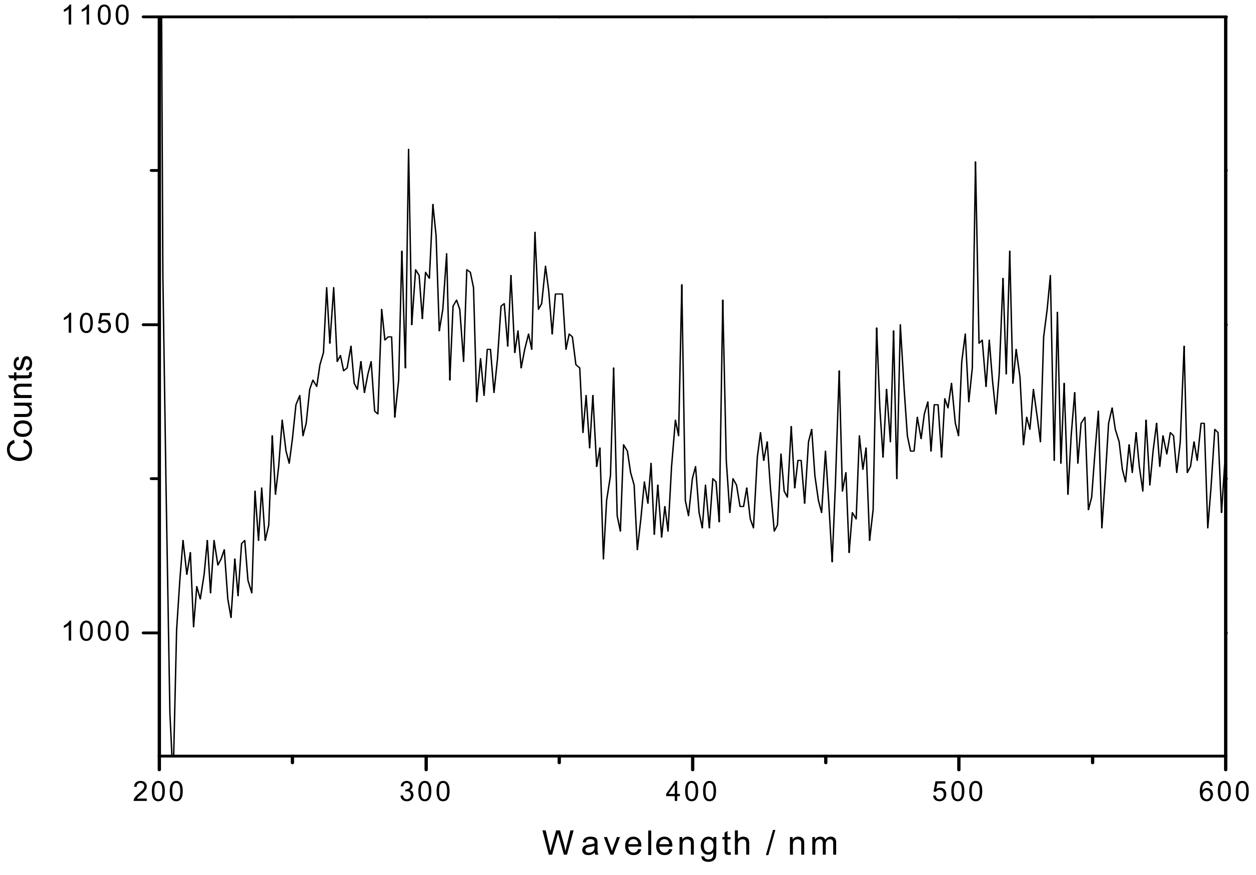

Figure 6.14: Dispersed fluorescence spectra of CF_3Br taken with photoexcitation energy of 14.90 eV, using the UV turret and 100 grooves mm^{-1} grating.

The dispersed fluorescence spectrum of CF_3Br taken using the UV turret and the 100 grooves mm^{-1} grating on the secondary Triax monochromator, is show in figure 6.13. This spectrum has not been normalised to the sensitivity of the CCD (chapter 2) due to the weakness of the dispersed signal. Two bands are seen, the first band is a very weak band between 200 and 275 nm. The second band is a much stronger band between 450 and 800 nm with a peak at 600 nm. These bands are both seen in the CF_3H and CF_3Cl spectra taken with photoexcitation energies of 11.7 eV and 11.0 eV respectively. The bands are also assigned to emission from the CF_3* radical. The first band is a result of a transition between the $^2A_1$' (4s) Rydberg state and the $\tilde{X}$ $^2A_1$ ground state of CF_3. The second band is assigned to a Rydberg – Rydberg transition between an excited state of either ^2E' or $^2A_2$" symmetry and a repulsive lower state of $^2A_1$' symmetry.

The dispersed fluorescence spectrum of CF_3Br taken with a photoexcitation energy of 14.9 eV is shown in figure 6.14. This spectrum has not been normalised to the sensitivity of the CCD due to the weakness of the signal. The spectrum shows bands with peaks at 280 and 300 nm. These bands are also seen in the dispersed fluorescence spectra of CF_4, CF_3H and CF_3Cl taken at photoexcitation energies of 15.7 eV, for both CF_4 and CF_3H, and at 16.0 eV for CF_3Cl. Both these peaks have been assigned as emission from the CF_2 $\tilde{A}$ $^1B_1$ - $\tilde{X}$ $^1A_1$ transition. The two bands are probably a result of a bimodal vibrational distribution resulting from two different dissociation channels of CF_3Br to produce the CF_2^* radical. A further band with a peak at *ca.* 350 nm is also seen. This peak is not seen in the either the CF_4 or CF_3H spectra taken at 15.7 eV. We do see a similar peak in the CF_3Cl spectrum at *ca.* 340 nm, but the peak in figure 6.14 is significantly stronger. Again we would suggest the emitter is not common to these molecules and it contains the Br atom. The $\tilde{A}$ $^1A''$ - $\tilde{X}$ $^1A'$ system of CFBr between 420 and 450 nm is known [3, 14, 15] and is probably what is being detected here.

6.2.5 CF_3I

The electronic configuration of CF_3I is …..$(3a_1)^2(2e)^4(3e)^4(1a_2)^2(4a_1)^2(4e)^4$ where the numbering scheme is restricted to outer-valence molecular orbitals. The flux-normalised fluorescence excitation spectrum of CF_3I taken using the MEG with a resolution of 0.2 nm is shown in figure 6.15. The CF_3I fluorescence excitation spectrum is much more complicated than any of the other molecules in the CF_3X series. We see peaks between 9 and 22 eV the majority appear to be resonant, but some of the peaks at hν > 18 eV may have non-resonant character. The main peaks are seen at 10.30, 13.00, 16.98 and 20.00 eV. The first of these peaks at 10.30 eV, probably corresponds to the lowest-energy peaks in the CF_4, CF_3H, CF_3Cl and CF_3Br fluorescence excitation spectra. Therefore the signal is most likely due to emission from the CF_3^* radical. The second major peak at 13 eV is a sharp narrow band most likely due to emission from the CF_2^* radical. The energetics of the different dissociation channels of CF_3I are presented in table 6.5. The thermochemical threshold for the production of both CF_3* and CF_2* fragments are below these peaks, therefore these channels are energetically open.

There is a broad feature at higher energy which has an onset at 17.60 eV and peaks at 19.82 eV. This band is probably a result of fluorescence coming from more than one emitter. By analogy with CF_3Br there is probably some emission originating from A $^2\Sigma^+$ and B $^2\Delta$ states of the CF radical. Emission from the CF_3I^+ parent ion could also be present. This broad band also shows signs of containing emission from both CO_2^+ and N_2^+. The CO_2^+ $\tilde{A}^2\Pi_u - \tilde{X}^2\Pi_g$ transition has a signal onset of 17.34 eV (chapter 2). The features at higher energy to the onset of this peak at 17.60 eV, have similar characteristics to the CO_2 excitation spectrum at this energy. The small peak at 18.22 eV is at the same energy we would expect the CO_2^+ $\tilde{B}^2\Sigma_u^+ - \tilde{X}^2\Pi_g$ emission to occur. Within the broad peak we also see a sharp increase in signal with an onset at 18.76 eV. At this energy we would expect to see emission from the N_2^+ $B^2\Sigma_u^+ - X^2\Sigma_g^+$ band. This N_2^+ and CO_2^+ signal may be due to impurities contained in the gas bottle or the sample line.

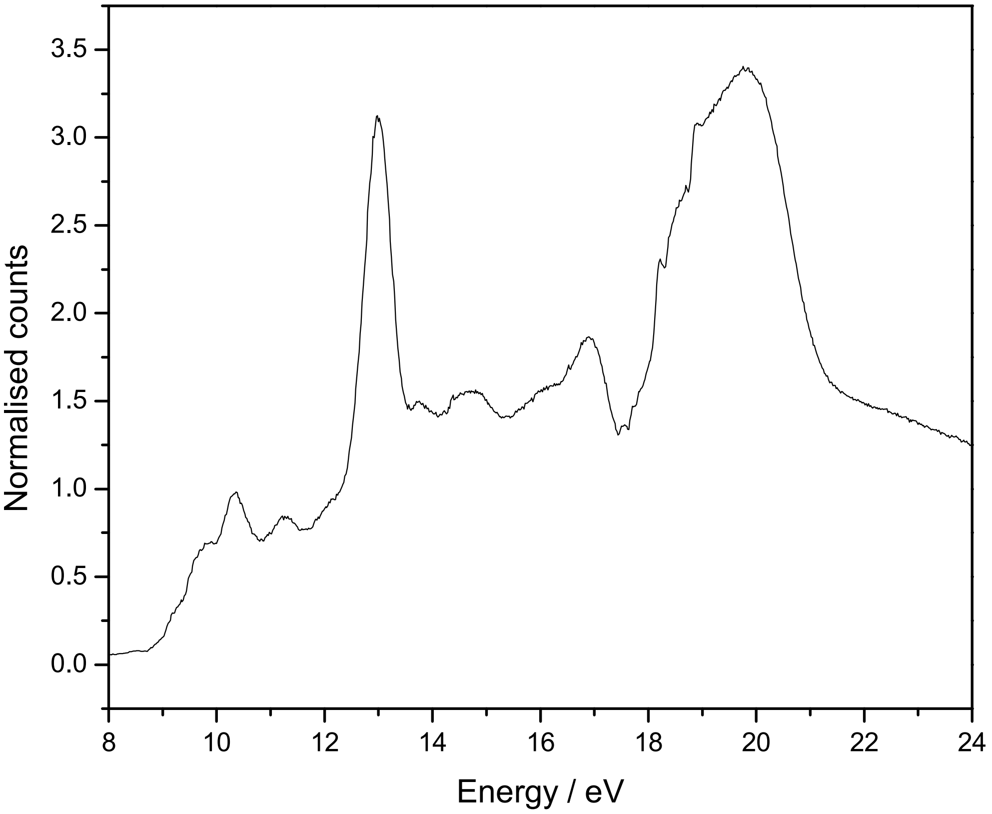

Figure 6.15: The undispersed fluorescence excitation spectrum of CF_3I, taken using the MEG at a resolution of 0.2 nm.

The dispersed fluorescence spectrum of CF_3I taken at a photoexcitation energy of 10.30 eV, using the UV turret in combination with the 100 grooves mm^{-1} grating is shown in figure 6.16. The spectrum shows a small band peaking at 350 nm followed by a sharper peak at 485 nm. A broad band is also seen which peaks at 570 nm. These bands are new in the series of molecules we have discussed in this chapter. Therefore the emission should be due to a fragment containing an I atom. No thermochemical data is available in the literature for the CFI fragment, hence the energetics for the dissociation channels involving CFI are not available. In work done by our group on the CH_3F molecule using a Lyman-α discharge lamp (10.2 eV) as an excitation source and using this same detection system, we observed CHF emission as the sole emission [16]. The thermochemical threshold for that emission was 7.93 eV, hence energetically the production of CFI from CF_3I excited at 10.30 eV is possible. Theoretical calculations have predicted the CFI transition energy of $\tilde{A}\ {}^1A''$ (000) - $\tilde{X}\ {}^1A'$ (000) to occur between 570 and 588 nm [17]. So the strongest bands seen in figure 6.16 at 485 nm could be due to CFI $\tilde{A}\ {}^1A''$ - $\tilde{X}\ {}^1A'$. There may also be some weak underlying emission from the CF_3* radical.

Neutral/parent ion	Dissociation channel	Dissociation energy / eV	Vertical IE / eV
	CF B $^2\Delta$ + I + 2F	17.81	
	CF A $^2\Sigma^+$ + I + 2F	16.97	
	CF B $^2\Delta$ + F_2 + I	15.99	
	CF A $^2\Sigma^+$ + F_2 + I	15.15	
	CF X $^2\Pi$ + I + 2F	11.50	
	CF X $^2\Pi$ + F_2 + I	9.86	
	CF_2 $\tilde{B}$ + IF	15.17	
	CF_2 $\tilde{A}$ $^1B_1$ + I + F	10.77	
	CF_2 $\tilde{X}$ $^1A_1$ + I + F	6.15	
	CF_3 $^2A_1'$ (4s) + I	8.75	
	CF_3 $^2A_2''$ / $^2E'$ (3p) + I	8.74	
	CF_3 $\tilde{X}$ $^2A_1$ + I	2.34	
CF_3I $\tilde{X}$ $^1A_1$			

Table 6.5: Dissociation channels of CF_3I

The dispersed fluorescence spectrum taken with a photoexcitation energy of 13.0 eV is shown in figure 6.17. The first two peaks are seen at 280 and 300 nm. These peaks have also been seen for the other molecules in the CF_3X series and have been assigned as emission from the CF_2 $\tilde{A}$ $^1B_1$ - $\tilde{X}$ $^1A_1$ transition. Further peaks are seen at 340 and 485 nm with a shoulder at *ca.* 440 nm. Figure 6.18 shows the dispersed fluorescence spectrum of CF_3I taken with a photoexcitation energy of 16.98 eV. This spectrum shows features very similar to the spectrum taken at 13.0 eV between 330 and 800 nm. The spectrum taken at 16.98 eV has been assigned to emission from different vibrational levels of the CFI $\tilde{A}$ $^1A''$ state to the ground state $\tilde{X}$ $^1A'$. The three spectra taken at 10.3, 13.0 and 16.98 eV all contain peaks at 485 and the shoulder at 440 nm. The peak at 340 nm appears in the 13.0 eV spectrum along with CF_2 $\tilde{A}$ $^1B_1$ - $\tilde{X}$ $^1A_1$ emission. In the spectrum taken at 16.98 eV the CF_2^* emission has disappeared and the two peaks at 340 and 485 nm with further peaks at 660, 720 and 740 nm are present.

We can assume that for the photoexcitation energy of 10.3 eV we see CFI $\tilde{A}$ $^1A''$ - $\tilde{X}$ $^1A'$ emission. At 13.0 eV we see emission from CF_2 $\tilde{A}$ $^1B_1$ - $\tilde{X}$ $^1A_1$ as well as the emission bands we see at 10.3 eV assigned to CFI. The peak at 340 nm is also due to CFI emission. This time because of the extra photoexcitation energy we are able to populate higher vibrational levels of the CFI $\tilde{A}$ $^1A''$ state. As we go up in photoexcitation energy to 16.98 eV we lose the signal due to the CF_2^* radical. Now only the CFI $\tilde{A}$ $^1A''$ - $\tilde{X}$ $^1A'$ emission is observed.

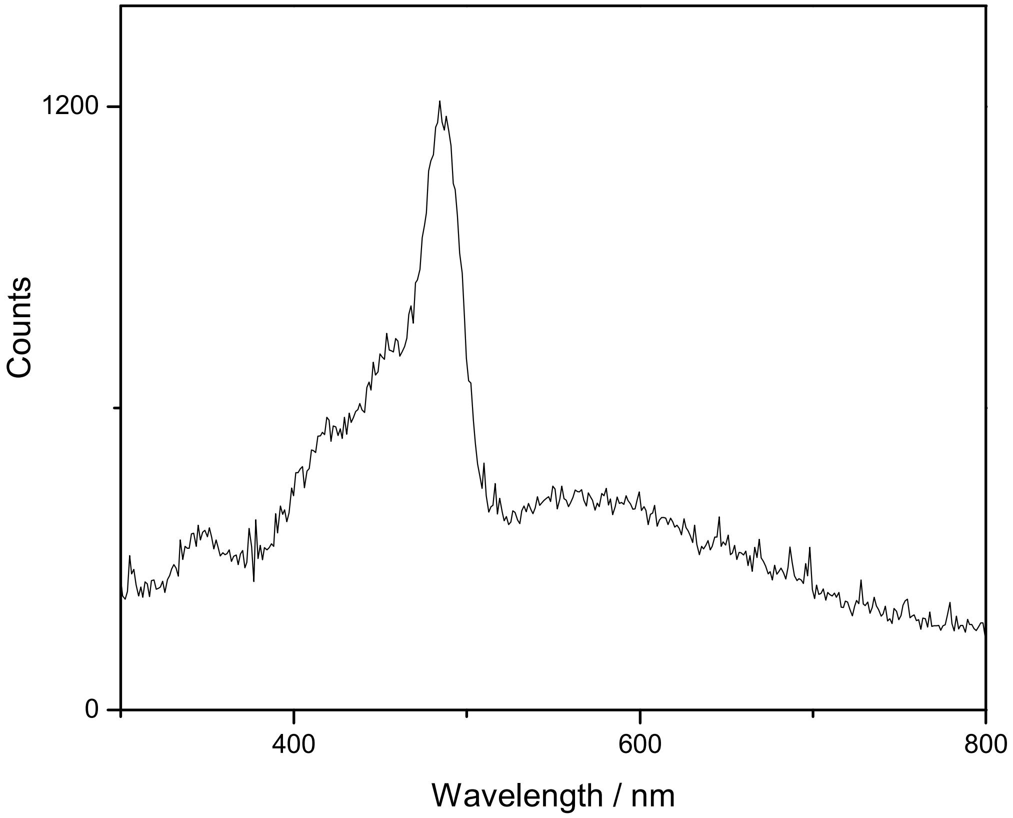

Figure 6.16: Dispersed fluorescence spectra of CF_3I taken with photoexcitation energy of 10.3 eV, using the UV turret and 100 grooves mm^{-1} grating.

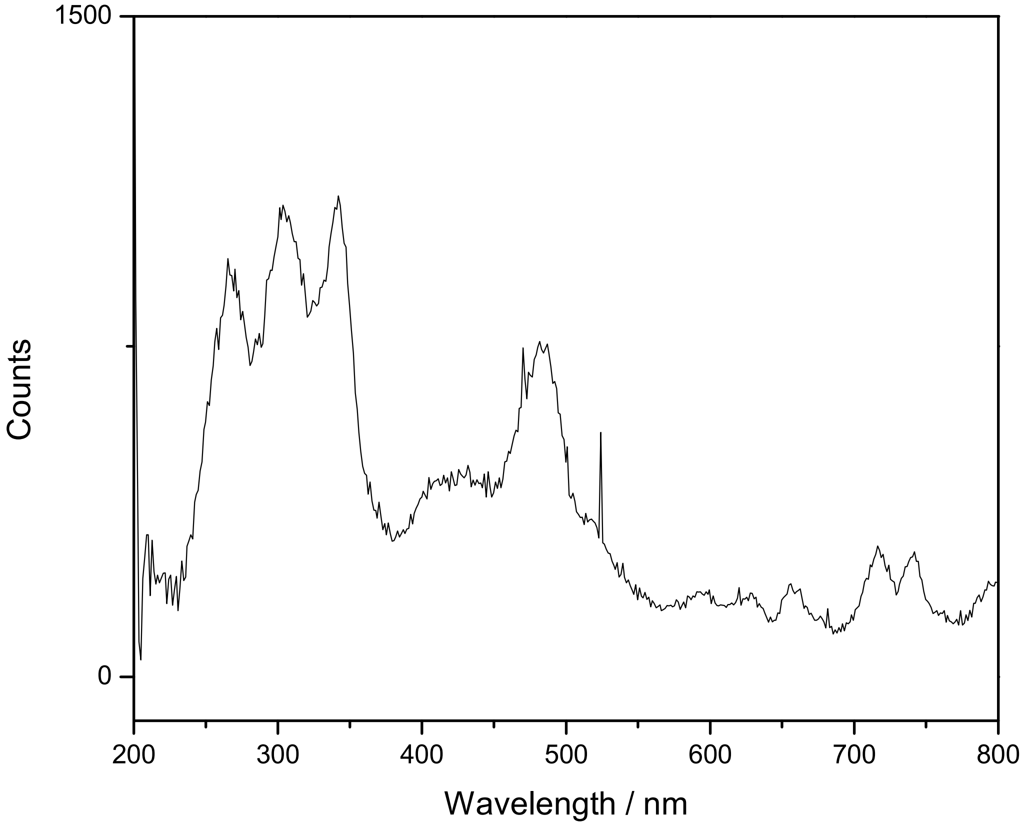

Figure 6.17: Dispersed fluorescence spectra of CF_3I taken with photoexcitation energy of 13.0 eV, using the UV turret and 100 grooves mm^{-1} grating.

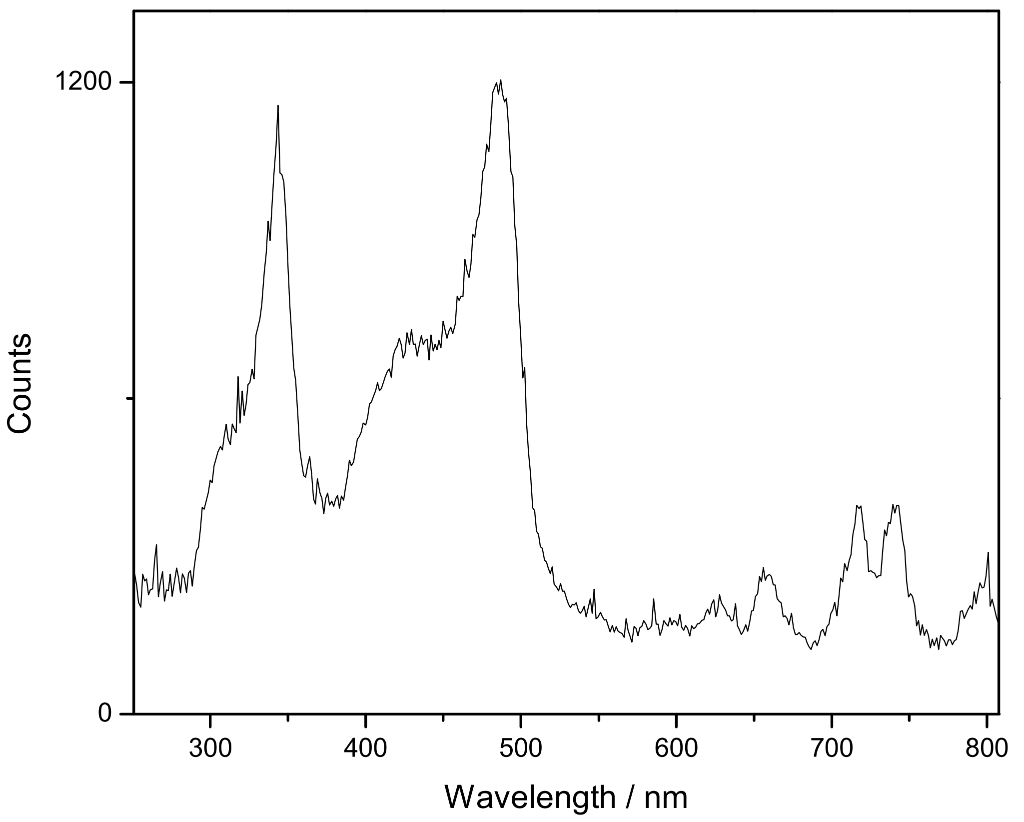

Figure 6.18: Dispersed fluorescence spectra of CF_3I taken with photoexcitation energy of 16.98 eV, using the UV turret and 100 grooves mm^{-1} grating.

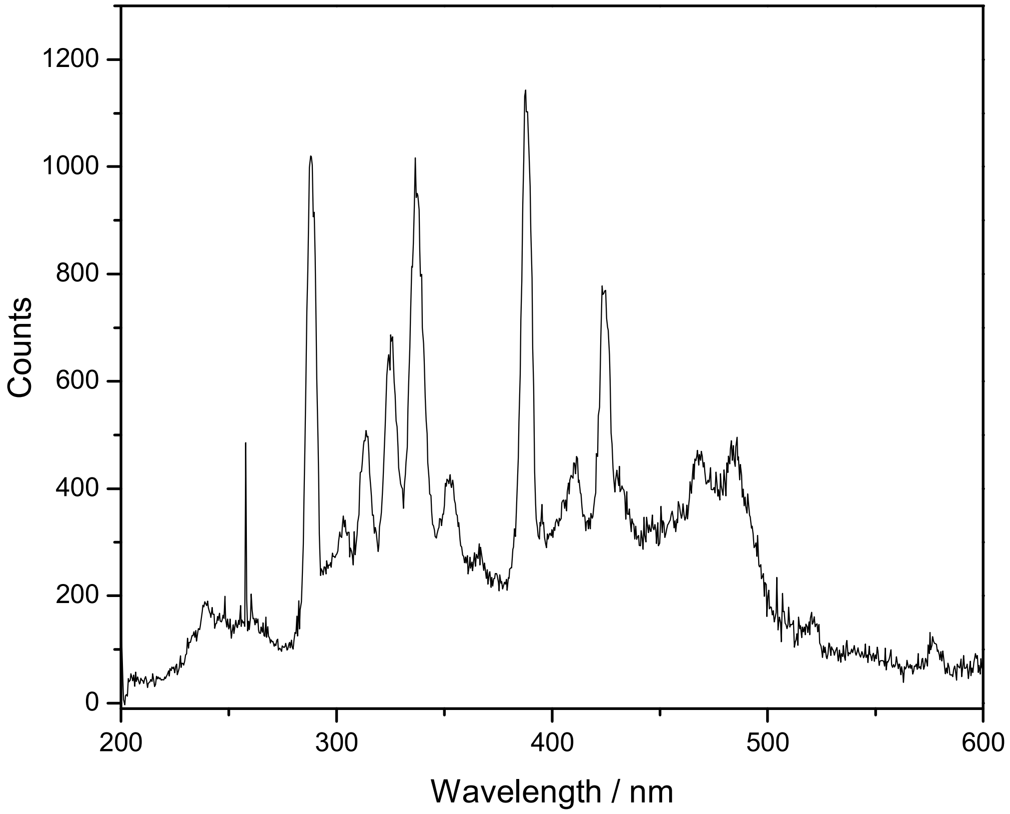

Figure 6.19: Dispersed fluorescence spectra of CF_3I taken with photoexcitation energy of 20.0 eV, using the UV turret and 300 grooves mm^{-1} grating.

The dispersed fluorescence spectrum of CF_3I taken at a photoexcitation energy of 20.0 eV is shown in figure 6.19. The spectrum is dominated by signal from CO_2 and N_2. The sharp peaks between *ca*. 280 and 380 nm are due to CO_2^+ emission via the $\tilde{A}^2\Pi_u - \tilde{X}^2\Pi_g$ and $\tilde{B}^2\Sigma_u^+ - \tilde{X}^2\Pi_g$ transitions (chapter 2). The two sharp intense peaks at *ca*. 390 and 430 nm is a result of emission from N_2^+ $B^2\Sigma_u{}^+ - X^2\Sigma_g{}^+$. Assignment of any parent ion emission or that from the CF radical is now difficult because of the intense nature of the CO_2^+ and N_2^+ bands. Shortage of beam time did not allow us to complete this study.

6.3 Conclusions

In this chapter we have presented the VUV fluorescence spectra of CF_3X (X=F,H,Cl,Br,I). The fluorescence excitation spectra are very similar to the previous spectra recorded at BESSY 1 with the relative intensities being different. Fluorescence emissions are a result of transitions from excited states of CF, CF_2, CF_3 and parent ion CF_4^+, CF_3H^+. Further bands assigned to CFCl, CFBr and CFI have also been observed.

6.4 References

[1] L.C. Lee, J.C. Han, C. Ye and M. Suto, *J. Chem. Phys*. **92** (1990) 133.

[2] M Suto and L C Lee , *J Chem. Phys*, **79** (1983) 1127

[3] I.R. Lambert, S.M. Mason, R.P. Tuckett and A. Hopkirk, *J. Chem. Phys*. **89** (1988) 2683.

[4] H. Biehl a, K.J. Boyle a, R.P. Tuckett a,*, H. BaumgErtel b, H.W. Jochims *Chemical Physics* **214** (1997) 367

[5] J.C. Creasey, I.R. Lambert, R.P. Tuckett and A. Hopkirk, *Mol. Phys*. **71** (1990) 1355.

[6] J.C. Creasey, I.R. Lambert, R.P. Tuckett and A. Hopkirk, *Mol. Phys*. **71** (1990) 1367.

[7] J.C. Creasey, P.A. Hatherly, I.R. Lambert and R.P. Tuckett, *Chem. Phys. Lett*. **188** (1992) 223.

[8] H. Biehl, K.J. Boyle, D.M. Smith and R.P. Tuckett, *Chem. Phys*. **214** (1997) 357.

[9] S. Eden a,*,1, P. Lima˜o-Vieira a,2, S.V. Hoffmann b, N.J. Mason *Chemical Physics* **323** (2006) 313–333

[10] P.J. Bassett and D.R. Lloyd, *J. Chem. Soc. A,* (1971) 641

[11] Mathews, C.W., *Can. J. Phys*., **45** (1967), 2355

[12] C. R. Brundle, M. B. Robin, *J. Chem. Phys.,* **53**, (1970), 2196

[13] N. Washida, M. Suto, S. Nagase, U. Nagashima and K. Morokuma, *J. Chem. Phys.* **78** (1983) 1025.

[14] J.R. Purdy and B.A. Thrush, Chem. Phys. Lett. **73** (1980) 228.

[15] R. Schlachta, G.M. Lask and V.E. Bondybey, *J. Chem. Soc. Faraday Trans*. **87** (1991) 2407.

[16] S Ali, *first year report,* University of Birmingham 2004

[17] I. Martin, E. Mayor, A. M. Velasco, *International Journal of Quantum Chemistry,* **104** (2005) 522

[18] C.E. Theodosiou, M. Inokuti and S.T. Mason, *Atomic Data and Nuclear Data Tables*, **35** (1986) 473.

7. VUV fluorescence Spectroscopy of SF_5CF_3

The work presented in this chapter has been published [1]. The experiments were carried out at three different synchrotron radiation sources: MAX-Lab (Lund, Sweden), SRS (Daresbury, UK) and Elettra (Trieste, Italy). The first two covered the VUV range 6 – 30 eV, the third the soft X-ray range 25 – 100 eV. All the data taken at the Daresbury SRS, which probably constitute the majority of the fluorescence spectra, were taken by me. I had no direct involvement in any of the experiments carried out at MAX-Lab or Electra. Although I was not the principal author for this paper, I was involved in the analysis. SF_5CF_3 can be regarded as a member of the CF_3X family (chapters 5 – 6), except that X is now a large polyatomic radical rather than an atom.

7.1 Introduction

SF_5CF_3 was discovered in the atmosphere in 2000 [2] and since then it has been catalogued as a powerful greenhouse gas. Entirely of anthropogenic origin [3, 4] (so far, the only known source of SF_5CF_3 is connected to the manufacture of fluorochemicals), this molecule shows a global warming potential 18000 times higher than CO_2. Although its concentration in air is still very low, the potential environmental danger of SF_5CF_3 urges the estimation of its impact in the atmosphere. A determination of the spectroscopic properties of SF_5CF_3 is therefore essential to characterize its behaviour. A brief summary of the main studies devoted to that end and their results are listed below.

Photoabsorption investigations [5 - 8] have shown that SF_5CF_3 does not absorb visible or UV light below 8 eV. This means that this molecule is not affected by the solar radiation in the lower parts of the atmosphere and only photons in the mesosphere and ionosphere can trigger its photolysis [9]. Studies on its interaction with charged particles has revealed that SF_5CF_3 has a high electron affinity. Ion-molecule reactions [10 -12] and especially electron dissociative attachment [13, 14] have been demonstrated to produce the fragmentation of the molecule, probably being the main cause of its destruction at altitudes above 50 km. Based on these results, scientists have concluded that the lifetime of SF_5CF_3 in the atmosphere is around 1000 years.

Important advances in the electronic structure and fragmentation dynamics of this molecule have recently been reviewed [15], there is still much to be done. By 2001, the threshold photoelectron - photoion coincidence studies of Chim et al. [16] provided the first ionisation potentials of the molecule but subsequent photoelectron measurements [7, 8] reported a richer electronic structure. Only recently have theoretical calculations been able to reproduce well the valence photoelectron spectrum of SF_5CF_3 and give some insight into its photoabsorption spectrum [17]. Threshold energies of several ions were determined by electron impact experiments [18], but up to date nothing is known about neutral fragments. Surprisingly enough, it is still unknown whether the molecule dissociates following excitation into its first photoabsorption band.

Photon induced fluorescence spectroscopy (PIFS) is a powerful technique for investigating the structure and dynamics of excited molecules. It is especially suitable to trace the production of neutral fragments and to find out the internal energies of the emitting species, thus providing complementary results to those obtained from techniques that detect charged particles. Likewise, the evolution of the fluorescence with excitation energy can also give information about electronic transitions and the dynamics of excited states of the molecule under study.

We report for the first time the total fluorescence and dispersed fluorescence spectra of SF_5CF_3 following vacuum-ultraviolet (VUV) photoexcitation. Apart from these novel data, a high-resolution photoabsorption spectrum is also presented to help the discussion. In order to interpret the spectra, we refer to the theoretical studies on the electronic structure of SF_5CF_3 [17, 19, 20] but even more substantially to the knowledge of the related SF_6 and CF_3X (X=H, F, Br, and Cl) molecules (chapter 6).

7.2 Experimental

Experiments were carried out at three different synchrotron radiation laboratories: MAX-Lab (Lund, Sweden), SRS (Daresbury, UK) and Elettra (Trieste, Italy). The photoabsorption spectrum and preliminary total fluorescence yield and dispersed fluorescence spectra of SF_5CF_3 (not included in the chapter) were recorded at the beam line 52 of the MAX I storage ring at the Swedish national synchrotron facility MAX-Lab, in Lund. The beam line, based on a bending magnet, uses a 1-m normal incidence monochromator and provides photons in the VUV range. Due to the low collection efficiency of fluorescence experiments, the slits of the monochromator were fully open (400 μm) during the experiments, giving a resolution of 0.06 eV at $h\nu = 15$ eV. The end-station has been described elsewhere [21]. In order to maximise collection of the fluorescence, two optical systems each consisting of a lens and a mirror, are mounted in a cylindrical gas cell inside the experimental chamber. One of the collecting systems directs the light out of the chamber to an external lens that focuses it onto a 0.46-m spectrograph (Jobin-Yvon HR460). The other optical system, perpendicular to the previous one, projects the collected light to a photo multiplier tube (PMT) for undispersed, total fluorescence measurements. The PMT (Hamamatsu R647) detects emission in the spectral window of 300-650 nm. The rear part of the station includes a Si photodiode to measure the photon flux of the beam line. Dispersed and undispersed fluorescence experiments were also carried out using the new Wadsworth monochromator (station 3.1) of the Synchrotron Radiation Source (SRS) at Daresbury (UK) [22]. Full details are reported in chapter 2.

At Elettra, dispersed and undispersed fluorescence experiments were performed at the Gas Phase Photoemission beam line, which uses undulator radiation at photon energies from 13 - 1000 eV. Exciting radiation is monochomatized by a spherical grating monochromator (five interchangeable gratings are available) equipped with a planar pre-mirror. The incident radiation hits the molecular jet emanating from a hypodermic needle. The fluorescence emitted into a cone along the electric vector of the incident radiation was collimated with a spherical mirror, exited the vacuum chamber through a quartz window, and was focused into the entrance slit of the 300-mm Acton spectrograph. The light was dispersed by a 1200 lines/mm grating and detected by a nitrogen cooled CCD detector (PRINCETON 10:100B).

The sample gas SF_5CF_3 with a stated purity of 99 % was purchased from Apollo Scientific Ltd and Fluorochem Ltd. It was used without further purification. The energy scales of the spectra are calibrated according to the literature values [7]. None of the dispersed spectra have been normalized to the wavelength sensitivity of the different fluorescence systems, and this is significant when comparing emission spectra from different spectrometers.

7.3 Results

7.3.1 Photoabsorption spectrum

The photoabsorption spectrum of SF_5CF_3 was acquired at MAX-Lab in the 10-21 eV energy range in steps of 0.25 nm using a Si photodiode. As with experiments performed at BESSY 1 (chapter 3 and 5), a generic absorption spectrum was obtained by measuring the intensity of the exciting light beam passing through the experimental cell without and with gas and then, by normalizing the ratio of these two current curves to the ring current and pressure fluctuations. Unlike the BESSY 1 data, however, absolute values of the cross-sections are not determined since the gas density and the interaction length are now difficult to estimate. The resulting spectrum (Fig. 7.1) agrees very well with the reported absorption spectra in the literature [7, 8], revealing the same structures over an increasing background. Because of the contribution of second-order radiation from the NIM monochromator output of the beam line 52 at MAX I, the absorption threshold at 8 eV and the first resonance with the maximum at 9.3 eV could not be recorded.

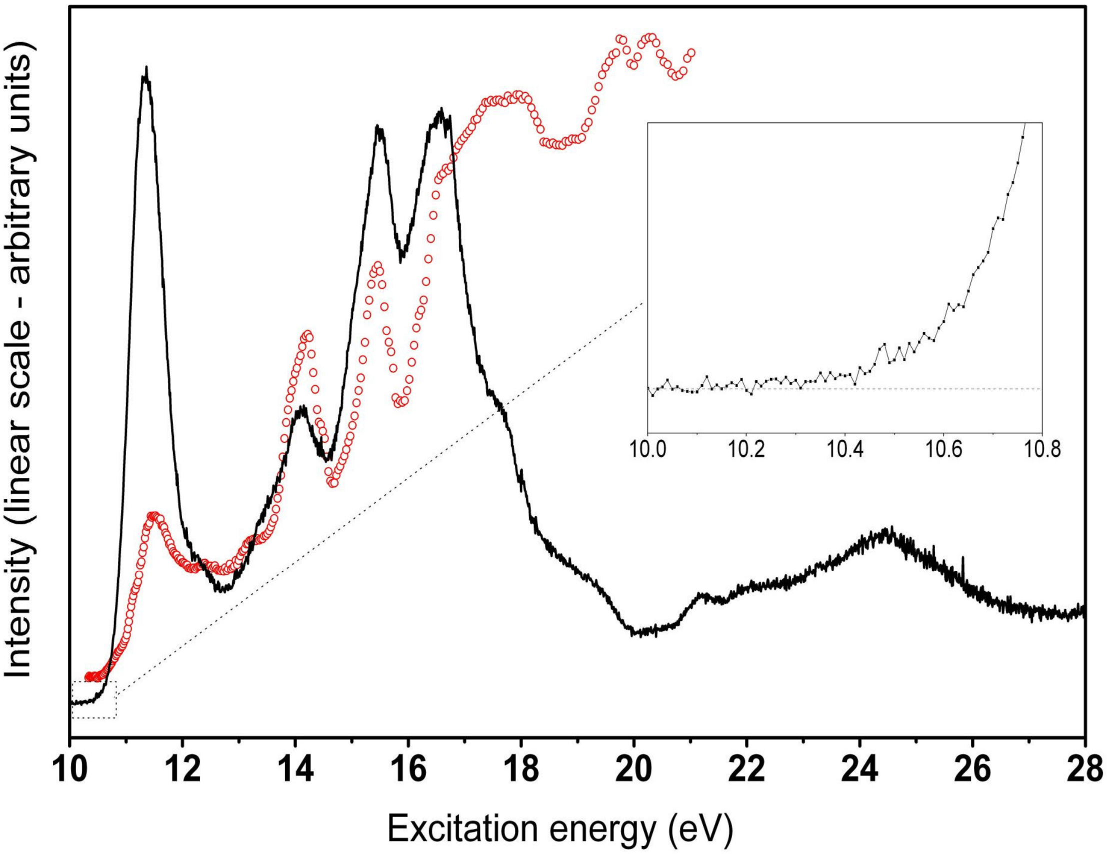

Figure 7.1. Circles: Photoabsorption spectrum of SF_5CF_3 obtained with a silicon photodiode measured at Max-Lab, beam line 52. Black line: Total fluorescence yield in the UV-Vis region of SF_5CF_3 measured at Daresbury, beam line 3.1. The insert corresponds to a magnified view of the initial part in the total fluorescence yield spectrum. Both spectra have been normalized to the flux of the beam lines.

The lack of theoretical predictions about the excited states of SF_5CF_3 limited the interpretation of its absorption spectrum in previous studies [7, 8], and the assignment of its different features is still under debate. Based on quantum defect analysis, Limão-Vieira et al. [7] assigned all the absorption features to Rydberg transitions converging to the first five ionisation potentials. Holland et al. [8] compared the absorption spectrum of SF_5CF_3 with those of SF_6 [23] and CF_4 [24], assuming that the structures present in the absorption spectra of these two molecules would have their counterparts in the spectrum of SF_5CF_3. The valence photoabsorption spectrum of SF_6 is dominated by excitations to unoccupied molecular orbitals, while Rydberg transitions have much smaller cross sections [25]. In contrast, the photoabsorption features of the CF_3X (X=H, F, Br, and Cl) molecules are most often attributed to Rydberg transitions [26, 27, 28] (chapter 5). Holland et al. [8] argued that excitations to molecular orbitals could still play the main role in the case of CF_4. Thus they interpreted the photoabsorption spectrum of SF_5CF_3 in terms of intravalence transitions.

Theoretical calculations of Turki and Eisfeld [17] favoured the predominance of Rydberg excitations in the region below the first ionization potential (13.96 eV [7]). In particular, the calculated energy for the excitation from the highest occupied molecular orbital (HOMO) to the 4s orbital matched very accurately with the energy of the first absorption feature (11.4 eV) in Fig. 7.1. The lowest energy absorption feature at 9.33 eV was assigned to the HOMO → LUMO transition (LUMO = lowest unoccupied molecular orbital), as earlier suggested by Chim et al. [16].

7.3.2 Total Fluorescence yield

Figure 7.1 also presents the total fluorescence yield (TFY) of SF_5CF_3 following photoexcitation in the range 10-28 eV from station 3.1 at the SRS in Daresbury. The fluorescence was measured using a PMT which allowed the detection between 190 and 800 nm, approximately. The threshold for fluorescence emission is 10.2 ± 0.2 eV, as shown in the insert of Figure 7.1. Several features are observed, the most prominent being centred at the energies 11.4, 14.1, 15.5, 16.6 and 24.5 eV. The three first energies coincide with the peaks in the photoabsorption spectrum, indicating that these excitations lead to fluorescence emission.

Following one of the approaches employed to interpret the photoabsorption spectrum, we analyze the TFY spectrum of SF_5CF_3 by comparing it to those of its constituents. On the one hand, the comparison to SF_5 is straightforward. Recent PIFS investigations of SF_6 have shown that no emission in the 400-1000 nm range occurs below ~30 eV [29], although an early electron-impact induced fluorescence study on SF_6 [30] reported molecular emission around 300 nm for excitation energies above 13.5 eV. We show later that the TFY spectrum of SF_5CF_3 shows no contributions from sulphur-containing species SF_x. On the other hand, CF_3X (X=H, F, Br, and Cl) molecules emit in the ultraviolet and visible when excited with photons above 10 eV and this emission has been extensively studied [31] (see chapter 6). The TFY spectra of the CF_3X molecules typically show structures in three regions. Their positions vary slightly depending on the molecule, the first one being at 10-12 eV, the second one around 15 eV and the third one slightly above 20 eV. The structures in the first two regions have been correlated to excitations to different Rydberg states of the molecules. These states are unstable and can dissociate yielding excited CF_3 and/or CF_2 fragments which fluoresce. The features in the total fluorescence spectra at higher energies have a different origin, and they have been interpreted in terms of radiative decay of excited states of the parent ion and of excited CF radicals.

The gross features of the total fluorescence yield of SF_5CF_3 are quite similar to those in the CF_3X molecules, although there is more fine structure in SF_5CF_3 due to the more complicated electronic structure. These similarities in the fluorescence yields strongly suggest that the fluorescence emission of SF_5CF_3 at photon energies between 10-18 eV is due to the CF_3 and CF_2 fragments. However, the TFY spectrum of SF_5CF_3 above 20 eV is less likely attributable to the emission of the parent ion ($SF_5CF_3^+$) since this ion has not been observed at all in any mass spectroscopic study [6,16,18]. Nevertheless, there exists the possibility that excited states of $SF_5CF_3^+$ could fluoresce before dissociation, since mass spectrometry detects ions with lifetimes of the order of microseconds, while fluorescence occurs much faster on a nanosecond timescale.

7.3.3 Dispersed fluorescence

The validity of the above assumptions was checked by performing dispersed fluorescence measurements at the most representative excitation energies. At the SRS we used the 0.19 m Triax spectrometer and a UV300 l/mm grating, and Fig. 7.2 presents the recorded spectra. They have not been normalized to the wavelength sensitivity of the fluorescence collecting system, but as a guideline and according to the manufacturers' specifications, the sensitivity of the spectrometer peaks at ca. 300 nm, reducing to approximately 50% at 200 and 600 nm (chapter 2 figure 2.6)

As discussed above, the fluorescence spectrum of SF_5CF_3 could show emission due to the excited CF_3 and CF_2 fragments. In our spectra, there is a broad structure in the 500–800 nm range, similar to the emission band in the CF_3X molecules and attributed to the $\tilde{B}$ $^2A_2$" → $\tilde{A}$ $^1A_1$' and $\tilde{C}$ ^2E' → $\tilde{A}$ $^2A_1$' transitions in the CF_3 radical [32]. Fig. 7.2 shows that the maximum of this emission band shifts to lower wavelengths as the excitation energy increases. This effect has also been observed in CF_3Br and CF_3Cl [33], indicating that higher vibrational levels of CF_3* (where * indicates an electronically-excited species) are more likely to be populated at larger excitation energies. In the absence of vibrational relaxation, this will produce a shift to lower wavelengths in the observed emission. The fluorescence spectrum measured at the lowest excitation energy (11.3 eV) also shows a weak emission band around 200-250 nm, similar to the dispersed fluorescence spectra of the CF_3X molecules measured at the photon energies 10-12 eV [31, 33, 34]. The low intensity of this band in SF_5CF_3 may be partly due to decreased detection efficiency in the wavelength range 200-250 nm. This band has also been attributed to the CF_3 fragment and is possibly due to the $\tilde{E}$ $^2A_1$' → $\tilde{X}$ $^2A_2$" transition [35], although the emitting state may also be a valence state with A_2 symmetry [32]. The upper states of the UV and visible bands should lie very close in energy, since the threshold energies above the CF_3 ground state were found to be practically the same, 6.4 eV, for both emissions [35]. These measurements show that photon absorption in the band with the maximum at 11.4 eV leads to the dissociation of the molecule. At excitation energies of 13.51 eV and higher, an emission band centred around 300 nm is observed in the fluorescence spectra of SF_5CF_3. The CF_3X molecules typically show an emission band centred at slightly smaller wavelengths (around 280 nm) [31, 36], but it can also peak at 300 nm depending on experimental conditions [34]. This band has been attributed to the $\tilde{A}$ $^1B_1$ → $\tilde{X}$ $^1A_1$ transition in CF_2. We assign the observed band at 250-350 nm in SF_5CF_3 to this emission.

As mentioned above, the electron-impact induced fluorescence of SF_6 showed emission around 300 nm for electron energies above 13.5 ± 1.5 eV [30]. The emission was tentatively assigned to SF_5, SF_4 or SF_3 fragments but we believe that it may come directly from SF_6. (We note that there have been no other observations in the literature of emissions in the UV / visible assigned to SFx fragments.) In the electron energy loss spectrum of SF_6 [37], there is a peak at 13.3 eV whose energy coincides with the onset of the electron-impact induced fluorescence emission. According to the photoabsorption spectrum of Holland et al [23], this peak corresponds to the $1t_{1g} \rightarrow 6t_{1u}$ transition. The excited SF_6 could undergo fluorescence decay to the lowest $(1t_{1g})^{-1}$ $(6a_{1g})^{-1}$ excited state at around 9.8 eV [37], emitting around the cited wavelength (300-400 nm). Thus, we propose such a mechanism and assign the emission to excited states of the SF_6 molecule. This assignment should be confirmed by ultra-sensitive PIFS studies on SF_6 at those excitation energies. However, any such contribution from the SF_5 component of SF_5CF_3 is ruled out in our SF_5CF_3 spectra because a F atom would need to migrate across the C-S bond, forming electronically-excited SF_6. This seems unlikely. There is another reason which indicates that the fluorescence observed by Zabbour *et al.* [30] is not present in our spectra; the broad shape of the emission band in our high-resolution dispersed spectrum (Fig.7.4) differs significantly from the emission observed in the electron-impact induced fluorescence of the SF_6 molecule. At excitation energies above 19.2 eV, a weak emission feature develops around 400 nm, most likely due to N_2^+ B $^2\Sigma_u^+$ (v'=0) X $^2\Pi_g^+$ (v"=0) emission from a small N_2 impurity (see below).

Finally, we discuss the possibility of other emitters being responsible for the bands observed in the dispersed fluorescence spectra of SF_5CF_3. The CF radical has two known emission systems: A $^2\Sigma^+$ - X $^2\Pi$ and B $^2\Delta$ - X $^2\Pi$ with emission wavelengths in the wavelength regions 223-256 nm and 197-220 nm, respectively [38]. These systems, particularly the former one, could in principle contribute to the observed spectra. However, the creation of the CF fragment from the SF_5CF_3 molecule would require the breaking of three bonds, needing an energy of approximately 12.7 eV [39]. Since the excitation energy of the CF radical in the A $^2\Sigma^+$ state is 5.29 eV [40], the CF fragment should not give any contribution to fluorescence emission at excitation energies below ca. 18 eV. Fluorescence could also take place between the excited states of the neutral and/or ionic SF_5CF_3 molecule itself, but if present in our spectra we could not identify them.

The higher flux of the Gas Phase beam line and the better spectral resolution of the spectrometer at Elettra allowed us to investigate the intensity behaviour of the CF_3 and CF_2 fluorescence with excitation energy. Two fluorescence regions, one from 550 to 650 nm (CF_3 emission) and the other from 250 to 310 nm (CF_2 emission), were selected and measured in the photon energy range 13.6 - 27.0 eV in steps of 0.1 eV. Fig. 7.3 presents both excitation functions together with a total fluorescence yield obtained with the Elettra fluorescence spectrograph working in zero order. The difference in the relative intensities of the peaks in the TFY obtained at Elettra from those measured at Daresbury (Fig. 7.1) is explained by the difference in the quantum efficiency of the detectors; the CCD spectrograph at Elettra is more sensitive to visible light than the EMI 9883 QB photomultiplier tube used at Daresbury. The fluorescence around 550 nm follows the profile of the TFY, whereas the fluorescence of region 280 nm resembles more that of the TFY from Daresbury. Both excitation functions reveal the same structures but with different relative intensities. However, the two partial fluorescence yields peak at slightly different energies in the interval 15.0 -16.0 eV. This may be caused by two different excited states of SF_5CF_3 being responsible for dissociation to the emitting states of CF_3 and CF_2.

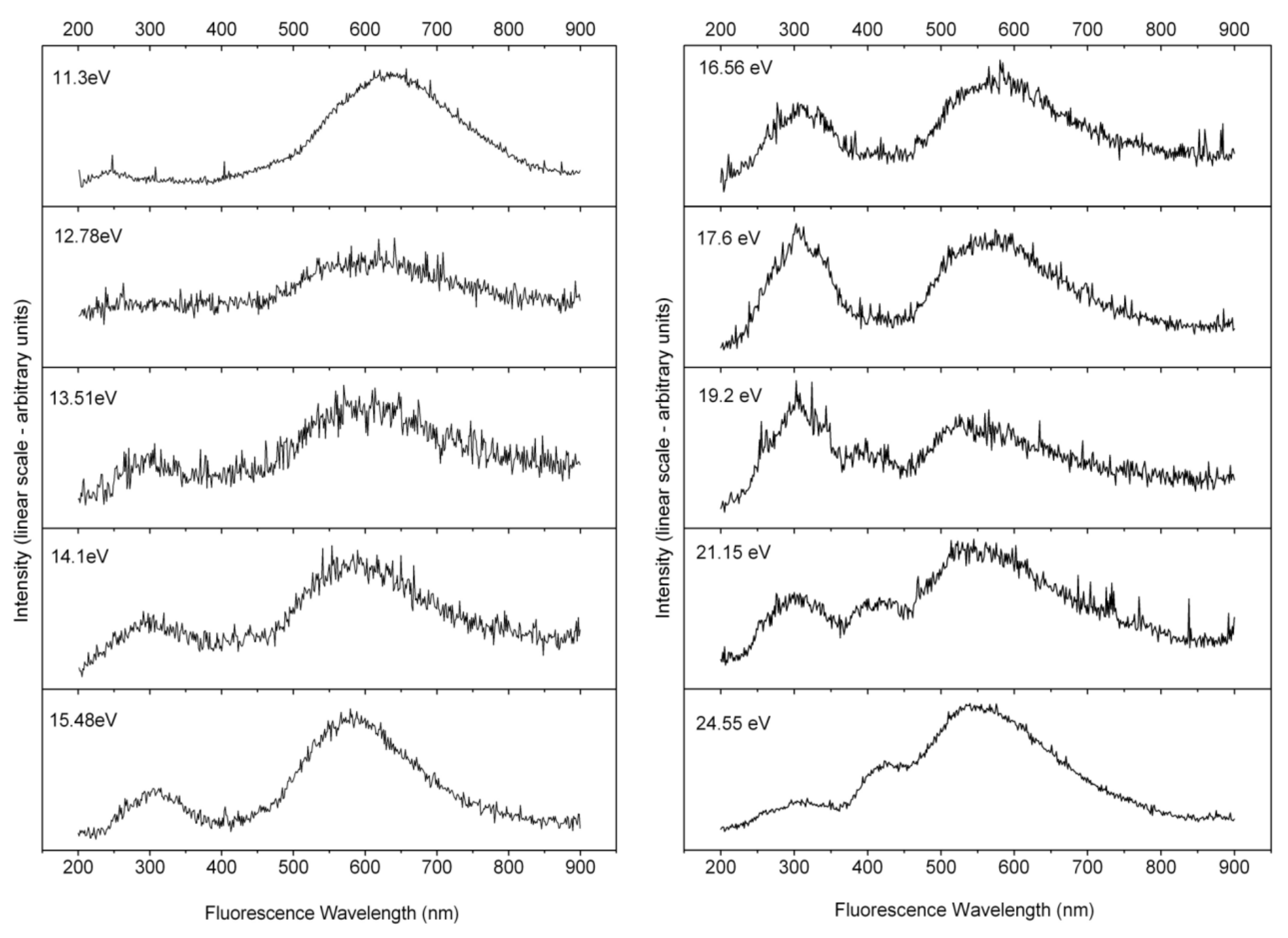

Figure 7.2 Dispersed fluorescence spectra of SF_5CF_3 at ten different excitation energies. Data taken using station 3.1 at the Daresbury SRS.

Higher-resolution dispersed fluorescence spectra were also recorded at the Gas Phase Beam line using the 300-mm ACTON fluorescence spectrometer with a 1200 lines/mm grating. The wavelength range 200-1000 nm was measured in several 70 nm windows, and the final spectrum was obtained by joining them together (Fig.7.4). At an excitation energy of 16.5 eV , the spectrum is very similar to that obtained at Daresbury (Fig. 7.2), showing fluorescence due to the CF_3 and CF_2 fragments. At 24.5 eV, the larger number of rulings per mm of the grating allow us to resolve the narrow bands at 390 nm and 427 nm that are due to the B - X transitions in the N_2^+ molecular ion. Despite the low amount of the N_2 impurity (~1%) in the sample, these emission bands are intense due to the high photoionization cross section of the N_2^+ B $^2\Sigma_u^+$ state just above its threshold. The fluorescence spectrum taken at a photon energy of 46 eV reveals numerous sharp lines. The most intense of them in the range 650-750 nm and around 920 nm can be assigned to transitions in neutral F and S atoms, respectively [41]. Some fluorine lines are also visible in the spectrum measured at 16.5 eV photon energy, but they must be caused by higher-order radiation from the beamline monochromator, since the upper states of these transitions have at least 14.5 eV of internal energy [41]. Therefore, the excitation functions of the fluorine lines at 731.1 and 739.9 nm, shown in Figure 6, should be inspected with caution (see Discussion). The dispersed fluorescence spectrum at 46 eV also shows molecular-like bands around 420 nm and 500 nm, but the signal-to-noise ratio of the spectrum is insufficient to identify the species responsible for these emissions. However, it is likely that fluorescence from the CF_3 radical may still account for the band at 500 nm.

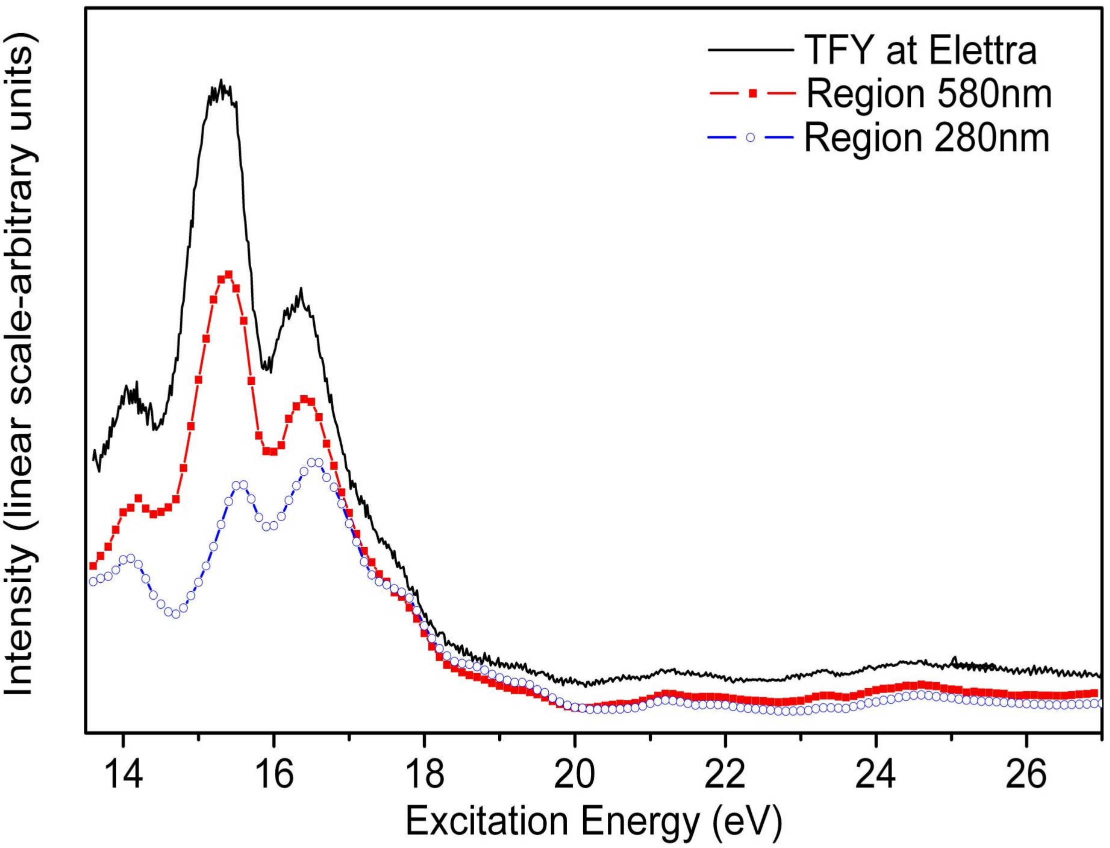

Figure 7.3. Excitation functions of fluorescence regions 250-310 and 550-650 nm, and the total fluorescence yield of SF_5CF_3 measured at Elettra. The spectra have been normalized to the flux of the beamline.

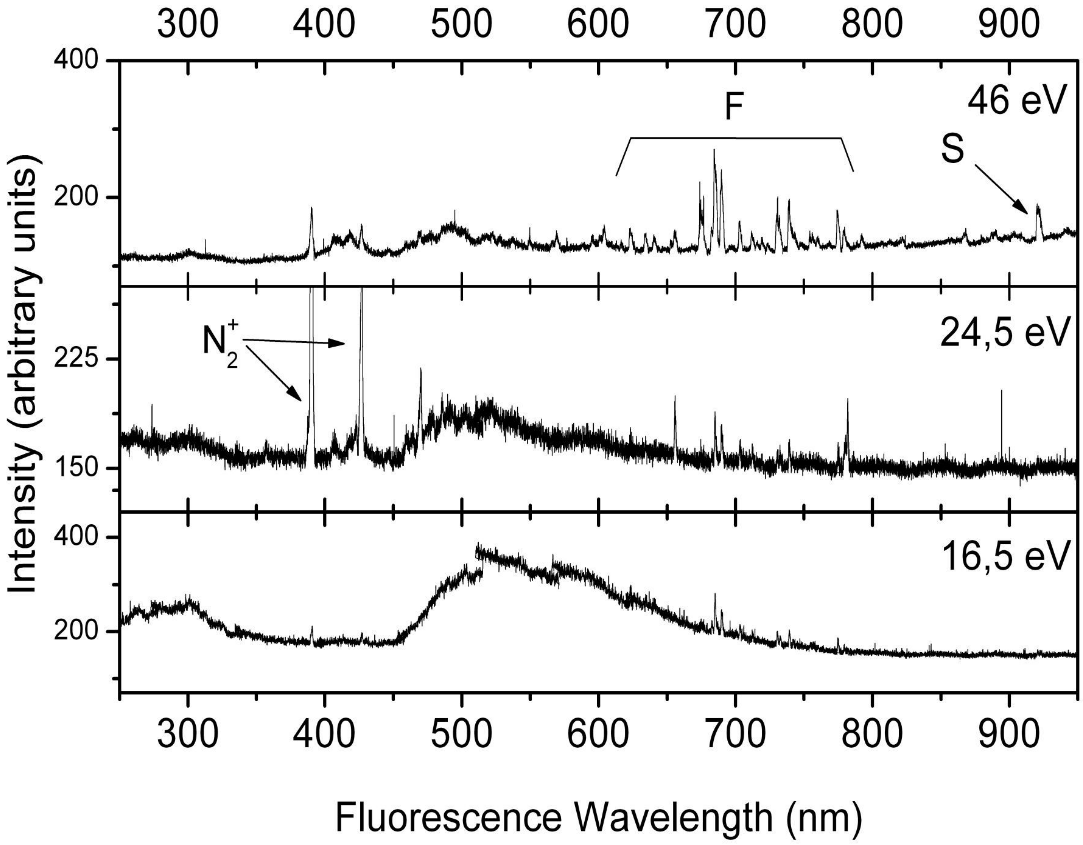

Figure 7.4. Dispersed fluorescence spectra of SF_5CF_3 measured at Elettra. The abnormal shape of the fluorescence spectrum for wavelengths around 500-600 nm at 16.5 eV is due to the quantum efficiency of the detector at these wavelengths.

7.4 Discussion

The identification of the CF_3 fragment as responsible for the fluorescence emission in SF_5 CF_3 at the lowest photon energies allows us to conclude that photon absorption within the band which has a maximum at 11.4 eV can lead to dissociation of the molecule. Furthermore, we can estimate the energy needed to break the SF_5CF_3 bond. In the CF_3X molecules, the emission observed at 10-12 eV excitation energy was attributed to the excited states lying about 6.4 eV above the ground state of the CF_3 fragment [35]. This corresponds to the dissociation $CF_3X \rightarrow CF_3^* + X$. For SF_5CF_3, the lowest energy to produce a CF_3 fragment is that for the reaction $SF_5CF_3 \rightarrow CF_3 + SF_5$. So if we begin to observe the excited CF_3 fragment at 10.2 ± 0.2 eV (Fig. 7.1) and the internal energy of the CF_3^* fragment is 6.4 eV, we determine an upper limit for the SF_5CF_3 bond dissociation energy of 3.8 ± 0.2 eV. This value, however, is subject to some uncertainties. Firstly, the excitation energy of the CF_3 fragment determined in ref. 35 relies on the correct vibrational numbering of the discrete CF_3 emission spectrum [34]. If this numbering is indeed correct, then the internal energy should actually be 6.29 eV, which increases the value for the bond dissociation energy to 3.9 ± 0.3 eV. Secondly, it is possible that in this study by Suto and Wahida [34] either or both electronically-excited CF_3 and ground-state SF_5 fragments are not formed in their lowest vibrational state. In that case, the determined SF_5CF_3 bond dissociation energy would be too high. Our result yields a slightly lower value than, but within error limits, for the SF_5CF_3 bond dissociation energy from that determined by threshold photoelectron – photoion coincidence spectroscopy, 4.06 ± 0.45 eV [6]. The calculated SF_5CF_3 bond dissociation energy is slightly lower, 3.50 eV [14].

In the CF_3X molecules, the appearance energy for the CF_2 emission is 2.02 eV higher than for the CF_3 emission [36]. This corresponds to the dissociation $CF_3X \rightarrow CF_2^* + X + F$. In SF_5CF_3 the appearance energy for CF_2 emission should be around 12.2 eV (= 10.2 eV + 2.02 eV). Unfortunately, partial fluorescence measurements could not be done across this threshold. The measurements of Figure 7.3 show that the CF_2 emission is already intense at 13.6 eV, although we note that this band is not visible with the excitation energy of 12.78 eV in Figure 7.2.

The CF_2 and CF_3 fluorescence yields have intensity maxima at the same energies as the peaks in the photoabsorption spectrum. This observation indicates that excited states of SF_5CF_3 dissociate along potential energy curves that yield excited CF_3 (which either emits light or further dissociates into excited CF_2). A similar behaviour has also been observed in the fragmentation of the ground and excited states of $SF_5CF_3^+$ [15]. The parent ion preferentially dissociates to CF_3^+ + SF_5 and not to SF_5^+ + CF_3, as can be concluded from the CF_3^+ ion yield which mirrors the threhold photoelectron spectrum of SF_5CF_3 [16]. Such a property is typical of small molecules, dissociating only on one repulsive potential energy surface with no curve crossing. It appears that SF_5CF_3 can behave as a pseudo-diatomic molecule, with a much lower density of vibronic states that it actually possesses. Fluorescence is just one of many decay channels for excited states of the parent molecule and therefore the absorption spectrum probably contains much intensity due to excitations that are "dark" to radiative decay; for example, dissociation to ground-state CF_3 and electronically-excited SF_5 will not be observed in these experiments, because SF_5 does not emit in the UV / visible. However, the similar trend of fluorescence yield and the absorption spectrum strongly suggests that excitations on SF_5CF_3 have an important molecular CF_3 character. It should be noted that absolute values of fluorescence quantum yields are not determined in these experiments.

As already described, the fluorescence emission up to around 16 eV in the CF_3X molecules has been attributed to Rydberg excited states of the parent molecule [31]. In SF_5CF_3, the corresponding region in the total fluorescence yield can extend up to 18 eV (up to this energy the CF_3 emission stays intense). Based on this reasoning, we attempt to assign the features in the TFY to Rydberg excitations. The energies of the Rydberg excitations converging to the ionization energies of the valence orbitals can be estimated using the calculated term values of Turki and Eisfeld [17] and the ionization energies reported by Holland et al [8]. As the number of possible Rydberg excitations is large, the energies of some will inevitably coincide with experimental values. Therefore, we consider only transitions to the lowest Rydberg 4s and 4p orbitals, which according to the calculations can be expected to have the highest oscillator strengths [17]. The results are shown in Fig.7.5 where the possible Rydberg transitions are displayed with bars (the heights of the bars are arbitrary). Obviously, definite assignments for the features cannot be given by the energy basis only. However, it seems that transitions to the 4s Rydberg orbital could account for the most intense features in the TFY. The TFY peak at 11.4 eV shows a rather clear shoulder at 12.3 eV that can be due to the excitation to the 4p orbital, as calculated in [17]. We note that the Rydberg orbitals of d type were not taken into account in the calculations of ref. 17. In the CF_3X molecules, such excitations have also been suggested to be responsible for fluorescence emission [31].

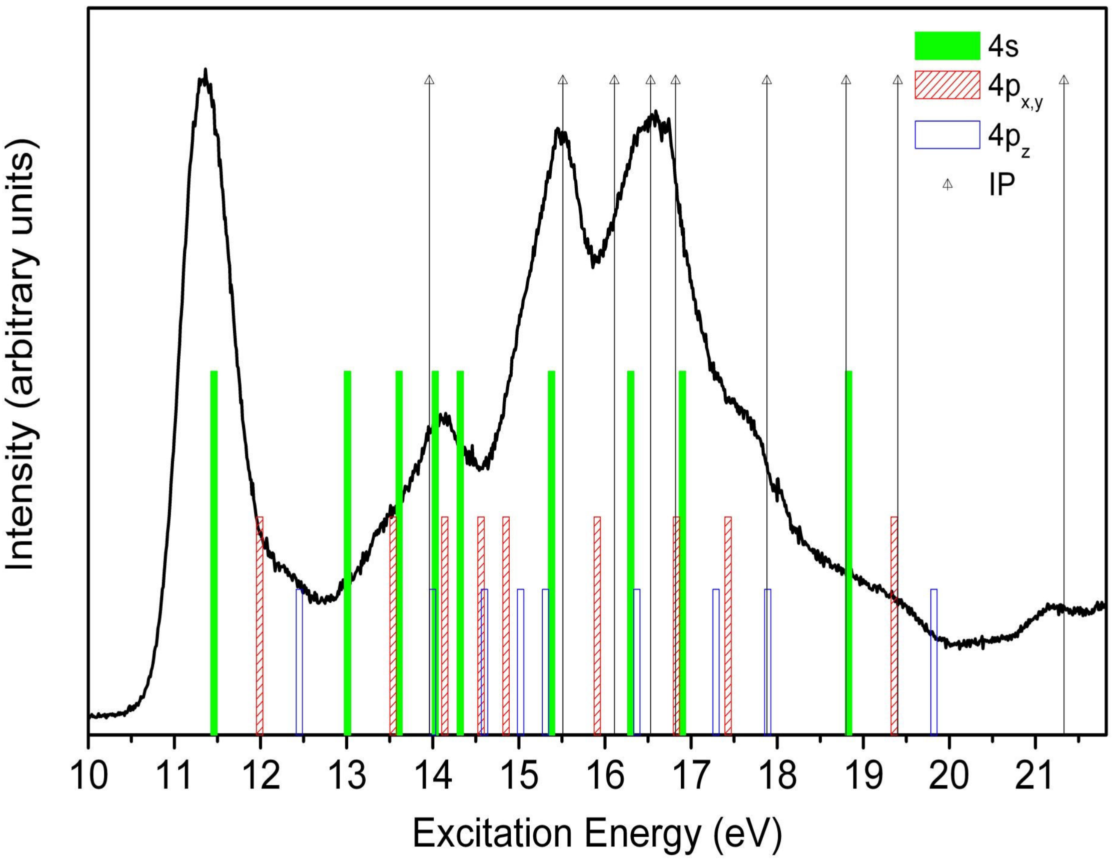

Figure 7.5. The solid curve displays the TFY measured at Daresbury (taken from Fig.7.1). The bars show the estimated positions of Rydberg transitions (the heights of the bars are arbitrary), while thin arrowed lines present the ionisation energies of the different valence orbitals as reported by Holland et al [8].

At higher excitation energies, excited ionic fragment CF_3^+ could, in principle, start to emit around 20 eV, but it was not found to contribute significantly to the observed fluorescence in the CF_3X molecules [36]. Thus, the intensity in the TFY spectrum (Fig. 7.1) could still be caused mostly by the CF_3 and CF_2 fragments. The partial fluorescence measurements of Fig. 3 reveal that there is fluorescence intensity in the corresponding wavelength regions. No other emitters, apart from N_2^+, have been identified in the dispersed spectra. In particular, no evidence of emission from the parent molecular ion, $SF_5CF_3^+$, has been encountered, in contrast to the CF_3X molecules where CF_4^+, CF_3Cl^+ and CF_3H^+ all show radiative decay from electronically-excited states [31].

Atomic emission due to excited fluorine fragments could begin around 17.8 eV. The upper limit for the dissociation $SF_5CF_3 \rightarrow SF_4CF_3 + F$ has been estimated to be 3.4 eV [14] and the excited F atoms, which fluoresce in the visible or near infra red, have internal energies of 14.37 eV or more [41]. This energy occurs in the photon energy range where the second order radiation gives a strong contribution to the excitation function (Fig. 7.6) which, added to the presence of the molecular emission background, masks any onset of a new emission. However, the excitation functions of the fluorine transitions at 731.1 and 739.9 nm, due to the $2p^4(^3P)3p(^2S) \rightarrow 2p^4(^3P)3s(^2P)$ and $2p^4(^3P)3p(^4P) \rightarrow 2p^4(^3P)3s(^4P)$ transitions respectively [41], show some features at different excitation energies. The most prominent one begins at around 20.5 eV and we tentatively assign it to the fluorine production channel $SF_5CF_3 \rightarrow SF_5^* + CF_3 \rightarrow SF_4 + F^* + CF_3$. This process requires an energy of 20.2 eV (= 5.84 + 14.37 eV), where the former energy has been calculated using the enthalpies of formation given in ref. 39 and the latter value is the internal energy of the F atom. This energy coincides quite well with the onset of the resonance. The rest of the features around 19, 23 and 24.5 eV are weak enough to be considered ambiguous but still worth noting as possible different dissociation limits that produce excited F atoms.

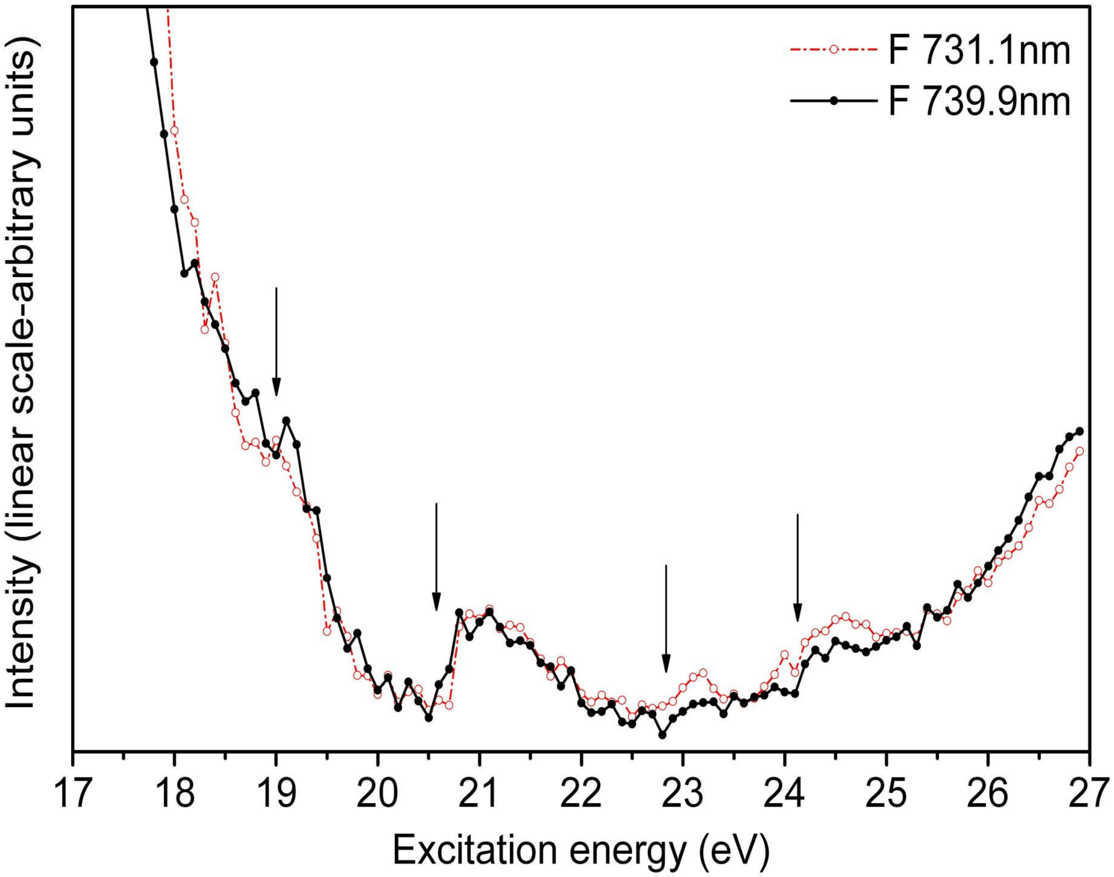

Figure 7.6: Excitation function of F 731.1 (dashed line) and 739.9 nm (continuous line) atomic transitions recorded after excitation of SF_5CF_3 with 17-27 eV photons. The arrows indicate the appearance threshold of the resonances discussed in the text.

The dispersed fluorescence spectrum (Fig.7.4) shows that at 24.5 eV excitation energy the total intensity of the atomic fragment lines is far lower than that of the molecular fragments. Atomic emission becomes proportionally more important at higher photon energies, as evidenced by the spectrum excited with 46 eV photons. At this excitation energy, a fluorescence feature at 922 nm can be attributed to the $3p^3(^4S)4p(^5P) \rightarrow 3p^3(^4S)4s(^5S)$ transitions in neutral sulphur atoms [41]. The same transitions in the SF_6 molecule were observed to have a resonant behaviour in the photon energy range 32-50 eV [29]. From the energy considerations, the emission was concluded to follow from the neutral dissociation of SF_6. The same effect could occur also in SF_5CF_3, this time resulting from an excitation in the SF_5 side of the molecule.

7.5 Conclusions

Photon induced fluorescence experiments have been performed for the SF_5CF_3 molecule in the vacuum-UV excitation energy range. The total fluorescence yield and dispersed fluorescence spectra of SF_5CF_3 resemble those of the CF_3X (X=H, F, Cl, and Br) molecules, showing molecular bands due to the excited CF_3 and CF_2 fragments at similar excitation energies. The emission due to the excited CF_3 fragment has a threshold of 10.2 ± 0.2 eV, leading to an upper-limit estimate of the SF_5CF_3 bond dissociation energy of 3.9 ± 0.3 eV. The CF_3 and CF_2 emissions are most likely caused by excitations of electrons from valence orbitals into Rydberg orbitals in the CF_3 side of the molecule. Thus, we proposed a partial explanation of the total fluorescence yield spectrum in terms of those Rydberg transitions. The photoabsorption spectrum shows peaks at the same energies as the total and partial fluorescence yields, implying the same origin for these features. However, the photoabsorption spectrum obviously displays other structures also due to intravalence transitions (especially in the SF_5 side), which will not be followed by fluorescence decay.

The emission due to the CF_3 and CF_2 fragments is an important contributor to the total fluorescence in the 200-1000 nm range also at photon energies above 20 eV. Fluorescence emission due to ionic molecular fragments is negligibly weak, while fluorescence in atomic fragments, especially in fluorine atoms, becomes proportionally more intense between 25 and 46 eV photon energy. The fluorescence emission of SF_5CF_3 provides one more hint that the structural parts (SF_5 and CF_3) of this molecule behave independently, and in part it does behave as another member of the CF_3X family (chapter 7).

7.6 References

[1] J A Ruiz, A Kivimäki, M Stankiewicz, E M García, M Coreno, S Ali, J Koperski, E Rachlew, G Vall-llosera i Serrano, V Feyer and R P Tuckett, *Phys. Chem. Chem. Phys*, **8** (2006), 5199

[2] W.T. Sturges, T. J. Wallington, and M. D. Hurley, *Science*, (2000) **289**, 611.

[3] M. A. Santoro, *Science*, **290** (2000), 935.

[4] H. Hou, L. Huang, L. Zhu, X. Pan, J. Zhang, and B. Ouyang, *Atmospheric Environment*, **39** (2005), 1641.

[5] N. J. Mason and P. A. Kendall, *J. Electron Spectrosc. Relat. Phenom.*, **120** (2001) 27.

[6] R.Y.L. Chim, R.A. Kennedy, and R.P. Tuckett, *Chem. Phys. Lett.,* **367** (2003), 697.

[7] P. Limão-Vieira, S. Eden, P.A. Kendall, N.J. Mason, A. Giuliani, J. Heinesch, M.-J. Hubin-Franskin, J. Delwiche and S.V. Hoffmann, *Int. J. Mass Spectrom.,* **233** (2004), 335.

[8] D.M.P. Holland, D.A. Shaw, I.C. Walker, I.J. McEwen, E. Aprà, and M.F. Guest, *J. Phys. B.,* **38** (2005), 2047.

[9] Chemical Kinetics and Photochemical Data for Use in Stratospheric Modeling (Evaluation Number 12, NASA JPL, 1997)

[10] C. Atterbury, R.A. Kennedy, C.A. Mayhew and R.P. Tuckett, *Phys. Chem. Chem. Phys.,* **3** (2001), 1949.

[11] C. Atterbury, A.D.J. Critchley, R.A. Kennedy, C.A. Mayhew and R.P. Tuckett, *Phys. Chem. Chem. Phys.,* **4** (2002), 2206.

[12] S.T. Arnold, T.M. Miller, A.A. Viggiano and C.A. Mayhew, *Int. J. Mass Spectrom.,* **223** (2003), 403.

[13] C.A. Mayhew and R.A. Kennedy, *Int. J. Mass Spectrom.,* **206** (2001), i-iv.

[14] W. Sailer, H. Drexel, A. Pelc, V. Grill, N.J. Mason, E. Illenberger, J.D. Skalny, T. Mikoviny, P. Scheier and T.D. Märk, *Chem. Phys. Lett.,* **351** (2002), 71.

[15] R.P. Tuckett. *Advances in Fluorine Science*, **1** (2006), 89 (publ. Elsevier)

[16] R.Y.L. Chim, R.A. Kennedy, R.P. Tuckett, W. Zhou, G.K. Jarvis, D.J. Collins, and P.A. Hatherly, *J. Phys. Chem. A*., **105** (2001), 8403.

[17] M. Turki and W. Eisfeld, *Phys. Chem. Chem. Phys.,* **7** (2005), 1700.

[18] B. Gstir, G. Hanel, J. Fedor, M. Probst, P. Scheier, N.J. Mason, and T.D. Märk., *J. Phys. B.,* **35** (2002), 2567.

[19] D.W. Ball, *J. Mol. Struc. (Theochem)*, **578** (2002), 29.

[20] Z. Li, J. Yang, J.G. Hou and Q. Zhu, *Chem. Phys. Lett.,* **359** (2002), 321.

[21] M. Stankiewicz, E. Melero Garcia, J. Alvarez Ruiz, P. Erman, P.A. Hatherly, A. Kivimäki, E. Rachlew and J. Rius i Riu, *Rev. Sci. Instrum. A*, **75** (2004), 2402.

[22] C.R. Howle, S. Ali, R.P. Tuckett, D.A. Shaw and J.B. West, *Nucl. Instr and Methods B*, **237** (2005), 656.

[23] D.M.P. Holland, D.A. Shaw, A. Hopkirk, M.A. MacDonald, and S.M. McSweeney, *J. Phys. B*.**, 25 (**1992), 4823 and references therein.

[24] J.W. Au, G.R. Burton and C.E. Brion, *Chem. Phys.,* **221** (1997), 151.

[25] J. L. Dehmer, *J. Chem. Phys.,* **56** (1972)**,** 4496.

[26] W.R. Harshbarger, M.B. Robin, and E.N. Lassettre, *J. Electron Spectrosc.,* **1** (1972), 319.

[27] G.C. King and J.W. McConkey, *J. Phys. B*.**, 11** (1978), 1861.

[28] L.C. Lee, X. Wang, and M. Suto, *J. Chem. Phys.,* **85** (1986), 6294.

[29] J. Alvarez Ruiz, E. Melero-Garcia, A. Kivimäki, M. Coreno, P. Erman, E. Rachlew, and R. Richter, *J. Phys. B.*, **38** (2005), 387.

[30] Z.J. Jabbour, K.A. Blanks, K.E. Martus and K. Becker, *J. Chem. Phys*., **88** (1988), 4252.

[31] H. Biehl, K.J. Boyle, R.P. Tuckett, H. Bäumgärtel, and H.W. Jochims, *Chem. Phys.,* **214** (1997), 367 and references therein.

[32] C. Larrieu, M. Chaillet, and A. Dargelos, *J. Chem. Phys.,* **96** (1992), 3732.

[33] M. Suto, N. Washida, H. Akimoto, and M. Nakamura, *J. Chem. Phys.,* **78** (1983), 1019.

[34] M. Suto and N. Washida, *J. Chem. Phys.,* **78** (1983), 1007.

[35] N. Washida, M. Suto, S. Nagase, U. Nagashima, and K. Morokuma, *J. Chem. Phys.,* **78** (1983), 1025.

[36] L.C. Lee, J.C. Han, C. Ye, and M. Suto, *J. Chem. Phys.,* **92** (1990), 133.

[37] S. Trajmar and A. Chutjian, *J. Phys. B*., **10** (1977), 2943.

[38] P.K. Carroll and T.P. Grennan, *J. Phys. B*., **3** (1970), 865.

[39] NIST Chemistry Webbook, http://webbook.nist.gov/chemistry

[40] K.P. Huber and G.Herzberg, "Constants of Diatomic Molecules" (data prepared by J.W. Gallagher and R.D. Johnson, III) in NIST Chemistry WebBook, NIST Standard Reference Database Number 69, Eds. P.J. Linstrom and W.G. Mallard, June 2005, National Institute of Standards and Technology, Gaithersburg MD, 20899 (http://webbook.nist.gov).

[41] NIST Atomic Spectra Database, NIST Standard Reference Database Number 78 (2006), http://physics.nist.gov/PhysRefData/ASD/index.html

8. VUV fluorescence spectroscopy of BF_3, BCl_3 and BBr_3

8.1 Introduction

In this chapter we present the VUV fluorescence spectra of BF_3, BCl_3 and BBr_3. All the spectra were taken using beamline 3.1 at the Daresbury SRS. Because of their potency as Lewis acids boron trihalides are used extensively as catalysts in organic synthesis. They are also used in the manufacture of resistors and in the plasma etching of semiconductor devices. Of the three molecules BBr_3 is probably the least well studied molecule in the VUV range. The VUV spectroscopy of the boron trihalides has been investigated by several groups using a number of different experimental techniques. Bassett and Lloyd [1] have recorded low resolution photoelectron spectra of each of the boron trihalides. Their results including vertical ionization energies are summarized along with calculated thermodynamic dissociation energies for different fragmentation channels in tables 8.1, 8.3 and 8.4. Their photoelectron assignments suggested that the sequence of the six highest occupied valence molecular orbitals in BBr_3 is slightly different from that in BF_3 and $BC1_3$. This chapter describes work that probes the highly excited electronic states of these molecules by use of VUV fluorescence spectroscopy. Emissions from products of these excited electronic states provide information which is fundamental to understanding their chemical dynamics.

Fluorescence spectroscopy has been performed by Tuckett *et al.* [2 - 5] on all three molecules both at the BESSY 1 synchrotron radiation source in Berlin and at the Daresbury SRS. It was found for excitation energies in the range 13 – 17 eV, photodissociation of Rydberg states of BF_3 produced a substantial branching ratio into two, possibly three, excited valence states of the BF_2 radical [2,4]. Fluorescence from BCl_3 photoexcited in the range 9 – 22 eV was found to be more complicated, with emissions being observed and mostly assigned to BCl_2 ,BCl, BCl_3^+ , BCl_2^+ and B [3,4]. BBr_3 fluorescence spectra were recorded between 8 and 20 eV [5] where emission from BBr_2 was identified by use of dispersed fluorescence spectroscopy between 240 and 390 nm. Parent ion BBr_3^+ ion emission was also observed between 350 and 440 nm and were assigned as originating from $BBr_3^+ \tilde{D}\ {}^2E'$. Analogous emission in BBr, BBr_2^+ and B were also observed.

8.2 Results

8.2.1 BF_3

The electronic configuration of the outer-valence molecular orbitals of BF_3 in D_{3h} symmetry is …..$(2a_1')^2(2e')^4(la_2'')^2(3e')^4(le'')^4(la_2')^2$. The numbering scheme does not include the core orbitals. The vertical ionisation energies for the five outermost occupied valence orbitals have been measured to be 15.95 ($1a_2'$), 16.67 ($1e''$), 17.14 ($3e'$), 19.13 ($1a_2''$), and 21.09 ($2e'$) using He(I) and He(II) photoelectron spectroscopy [1]. The quantum defects of ns, np and nd Rydberg orbitals centred on B (F) atoms are predicted to be 0.86 (1.20), 0.47 (0.75), and 0.01 (0.003) [6]. The flux-normalised fluorescence excitation spectrum of BF_3 taken using the medium energy grating (MEG) at a resolution of 0.2 nm on the primary monochromator is shown in figure 8.1. Resonant bands are seen between *ca.* 12 and 17 eV, with peaks at 13.16, 14.10 and 15.72 eV, and weaker shoulders at 14.65 and 15.30 eV. The low-energy band at 13.16 eV has a wider width than the other bands in this spectrum.

Using the Rydberg formula and vertical ionisation energies of BF_3, the peaks in this fluorescence excitation spectrum have been assigned [2,4]. The lowest-energy peak at 13.16 eV is assigned as originating from the $(3e')^{-1}$ 3s Rydberg state. The energetics and dissociation channels of BF_3 are presented in table 8.1. The first ionisation energy of BF_3 is at 15.95 eV. Hence any signal seen below the photoexcitation energy of 15.95 eV cannot be due to emission from the parent ion. The BF radical can be produced in its ground state with a photoexcitation energy of 10.57 eV. The lowest-lying electronic transition of BF is A $^1\Pi$ - X $^1\Sigma^+$ at 195 nm or 6.3 eV [2,4]. When combined with the thermochemical threshold for BF fragment production, this energy exceeds that of the excitation photon. The thermochemical threshold for production of the BF_2 radical in the $\tilde{A}$ state is at 10.83 eV, and energetically the fluorescence signal seen at 13.16 eV can only result from the BF_2 fragment. The next band with a peak at 14.10 eV has been assigned as originating from the $(1a_2')^{-1}$ 3p Rydberg state [2]. Some partially-resolved discrete structure can be seen. The weak shoulder at 14.65 eV has also been assigned as originating from the $1a_2'$ molecular orbital of BF_3. Absorption of a photon leads to excitation to the $(1a_2')^{-1}$ 3d Rydberg state. Fragmentation, either via direct dissociation from a repulsive surface or by predissociation, occurs to produce the BF_2 fragment in an excited state and fluorescence emanates from this state. The band with a peak at 15.72 eV has been assigned as originating from the $(3e')^{-1}$ 4s Rydberg state. Again, energetically this peak can only be a result of emission emanating from the BF_2 fragment. At higher energies a very weak non-resonant band is seen above *ca.* 21 eV. Here we have enough energy to ionise the BF_3 molecule. Therefore emission can emanate from the parent ion, BF_3^+. The observed signal is very weak, but does agree with earlier studies [2] and is probably due to BF_3^+ $\tilde{E}$ $^2A_1'$.

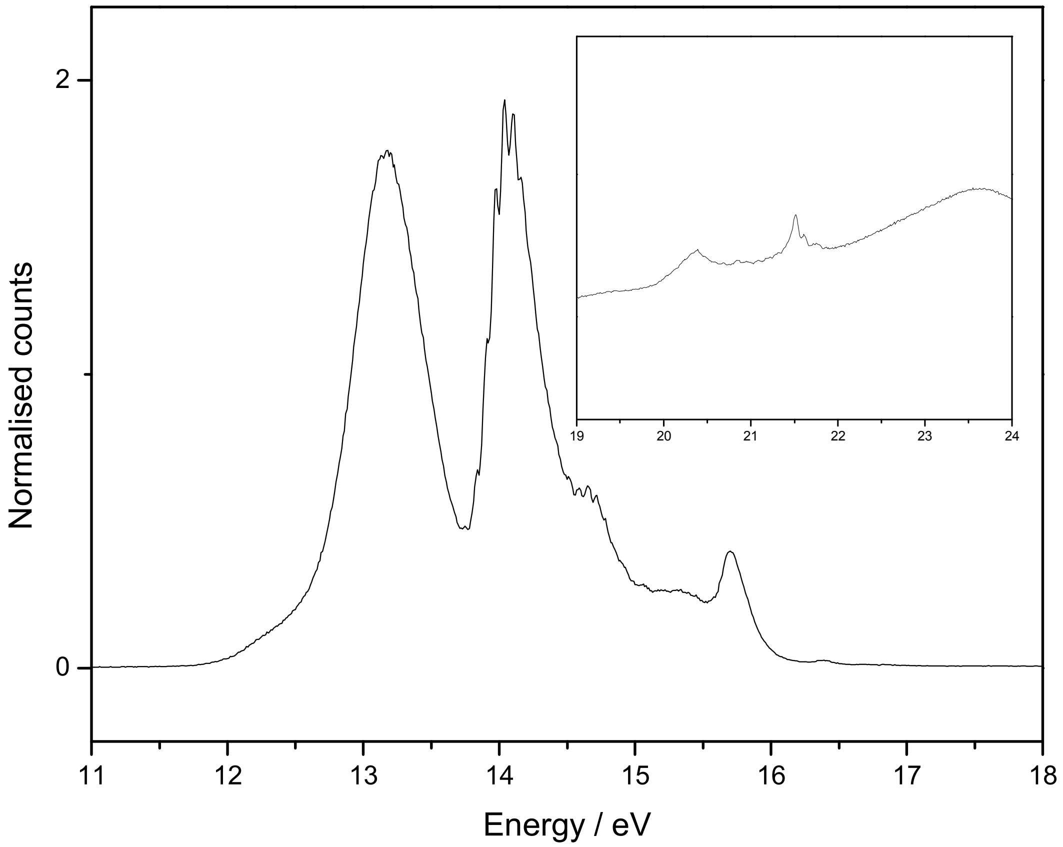

Figure 8.1: The undispersed fluorescence excitation spectrum of BF_3, taken using the MEG at a resolution of 0.2 nm. Insert show part of spectra taken using the HEG between 19 and 24 eV with a resolution of 0.1 nm.

Neutral / Parent ion	Dissociation channel	Dissociation energy / eV	Vertical IE / eV
$\tilde{E}$ $^2A_1'$			21.57
$\tilde{D}$ $^2E'$			21.09
$\tilde{C}$ $^2A_2''$			19.13
	B + 3F	20.1	
	B + F_2 + F	18.45	
$\tilde{B}$ $^2E'$			17.14
$\tilde{A}$ $^2E''$			16.67
BF_3^+ $\tilde{X}$ $^2A_2'$			15.95
	BF + 2F	12.22	
	BF + F_2	10.57	
	BF_2^+ + F	15.88	
	BF_2 $\tilde{C}$ $^2B_2$ + F	14.3[a]	
	BF_2 $\tilde{B}$ $^2A_1$+ F	13.8[a]	
	BF_2 $\tilde{A}$ $^2B_1$+ F	10.83[a]	
	BF_2 $\tilde{X}$ $^2A_1$+ F	6.48	
BF_3		0	

Table 8.1. The energetics and dissociation channels of BF_3 neutral and parent ion.
[a] From reference [2]

The dispersed fluorescence spectrum of BF_3, taken with a photoexcitation energy of 13.16 eV and using the UV turret and 300 grooves mm^{-1} grating on the secondary Triax monochromator, is shown in figure 8.2. The spectrum has been normalised to the sensitivity of the CCD detection system (chapter 2). Three bands are seen with peaks at 305, 340 and 405 nm. On thermodynamic grounds the only species that could be responsible for the emission at 13.16 eV is the BF_2* radical. We have enough energy to populate the BF_2 $\tilde{A}$ state. The $\tilde{B}$ state of BF_2 has a thermochemical threshold at 13.80 eV (table 8.1). Hence any bands seen at 13.16 eV can only result from BF_2 $\tilde{A}$ - $\tilde{X}$ emission. The peak at 305 nm can now be assigned as emission resulting from the BF_2 $\tilde{A}$ - $\tilde{X}$ transition. The two peaks at 340 and 405 nm pose a problem. From previous experiences of beamline 3.1, we know that second-order effects from the primary Wadsworth monochromator are a particular problem between *ca.* 12 and 16 eV on the MEG. We reason that the latter two bands may be second-order signal from parent ion emission at 26.32 eV. Figure 8.5 shows the dispersed spectrum taken with a photoexcitation energy of 21.5 eV. We see two bands with peak wavelengths at

345 and 400 nm. Hence, we conclude that the two latter bands seen in the spectrum taken at 13.16 eV are indeed due to second-order signal from 26.32 eV.

Figure 8.3 shows the dispersed fluorescence spectra of BF_3, taken at photoexcitation energies of 14.10 and 15.7 eV, using the UV turret and the 300 grooves mm^{-1} grating on the secondary Triax monochromator. Both spectra are very similar, the major peaks are at the same wavelengths, with only the relative intensities of the peaks being different. The peaks are seen at wavelengths of 240, 265, 300, 335 and 405 nm. The latter two peaks are from second-order signal coming from the primary monochromator. The peak at 300 nm could be due to emission resulting from the BF_2 $\tilde{A}$ - $\tilde{X}$ transition. The first two bands are not seen in the dispersed spectrum taken at 13.16 eV. The thermochemical threshold for the production of BF_2 $\tilde{B}$ state is at 13.80 eV. Therefore we can say that these two bands are probably a result of emission emanating from the BF_2 $\tilde{B}$ state. Again on thermodynamic grounds no other possible emitter exists at 14.10 eV. At a photoexcitation energy of 15.7 eV we have enough energy to populate the BF_2 $\tilde{C}$ state. The two bands with peaks at 240 and 265 nm are seen in both the spectra shown in figure 8.3. Therefore we must assume the emitting state in the BF_2 radical is common to both spectra. Hence it is unlikely that we see any fluorescence emanating from the BF_2 $\tilde{C}$ state at 15.7 eV.

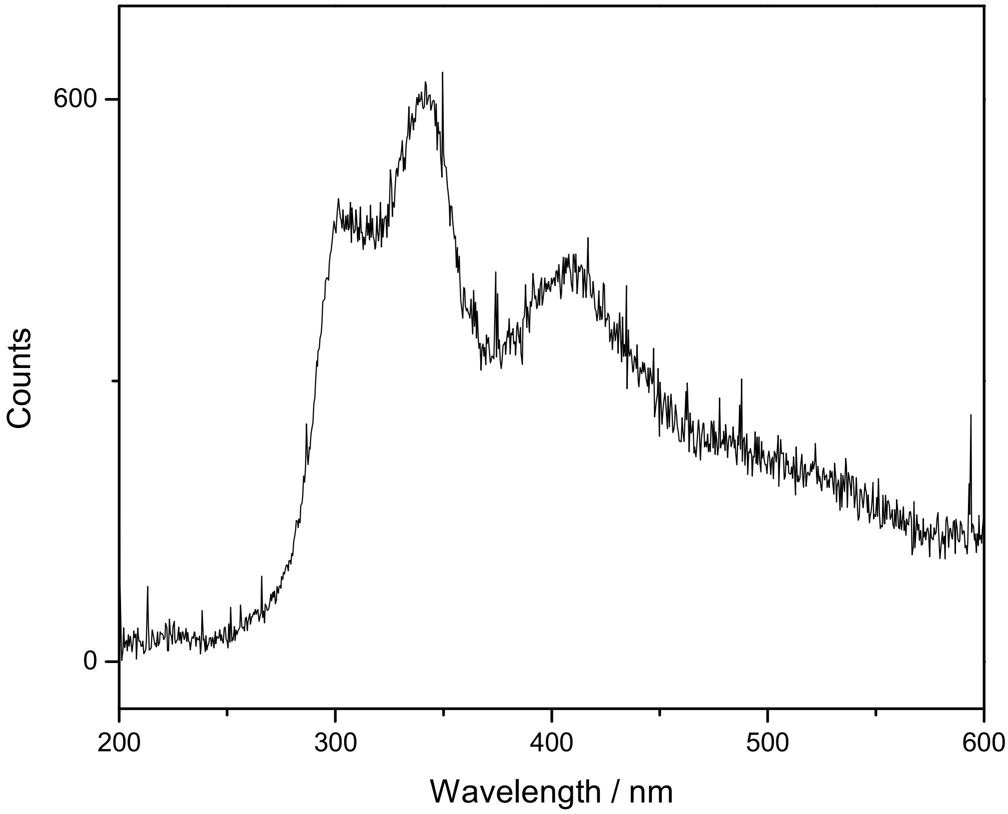

Figure 8.2: Dispersed fluorescence spectra of BF_3 taken with a photoexcitation energy of 13.16 eV using the UV turret and 300 grooves mm^{-1} gratings. The slits on the secondary Triax monochromator were set at 1mm.

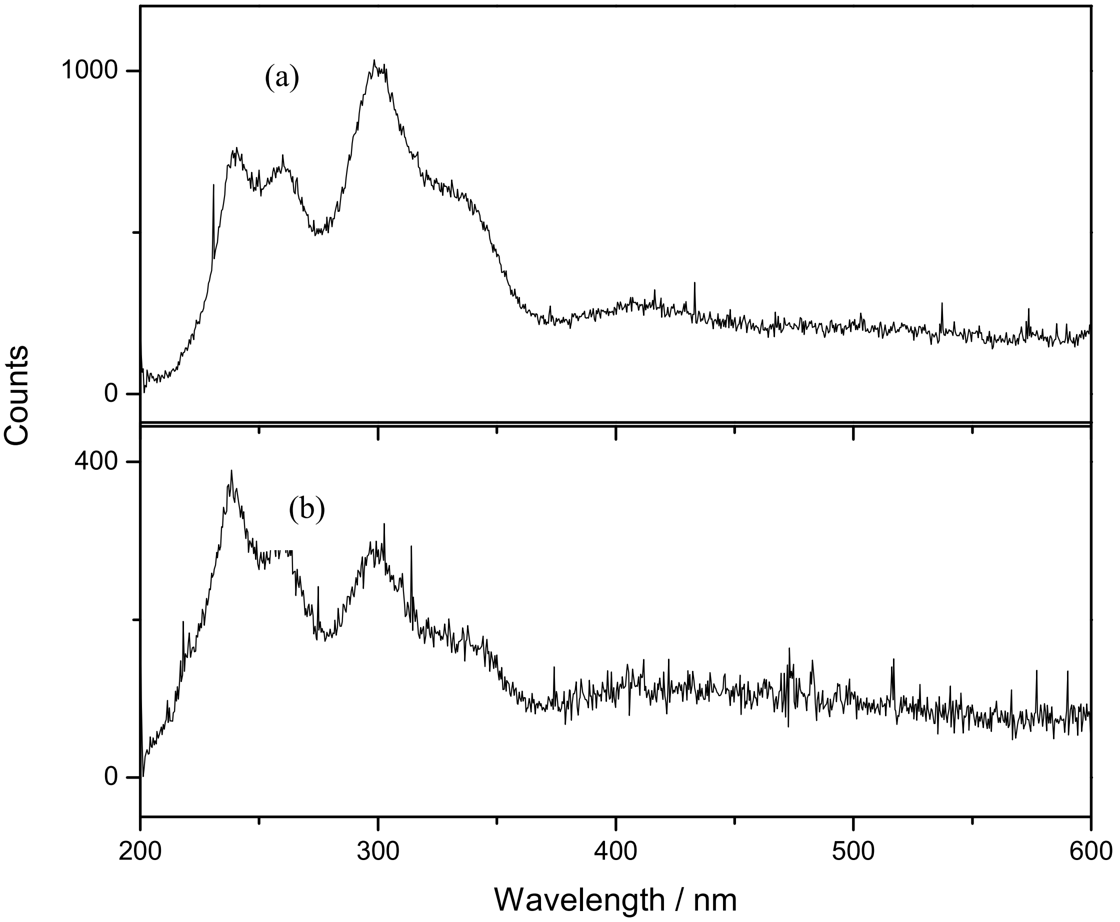

Figure 8.3: (a) Dispersed fluorescence spectra of BF_3 taken with a photoexcitation energy of 14.10 eV (b) taken with a photoexcitation energy of 15.7 eV. Both spectra were taken using the UV turret and 300 grooves mm^{-1} grating. The slits on the secondary Triax monochromator were set at 1 mm.

Figure 8.4 shows a higher resolution spectrum taken at a photoexcitation energy of 14.10 eV. The spectrum was dispersed using the UV turret in combination with the 1200 grooves mm^{-1} grating on the secondary Triax monochromator. The slits on the Triax were set to 1 mm giving an optical resolution of 3.5 nm. In this spectrum a long progression of vibrational structure can be seen. The observed line positions are listed in table 8.2. The first major progression has an average line spacing of 520 cm^{-1}, and the second weaker progression has an average line spacing of 526 cm^{-1}. Previous work by Tuckett *et al.*, using He* 2 ^3S metastable impact as the excitation source (energy 19.82 eV), also observed these progressions [2] and there is reasonable agreement in the absolute energies of the peaks. The average line spacing obtained was 525 cm^{-1} for both progressions closely agreeing with the results obtained here. The lines were assigned to two overlapping vibronic transitions in the BF_2 radical, both to the v_2 bending mode manifold in the $\tilde{X}$ state. High resolution spectra for the peaks at 13.16, 14.65 and 15.70 eV were also recorded, using identical conditions to the spectrum taken at 14.10 eV. Very surprisingly, no discrete structure was observed for any of these spectra.

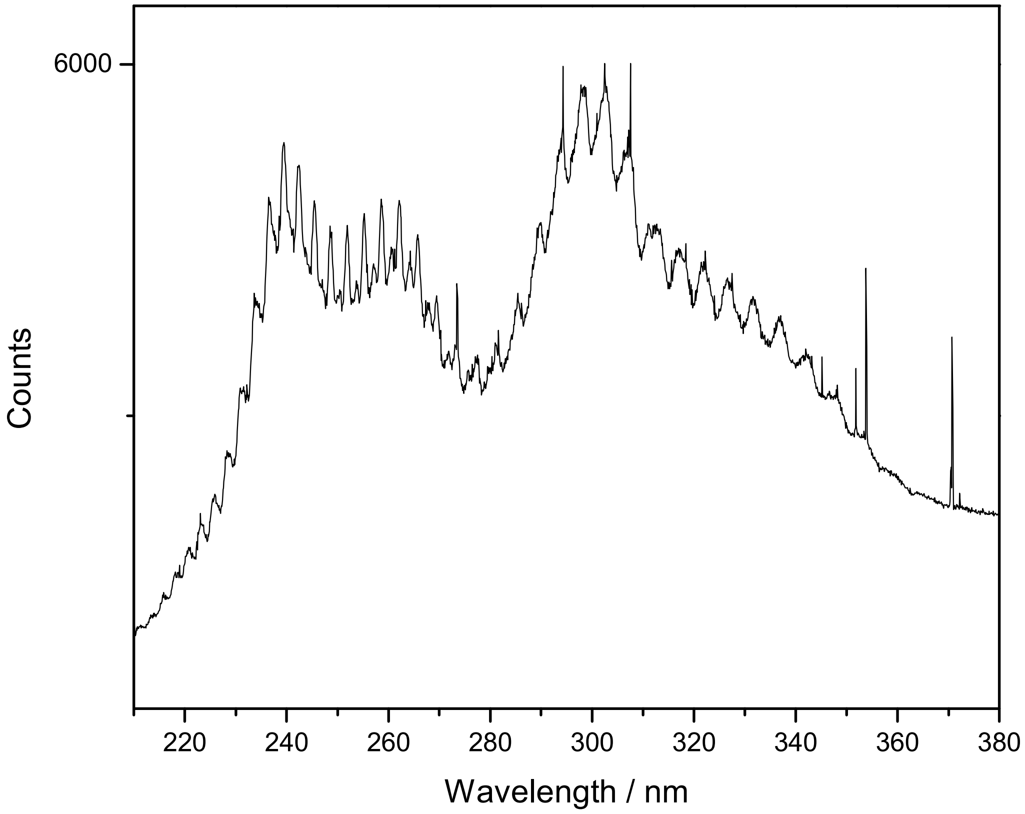

Figure 8.4: Dispersed fluorescence spectra of BF_3 taken with a photoexcitation energy of 14.10 eV using the UV turret and 1200 grooves mm^{-1} gratings. The slits on the secondary Triax monochromator were set at 1mm.

1st Progression / nm	cm^{-1}	Δv	2nd Progression / nm	cm^{-1}	Δv
218.35	45798		251.35	39785	
		561			509
221.06	45237		254.61	39276	
		473			530
223.40	44764		258.09	38746	
		525			516
226.05	44238		261.58	38229	
		557			524
228.93	43682		265.22	37705	
		509			510
231.63	43173		268.85	37195	
		546			537
234.59	42627		272.79	36658	
		481			522
237.27	42146		276.73	36136	
		490			555
240.06	41656		281.05	35581	
		507			
243.02	41149				
		541			
246.25	40608				
		504			
249.35	40104				
		536			
252.73	39568				
		526			
256.13	39042				
		520			
259.59	38522				
		515			
263.11	38007				
		530			
266.83	37477				
		507			
270.49	36970				
		529			
274.42	36441				

Table 8.2: Vibrational progression in BF_2*

The dispersed fluorescence spectrum of BF_3 taken, at a photoexcitation energy of 21.7 eV, using the UV turret in combination with the 100 grooves mm^{-1} grating on the secondary Triax monochromator is shown in figure 8.5. The spectrum shows two bands, the first between *ca.* 250 and 360 nm, and a second band with a peak at *ca.* 410 nm. Both these bands are probably due to emission emanating from the BF_3^+ $\tilde{D}$ $^2E'$state. The first band is assigned to the BF_3^+ $\tilde{D}$ $^2E'$- $\tilde{X}$ $^2A_2'$ transition and the second band is assigned to the BF_3^+ $\tilde{D}$ $^2E'$ - $\tilde{B}$ $^2E'$ transition. Both transitions are electric dipole allowed in D_{3h} symmetry.

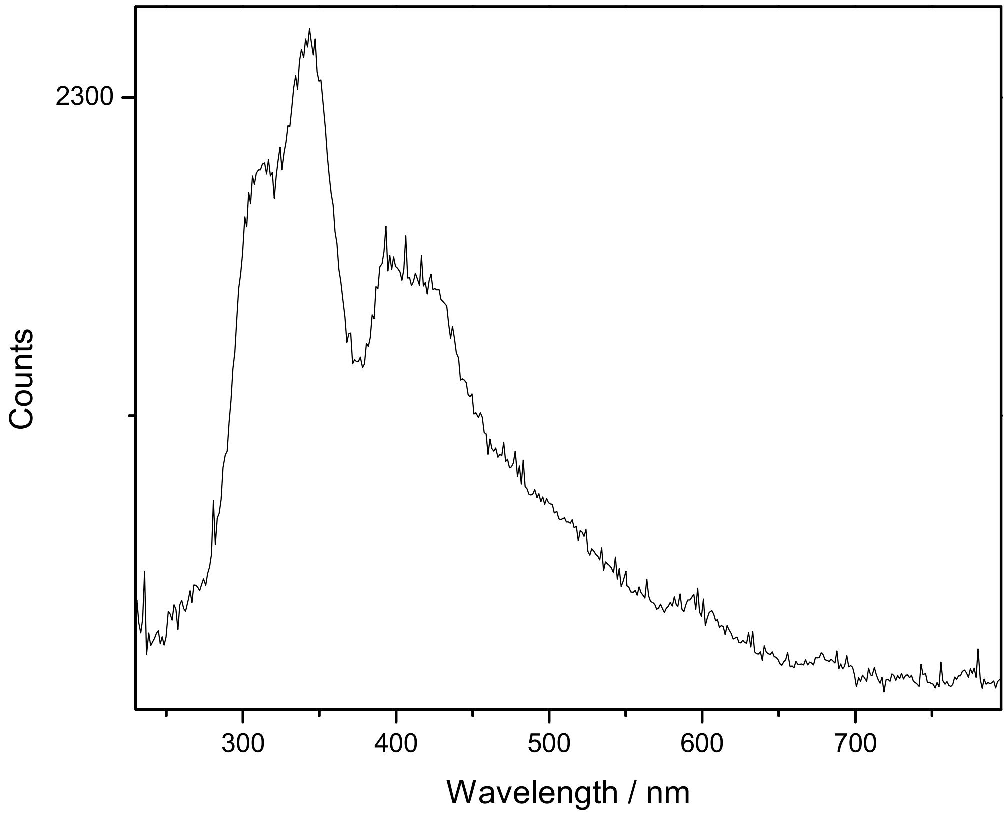

Figure 8.5: Dispersed fluorescence spectra of BF_3 taken with a photoexcitation energy of 21.7 eV using the UV turret and 100 grooves mm^{-1} gratings. The slits on the secondary Triax monochromator were set at 1mm

8.2.2 BCl$_3$

The electronic configuration of the outer-valence molecular orbitals of BCl$_3$ is also…..$(2a_1')^2(2e')^4(la_2'')^2(3e')^4(le'')^4(la_2')^2$. The numbering scheme here does not include the core orbitals. The vertical ionisation energies for the five outermost occupied valence orbitals have been measured to be 11.73 ($1a_2'$), 12.39 ($1e''$), 12.66 ($3e'$), 14.42 ($1a_2''$), and 15.54 ($2e'$) using He(I) and He(II) photoelectron spectroscopy [1].

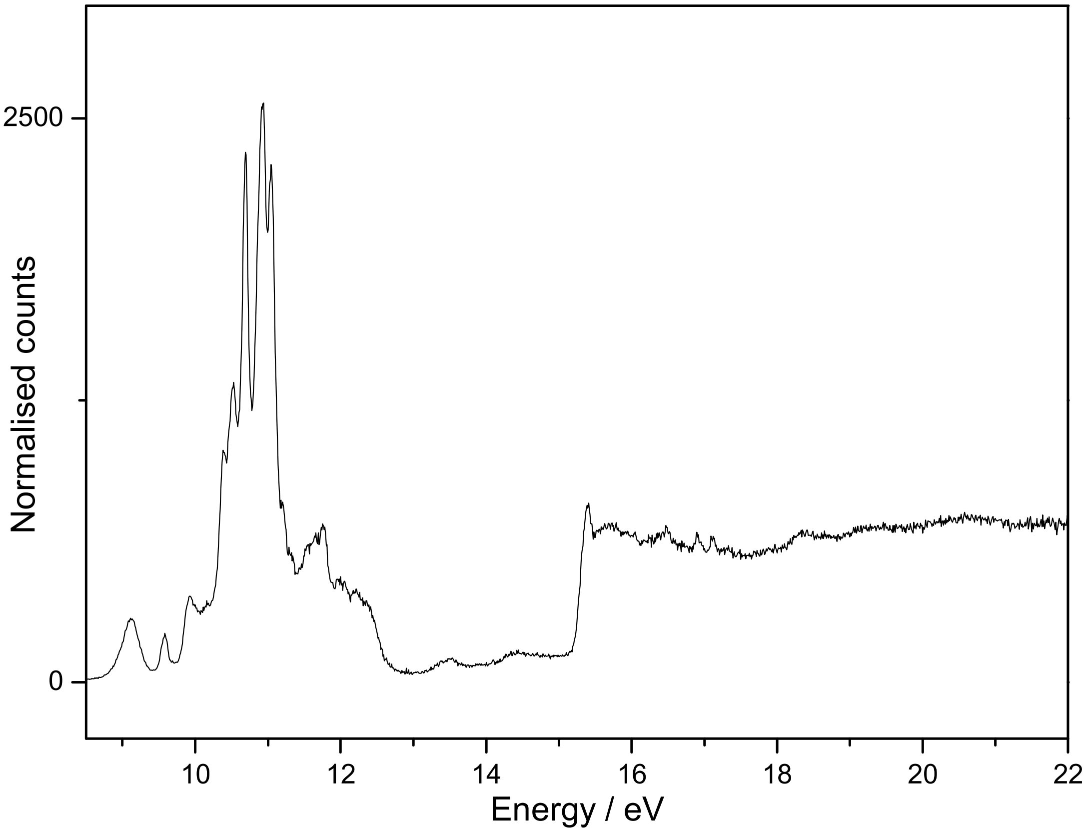

Figure 8.6: The undispersed fluorescence excitation spectrum of BCl$_3$, taken using the MEG at a resolution of 0.2 nm.

Neutral / Parent ion	Dissociation channel	Dissociation energy / eV	Vertical IE / eV
$\tilde{D}\ ^2E'$			15.54
$\tilde{C}\ ^2A_2''$			14.42
	B + 3Cl	13.8	
	B + Cl_2 + Cl	11.28	
$\tilde{B}\ ^2E'$			12.66
	$BCl_2^+\ \tilde{X}$ + Cl	12.41	
$\tilde{A}\ ^2E''$			12.39
BCl_3^+ $\tilde{X}\ ^2A_2'$			11.73
	BCl + 2Cl	8.16	
	BCl + Cl_2	5.64	
	$BCl_2\ \tilde{C}\ ^2A_1$ + Cl	11.94[a]	
	$BCl_2\ \tilde{B}\ ^2B_2$ + Cl	10.92[a]	
	$BCl_2\ \tilde{A}\ ^2B_1$ + Cl	7.22[a]	
	$BCl_2\ \tilde{X}\ ^2A_1$ + Cl	4.61	
BCl_3		0	

Table 8.3. The energetics and dissociation channels of BCl_3 neutral and parent ion.
[a] Reference (6, 7)

The flux-normalised fluorescence excitation spectrum of BCl_3 taken using the MEG at a resolution of 0.2 nm is shown in figure 8.6. Resonant peaks are seen between 9 and 13 eV and in addition a strong non-resonant peak with an onset at 15.26 eV is also observed. The peaks between 9 and 13 eV were assigned to states of BCl_3 arising from electron excitation from either the 3e' or $1a_2'$ valence orbitals to s, p or d Rydberg orbitals [3]. As in the BF_3 spectrum, the lowest-energy $(3e')^{-1}$ 3s Rydberg peak at 9.17 eV is broader than the other peaks. This peak is probably broadened by lifetime effects. By analogy with BF_2, we would assume this emission is a result of $BCl_2\,\tilde{A}$ - $\tilde{X}$ transition. Table 8.3 shows the energetics and dissociation channels of BCl_3. Energetically, at a photoexcitation energy of 9.17 eV only the $BCl_2\,\tilde{A}$ state is accessible. The other Rydberg peaks in figure 8.6 are narrower than the peak at 9.17 eV, their width being determined by the resolution of the photoexcitation source. Studies using a range of UV/Visible filters by Tuckett *et al.* [3,4] have shown that emission from these states is predominantly in the UV between 200 and ~ 400–450 nm. The non-resonant band at higher energy has a threshold at 15.26 eV. This threshold energy is in good agreement with the adiabatic ionisation energy of the $\tilde{D}$ ^{2}E’ of BCl_3^+ and the form of the excitation spectrum is characteristic of a non-resonant photoionization process (chapter 1).

Dispersed fluorescence spectra taken between 9 and 13 eV are shown in figure 8.7. The spectra were taken using the UV turret in combination with the 100 grooves mm^{-1} grating on the secondary Triax monochromator. All the spectra have been normalised to the sensitivity of the CCD/Triax detection system and the readout noise subtracted. The spectra were dispersed at energies of 9.17, 9.61, 9.94, 10.75 and 10.96 eV. Figure 8.7(a) and (b) present the dispersed fluorescence spectrum taken at 9.17 eV and 9.61 eV, both of which show a broad band between *ca.* 400 and 800 nm. These bands have been assigned as BCl_2 $\tilde{A}$ - $\tilde{X}$ emission. The next spectrum taken at 9.94 eV (figure 8.7 (c)) also shows a broad band between *ca.* 400 and 800 nm. A further band not seen in the previous two spectra now appears between 300 and 380 nm. Intuitively we would assign this band to emission resulting from BCl_2 $\tilde{B}$ - $\tilde{X}$ transition. The values for the electronic energy levels of the BCl_2* radical shown in table 8.3 are taken from a theoretical paper of Warschkow *et al.* [7]. These values suggest that at 9.94 eV only the BCl_2 $\tilde{A}$ state is accessible, so clearly if our assignment is correct there are errors in the absolute energies of this *ab initio* study.

The last two spectra in figure 8.7 also show the broad band between *ca.* 400 and 800 nm as well as another band between 250 and 380 nm. This second band is broader than the band seen in figure 8.7 (c). This is probably a result of an appearance of a new band in close proximity to the band seen in figure 8.7 (c). Again intuitively this band could be thought of as emission resulting from a BCl_2 $\tilde{C}$ - $\tilde{X}$ transition. We note, however, that at 10.75 eV according to the thermochemistry of reference [7] only the BCl_2 $\tilde{A}$ state channel is open. Weak evidence supporting these assignments for three excited states of BCl_2 can be found using the thermochemical values in table 8.3. The BCl_2 $\tilde{B}$ - $\tilde{X}$ and $\tilde{C}$ - $\tilde{X}$ emission are calculated to be *ca.* 30 nm apart and the peaks of the two bands (figure 8.7 (c) and (d)) are also *ca.* 30 nm apart. It is important to note that for the energies and orbital symmetries of the three lowest excited states of BF_2 and BCl_2, we have quoted values which were calculated at the geometry of the ground state of these two radicals by Atkinson *et al* [8] and Warschkow *et al* [7]. From the more extensive calculations performed on BF_2 by Peric and Peyerimhoff [9,10], the energies of these states were dependent markedly on both bond angle and the B–F bond length. Finally, we note that the calculation predict that the symmetry of the 2nd and 3rd excited states are reversed in BF_3 and BCl_3.

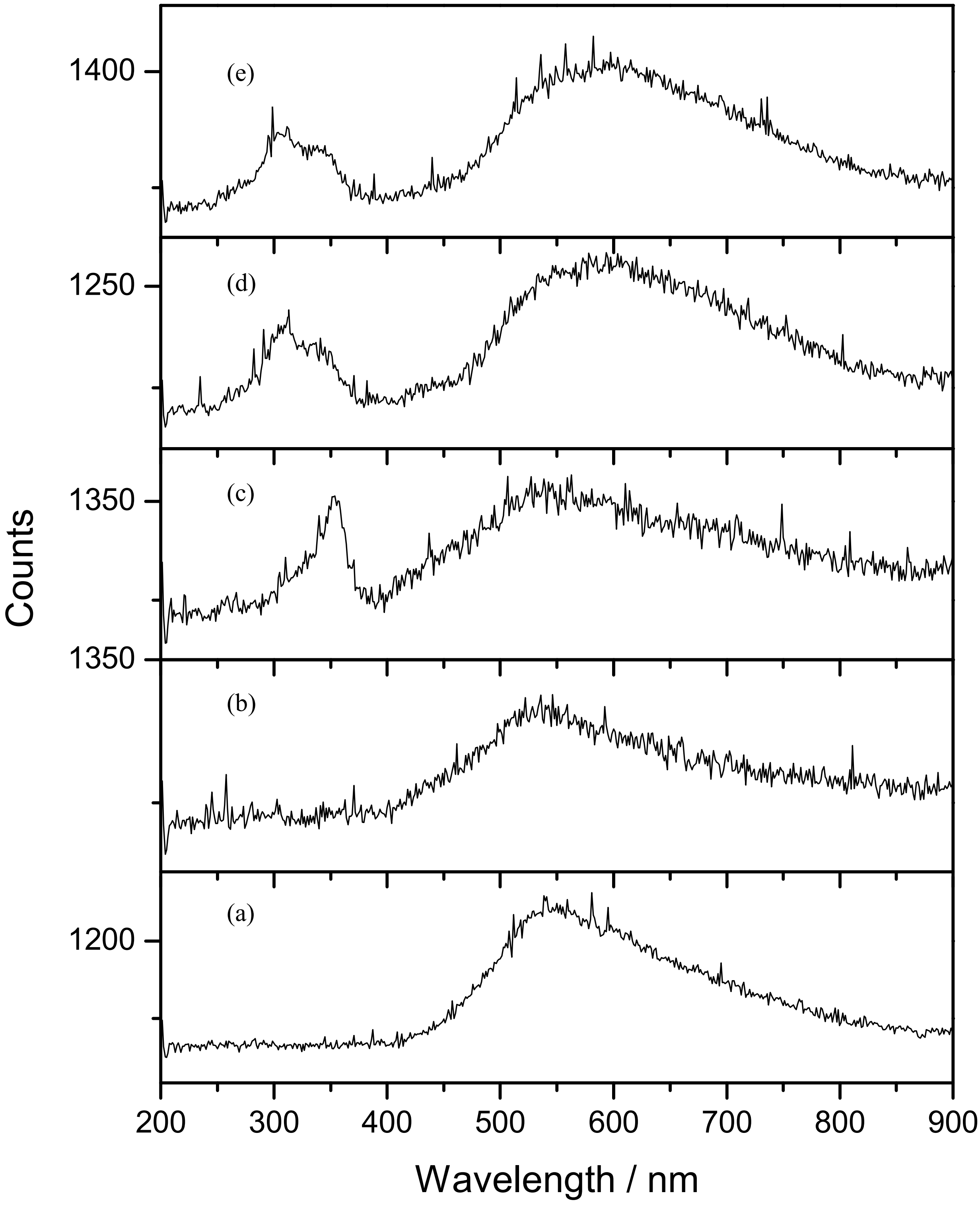

Figure 8.7: (a) Dispersed fluorescence spectra of BCl_3 taken with a photoexcitation energy of 9.17 eV (b) taken with a photoexcitation energy of 9.61 eV (c) taken with a photoexcitation energy of 9.94 eV (d) taken with a photoexcitation energy of 10.75 eV (e) taken with a photoexcitation energy of 10.96 eV All the spectra were taken using the UV turret and 100 grooves mm^{-1} grating. The slits on the secondary Triax monochromator were set at 1 mm.

Figure 8.8 show the dispersed fluorescence spectra of BCl_3 taken at photoexcitation energies of 15.49 and 17.70 eV using the UV turret in combination with the 100 grooves mm^{-1} grating on the Triax. The spectrum taken at 15.49 eV shows three bands with peaks at wavelengths of 278, 352 and 495 nm. The first band is the narrowest, and has been assigned to emission due to BCl A $^1\Pi - X\ ^1\Sigma^+$. The bands with peak wavelengths at 352 and 495 nm are due to emission emanating from the parent ion BCl_3^+. The first of these bands is probably due to emission from the electric-dipole-allowed $BCl_3^+\ \tilde{D}\ ^2E' - \tilde{X}\ ^2A_2'$ transition. This spectrum was taken at low resolution hence any discrete structure present is not detected. The second band at 495 nm also has its origins in the $BCl_3^+\ \tilde{D}\ ^2E'$ state. This time it results from a transition to the $\tilde{B}\ ^2E'$ state of BCl_3^+. At the photoexcitation energy of 17.70 eV, in comparison to the previous spectrum, we see a much weaker band at 278 nm followed by two further bands at 352 and 495 nm. At this energy the channel that leads to the fluorescence emanating from the BCl* radical becomes diminished while the parent ion bands do not lose any intensity.

Figure 8.9 shows a higher resolution spectrum taken at a photoexcitation energy of 17.70 eV using the UV turret and the 1200 grooves mm^{-1} grating on the Triax. The slit on the secondary Triax monochromator were set at 1 mm giving a resolution of 3.5 nm. This new band is not seen at 15.49 eV and shows a clearly resolved vibronic progression with a spacing of *ca.* 650 cm^{-1}. Previous work by Tuckett *et al.* also observed this emission [3]. In that study an action spectrum, where the secondary monochromator is set to a peak in the band while the primary monochromator is scanned, were performed from 12 to 25 eV. This kind of spectrum will give information on the threshold energy for a fluorescent band and here it was found to be 16.75 eV. Furthermore, the form of the excitation function was similar to that of a non-resonant, parent-ion production process. The emitter cannot be the parent ion of BCl_3 because no electronic state of BCl_3^+ is observed in the threshold [11] or He I photoelectron spectrum [1] of BCl_3 at this energy. On thermochemical grounds the most likely emitter is BCl_2^+. Threshold photoelectron coincidence techniques have established that the ground state of BCl_2^+ appears at $\leq$ 12.30 eV [11]. The emission band in figure 8.9 appears between *ca.* 280 and 350 nm (4.4 – 3.5 eV). The energetics would suggest that the emission is a result of an electronic transition from an excited state of BCl_2^+ with a threshold at 16.75 eV. This has been assigned in the previous work as emission resulting from the $BCl_2^+\ \tilde{A} - \tilde{X}$ transition [3,4]. The vibrational progression with spacing of 650 ± 30 cm^{-1} was assigned by Tuckett *et al*. [3] to the v_2 bending mode of the ground or excited state of BCl_2^+.

Experiments at photoexcitation energies ≥ 20 eV were performed but spectra showing atomic emission seen in previous work [3,4] from B* 2p – 2s were of poor quality.

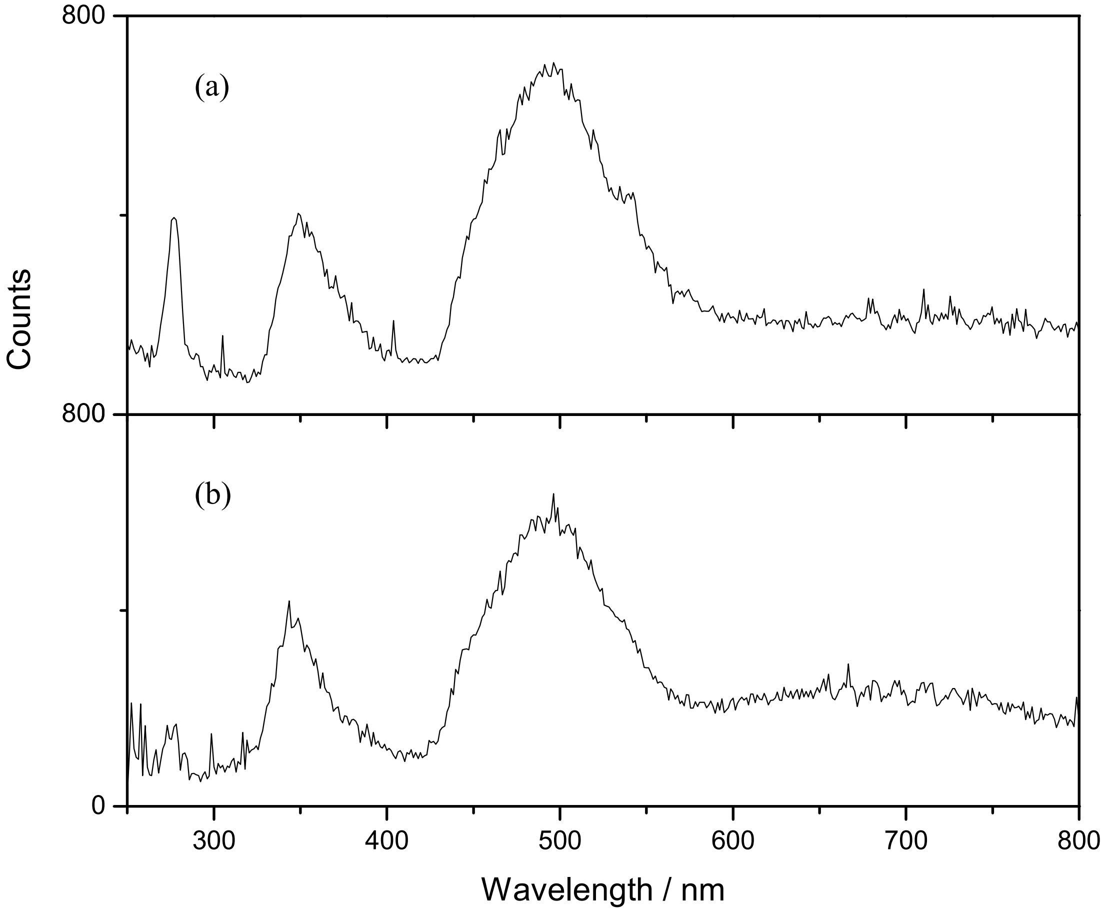

Figure 8.8: (a) Dispersed fluorescence spectra of BCl_3 taken with a photoexcitation energy of 15.49 eV (b) taken with a photoexcitation energy of 17.7 eV. Both spectra were taken using the UV turret and 100 grooves mm^{-1} grating. The slits on the secondary Triax monochromator were set at 1 mm.

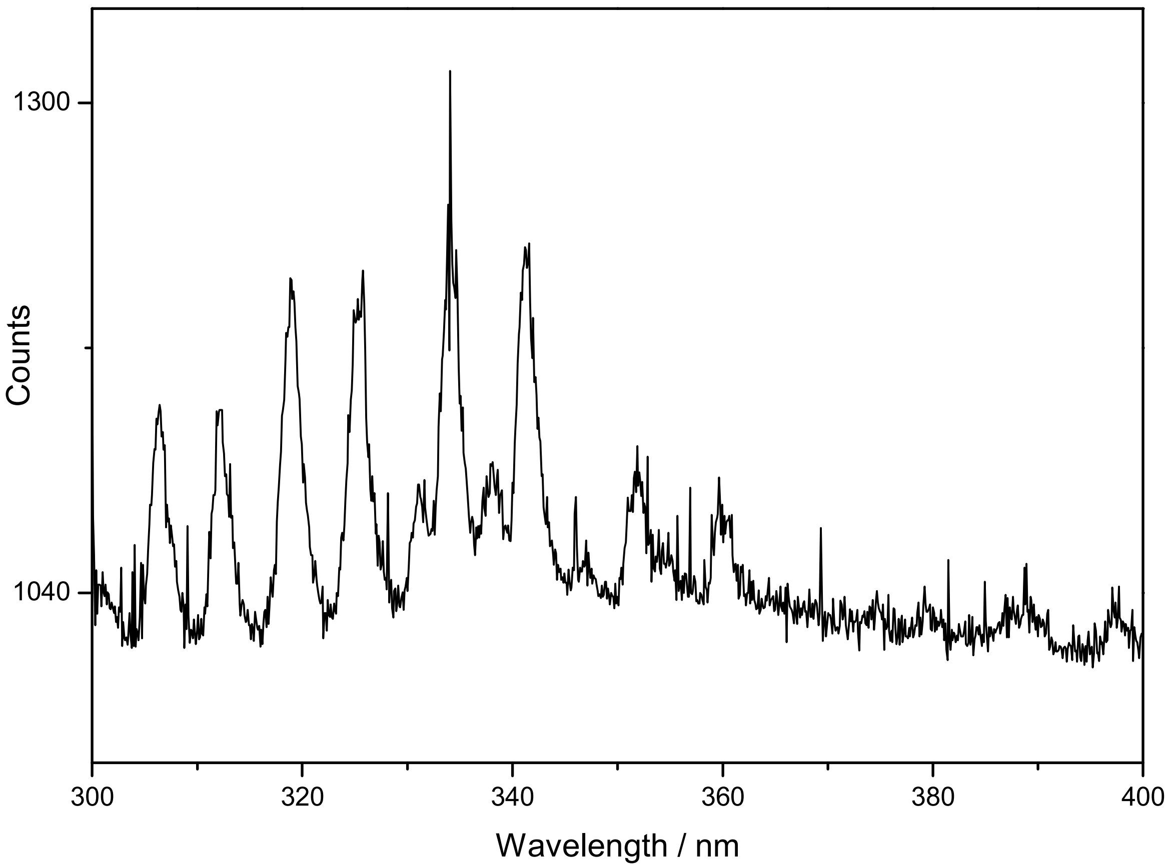

Figure 8.9: Dispersed fluorescence spectra of BCl_3 taken with a photoexcitation energy of 17.7 eV using the UV turret and 1200 grooves mm^{-1} gratings. The slits on the secondary Triax monochromator were set at 1mm.

8.2.3 BBr_3

The electronic configuration of BBr_3 is most likely ....$(2a_1')^2(2e')^4(1a_2'')^2(3e')^4(1e'')^4(1a_2')^2$ same as both the BF_3 and BCl_3 molecules. The numbering scheme here also does not include the core orbitals. The true assignment of the photoelectron spectrum and ordering of the molecular orbitals of BBr_3 is still uncertain [5]. The vertical ionisation energies for the five outermost occupied valence orbitals have been measured to be 10.65 ($1a_2'$), 11.36/11.71 ($1e''/3e'$), 13.18 ($1a_2''$), and 14.20 ($2e'$) using He(I) and He(II) photoelectron spectroscopy [1].

The flux-normalised fluorescence excitation spectrum of BBr_3 taken using the MEG at a resolution of 0.2 nm is shown in figure 8.10. The spectrum is very similar to earlier work [5] except for the relative intensities. Resonant peaks are seen between *ca.* 8.8 and 12 eV. By analogy with the BF_3 and BCl_3 spectra we would expect the emitter to be the BBr_2^* radical. The thermochemistry would suggest that the emitter could be either the BBr_2^* or BBr^* radical. Two non-resonant features with thresholds at 14.05 and 16.05 eV are observed at higher energies. The first onset at 14.05 eV is close to the adiabatic ionisation energy of the $\tilde{D}\ ^2E'$state of BBr_3^+ at 13.67 eV. Therefore the most likely origin for this emission is probably the $\tilde{D}\ ^2E'$state of BBr_3^+. The second threshold is close to the thermochemical threshold of the ^2S excited state of the B atom.

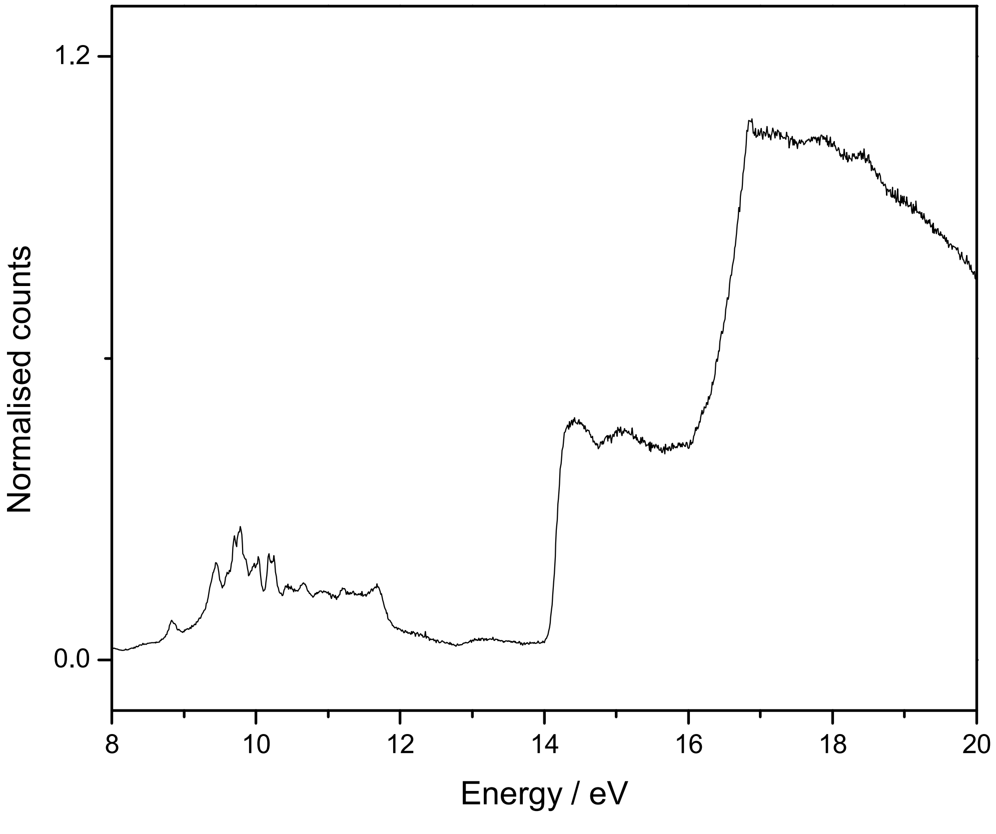

Figure 8.10: The undispersed fluorescence excitation spectrum of BBr_3, taken using the MEG at a resolution of 0.2 nm.

Neutral / Parent ion		Dissociation channel	Dissociation energy / eV	Vertical IE / eV
	$\tilde{E}\ ^2A_1'$			16.63
	$\tilde{D}\ ^2E'$			14.20
	$\tilde{C}\ ^2A_2''$			13.18
	$\tilde{B}\ ^2E'$			11.71
		B + 3Br	11.45	
		B + Br_2 + Br	9.13	
	$\tilde{A}\ ^2E''$			11.36
BBr_3^+	$\tilde{X}\ ^2A_2'$			10.65
		BBr + 2Br	6.86	
		BBr + Br_2	4.54	
		BBr_2 $\tilde{X}$ + Br	3.93	
BBr_3			0	

Table 8.4. The energetics and dissociation channels of BBr_3 neutral and parent ion. Symmetry of the states in the parent ion is in dispute [5].

The dispersed fluorescence spectra taken between 8.8 and 12 eV is shown in figure 8.11. All the spectra were taken using the UV turrent in combination with the 100 grooves mm^{-1} grating on the secondary Triax monochromator. These spectra have ***not*** been normalised to the sensitivity of the CCD/Triax system because of the weak nature of the signal. The spectra were dispersed at energies of 8.80, 9.44, 9.75, 10.18 and 10.60 eV. Figure 8.11 (a) and (b) present the dispersed fluorescence spectrum taken at 8.8 eV and 9.44 eV, both of which show a broad band between *ca.* 260 and 430 nm and a second band between *ca.* 470 and 800 nm. By analogy with the BF_3 and BCl_3 spectra, we assign these bands to emission emanating from excited states of BBr_2 to the ground state. The higher wavelength band between *ca.* 470 and 800 nm is probably due to the BBr_2 $\tilde{A}$ - $\tilde{X}$ transition.

The first band between *ca.* 260 and 430 nm is probably due to emission from one or both of the $\tilde{B}$ and $\tilde{C}$ states of BBr_2. Figure 8.11 (c) shows the dispersed spectrum taken at 9.75 eV. This spectrum shows the two bands seen in the previous spectra, as well as signs of a new band emerging at 540 nm. All these spectra were taken with the LiF window in place before the post-focusing mirror box. Therefore no second-order effects will be observed here. As we increase the photoexcitation energy to 10.18 and 10.60 eV this band becomes more and more dominant while the intensity of the other bands decrease. In the last spectrum figure 8.8

(e) the two other bands have almost disappeared and the new band dominates the spectrum. Assignment of this band is difficult as data on the electronic states of BBr_3 and its fragments are limited. We can say the emission is probably due to one of two fragments, either BBr_2^* or the BBr* radical. The only previous fluorescence work done on this molecule observed emission at 295 nm for photoexcitation energies between *ca.* 11.7 and 13.9 eV [5]. It was assigned to BBr A $^1\Pi - {}^1\Sigma^+$. Therefore emission from the BBr* radical can probably be discounted. It was suggested earlier that emission in the range 260 – 430 nm was due to BBr_2 $\tilde{B}$ - $\tilde{X}$ and $\tilde{C}$ - $\tilde{X}$. If we assign the peak wavengths of 300 and 350 nm to the origins of the $\tilde{C}$ - $\tilde{X}$ and $\tilde{B}$ - $\tilde{X}$ transitions, respectively, and the peak wavelength of 580 nm to the origin of $\tilde{A}$ - $\tilde{X}$ transition (figure 8.11 (c)), then the transition energy for the 3 peaks are 4.1, 3.5 and 2.1 eV. The new band at 540 nm or 2.3 eV in figure 8.11 (e) might possibly be assigned to BBr_2 $\tilde{C}$ - $\tilde{A}$. The previous dispersed fluorescence study performed at BESSY 1 [5] did not detect the band at 540 nm. The detection system used in that work had a rapid loss of sensitivity from *ca.* 400 nm while the present CCD/Triax system has good sensitivity to *ca.* 800 nm (chapter 2).

The dispersed fluorescence spectra taken at the higher photoexcitation energies of 13.2, 14.2 eV and 19.1 eV are shown in figure 8.12. At an energy of 13.2 eV we see a band with a peak at 300 nm followed by two further bands at higher wavelengths. This emission has been seen in the previous work [5] and has been assigned as BBr A – X emission. The two higher-wavelength bands are probably a result of second-order signal from the primary monochromator. At 14.2 eV we are above the thermochemical threshold for the BBr_3^+ $\tilde{D}$ state. Therefore the emission observed has been assigned as originating from that state. The first band between *ca.* 350 and 430 nm is assigned to the BBr_3^+ $\tilde{D}$ - $\tilde{X}$ transition. The band between *ca.* 430 and 610 nm is assigned to the BBr_3^+ $\tilde{D}$ - $\tilde{B}$ transition. Both of these transitions are electric dipole allowed in D_{3h} symmetry while the $\tilde{D}$ - $\tilde{A}$ transition is formally forbidden. The band to higher wavelengths could be due to BBr_3^+ $\tilde{C}$ - $\tilde{A}$. The spectrum taken at 19.1 eV shows all the bands present in the spectrum taken at 14.2 eV in addition to signal coming from atomic B.

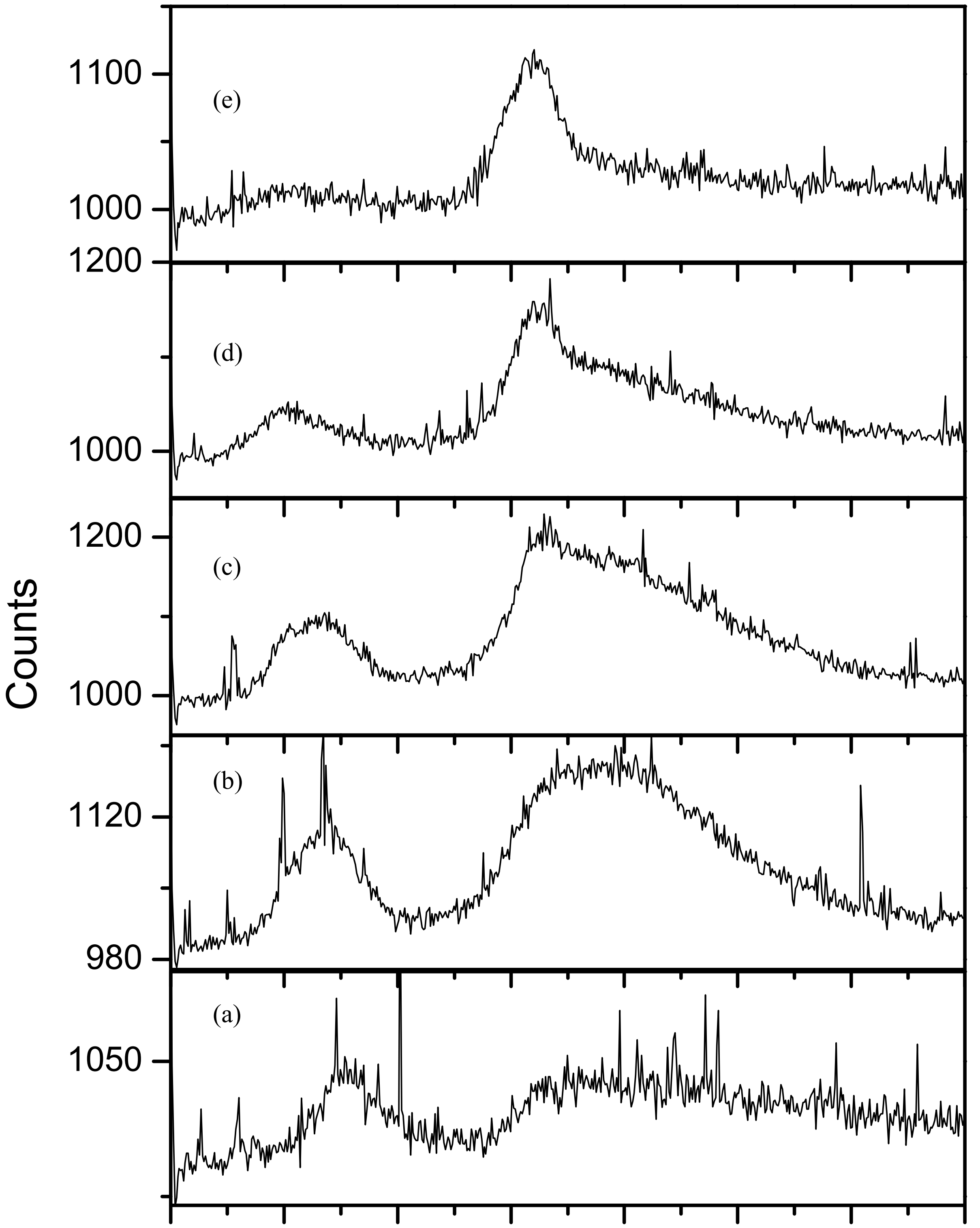

Figure 8.11: (a) Dispersed fluorescence spectra of BBr_3 taken with a photoexcitation energy of 8.8 eV (b) taken with a photoexcitation energy of 9.44 eV (c) taken with a photoexcitation energy of 9.75 eV (d) taken with a photoexcitation energy of 10.18 eV (e) taken with a photoexcitation energy of 10.60 eV All the spectra were taken using the UV turret and 100 grooves mm^{-1} grating. The slits on the secondary Triax monochromator were set at 1 mm. All the spectra were taken with the LiF window in place before the post-focusing mirror box.

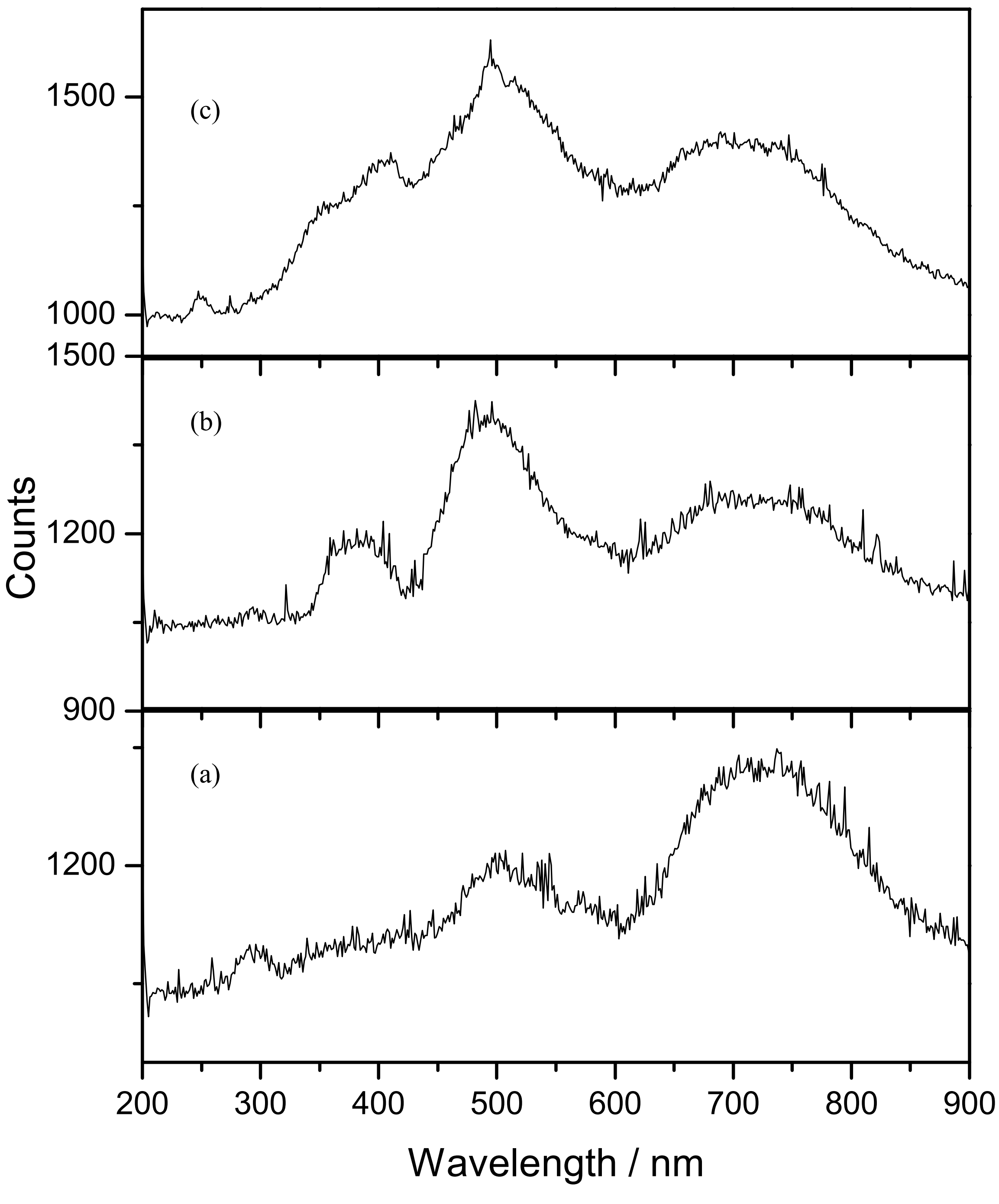

Figure 8.12: (a) Dispersed fluorescence spectra of BBr_3 taken with a photoexcitation energy of 13.20 eV (b) taken with a photoexcitation energy of 14.20 eV. (c) taken with a photoexcitation energy of 19.10 eV Both spectra were taken using the UV turret and 100 grooves mm^{-1} grating. The slits on the secondary Triax monochromator were set at 1 mm.

8.3 Conclusions

The VUV fluorescence spectroscopy of BX_3(X = F, Cl, Br) have been presented. In BF_3 the observed emissions have been assigned to fluorescence emanating from BF_2 and BF_3^+. Fluorescence spectra of BCl_3 showed emission emanating from BCl_2, BCl, BCl_3^+ and BCl_2^+. New emission bands were seen in the BCl_3 spectra assigned to both BCl_2 and parent ion BCl_3^+. We observed BBr_3 emission emanating from excited states of BBr_2, BBr and BBr_3^+. New emission bands have been assigned to excitated states of BBr_2 and parent ion BBr_3^+.

8.4 References

[1] P.J. Bassett and D.R. Loyd, J. *Chem. Soc*. A, (1971) 1551

[2] J.C. Creasey, P.A. Hatherly, H.M. Jones, I.R. Lambert, and R. P. Tuckett, *Molec. Phys.,***78** (1993) 837.

[3] J.C. Creasey, P.A. Hatherly, H.M. Jones, I.R. Lambert, and R. P. Tuckett, *Molec. Phys*,**79** (1993) 413.

[4] K J Boyle, D P Seccombe, R P Tuckett, H Baumgartel and H W Jochims, *J. Phys. B: At. Mol. Opt. Phys*. **32** (1999) 2569

[5] H. Biehl., J.C. Creasey, D. M. Smith, R. P. Tuckett, K. R. Yoxall, H. Baumgartel, H. W. Jochims, and U. Rokland,, *Molec. Phys*, **87** (1996)1199

[6] C.E. Theodosiou, M. Inokuti and S.T. Mason, *Atomic Data and Nuclear Data Tables,* **35** (1996) 473

[7] O. Warschkow, E. P. F Lee and T. G. Wright, *J. Chem. Soc. Faraday Trans*, **93** (1997) 53

[8] D. B. Atkinson, K. K. Irikura and J. W. Hudgens, *J. Phys. Chem. A,* **101** (1997) 2045

[9] M. Peric and S. D. Peyerimhoff *Molec. Phys*. **78** (1993a) 855

[10] M. Peric and S. D. Peyerimhoff *Molec. Phys.* **79** (1993a) 877

[11] H. Biehl., J.C. Creasey, D. M. Smith, R. P. Tuckett, K. R. Yoxall, H. Baumgartel, H. W. Jochims, and U. Rokland, *J. Chem. Soc. Faraday Trans*, **91** (1995) 3073.

[12] M. Suto, J. C. Han, and L. C. Lee, *J. Chem. Phys*., **89** (1988) 6653.

[13] L. C. Lee, J. C. Han, and M. Suto, *J. Chem. Phys*., **91** (1989) 2036.

[14] G. H King, S. S. Krishnamurthy, M. F. Lappert, and J. Pedley, *Discuss. Faraday Soc*., **54** (1993) 70

9. VUV fluorescence spectroscopy of PF_3 and PCl_3

9.1 Introduction

In this chapter we present the VUV fluorescence spectra of the molecules PF_3 and PCl_3. Spectra were recorded for PBr_3 but the quality of the spectra were poor. There was no time available to repeat the experiments, therefore none of the fluorescence spectra for this molecule is presented here. The spectra were taken using beamline 3.1 at the Daresbury SRS. The VUV fluorescence spectra of both the PF_3 and PCl_3 have been recorded before by Tuckett *at al.* using synchrotron radiation both at the Daresbury SRS and BESSY 1 in Berlin [1,2]. The increased sensitivity of our current dispersed fluorescence apparatus and the commissioning of the new Wadsworth monochromator with its higher flux output at Daresbury encouraged a repeat of these experiments. Other work done on these molecules include absorption spectroscopy in the VUV range [3-7], as well as several studies on the electronic emission spectroscopy of fragments [8-10]. Several *ab initio* studies have also been carried out on the positions and geometries of the excited states of PF_2, PF, PCl_2 and PCl [11-14]. Photoionisation studies have been performed by several groups [15-24] using techniques including photoelectron and coincidence spectroscopy. As a general statement, the electronic spectroscopy pf PF_2 and PCl_2 is not well understood, whereas that of PF and PCl is more mature. This chapter describes work that probes highly excited electronic states of these molecules by use of VUV fluorescence spectroscopy. Emissions from products of these excited electronic states provide information which is fundamental to understanding their chemical dynamics.

9.2 Results

9.2.1 PF_3

The electronic configuration of the outer-valence molecular orbitals of PF_3 in C_{3v} symmetry is …..$(2a_1)^2(2e)^4(3a_1)^2(3e)^4(4e)^4(la_2)^2(4a_1)^2$. The numbering scheme does not include the core orbitals. The vertical ionisation energies for the five outermost occupied valence orbitals have been measured to be 12.27 ($4a_1$), 15.89 ($1a_2$), 16.44 (4e), 17.47 (3e), and 18.60 ($3a_1$) eV [17]. The flux-normalised fluorescence excitation spectrum of PF_3 taken using the high-energy grating at a resolution of 0.1 nm on the primary monochromator is shown in figure 9.1. The spectrum can be divided into two regions, a low energy region from 9 – 13 eV, and a high energy region from 14 – 20 eV. If we compare the fluorescence excitation spectrum presented in this chapter to the one taken by Tuckett *et al.* [1], we see very good agreement between the peak energies but the relative intensities of the normalised spectra are significantly different. The low-energy region in the earlier work had greater intensity than the high-energy region, whereas now the high-energy region shows the greater intensity. We see similar trends in almost all of the fluorescence excitation spectra taken for this thesis. During many of the experiments carried out at the Daresbury SRS, both the MEG and HEG were used to record a particular energy range of the fluorescence excitation spectra for a particular molecule. Flux-normalisation of these spectra were carried out using flux curves shown in chapter 2. We find that the relative intensities of the two spectra, in almost all cases, are very similar. This suggests that our method of flux-normalisation used on this thesis with the new apparatus (chapter 2) is correct. The differences from the spectra recorded *ca.* 10 years ago are probably a result of a different method of flux normalisation on the earlier apparatus. In the earlier work flux curves were taken at the same time as the fluorescence excitation experiment. In the present work this is done in the absence of any gas.

Figure 9.2 shows an expanded version of the low energy region between 9 – 13 eV. This region exhibits resolved vibrational structure which have been shown by the use of filter experiments by Tuckett *et al.* [1] to give rise to visible radiation at $\lambda > 400$ nm. Three different vibrational progressions are evident, their line positions and spacing have been recorded and are presented in table 9.1. The three bands centred at 9.75, 11.05 and 11.55 eV have been found to give rise to fluorescence over slightly different wavelengths in the visible region [1]. Thermochemistry tells us that there are two excited states of PF_2 that could be responsible for this emission (table 9.2). The first two bands have also been seen at vibrational resolution in absorption spectroscopy by Humphries *et al.* [5]. These bands have been assigned previously to the $(4a_1)^{-1}$ 4p, $(4a_1)^{-1}$ 5p and $(4a_1)^{-1}$ 6p Rydberg states of PF_3 [ref]. The $4a_1$ highest-occupied molecular orbital is essentially a lone-pair orbital located on the phosphorus atom [17] and therefore quantum defect values obtained should reflect those for an isolated P atom. The average vibrational spacing for the three bands are 447, 461 and 464 cm^{-1}, respectively. This is in good agreement with the previous study where a constant vibrational spacing of 458 cm^{-1} was obtained [1]. Using the intensity distribution of the vibrational structure Tuckett *et al.* [25] estimated the change in FPF bond angle between the ground state and Rydberg states of PF_3. As the Rydberg states are converging on the PF_3^+ $\tilde{X}$ $^2A_1$ state, it was assumed that both states have the same geometry, and so an estimation of the change in bond angle was made upon ionisation of PF_3 to PF_3^+, 14 ± 1°. Since the ground state of PF_3 has a bond angle of 98°, the bond angle of the ion is 112°, the ion retains C_{3v} symmetry and therefore is not planar. The higher-energy region between 14 and 20 eV show four resonant bands with peak energies of 14.28, 16.10, 17.16 and 19.40 eV. These bands have been shown by Tuckett *et al.* to give rise to emission predominantly in the UV region at $\lambda < 400$ nm. At these higher photoexcitation energies the observed emission according to the thermochemistry could be due to different electronic states of PF_2 or PF. Atomic emission from either the F* or P* fragment could also be occurring. Parent ion PF_3^+ emission is unlikely to be occurring due to the resonant nature of the bands observed in figure 9.1.

The dispersed fluorescence spectra of PF_3 taken with photoexcitation energies of 9.75 and 11.10 eV are shown in figure 9.3. The spectra were taken using the UV turret and 100 grooves mm^{-1} grating on the secondary Triax monochromator. The spectrum taken at 9.75 eV shows a broad band between *ca.* 350 and 750 nm and has a peak at *ca.* 530 nm. This band was assigned in the previous work to emission from PF_2 $\tilde{A}\ ^2A_1$ - $\tilde{X}\ ^2B_1$ [1]. In that work they also observed a further band between 300 and 360 nm. This band, due to PF A $^3\Pi$ – X $^3\Sigma^-$, was assigned as weak second-order emission coming from the primary monochromator at 19.60 eV. The spectra shown in figure 9.3 were both taken with the lithium fluoride in place before the post-focusing mirror box so any higher-order radiation would not reach the interaction region. The absence of this peak in the presence of the lithium fluoride window is strong confirmation that this emission band is indeed due to second-order radiation from the primary monochromator.

Figure 9.3 (b) shows the spectrum taken at a photoexcitation energy of 11.10 eV. Two bands are seen in this spectrum, the first is a broad band spanning *ca.* 350 - 700 nm, with a peak at *ca.* 400 nm. The second is a much narrower band between *ca.* 270 - 330 nm with a peak at 310 nm. Both of these bands are probably due to emission emanating from the PF_2 radical. The band with a peak wavelength of *ca.* 400 nm is assigned to PF_2 $\tilde{A}\ ^2A_1$ - $\tilde{X}\ ^2B_1$. If we compare this to the previous spectrum the peak of this band has shifted to lower wavelength. This shift may be due to two factors. First, the excited state of PF_2 is probably produced vibrationally hot as we have more excess energy available to populate higher vibrational levels. Second, when the spectrum is normalised to the sensitivity of the CCD/Triax system (figure 2.6) we see a shift in the peak to lower wavelengths for the higher-energy spectrum; if the un-normalised spectra are compared directly, the two peaks appear at 540 and 530 nm for the spectra taken at 9.75 and 11.10 nm, respectively.

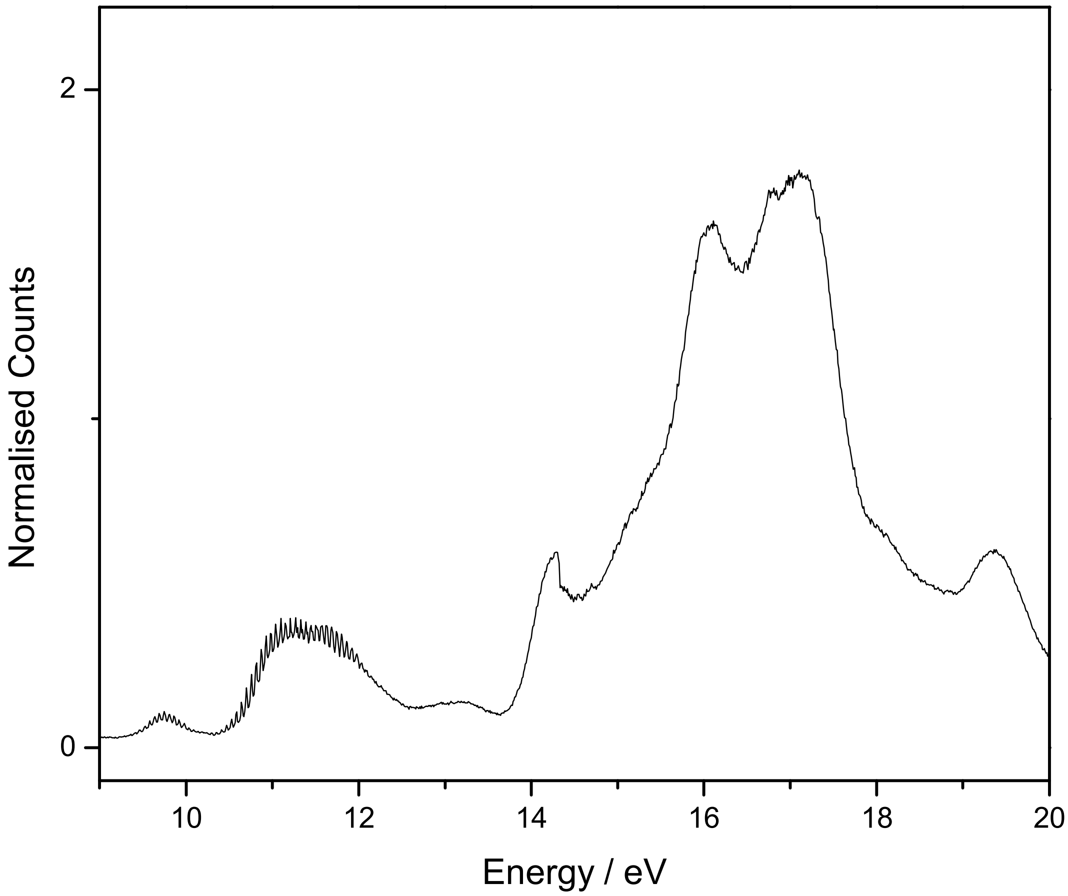

Figure 9.1: The undispersed fluorescence excitation spectrum of PF_3, taken using the HEG at a resolution of 0.1 nm. No filter, so PMT detects 190 – 800 nm.

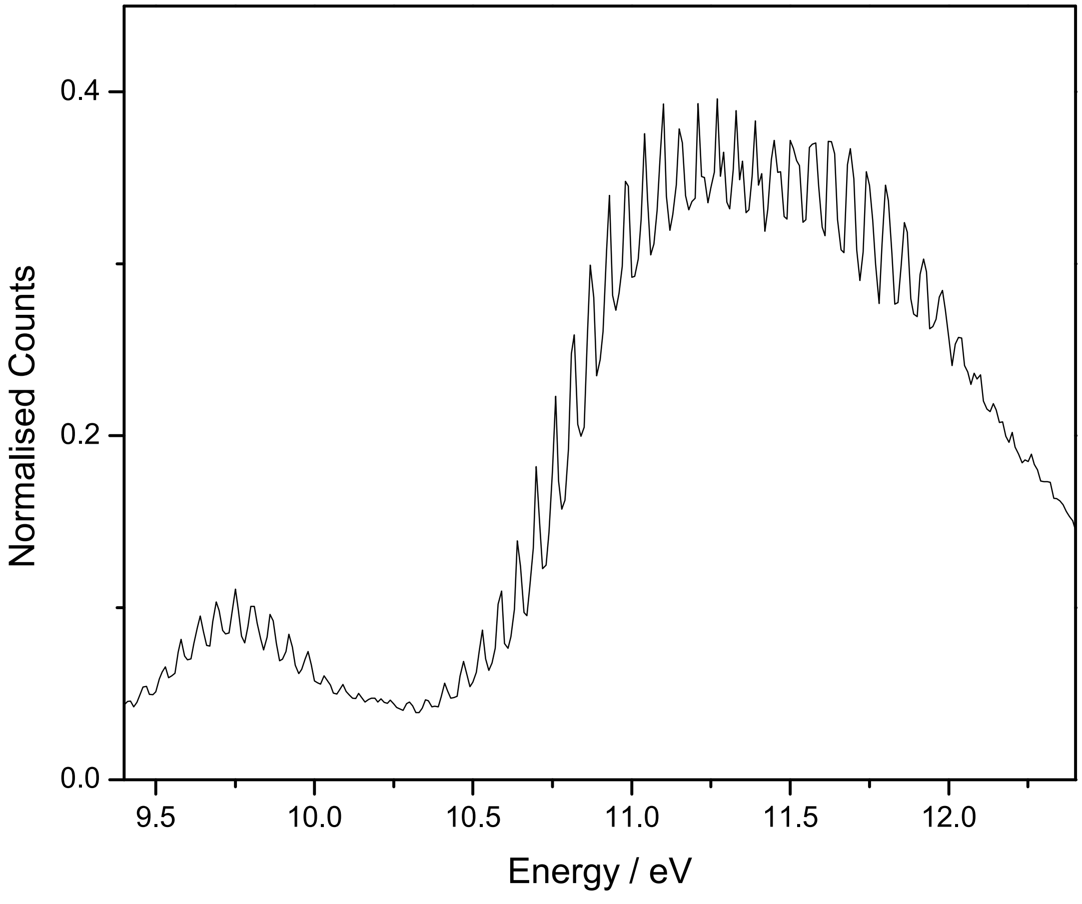

Figure 9.2: The undispersed fluorescence excitation spectrum of PF_3 expanded between 9.4 and 13.4 eV showing vibrational resolution.

1st progression / eV	/ cm^{-1}	Δv	2nd progression / eV	/ cm^{-1}	Δv	3rd progression / eV	/ cm^{-1}	Δv
9.42	75977		10.41	83962		11.29	91060	
		403			484			484
9.47	76381		10.47	84446		11.35	91544	
		484			484			484
9.53	76865		10.53	84930		11.41	92028	
		403			484			484
9.58	77268		10.59	85414		11.47	92512	
		484			403			484
9.64	77752		10.64	85817		11.53	92996	
		403			484			403
9.69	78155		10.70	86301		11.58	93399	
		484			484			484
9.75	78639		10.76	86785		11.64	93883	
		403			484			403
9.80	79042		10.82	87269		11.69	94286	
		484			403			403
9.86	79526		10.87	87672		11.74	94689	
		484			484			484
9.92	80010		10.93	88156		11.80	95173	
		484			403			484
9.98	80494		10.98	88560		11.86	95657	
		403			484			484
10.03	80897		11.04	89044		11.92	96141	
		484			484			484
10.09	81381		11.10	89527		11.98	96625	
		403			403			
10.14	81785		11.15	89931				
					484			
			11.21	90415				

Table 9.1: Vibrational progressions in PF_3.

Neutral / Parent ion	Dissociation channel	Dissociation energy / eV	Vertical IE / eV
$\tilde{E}\ ^2E$			19.50
$\tilde{D}\ ^2A_1$			18.60
$\tilde{C}\ ^2E$			17.46
$\tilde{B}\ ^2E$			16.30
$\tilde{A}\ ^2A_2$			15.88
PF_3^+ $\tilde{X}\ ^2A_1$			12.25
	PF A $^3\Pi$ + 2F	14.68	
	PF X $^3\Sigma^-$ + 2F	11.00	
	PF A $^3\Pi$ + F_2	13.03	
	PF X $^3\Sigma^-$ + F_2	9.35	
	PF_2 $\tilde{G}\ ^2A_2$ + F	13.33	
	PF_2 $\tilde{F}\ ^2A_2$+ F	13.11	
	PF_2 $\tilde{E}\ ^2B_1$+ F	11.95	
	PF_2 $\tilde{D}\ ^2B_2$+ F	11.85	
	PF_2 $\tilde{C}\ ^2A_1$ + F	11.07	
	PF_2 $\tilde{B}\ ^2B_2$+ F	8.81	
	PF_2 $\tilde{A}\ ^2A_1$+ F	7.94	
	PF_2 $\tilde{X}\ ^2B_1$+ F	5.65	
PF_3		0	

Table 9.2. The energetics and dissociation channels of PF_3 neutral and parent ion. Values used in this table are taken from reference [1,17, 26]

According to the thermochemistry the only new electronic states of PF_2 that could be responsible for this emission at 310 nm are the bent $\tilde{B}\ ^2B_2$ or the linear $\tilde{a}\ ^4B_1$ states. The PF_2 $\tilde{a}\ ^4B_1$ - $\tilde{X}\ ^2B_1$ transition is both spin-forbidden and has a large change in FPF bond angle. The $\tilde{B}\ ^2B_2$ - $\tilde{X}\ ^2B_1$ transition is electric dipole forbidden but has a much smaller change in FPF bond angle [1, 25]. The lifetime of this emitting state is relatively long ($\tau > \sim$ 500 ns) [1]. This band is therefore assigned to the forbidden PF_2 $\tilde{B}\ ^2B_2$ - $\tilde{X}\ ^2B_1$ transition.

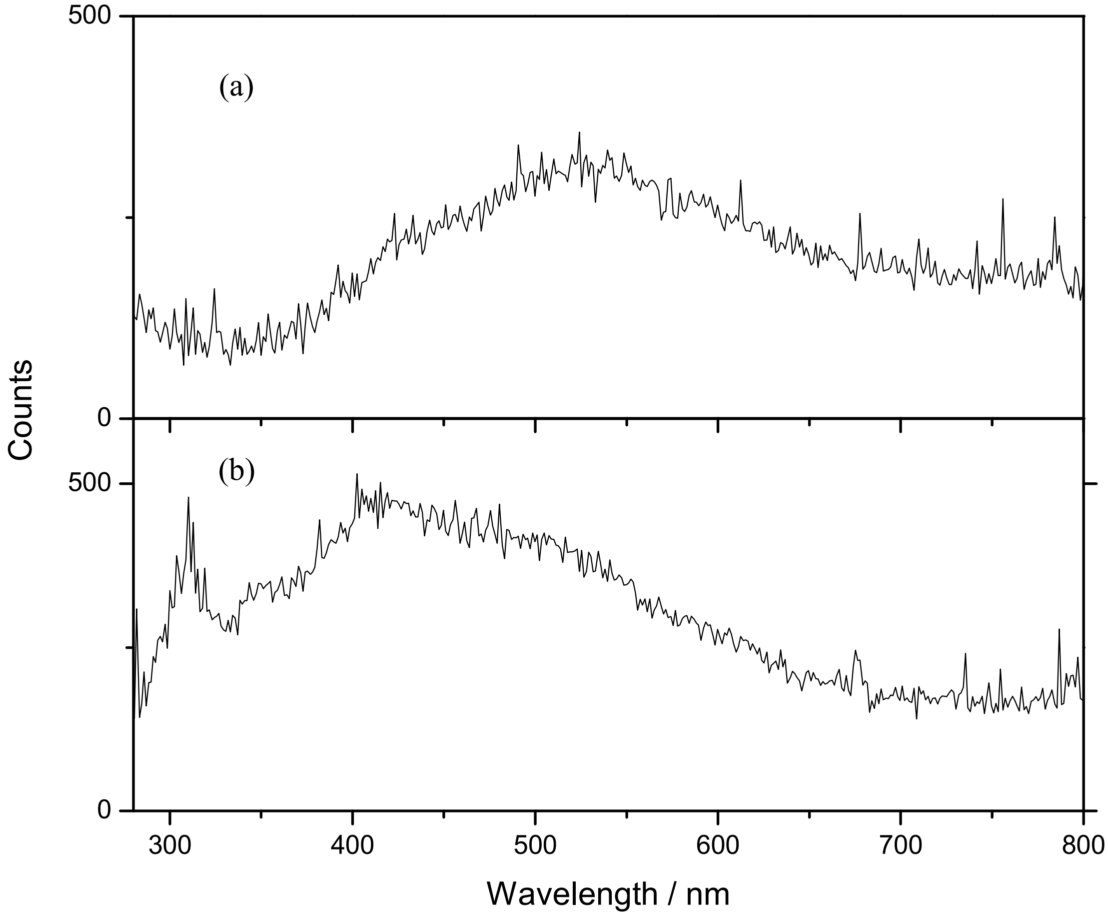

Figure 9.3: (a) Dispersed fluorescence spectra of PF_3 taken with a photoexcitation energy of 9.75 eV (b) taken with a photoexcitation energy of 11.1 eV. Both spectra were taken using the UV turret and 100 grooves mm^{-1} grating. The slits on the secondary Triax monochromator were set at 1 mm.

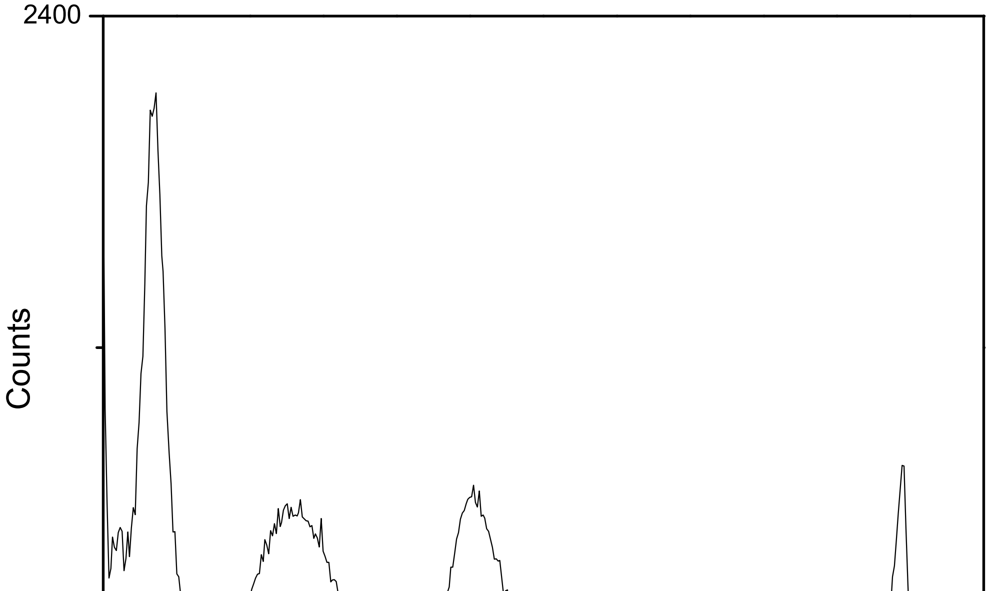

Figure 9.4: Dispersed fluorescence spectra of PF_3 taken with a photoexcitation energy of 14.40 eV using the UV turret and 100 grooves mm^{-1} gratings. The slits on the secondary Triax monochromator were set at 1mm. no LiF window, so could also be 2 x 14.4 eV.

The dispersed fluorescence spectrum of PF_3 taken at a photoexcitation energy of 14.40 eV using the UV turret and 100 grooves mm^{-1} grating on the secondary monochromator is shown in figure 9.4. Four bands are seen with peak wavelengths of 235, 328, 452 and 744 nm. The first band at 235 nm is narrow and by far the most intense of the four bands. The second band at 328 nm is broader and less intense. At a photoexcitation energy of 14.40 eV the $\tilde{C}\ ^2A_1$ to $\tilde{G}\ ^2A_2$ states of doublet symmetry are energetically open, and these two bands have been assigned to the $\tilde{C}\ ^2A_1$ - $\tilde{X}\ ^2B_1$ and $\tilde{E}\ ^2B_1$ - $\tilde{A}\ ^2A_1$ transitions. It is noted that both these transitions are dipole allowed under formal selection rules. In the previous study the band at 452 nm was assigned to second-order signal from the PF_2 $\tilde{C}\ ^2A_1$ - $\tilde{X}\ ^2B_1$ band at 235 nm [1]. In that study this band was observed very weakly with a peak at *ca.* 444 nm. The sensitivity of the secondary monochromator used dropped rapidly for wavelengths greater than 400 nm (chapter 4). It is believed that this assignment is probably correct. However, we cannot discount the possibility that the emission could be due to PF_2 $\tilde{D}\ ^2B_2$ - $\tilde{B}\ ^2B_2$ (calculated at 3.04 eV or 408 nm) which is an allowed transition under the C_{2v} selection rules.

The final peak in this spectrum is at 744 nm. It is the narrowest of the bands and probably is a result of atomic emission. At a photoexcitation energy of 14.40 eV it is not possible energetically to produce F* emission. Data from atomic emission tables [26] predict a possible F emission band emanating from the $2s^22p^43p^1\ ^4P_{3/2}$ state to appear at 739.8 nm. The energy required to dissociate PF_3 and produce PF_2 and F in their ground states is 5.65 eV (table 9.2). The F $2s^22p^43p^1\ ^4P_{3/2}$ state is at 116042 cm^{-1} or 14.39 eV above the ground state. To produce PF_2 + F* would require radiation with an energy of 20.04 eV. Therefore, energetically it should not be possible for atomic emission from fluorine to be occurring here. However, experience using beamline 3.1 at Daresbury tells us that when the LiF window is not in place, particularly at the lower-energy range of both gratings, we see second-order signal from the primary monochromator. Here, we believe the band at 744 nm is a result of second-order radiation coming from the primary monochromator at 28.8 eV. This band is therefore assigned as second-order F $2s^22p^43p^1\ ^4P_{3/2} \rightarrow 2s^22p^43s^1\ ^4P_{3/2}$ emission. This assignment is allowed under atomic selection rules. Figure 9.5 shows the dispersed fluorescence spectra taken at a photoexcitation energy of 16.10 eV. The spectrum shows a band with a peak at *ca.* 330 nm. This peak has been seen previously and has been assigned to the PF A $^3\Pi$ – X $^3\Sigma^-$ transition. Dispersed were also taken at peak energies of 17.16 and 19.40 eV, both show this same PF band at 330 nm.

In this section we have confirmed all of the assignment from the 1998 study [1] and with a comparable signal/noise ratio. We have also observed a new F* peak in second-order.

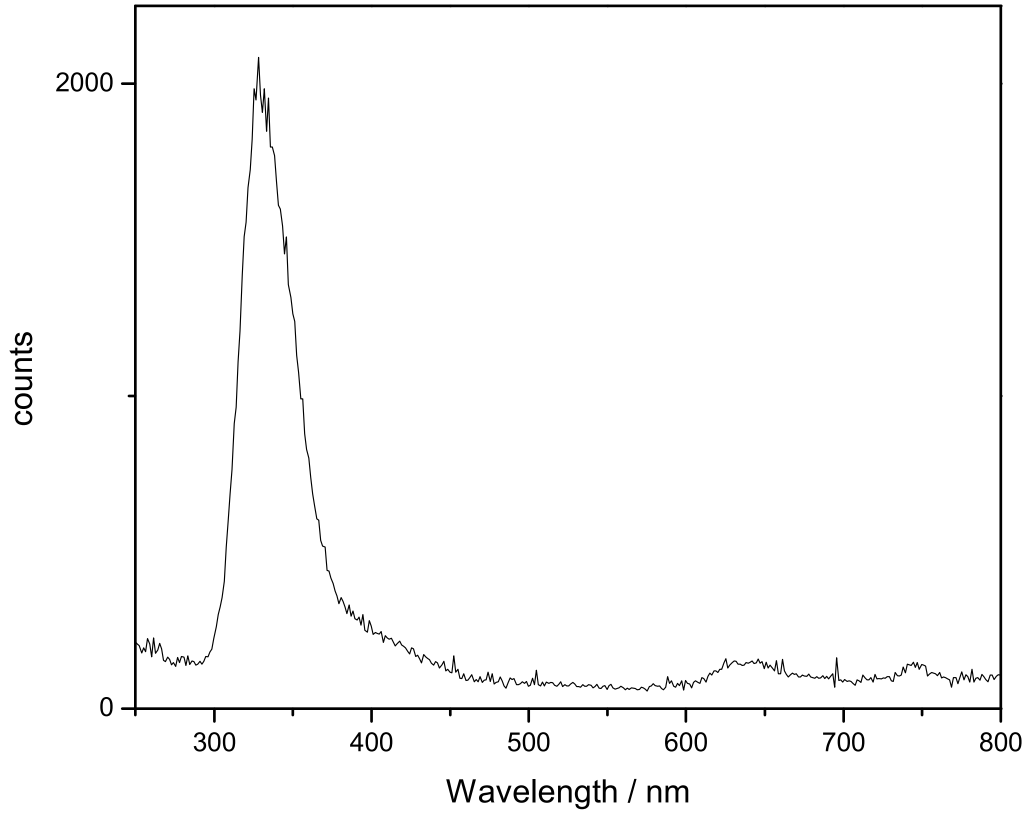

Figure 9.5: (a) Dispersed fluorescence spectra of PF_3 taken with a photoexcitation energy of 16.10 eV. The slits on the secondary Triax monochromator were set at 1 mm.

9.2.2 PCl_3

The electronic configuration of the outer-valence molecular orbitals of PCl_3 in C_{3v} symmetry is also…..$(2a_1)^2(2e)^4(3a_1)^2(3e)^4(4e)^4(1a_2)^2(4a_1)^2$. The numbering scheme does not include the core orbitals. The vertical ionisation energies for the six outermost occupied valence orbitals have been measured to be 10.52 ($4a_1$), 11.69 ($1a_2$), 11.97 (4e), 12.94 (3e), 14.23 ($3a_1$) and 15.19 (2e) eV [23]. The flux-normalised fluorescence excitation spectrum of PCl_3 taken using the medium energy grating at a resolution of 0.2 nm on the primary monochromator is shown in figure 9.6. We can divide the spectrum into two regions, a low energy region from 9 – 13 eV, and a high energy region from 14 – 18 eV. In the low energy region two bands with resonant peaks at 10.40 and 11.30 eV are observed. These peaks have the shape characteristic of a resonant dissociative process where the initially populated Rydberg states of the neutral molecule dissociate to a fluorescing fragment. Thermochemistry tells us that emission could be due to either the PCl* or PCl_2* fragment. By analogy with the PF_3 spectrum we would expect the emission to be solely from the excited states of PCl_2.

In the high-energy region we see bands with peaks at 15.10 and 17.32 eV. The shape of the higher energy band is characteristic of a non-resonant photoionisation process and probably a result of emission from the PCl_3^+ $\widetilde{E}$ ^{2}E state which has a adiabatic ionisation energy of 14.6 eV [23]. We also see an overlapping resonant band whose threshold is unknown. If we compare this spectrum to earlier work [2], we can see again that the peak energies of the bands are the same while the relative intensities differ. Note however on this occasion we se greater intensity in the low-energy range.

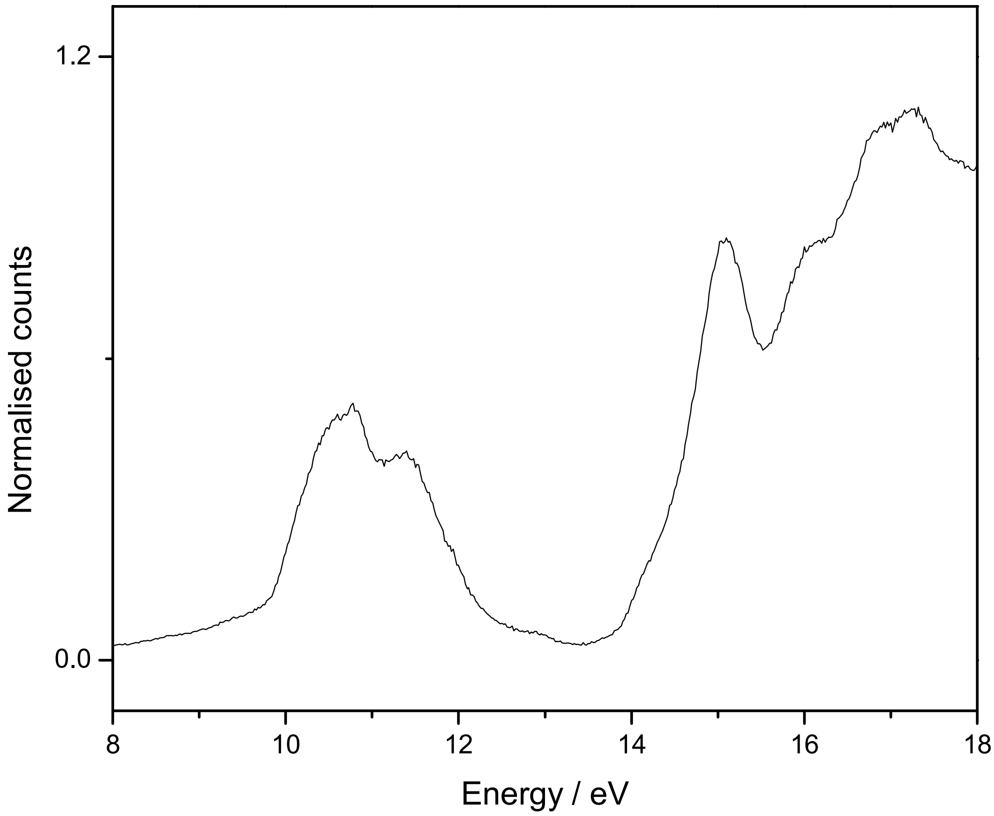

Figure 9.6: The undispersed fluorescence excitation spectrum of PCl_3, taken using the MEG at a resolution of 0.2 nm. No filter, so PMT detects 190-800 nm.

Neutral / Parent ion		Dissociation channel	Dissociation energy / eV	Vertical IE / eV
	$\tilde{E}$ ^{2}E			15.19
	$\tilde{D}$ $^2A_1$			14.23
	$\tilde{C}$ ^{2}E			12.94
	$\tilde{B}$ ^{2}E			11.97
	$\tilde{A}$ $^2A_2$			11.69
PCl_3^+	$\tilde{X}$ $^2A_1$			10.52
		PCl A $^3\Pi$ + 2Cl	10.02	
		PCl X $^3\Sigma^-$ + 2Cl	6.79	
		PCl A $^3\Pi$ + Cl_2	7.54	
		PCl X $^3\Sigma^-$ + Cl_2	4.31	
		PCl_2 $\tilde{B}$ $^2B_2$+ Cl	6.40	
		PCl_2 $\tilde{A}$ $^2A_1$+ Cl	5.40	
		PCl_2 $\tilde{X}$ $^2B_1$+ Cl	3.31	
PCl_3			0	

Table 9.3. The energetics and dissociation channels of PCl_3 neutral and parent ion. Values used taken from reference [2, 24, 26]

The dispersed fluorescence spectrum of PCl_3 taken with a photoexcitation energies of 10.40 eV is shown in figure 9.7. The spectra were taken using the UV turret and 100 grooves mm^{-1} grating on the secondary Triax monochromator. The spectrum shows two bands with peak wavelengths of *ca.* 440 and 550 nm. From the data shown in table 9.3 the band origins of the PCl_2 $\tilde{A}$ $^2A_1$ - $\tilde{X}$ $^2B_1$ and $\tilde{B}$ $^2B_2$ - $\tilde{X}$ $^2B_1$ transitions are predicted to be at 593 and 401 nm. We assign the band with a peak at 550 nm to the PCl_2 $\tilde{A}$ $^2A_1$ - $\tilde{X}$ $^2B_1$ transition. The band with a peak at 440 nm is assigned to the dipole-forbidden PCl_2 $\tilde{B}$ $^2B_2$ - $\tilde{X}$ $^2B_1$ transition. In the previous work Tuckett *et al* [2] only observed the one band with a peak at 420 nm. This band was assigned to the dipole-forbidden PCl_2 $\tilde{B}$ $^2B_2$ - $\tilde{X}$ $^2B_1$ transition due to the relatively long lifetime observed. The extra sensitivity of our detection at this region enables us to detect the emission from both of these states.

The dispersed fluorescence spectra of PCl_3 taken with photoexcitation energies of 15.10 and 17.28 eV are shown in figure 9.8. The spectra were taken using the UV turret and 100 grooves mm^{-1} grating on the secondary Triax monochromator. The spectrum taken at 15.10 eV shows six bands with peak wavelengths at *ca.* 241, 254, 306, 348, 382 and 427 nm. At the photoexcitation energy of 15.10 eV we probably have the two bands (15.10 and 17.32 eV) overlapping. Therefore, dispersed emission spectra from both these bands is probably being observed. Using table 9.3 the calculated wavelengths for emission emanating from the PCl_3^+ $\tilde{E}$ ^2E state to the $\tilde{C}$ ^2E, $\tilde{B}$ ^2E, $\tilde{A}$ $^2A_2$ and $\tilde{X}$ $^2A_1$ states are 550, 385, 355 and 265 nm. All these transition are dipole allowed under formal selection rules. We can assign three of the six bands in figure 9.8 (a) to the latter three transitions above. The two bands seen at 385 and 355 nm are a result of transitions to the $\tilde{B}$ ^2E, and $\tilde{A}$ $^2A_2$ states. The lowest wavelength peak at 241 nm is probably due to PCl_3^+ $\tilde{E}$ ^2E - $\tilde{X}$ $^2A_1$ emission. Tuckett *et al.* [2] observed a band at 258 nm which was assigned to Cl_2 D' 2 $^3\Pi_g$ – A' 2 $^3\Pi_u$. The band we see at 254 nm is assigned to this Cl_2 transition. Finally the bands at 306 and 427 nm are assigned to the dipole-allowed PCl_3^+ $\tilde{D}$ $^2A_1$ - $\tilde{X}$ $^2A_1$ and $\tilde{C}$ ^2E - $\tilde{X}$ $^2A_1$ transitions respectively.

The spectrum taken at 17.28 eV shows all the bands observed in the previous spectrum. The intensity of the parent ion bands has significantly diminished, whereas the Cl_2 D' 2 $^3\Pi_g$ – A' 2 $^3\Pi_u$ band has gained in relative intensity. This would suggest that the band in the fluorescence excitation spectrum at 15.10 eV is probably due to parent ion emission. The higher-energy band, with a peak at 17.28 eV, is mostly a result of emission coming from Cl_2*.

9.3 Conclusions

We have presented the dispersed and undispersed fluorescence spectra of PF_3 and PCl_3. These spectra have been compared to previous work and confirm previous assignments. We see a new emission in PF_3 assigned to the F $2s^22p^43p^1$ $^4P_{3/2}$ → $2s^22p^43s^1$ $^4P_{3/2}$ transition obtained with second-order radiation from the VUV excitation source. New bands are also seen in PCl_3 which have been assigned to parent ion emission emanating from the PCl_3^+ $\tilde{E}$ ^2E, $\tilde{D}$ $^2A_1$ and $\tilde{C}$ ^2E states.

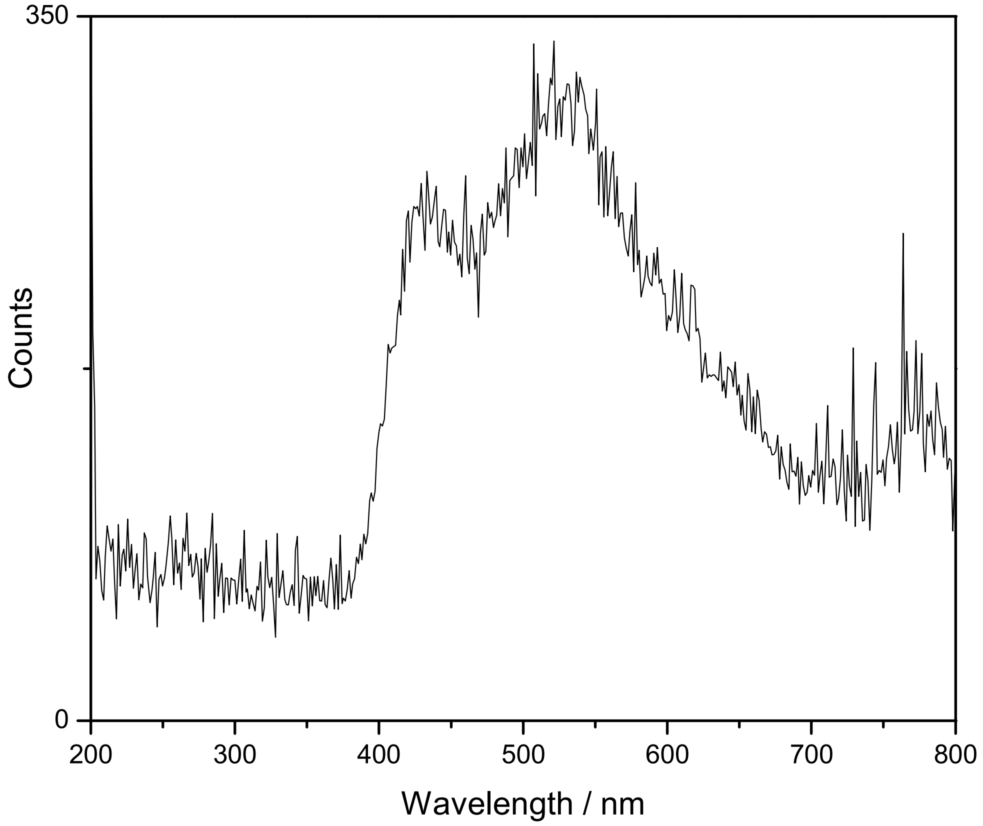

Figure 9.7: Dispersed fluorescence spectra of PCl_3 taken with a photoexcitation energy of 10.40 eV using the UV turret and 100 grooves mm^{-1} gratings. The slits on the secondary Triax monochromator were set at 1mm

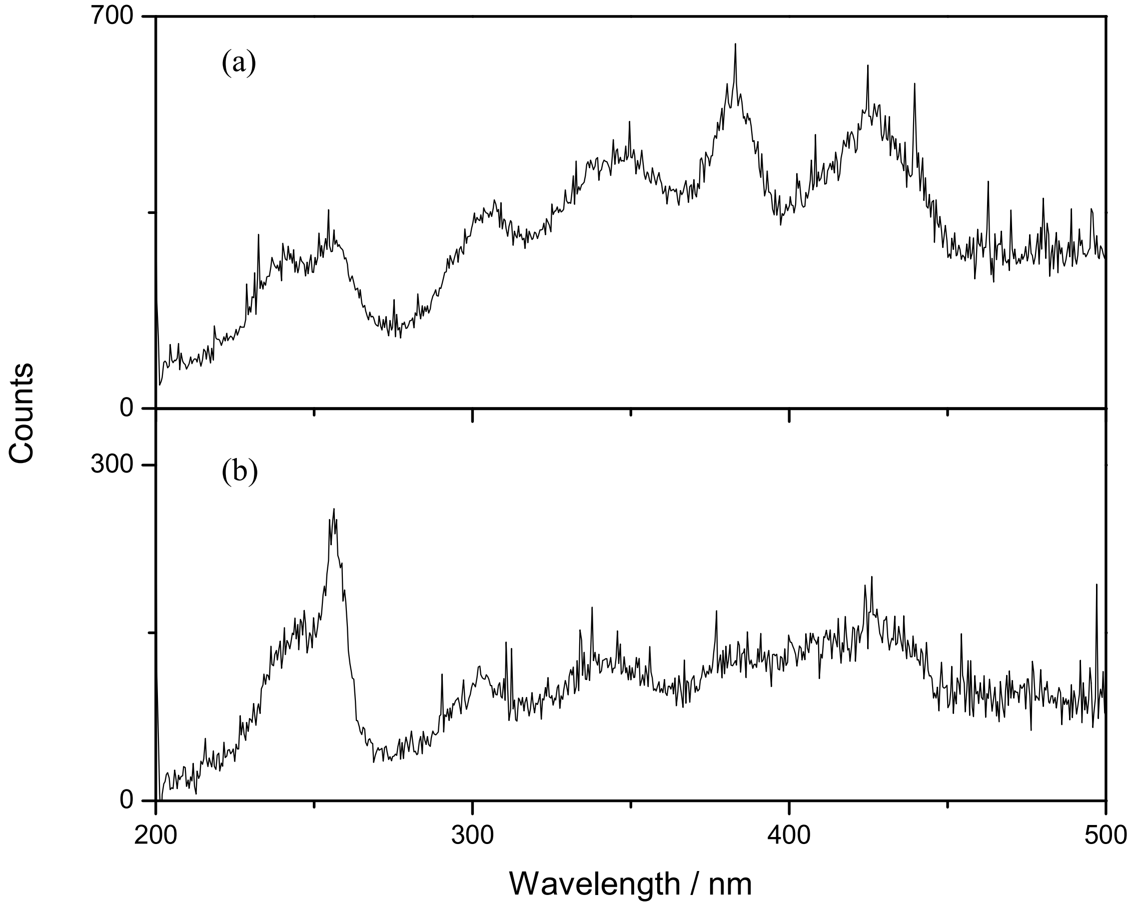

Figure 9.8: (a) Dispersed fluorescence spectra of PCl_3 taken with a photoexcitation energy of 15.10 eV (b) taken with a photoexcitation energy of 17.28 eV. Both spectra were taken using the UV turret and 100 grooves mm^{-1} grating. The slits on the secondary Triax monochromator were set at 1 mm.

9.4 References

[1] H Biehl, K J Boyle, D P Seccombe, R P Tuckett, H Baumgartel and H W Jochims, *J. Chem. Phys*. **3** (1998) 108

[2] K J Boyle, G K Jarvis, R P Tuckett, H Baumgartel and H W Jochims, *J. Chem. Soc. Faraday Trans.* **94** (1998) 2073

[3] C E Humphries, A D Walsh and P A Warsop, *Faraday Discuss. Chem. Soc*, **35** (1963), 148

[4] M J Mcadams and B R Russell, *Chem. Phys. Lett*, **18,** (1973), 402

[5] J W Au, G Cooper and C E Brion, *Chem. Phys*, **215**, (1997), 397

[6] Y Zhao and D W Setser, *Chem. Phys. Lett*, **210**, (1993), 362

[7] R D Johnson and K K Irikura, *Chem. Phys. Lett*, **228**, (1994), 273

[8] L Latifzadeh and K Balasubramanian, *Chem. Phys. Lett*, **228**, (1994), 463

[9] N Basco and K K Lee, *J Chem. Soc. Chem. Comm*, (1997) 1146

[10] J A Coxon and M A Wickramaaratchi, *J. Mol. Spectros*, **68** (1977) 372

[11] E P F Lee, D C Wang and F T Chau, *J. Phys. Chem*, **100**, (1996) 19795

[12] A E Douglas and M Frackowiak, *Can. J. Phys*., **40**, (1962) 832

[13] L Latifzadeh and K Balasubramanian, *Chem. Phys. Lett*, **243**, (1995), 243

[15] L Latifzadeh and K Balasubramanian, *Chem. Phys. Lett*, **241**, (1995), 13

[16] M T Nguyen, *Mol. Phys*, **59** (1986) 547

[17] J P Maier and D W Turner, *J. Chem. Soc. Faraday Trans* 2, **68** (1972) 711

[18] D J Reynolds, E H Van Kreef and I Powis, *J Chem. Phys*, **95** (1991) 8895

[19] M J Bramwell, S E Jaeger and J C Whitehead, *Chem. Phys. Lett*, **196**, (1992) 547

[20] M J Bramwell, C Hughes, S E Jaeger and J C Whitehead, *Chem. Phys*. **183**, (1994) 127

[21] J L Brum and J W Hudgens, *J. Phys. Chem*, **98** (1994) 5587

[22] A Papakondylis, A Mavridis and A Metropoulos, *J. Phys. Chem*, **99** (1995) 10759

[23] P A Cox, S Evans, A F Orchard, N V Richardson and P J Roberts, *J Chem. Soc. Faraday. Discuss*, **44** (1972) 26

[24] K J Boyle, G K Jarvis and R P Tuckett, *J Chem. Soc. Faraday Trans*, **94** (1998) 1045

[25] R P Tuckett and P J Knowles, *Chem. Phys. Lett*, **261** (1996) 486

[26] http://webbook.nist.gov/chemistry/

10. Conclusions

In this thesis we have presented the VUV spectroscopy of a series of small halogenated polyatomic molecules. The newly commissioned beamline 3.1 of the Daresbury SRS was used to take the majority of the fluorescence spectra. Photoabsorption spectra recorded in the last year of the operation of BESSY 1 have been analysed and presented. Spectra collected using a new dispersed fluorescence spectrometer, using a CCD detection system, were compared to similar spectra taken using a different dispersed spectrometer at the BESSY 1 synchrotron source.

The first series of molecules presented were CCl_4, $SiCl_4$ and $GeCl_4$. Analysis of the photoabsorption spectra resulted in assignments of the absorption peaks to transitions that mainly produced a Rydberg state. Fluorescence spectra confirmed the assignments of the earlier BESSY 1 work with a favourable comparison of the signal/noise ratio. New emission assigned to the $SiCl_2/GeCl_2$ $\tilde{a}\,^3B_1$ - $\tilde{X}\,^1A_1$ transitions were also observed.

The second set of molecules presented were the CF_3X series (X=H,F,Cl,Br,I). The peaks in the photoabsorption spectra were mainly assigned to Rydberg transitions. Fluorescence spectra confirmed earlier studies and were found to be manly due to CF_3, CF_2 and CF emission. Parent ion CF_4^+ and CF_3H^+ emission were also observed. Observed emissions were also tentatively assigned to the CFCl, CFBr and CFI fragments. New bands due to CF_3H^+ emission have been recorded. The fluorescence spectra of the CF_3I molecule are presented here for the first time. The first fluorescence study of the SF_5CF_3 molecule, which can be thought of as part of the CF_3X series is also shown. The fluorescence spectra provided some evidence that the structural parts (SF_5 and CF_3) of this molecule behave independently. Fluorescence emission bands were due mainly to CF_3 and CF_2 fragments.

The fluorescence spectra of the BF_3, BCl_3 and BBr_3 series were recorded. Emission has been observed from BF_2 and parent ion BF_3^+. Dispersed spectra taken at a photoexcitation energy of 14.10 eV showed two vibrational progressions with line spacing of 520 and 526 cm^{-1}. New emission bands were seen in the BCl_3 spectra assigned to both BCl_2 and parent ion BCl_3^+. BCl_2^+ emission seen in one of our earlier studies but unverified by several other studies have been confirmed here. Bands have also been observed for the first time and assigned to transitions between different states of BBr_2 and BBr_3^+.

The final chapter shows the fluorescence spectra of PF_3 and PCl_3 which have been compared to previous work and confirm previous assignments. New emission in PF_3 assigned to the F $2s^22p^43p^1\ ^4P_{3/2} \rightarrow 2s^22p^43s^1\ ^4P_{3/2}$ transition obtained with second-order radiation from the VUV excitation source have been observed. New bands are also seen in PCl_3 which have been assigned to parent ion emission emanating from the PCl_3^+ $\tilde{E}\ ^2E$, $\tilde{D}\ ^2A_1$ and $\tilde{C}\ ^2E$ states.

The new dispersed fluorescence spectrometer with CCD detection has provided spectra which are at least as good as previous spectra taken using PMT detection with the added advantage of a much shorter detection time. In practice maximum integration time per single scan is *ca.* 40 minutes. Even with two accumulations and the cosmic ray removal tool applied scans with longer integration times often resulted in the appearance of larger quantities of cosmic rays that obscured the acquired data. Even with this disadvantage the system is superior and can be still used to study fluorescing electronic states which produce weak fluorescence signals. Future systems of study could include the CCl_3X series (X=H, F, Br), and a repeat of the CF_3I spectra.